

Report Documentation Page

Form Approved
OMB No. 0704-0188

Public reporting burden for the collection of information is estimated to average 1 hour per response, including the time for reviewing instructions, searching existing data sources, gathering and maintaining the data needed, and completing and reviewing the collection of information. Send comments regarding this burden estimate or any other aspect of this collection of information, including suggestions for reducing this burden, to Washington Headquarters Services, Directorate for Information Operations and Reports, 1215 Jefferson Davis Highway, Suite 1204, Arlington VA 22202-4302. Respondents should be aware that notwithstanding any other provision of law, no person shall be subject to a penalty for failing to comply with a collection of information if it does not display a currently valid OMB control number.

1. REPORT DATE 25 FEB 2001		2. REPORT TYPE FINAL REPORT		3. DATES COVERED 06-01-2008 to 11-03-2010	
4. TITLE AND SUBTITLE MODELING COMPLEX DYNAMIC INTERACTIONS OF NONLINEAR, AEROELASTIC, MULTISTAGE, AND LOCALIZATION PHENOMENA IN TURBINE ENGINES				5a. CONTRACT NUMBER FA9550-08-1-0276	
				5b. GRANT NUMBER	
				5c. PROGRAM ELEMENT NUMBER	
6. AUTHOR(S) BODGAN EPUREANU; MATTHEW CASTANIER				5d. PROJECT NUMBER	
				5e. TASK NUMBER	
				5f. WORK UNIT NUMBER	
7. PERFORMING ORGANIZATION NAME(S) AND ADDRESS(ES) UNIVERSITY OF MICHIGAN,DEPARTMENT OF MECHANICAL ENGINEERING,2350 HAYWARD STREET,ANN ARBOR,MI,48109-2125				8. PERFORMING ORGANIZATION REPORT NUMBER ; AFRL-OSR-VA-TR-11-037	
9. SPONSORING/MONITORING AGENCY NAME(S) AND ADDRESS(ES)				10. SPONSOR/MONITOR'S ACRONYM(S)	
				11. SPONSOR/MONITOR'S REPORT NUMBER(S) AFRL-OSR-VA-TR-11-037	
12. DISTRIBUTION/AVAILABILITY STATEMENT Approved for public release; distribution unlimited					
13. SUPPLEMENTARY NOTES					
14. ABSTRACT Goals: To model and predict the nonlinear vibration response of a rotor with a cracked blade; account for multistage and aeroelastic coupling; (2) to provide a fundamental physical understanding of localization in rotors due to combined effects of cracks and mistuning; (3) To identify localization and nonlinear vibration characteristics associated with cracks so they can be used for detection and prognosis; (4) to develop a new aerolastic model capable of efficiently and accurately predicting aerodynamic loads on multistage mistuned bladed disks with nonlinear structural behavior. Impact: Provide cutting edge, new capabilities for accurately predicting the dynamics of a large class of cracked, aeroelastic systems and enabled fracture propagation and fatigue life predictions; (2) directly support established and emerging practices in damage assessment of aerospace vehicles to enable critical maintenance and repair decisions, thus increasing asset readiness; (3) provide fundamental physical insight for the development of advanced design and monitoring technology for systems with FSI.					
15. SUBJECT TERMS					
16. SECURITY CLASSIFICATION OF:			17. LIMITATION OF ABSTRACT Same as Report (SAR)	18. NUMBER OF PAGES 187	19a. NAME OF RESPONSIBLE PERSON
a. REPORT unclassified	b. ABSTRACT unclassified	c. THIS PAGE unclassified			

CONTENTS

1	INTRODUCTION	4
2	ACTIVITIES	6
2.1	Fluid-Structural Coupling Effects on the Dynamics of Mistuned Bladed Disks	6
2.2	Convergence Predictions for Aeroelastic Calculations of Tuned and Mistuned Bladed Disks	6
2.3	Estimation and Veering Analysis of Nonlinear Resonant Frequencies of Cracked Plates	7
2.4	An Efficient Reduced Order Modeling Technique for Nonlinear Vibration Analysis of Structures with Intermittent Contact	7
2.5	Node Sampling for Nonlinear Vibration Analysis of Structures with Intermittent Contact	7
2.6	Bilinear Modal Representations for Reduced-Order Modeling of Localized Piecewise-linear Oscillators	8
2.7	Reduced-Order-Modeling for Nonlinear Analysis of Cracked Mistuned Multi-Stage Bladed Disk Systems	8
2.8	A Statistical Characterization of the Effects of Mistuning in Multi-Stage Bladed Disks	9
2.9	Reduced-Order Models of Mistuned Cracked Bladed Disks	9
2.10	Detection of Cracks in Mistuned Bladed Disks using Reduced Order Models and Vibration Data	10
2.11	Reduced Order Models for Blade-to-Blade Damping Variability in Mistuned Blisks	10
3	FINDINGS	11
3.1	Fluid-Structural Coupling Effects on the Dynamics of Mistuned Bladed Disks	11
3.2	Convergence Predictions for Aeroelastic Calculations of Tuned and Mistuned Bladed Disks	11
3.3	Estimation and Veering Analysis of Nonlinear Resonant Frequencies of Cracked Plates	12
3.4	An Efficient Reduced Order Modeling Technique for Nonlinear Vibration Analysis of Structures with Intermittent Contact	12
3.5	Node Sampling for Nonlinear Vibration Analysis of Structures with Intermittent Contact	13

3.6	Bilinear Modal Representations for Reduced-Order Modeling of Localized Piecewise-linear Oscillators	14
3.7	Reduced-Order-Modeling for Nonlinear Analysis of Cracked Mistuned Multi-Stage Bladed Disk Systems	15
3.8	A Statistical Characterization of the Effects of Mistuning in Multi-Stage Bladed Disks	15
3.9	Reduced-Order Models of Mistuned Cracked Bladed Disks	16
3.10	Detection of Cracks in Mistuned Bladed Disks using Reduced Order Models and Vibration Data	17
3.11	Reduced Order Models for Blade-to-Blade Damping Variability in Mistuned Blisks	18
4	BENEFITS AND IMPACT	19
4.1	Cumulative List of People Involved in the Research	19
4.2	Cumulative List of Journal Publications Resulting from the Research	20
	REFERENCES	21

APPENDICES

5	FLUID-STRUCTURAL COUPLING EFFECTS ON THE DYNAMICS OF MISTUNED BLADED DISKS	36
5.1	Structural Reduced Order Model	39
5.2	Frequency Domain Unsteady Aerodynamic Model	40
5.3	Fluid-Structure Coupling Models	42
5.4	Case Study	47
6	CONVERGENCE PREDICTIONS FOR AEROELASTIC CALCULATIONS OF TUNED AND MISTUNED BLADED DISKS	55
6.1	Aeroelastic Model	57
6.2	Hybrid Technique: General Case	60
6.3	Hybrid Technique: Tuned Case	65
6.4	Results and Discussion	67
7	ESTIMATION AND VEERING ANALYSIS OF NONLINEAR RESONANT FREQUENCIES OF CRACKED PLATES	77
7.1	Cracked Plate Model	80
7.2	Linear Free Response Analysis	81
7.3	Nonlinear Forced Response Analysis	84
7.4	Bilinear Frequency Approximation	87
8	AN EFFICIENT REDUCED ORDER MODELING TECHNIQUE FOR NON-LINEAR VIBRATION ANALYSIS OF STRUCTURES WITH INTERMITTENT CONTACT	95
8.1	Background	96
8.2	Mathematical Formulation	100
8.3	Case study	107
9	NODE SAMPLING FOR NONLINEAR VIBRATION ANALYSIS OF STRUCTURES WITH INTERMITTENT CONTACT	113
9.1	Background	114
9.2	Mathematical Formulation	117
9.3	Case studies	125

10	BILINEAR MODAL REPRESENTATIONS FOR REDUCED-ORDER MODELING OF LOCALIZED PIECEWISE-LINEAR OSCILLATORS	134
10.1	Mathematical formulation: Piecewise linear structures in a mapped subspace	137
10.2	Proper orthogonal decomposition	139
10.3	Bilinear modal representation of the proper orthogonal modes	143
10.4	Case studies	146
11	REDUCED-ORDER-MODELING FOR NONLINEAR ANALYSIS OF CRACKED MISTUNED MULTI-STAGE BLADED DISK SYSTEMS	153
11.1	Background	154
11.2	Mathematical Formulation	156
11.3	Analysis	164
12	A STATISTICAL CHARACTERIZATION OF THE EFFECTS OF MISTUNING IN MULTI-STAGE BLADED DISKS	171
12.1	Methodology	173
12.2	Analysis	177

1 INTRODUCTION

The Air Force places high demands on operational capabilities of their aircraft that require increased performance and reliability. Among the most critical systems for the Air Force fleet are the turbine engines, especially considering that a fighter jet relies on a single engine that must meet high thrust-to-weight and durability targets for a large range of operating conditions. Current and next-generation turbine engines will increasingly depend on onboard health monitoring and prognosis systems to help ensure the reliability, safety, and readiness of air vehicles. In order to effectively interpret the measurement data required for monitoring and prognosis of turbine engines, efficient models that capture the essential complex dynamic interactions of nonlinear, aeroelastic, multistage, and localization phenomena must be employed. In this research, advanced structural dynamic and aeroelastic modeling techniques have been developed for turbine engine rotors, which will directly support the emerging structural health monitoring and system prognosis needs of Air Force engines and aircraft.

In contrast to this research, previous approaches often consider that bladed disks are isolated from their neighboring stages for structural dynamic analyses, i.e. that they are in vacuo, isolated from other stages, and free of cracks and other damage. In reality, a bladed disk in a gas turbine engine is one stage of a multistage rotor. The bladed disk is also subject to the effects of the fluid, which provides aerodynamic excitation, damping, and interblade coupling. Furthermore, the blades can suffer both foreign object damage and high cycle fatigue. In particular, a crack can form in one or more blades, introducing geometric changes and nonlinearities in the system that can qualitatively change the dynamics of the blade, the bladed disk, and the full multistage rotor.

The PIs and their collaborators have developed efficient vibration modeling and simulation capabilities for realistic turbine engine rotors that account for each of the following complexities: aeroelastic coupling, multistage coupling, and nonlinearities due to cracks. It has been shown that capturing these aspects of the system are critical to predicting the forced response, including the localization of the response about certain blades. It is well known that small, random blade-to-blade differences, called mistuning, can lead to localization. However, there are many other factors that can cause or influence localization phenomena such as cracks or multi-stage analysis. Vibration response that is coupled strongly across multiple stages has also been observed for other operating conditions. Furthermore, it has been shown that both structural and aerodynamic coupling between blades can have a strong influence on vibration localization and forced response levels.

Together, the nonlinear, multistage, and aeroelastic methods developed by the PIs comprise a critical collection of unique, advanced modeling techniques for turbine engine rotors. Therefore, it is strongly believed that combining these novel capabilities provides an unprecedented opportunity to develop substantially new predictive technologies that will have important applications to design and online structural health monitoring and system prognosis of turbine engines. Online monitoring is generally preferred to offline monitoring in most applications. However, technical difficulties faced by current methods and problems associated with accurately modeling operating conditions have limited the available techniques to mostly offline detection of large damage. Nevertheless, the use of on-board reasoners is an important feature of future air vehicles. These vehicles mandate a drastic reduction in

maintenance and turn-around time between missions to increase their responsiveness and operational capabilities. The research performed provides the necessary fundamental basis for the development of advanced online health monitoring where nonlinear and fluid-structural interactions are crucial. In contrast, existing methods focus on structures and have difficulty tackling the complexities found in fluid-structural systems.

A class of techniques used for damage detection are based on vibratory responses. Most such methods monitor changes in the frequencies and modes of vibration. Other current techniques use subspace identification and updating, wavelet analyses, evolutionary algorithms, Ritz or stochastic methods, and others. These techniques are designed for linear vibrations while far fewer apply to nonlinear systems. Some nonlinear methods are based on system identification, while others use neural networks, phase space reconstruction, or Lyapunov exponents. These nonlinear methods have important limitations, e.g. some have difficulty tackling high-dimensional systems, others do not predict the damage location or level, or do not detect simultaneous damages. The results of the PIs show that the use of nonlinear and localization phenomena for detecting damage holds great potential, especially for turbine engine rotors.

In early work, simplified models with only several degrees of freedom (DOF) were used to study the dynamics of mistuned bladed disks. While such simplified models (like lumped parameter models) are convenient for investigating the effects of major system parameters (mistuning, structural coupling), they are not adequate to study real/practical bladed disks. Instead, models based on the finite element method (FEM) are typically used to represent the actual bladed disks accurately. However, for a mistuned disk with a specific mistuning pattern, FEM requires a model for the whole bladed disks, which usually has millions of DOF. Thus, when multiple mistuning patterns are of interest, e.g., in the case of Monte Carlo simulations and parametric studies (e.g. during design stages), FEM becomes computationally formidable as every mistuning pattern requires a separate (full) analysis. Hence, accurate and efficient reduced-order models (ROMs) have been developed, including ROMs based on the subset of nominal modes (SNM) method and the component mode mistuning (CMM) method that use tuned system modes as a modal basis (which allows a more easy computation of the aerodynamic forces).

Previous work has shown that interblade structural coupling is a critical factor affecting the dynamics of mistuned bladed disks. In operating conditions, bladed disks are always interacting with flows, and hence, bladed disks exhibit both structural and aerodynamic coupling. Thus, aeroelastic calculations are necessary for accurate predictions. Although compact and accurate structural reduced-order models have been developed, only a few studies of the dynamics of mistuned bladed disks have been conducted with considerations of aerodynamic forces. Flow models have been developed to calculate the unsteady pressure on the blades by (usually) assuming linearity of the unsteady pressure with respect to the displacements of the blades. In addition, a model reduction of the unsteady aerodynamics can be employed. Although 2-D and 3-D computational fluid dynamics models for passage flows have been developed recently, most mistuning analyses utilizing ROMs are purely structural. However, the aerodynamic forces acting on the blades provide additional interblade coupling, which is critical for predicting the forced response of mistuned bladed disks, especially when the structural damping is relatively small and comparable with the aerodynamic damping.

In the following, a review of the research conducted (activities, findings and impact) which addresses the challenges outlined above through an integrated and comprehensive modeling effort for predicting the complex dynamic interactions of nonlinear, aeroelastic, multistage, and localization phenomena in turbine engines, is provided.

2 ACTIVITIES

2.1 *Fluid-Structural Coupling Effects on the Dynamics of Mistuned Bladed Disks*

Mistuning changes the vibration of bladed disks dramatically. Various aeroelastic models have been used to investigate the free vibration and forced response problems of mistuned bladed disks. Most of these models used simplified structural and/or aerodynamic models. The traditional way to incorporate the aerodynamic coupling in the high fidelity structural models is to use the cantilever-blade normal modes to calculate the unsteady aerodynamic forces. In this work, a new reduced order modeling approach is developed by using the tuned system modes to calculate the unsteady aerodynamic forces directly. This new approach is applied to an industrial rotor. The results show that aerodynamic coupling has significant effects on the vibration of bladed disks for the case studied. Also, constraint modes are needed to yield accurate results if cantilever-blade normal modes are used to calculate the unsteady aerodynamic forces. However, using the tuned system modes to calculate the unsteady aerodynamic forces saves a significant amount of computation time compared to the method using both cantilever-blade normal modes and constraint modes.

2.2 *Convergence Predictions for Aeroelastic Calculations of Tuned and Mistuned Bladed Disks*

Mistuning changes the dynamics of bladed disks significantly. Frequency domain methods for predicting the dynamics of mistuned bladed disks are typically based on iterative aeroelastic calculations. Converged aerodynamic stiffness matrices are required for accurate aeroelastic results of eigenvalue and forced response problems. The tremendous computation time needed for each aerodynamic iteration would greatly benefit from a fast method of predicting the number of iterations needed for converged results. A new hybrid technique is proposed to predict the convergence history based on several critical ratios and by approximating as linear the relation between the aerodynamic force and the complex frequencies (eigenvalues) of the system. The new technique is hybrid in that it uses a combined theoretical and stochastic/computational approach. The dynamics of an industrial bladed disk is investigated, and the predicted convergence histories are shown to match the actual results very well. Monte Carlo simulations using the new hybrid technique show that the aerodynamic ratio and the aerodynamic gradient ratio are the two most important factors affecting the convergence history.

2.3 Estimation and Veering Analysis of Nonlinear Resonant Frequencies of Cracked Plates

In this work, veering phenomena in the nonlinear vibration frequencies of a cantilevered cracked plate are investigated, and an efficient method for estimating these frequencies is proposed. Of particular interest is the vibration response in parameter regions where the natural frequency loci show veerings. For a representative finite element model, it is shown that the veerings due to crack length variation involve the switching of mode shapes and modal interactions. The nonlinearity caused by the crack closing effect is then introduced, and its effect on the vibration response near the veerings is discussed. The nonlinear forced response analysis is carried out using a hybrid frequency/time domain method, which is based on the method of harmonic balance. The nonlinear vibration response near loci veerings and crossings due to the variation of crack length is investigated in detail. Finally, a novel method for estimating the nonlinear resonant frequency is introduced by generalizing the concept of bilinear frequency approximation, and the method is validated with the results of nonlinear forced response analysis for several veering regions.

2.4 An Efficient Reduced Order Modeling Technique for Nonlinear Vibration Analysis of Structures with Intermittent Contact

In this work, a reduced order modeling framework for nonlinear vibration problems of elastic structures involving intermittent contact is proposed. Of particular interest is a vibration problem of plate-like elastic structures with a crack with a large number of degrees of freedom involved on the crack surfaces. Due to the localized nature of such nonlinearity, the number of degrees of freedom on the surfaces greatly affects the computational time of the analysis. Therefore, reducing the number of degrees of freedom on the crack surfaces without significantly sacrificing the accuracy of the results is a critical issue for conducting vibration analysis of such structures in a reasonable amount of time. The focus is placed on the development of an efficient algorithm to select a set of nodes on the crack surfaces, where nonlinear boundary conditions are imposed. The method is developed based on a procedure for selecting master degrees of freedom for Guyan reduction. The accuracy, efficiency, and optimality of the method are discussed in detail and compared with those aspects of previous methods. The advantages of the new method are demonstrated in terms of the accuracy of the frequency response and the resonant frequencies.

2.5 Node Sampling for Nonlinear Vibration Analysis of Structures with Intermittent Contact

In this work, a node sampling methodology for nonlinear vibration problems of elastic structures involving intermittent contact is proposed. Of particular interest is a vibration problem of plate-like elastic structures with a crack with a large number of degrees of freedom involved on the crack surfaces. Due to the localized nature of such nonlinearity, the number of degrees of freedom on the surfaces greatly affects the computational time of the analysis. Therefore, reducing the number of degrees of freedom on the crack surfaces without significantly sacri-

ficing the accuracy of the results is a critical issue for conducting vibration analysis of such structures in a reasonable amount of time. The focus is placed on the development of an efficient algorithm to select a set of nodes on the crack surfaces, where nonlinear boundary conditions are imposed. The method is developed based on a procedure for selecting master degrees of freedom for Guyan reduction. The accuracy, efficiency, and optimality of the method are discussed in detail and compared with those aspects of previous methods. The advantages of the new method are demonstrated in terms of the accuracy of the frequency response and the resonant frequencies.

2.6 Bilinear Modal Representations for Reduced-Order Modeling of Localized Piecewise-linear Oscillators

A novel reduced-order modeling method for vibration problems of elastic structures with localized piecewise-linearity is proposed. The focus is placed upon solving nonlinear forced response problems of elastic media with contact nonlinearity, such as cracked structures and delaminated plates. The modeling framework is based on observations of the proper orthogonal modes computed from nonlinear forced responses and their approximation by a truncated set of linear normal modes with special boundary conditions. First, it is shown that a set of proper orthogonal modes can form a good basis for constructing a reduced order model that can well capture the nonlinear normal modes. Next, it is shown that the subspace spanned by the set of dominant proper orthogonal modes can be well approximated by a slightly larger set of linear normal modes with special boundary conditions. These linear modes are referred to as bi-linear modes, and are selected by an elaborate methodology which utilizes certain similarities between the bi-linear modes and approximations for the dominant proper orthogonal modes. These approximations are obtained using interpolated proper orthogonal modes of smaller dimensional models. The proposed method is compared with traditional reduced order modeling methods such as component mode synthesis, and its advantages are discussed. Forced response analyses of cracked structures and delaminated plates are provided for demonstrating the accuracy and efficiency of the proposed methodology.

2.7 Reduced-Order-Modeling for Nonlinear Analysis of Cracked Mistuned Multi-Stage Bladed Disk Systems

In this work, a novel modeling methodology for the nonlinear vibration analysis of multi-stage bladed disk systems with small blade-to-blade mistuning and a cracked blade is proposed. The modeling strategy is based on an efficient stage-wise reduced order modeling method based on cyclic-symmetry analysis and component mode synthesis. Reduced order models are constructed for individual stages and assembled by projecting the motion of the interface of the neighboring stages onto a set of harmonic shape functions. The analysis procedure allows the stages to have different numbers of blades and mismatched computational grids on the interfaces of the neighboring stages. Furthermore, the modeling framework is independent of the modeling method for each stage, which enables the use of various existing modeling methods of single stages. Moreover, nonlinearity can also be included in the multi-stage computations, as long as the nonlinearity can be modeled for a single stage. To demonstrate

the capability of the modeling procedure, the nonlinear effect of crack opening and closing is considered, in conjunction with the effects of small mistuning. The accuracy and efficiency of the proposed methods are discussed.

2.8 A Statistical Characterization of the Effects of Mistuning in Multi-Stage Bladed Disks

A great deal of research has been conducted on the effects of small random variations in structural properties, known as mistuning, in single stage bladed disks. Due to the inherent randomness of mistuning and the large dimensionality of the models of industrial bladed disks, a reduced order modeling approach is required to understand the effects of mistuning on a particular bladed disk design. Component mode mistuning (CMM) is an efficient compact reduced order modeling method that was developed to handle this challenge in single stage bladed disks. In general, there are multiple stages in bladed disk assemblies, and it has been demonstrated that for certain frequency ranges accurate modeling of the entire bladed disk assembly is required because multi-stage modes exist. In this work, a statistical characterization of structural mistuning in multi-stage bladed disks is carried out. The results were obtained using CMM combined with a multi-stage modeling approach previously developed. In addition to the statistical characterization, a new efficient classification method is detailed for characterizing the properties of a mode. Also, the effects of structural mistuning on the characterization of the mode is explored.

2.9 Reduced-Order Models of Mistuned Cracked Bladed Disks

Predicting the influence of cracks on the dynamics of bladed disks is a very important challenge. Cracks change the structural response, which in turn changes the crack propagation characteristics. Hence, accurate and computationally effective means to model the dynamics of cracked bladed disks and blisks is particularly crucial in applications such as prognosis, guidance for repairs, characterization after repairs, design, and structural health monitoring. Most current models of bladed disks exploit cyclic symmetry to gain computational efficiency. However, the presence of cracks and mistuning destroys that symmetry and makes computational predictions much more expensive. In this work, we develop a new reduced order modeling methodology which can speed up computations by several orders of magnitude. There are two key components of the new methodology. First, the displacements and deformations of the crack surfaces are not modeled in absolute coordinates but relative coordinates. That allows for an effective model reduction based on (fixed-interface Craig-Bampton) component mode synthesis (CMS). The use of relative coordinates allows one to define one of the components in CMS as the pristine/uncracked structure (with mistuning). This approach is used in combination with a set of accurate approximations for the constraint modes used in CMS. Second, the effects of mistuning are captured by component mode mistuning (CMM) which allows the construction of extremely efficient reduced order models for the pristine/uncracked component with mistuning. The novel method is applied to a finite element model of an industrial blisk. The combined presence of mistuning and cracks is shown to have important effects. Also, the proposed approach is shown to provide accurate predictions for the overall blisk while requiring computations using single-sector

models only. The influence of various parameters on the accuracy of the reduced order models is investigated. Overall, the results show a very good agreement between full finite element analyses and the proposed reduced order modeling approach.

2.10 Detection of Cracks in Mistuned Bladed Disks using Reduced Order Models and Vibration Data

In this work, a novel methodology to detect the presence of a crack and to predict the nonlinear forced response of mistuned turbine engine rotors with a cracked blade and mistuning is developed. The combined effects of the crack and mistuning are modeled. First, a hybrid-interface method based on component mode synthesis is employed to develop reduced order models (ROMs) of the tuned system with a cracked blade. Constraint modes are added to model the displacements due to the intermittent contact between the crack surfaces. The degrees of freedom (DOFs) on the crack surfaces are retained as active DOFs so that the physical forces due to the contact/interaction (in the three-dimensional space) can be accurately modeled. Next, the presence of mistuning in the tuned system with a cracked blade is modeled. Component mode mistuning is used to account for mistuning present in the un-cracked blades while the cracked blade is considered as a reference (with no mistuning). Next, the resulting (reduced-order) nonlinear equations of motion are solved by applying an alternating frequency/time-domain method. Using these efficient ROMs in a forced response analysis, it is found that the new modeling approach provides significant computational cost savings, while ensuring good accuracy relative to full-order finite element analyses. Furthermore, the effects of the cracked blade on the mistuned system are investigated, and used to detect statistically the presence of a crack and to identify which blade of a full bladed disk is cracked. In particular, it is shown that cracks can be distinguished from mistuning.

2.11 Reduced Order Models for Blade-to-Blade Damping Variability in Mistuned Blisks

In this work, a novel reduced order modeling methodology to capture blade-to-blade variability in damping in blisks is developed. This new approach generalizes the concept of component mode mistuning (CMM) which was developed to capture stiffness and mass mistuning (and did not include variability in damping amongst the blades). This work focuses on modeling large variability in damping. Such variability is significant in many applications, and particularly important for modeling damping coatings. The damping in each of the blades is assumed to be structural at the blade level. However, variability in the damping coefficients of the blades means that the damping is not structural at the system (entire blisk) level. Similar to the CMM based studies, structural damping is used to capture the damping effects due to the mechanical energy dissipation caused by internal friction within the blade material. The steady state harmonic responses of the blades are obtained using the novel reduced order modeling methodology, and are validated by comparison with simulation results obtained using a full order model in ANSYS. The effects of damping mistuning are studied statistically through Monte-Carlo simulations. For this purpose, the blisk model is subjected to multiple traveling wave excitations. The uncertainty in the various mechanisms responsible for dissipation of energy and the uncontrollability of these dissipation mechanisms makes

it difficult to assign a reliable value for the loss factor of each blade. Hence, large variations (up to $\pm 80\%$) in the structural damping coefficients of the blades are simulated.

3 FINDINGS

3.1 *Fluid-Structural Coupling Effects on the Dynamics of Mistuned Bladed Disks*

In this study, the effects of aerodynamic coupling on the vibration response of bladed disks were investigated. An iterative method using the tuned system modes to calculate the aerodynamic coupling was developed. The results were compared with structure-only results and the results using the blade-alone normal modes. A bladed disk and aeroelastic configuration which exhibits relatively strong aerodynamic coupling was found in the case study herein. Also, the aerodynamic stiffness forces are strongly sensitive to interblade phase angle for the bladed disk studied.

For the case studied, it was shown that aeroelastic coupling may change the tuned and mistuned forced responses. Also, the statistical 95 percentile response levels are affected significantly by aerodynamic forces. Furthermore, the mistuned mode shapes change when aeroelastic coupling is introduced.

Mistuned mode crossing patterns are different for the results using the blade and system mode methods for the cases studied. Also, the one-step and converged aeroelastic coupling using the system mode methods yield similar results for the cases studied. However, when aeroelastic eigenvalues and mode shapes are of critical interest, multiple iterations and converged results should be used.

The constraint modes are necessary for obtaining accurate results when using the blade mode method for the case studied. However, the large number of constraint modes makes the computation time much larger than that of using the system mode method. Detailed results are presented in Section 5.

3.2 *Convergence Predictions for Aeroelastic Calculations of Tuned and Mistuned Bladed Disks*

A hybrid technique has been proposed to predict the convergence error of the aeroelastic calculation for mistuned bladed disks. The dependence of the aerodynamic forces on vibration frequencies has been approximated linearly by proposing an aero ratio based on two aerodynamic gradient matrices. Several other critical ratios have been defined to study their effects on the convergence error. Matrices randomly generated according to these critical ratios, as well as the exact matrices of an actual model, can be used in this hybrid technique. The hybrid technique has been validated using the exact matrices calculated for an actual industrial bladed disk. Monte Carlo simulations for general mistuned systems and tuned systems have been performed, and several conclusions have been obtained for the bladed disk

studied.

First, the aero ratio r_A and the gradient ratio r_G (details can be found in Section 6) have significant effects on the convergence error. For a system with both large r_A and r_G , an iterative calculation is likely to be unable to converge.

Second, the mistuned aeroelastic calculation is harder to converge than the corresponding tuned calculation. When the mistuning level is small, increases in the mistuning ratio r_M make the system harder to converge. While the mistuning level is large, the convergence error decreases slowly when r_M grows. In general, r_M has a moderate effect on the convergence error.

Third, a smaller veering ratio r_V or a smaller frequency ratio r_F makes the system harder to converge. However, the effect is relatively small. Finally, the structural damping γ has no significant effect on the convergence error. Detailed results are presented in Section 6.

3.3 Estimation and Veering Analysis of Nonlinear Resonant Frequencies of Cracked Plates

In this study, the linear and nonlinear vibration response of a cracked cantilevered rectangular plate have been investigated. In particular, the veering phenomena for the natural frequencies of the cracked plate were investigated. It was observed that veerings appear in plots of natural frequencies versus crack length or crack location ratio. It was shown that a wider veering region entails continuous interchanging between the modes, whereas a smaller veering (or crossing) region shows fast mode switching. Then, the nonlinear vibration response of the cracked plate due to contact of the crack surfaces was considered. A hybrid frequency/time-domain (HFT) method was applied to the calculation of nonlinear resonant frequencies in representative veering/crossing regions. It was shown that the characteristics of veerings/crossings are affected to some extent by the nonlinearity induced by the crack closing effect, although in general they are similar to those of the linear counterparts. Furthermore, an alternative method for estimating the nonlinear resonant frequencies was proposed by generalizing the bilinear frequency approximation. The results of the proposed method were validated with the resonant frequencies obtained by the nonlinear forced response analysis for three typical veering scenarios. Moreover, it was shown that the method works even for relatively large crack length ratio. Detailed results are presented in Section 7.

3.4 An Efficient Reduced Order Modeling Technique for Nonlinear Vibration Analysis of Structures with Intermittent Contact

In this study, a novel reduced order modeling framework for the nonlinear vibration analysis of elastic structures with intermittent contact was proposed. In Section 8.2, the modeling framework was developed based on a method of component mode synthesis. The master DOF selection scheme for Guyan reduction was formulated by considering the close relationship between the optimal master DOF selection and the optimal constraint locations for maximizing the fundamental frequency. The method is a combination of the sequential elimination method proposed by Henshell and Ong, and appropriate coordinate transformations to the

reduced order model. Another method for choosing the nodes was also introduced for the sake of comparative study, which is based on a method to optimally choose the measurement locations such that the measured mode becomes as linearly independent as possible. The method was then applied to a representative finite element model in Section 8.3. In Section 8.3.1, the methods were applied to a cracked plate model. Using the selected node patterns, forced response analysis was carried out to see the effects of the selection patterns on the frequency response. Furthermore the resonant frequencies were calculated by the application of bilinear frequency approximation. It was confirmed that the selected DOF resulted in accurate prediction of nonlinear resonant frequencies in comparison to the benchmark case of using all DOF on the crack surfaces. Moreover, a posteriori accuracy assessment procedure was introduced by examining the amount of penetration on the crack surfaces during a vibration cycle. For the methods examined, the node patterns selected using the proposed new method consistently showed the best results.

3.5 Node Sampling for Nonlinear Vibration Analysis of Structures with Intermittent Contact

In this study, a novel node sampling methodology for the nonlinear vibration analysis of elastic structures with intermittent contact was proposed. In Section 9.2, the modeling framework was developed based on component mode synthesis. The master DOF selection scheme for Guyan reduction was formulated by considering the close relationship between the optimal master DOF selection and the optimal constraint locations for maximizing the fundamental natural frequency. The method is a combination of the sequential elimination method proposed by Henshell and Ong and coordinate transformations to the reduced order model. Another method for choosing the nodes was also introduced for a comparative study. The alternate method is based on an approach to optimally choose measurement locations such that the truncated/measured modes become as linearly independent as possible. The method was then applied to a representative finite element model in Section 9.3. In Section 9.3.1, the methods were applied to a cracked plate model. Using the selected node patterns, forced response analysis was carried out to evaluate the effects of the selection patterns on the frequency response. Furthermore, the resonant frequencies were calculated by the application of bilinear frequency approximation. It was confirmed that the selected DOF resulted in accurate predictions of nonlinear resonant frequencies in comparison to the benchmark case of using all DOF on the crack surfaces. Furthermore, it was demonstrated that the method also achieves a significant reduction in CPU time for the nonlinear forced response calculations, without sacrificing the accuracy in the predicted forced response. Moreover, a method for a posteriori accuracy assessment was introduced by examining the amount of penetration on the crack surfaces during a vibration cycle. In Section 9.3.2, the method was also applied to a cracked blade model with a much larger number of DOF on the crack faces. The node selection patterns as well as the errors in the bilinear frequencies conform to the results in the example in Section 9.3.1. For the methods examined, the node patterns selected using the proposed new method consistently showed the best results.

Based on these results, the essential findings and contributions of this study can be summarized as follows.

- (1) It was shown mathematically that the selection of the nodes where the nonlinear boundary conditions should be applied for vibration problems with intermittent contact is closely related to the problem of maximizing the fundamental natural frequency of FE models by fixing some of the nodes.
- (2) The maximization problem can be (approximately) solved by the Henshell & Ong method in conjunction with the CMS method.
- (3) For simplified yet representative example models, the proposed method produced nodes that give accurate forced response predictions and nonlinear resonant frequencies when the nonlinear boundary conditions are applied on the selected nodes.
- (4) A posteriori accuracy assessment using numerical examples showed that the forced response analyses with the proposed method retain the largest impulse at the crack surfaces for the frequency ranges of interest

It should also be noted that the proposed method is independent of the geometry of the contact surfaces. That is because the selection procedure is solely dependent on the mass and stiffness of the structure. Therefore, for instance, even if there are distortions of the contact surfaces, the proposed method still works as long as the effects due to the distortions are reflected in the FE mass and stiffness matrices. In contrast, the limitation of the proposed approach is that the geometry of the contact surface has to be known a priori, and the domain of contact surfaces is assumed to remain unchanged during the vibration. That is, if the vibration problems of interest involve dynamic (fast) crack propagation, then the nodes selected by the proposed approach at some time instant might not necessarily be the optimal selection for the entire time duration of interest. However, this is not a problem if the contact problem of interest does not involve fast changes in the contact regions, such as the ones involving gap contact between mechanical components. In addition, local effects on the contact surfaces, such as variations in the grain size on the crack surfaces, were not considered in this study. These important issues are far beyond the scope of this study. However, the authors believe that the contributions of this study shall contribute to further expand the capabilities of model-based vibration analyses involving intermittent contact. Detailed results are presented in Section 9.

3.6 Bilinear Modal Representations for Reduced-Order Modeling of Localized Piecewise-linear Oscillators

A bi-linear modal representation of (localized) piecewise linear oscillators has been developed. First, the mathematical formulation for constructing reduced order models of piecewise linear oscillator with linear projection was developed in Section 10.1. Second, proper orthogonal decomposition of forced response results was examined using a vibration problem of a cracked plate, and a few key properties of the POMs were investigated (see Section 10.2). In particular, it was observed that the most dominant POM resembles the linear normal mode in the frequency range of interest, and the POMs can yield a compact ROM. More importantly, forced response analyses using the POMs revealed that capturing the local deformations near the discontinuous region is important for accurately predicting the nonlinear forced response. Several novel bi-linear modal representations of POMs were then proposed in Section 10.3 based on the observations on the POMs discussed in Section 10.2. Namely, it was shown that the most dominant POM can be well approximated by the corresponding

linear normal mode, and the POMs showing the local deformations can be represented by linear combinations of BLMs. To circumvent the difficulty in choosing the most adequate set of BLMs, BLM selection criteria using angle-based metrics have been proposed. In Section 10.4, the applicability of the proposed method including the BLM selection criteria, was investigated using case studies of a cracked plate and a delaminated plate. It was demonstrated that the proposed BLM representation successfully produces low-dimensional ROMs which accurately capture the vibration response of (localized) piecewise linear oscillators.

The proposed methods were applied to specific systems, such as the cracked plate and the delaminated plate. These systems exhibit complex behavior which was accurately captured by the proposed methodology. Hence, it is expected that the novel methods can be successfully applied to a broad category of systems with localized or piecewise-linear nonlinearity. Detailed results are presented in Section 10.

3.7 Reduced-Order-Modeling for Nonlinear Analysis of Cracked Mistuned Multi-Stage Bladed Disk Systems

A novel modeling methodology for combining single stage models (of different types) was introduced. The methodology was used to create reduced order models (ROMs) that combine a model of a single stage with a crack with a model of another single stage containing small blade-to-blade mistuning. The full order model of the stage with a crack was reduced using component mode synthesis (CMS), while the mistuned stage was reduced using cyclic-symmetry analysis, CMS, and component mode mistuning (CMM). The novel methodology enabled combining these two single stage ROMs with different modeling frameworks. The two stages were assembled by projecting the motion at the interface of the neighboring stages along a set of harmonic basis functions.

The results presented demonstrate the interaction between multi-stage effects and cracked-blade effects on the response of the overall system. It was demonstrated that performing a multi-stage analysis (as opposed to one single-stage analysis for each individual stage) is very important in certain frequency ranges for realistic industrial blades. It was also shown that, although the nonlinear forced response of a system with a cracked blade is bounded by the linear forced response of the system with a cracked blade and the response of a system without a cracked blade, this range can be very large and only through a nonlinear analysis can the true response be predicted. Detailed results are presented in Section 11.

3.8 A Statistical Characterization of the Effects of Mistuning in Multi-Stage Bladed Disks

A novel methodology was used to generate multi-stage reduced order models (ROMs) that requires only single sector full order models. This efficient methodology reduces the individual stages using a combination of component mode synthesis, component mode mistuning and cyclic symmetry analysis. The synthesis of the multi-stage ROM was completed in the reduced coordinates by projecting the motion along the interface between stages onto a set of harmonic basis functions and then enforcing geometric compatibility. The methodology was

applied to a two stage system to create a variety of ROMs and conduct statistical analyses. Additionally, a new classification scheme was developed for categorizing modes of multi-stage bladed disk systems. The classification scheme is based on sorting modes based on the energy distribution between the stages and the alignment of modes of the multi-stage system with modes from single stage systems.

Several conclusions can be drawn from this work. First, narrow frequency ranges can exist where single stage analyses are valid for *tuned* multi-stage systems. However, when considering mistuning, the modes in these frequency ranges often no longer match their single stage counterparts, thus significantly changing the forced response predictions although the energy does remain contained to the corresponding single stage. Additionally, outside of these narrow frequency ranges, multi-stage analyses are always required because multi-stage modes exist and therefore, a single stage analysis will be very inaccurate. Mistuning in multi-stage systems creates even more complex dynamics that need to be analyzed in a probabilistic manner. Therefore, many mistuning patterns need to be generated and efficient ROMs for performing calculations for the multi-stage system are critical. Also, it was observed that as the mistuning level is increased it has an increasing impact (increasing the amplification factor and decreasing the modal alignment). However, the influence levels off at approximately 5% standard deviation in the mistuning level for the two stage blisk investigated in this work. Detailed results are presented in Section 12.

3.9 Reduced-Order Models of Mistuned Cracked Bladed Disks

New reduced-order models (ROMs) for mistuned systems with cracked blades have been developed by treating the system as a combination of a tuned-system component (X), a relative component (X_r), and virtual blade mistuning components (CMM). The X - X_r -CMM approach has a number of attractive features.

- (1) The input data needed to construct accurate ROMs are relatively easy to generate. Only a finite element analysis of a sector with a cracked blade, a sector with a tuned blade, and a cantilevered blade are required. All input data can be expressed in terms of single-sector quantities, which minimizes computer memory and computational costs.
- (2) The transformation from usual physical coordinates to X - X_r coordinates is easily implemented by performing a simple linear transformation of the DOFs in the crack area. Using this approach, the usual tuned system model is obtained by simply deleting from the system matrices the elements corresponding to the relative DOFs.
- (3) The fixed-interface method used for the X - X_r model reduction converges quickly, and it employs only tuned system normal modes and constraint modes to represent the cracked system normal modes. Note that the use of relative coordinates has been observed to provide good convergence in the past. However, in contrast with the proposed method, in that work a standard CMS was used to model mistuning, and hence constructing ROMs required the use of full system matrices. Also, in that work, the bladed disk was partitioned differently than in this current approach.
- (4) The complexity of using system level information in the process of constructing the proposed ROMs is avoided. That is possible because the constraint modes are nonzero only in the sector with the cracked blade and approximately zero everywhere else.

- (5) Both small and large mistuning may easily be added to the X-X_r model by a variety of approaches. Herein, we focused on CMM. However, other mistuning projection techniques can be used as well. In particular, since mistuning is added only in the pristine/uncracked blades, the CMM method is one of the easiest methods to apply. Using this method, the mistuning projection is performed using the modal participation factors of cantilevered blade modes.
- (6) The proposed method can handle multiple cracks and large cracks. A key idea to accomplish this is the use of a modified Craig-Bampton CMS method which was introduced and shown to provide excellent results.
- (7) The X-X_r-CMM approach provides excellent accuracy. The approach was validated using an industrial turbo machinery blisk with a complex/realistic geometry and small as well as large cracks.
- (8) The estimated natural frequencies of the system with a cracked blade was shown to converge rapidly as the selected number of tuned system normal modes is increased. This feature ensures that the models obtained are small yet accurate.
- (9) The proposed approach is very efficient computationally. Predictions from X-X_r-CMM reduction and full finite element models were compared. The proposed approach was shown to provide large computational savings. For example, the mistuned finite element model with a cracked blade had 159,603 DOFs, whereas the reduced order model had 330 DOFs with the same accuracy.
- (10) Only sector level analyses and sector level information is needed to construct system level ROMs for full, cracked and mistuned bladed disks and blisks. That contrasts previous work where the full order constraint modes were needed in part because of the particularities of the partitions used there. Those partitions were needed to account for mistuning. In the proposed approach, mistuning is modeled by CMM, and a disadvantageous partition of the blisk is no longer needed.

3.10 Detection of Cracks in Mistuned Bladed Disks using Reduced Order Models and Vibration Data

An efficient and novel methodology to investigate the nonlinear forced response of mistuned bladed disks with a cracked blade has been developed. Efficient ROMs were developed from hybrid CMS and CMM. The forced response of the mistuned bladed disk with a cracked blade was obtained by using the proposed models and nonlinear time integration. The results were compared to those of a previous method. It was shown that blade mistuning can be projected efficiently to reduce the computational cost. This advantage plays an important role when computing system normal modes of a mistuned bladed disk is needed for many mistuning patterns. By investigating mode localizations due to cracks and mistuning, it was shown that cracks lead to mode localization which is different from localization due to mistuning. Also it was shown that cracks are distinguishable from mistuning by using the residuals of mode shapes of the mistuned bladed disk with a cracked blade relative to the mode shapes of the bladed disk without a crack. Furthermore, it was shown that the cracked blade is detectable statistically even in the presence of measurement noise and even when the nonlinearity due to the crack is not negligible.

Novel ROMs were developed to model damping mistuning. The damping in the blades was modeled as structural damping. The use of structural damping in general has been validated in a variety of publications and in particular by the analysis and validation of the CMM approach. This paper presents an extension to those studies, where damping was considered structural at a system level (and hence damping mistuning was ignored). The damping coefficients were considered distinct for each blade. This means that the damping is structural only at the blade level. When all the individual blade damping matrices are assembled together, the global structural damping matrix cannot be defined using one scalar value. Thus, the damping in the blisk as a whole cannot be defined as structural damping. A single structural damping coefficient (scalar value) was used to characterize damping in each blade in a frequency range of interest. Variation in damping within a single blade was not considered. If a real system exhibits damping which does not closely follow the assumptions of structural damping, then one alternate approach (used in the past) is to define different damping coefficients in different frequency ranges. The method proposed can be used in a similar fashion. Note that in various frequency ranges, the structural damping coefficients do not have to be the same values for each blade. Hence, the damping mistuning does not have to be the same in all frequency ranges. Thus, the methodology presented here is not limited to characterizing damping with a single scalar for all frequencies.

A FEM of a blisk was used to validate the novel ROMs. A maximum error of 0.3% between the amplitudes predicted by a ROM and the FEM was found for the case where only damping mistuning is present. When stiffness mistuning was included along with damping mistuning, a maximum error of 0.007% was obtained for the estimates of the resonant frequencies, and a maximum error of 4% for the amplitude of the resonant response. These errors are consistent with the errors obtained using CMM (i.e. with no damping mistuning). They are caused by the various approximations in CMM. Moreover, the novel ROMs are very simple to use and mathematically similar to CMM. The similarity comes from the fact that the equations for the ROM are alike. Thus, the novel ROMs can be very easily generalized and used to model not only damping mistuning, but also stiffness mistuning. The novel method developed adds to CMM the ability to model damping mistuning.

The computational efficiency of the new methodology enables the fast simulation of huge numbers of damping mistuning cases. The novel ROM was thus used to perform a statistical analysis to characterize the effects of random damping mistuning patterns. The blade amplification factors were calculated for many mistuning patterns with different standard deviations. The results show that for all random damping mistuning patterns with the same standard deviation, a random distribution of blade amplification factors can be obtained. As the standard deviation of the mistuning increases, the median, mean and the standard deviation of the distribution of the blade amplification factors also increases. This is true in general for all the engine order excitations. There is, however, no strong correlation between the engine order and the distribution of the blade amplification factors. Note that, such a statistical analysis can be helpful to determine the probability of the occurrence of certain blade amplification factors if the standard deviation of the mistuning pattern is known.

4 BENEFITS AND IMPACT

The novel modeling methodologies that capture nonlinear, aeroelastic, multistage, and localization phenomena have a solid potential to impact Air Force and civilian technology. The conducted research directly supports both established and emerging practices in damage assessment of aerospace vehicles. The techniques developed will thus help to enable critical maintenance and repair decisions by the flight line maintenance manager/officer. Furthermore, these techniques will contribute to the reduction of the development time for new air and space vehicles through increased use of modeling and simulation. Some specific benefits of the conducted research include:

- Fundamentally new capabilities for predicting the response of rotors with cracked blades, which make an important impact on increasing operational capabilities and readiness of Air Force engines and air vehicles;
- Novel, advanced techniques for system identification and damage detection in multistage rotors, which open the door to the next generation of realistic and practical structural health assessment for both onboard monitoring and offline maintenance inspections;
- The necessary fundamental physical insight for the development of advanced design and monitoring technology for systems in which nonlinear and fluid-structural interactions are crucial, thus generalizing existing methods that focus on structures and neglect important fluid-structural phenomena;
- More efficient yet higher fidelity predictions of nonlinear vibration response of cracked structures, which provide a quantum leap for estimating fracture propagation and fatigue life in complex structural and fluid-structural systems.

Finally, it is noted that the conducted research provides fundamental progress in modeling of a large class of cracked, aeroelastic structures. The modeling techniques have primarily been applied to turbine engines, but these new methods have broader applications to health monitoring and prognosis of the air vehicle as a whole. Therefore, these important contributions enable the Air Force to attain critical risk reduction goals by providing methods to improve the knowledge of system properties throughout the service life of each engine and air vehicle.

4.1 Cumulative List of People Involved in the Research

The following people were involved in the proposed research:

B. I. Epureanu, PI
M. P. Castanier, Co-PI
K. D'Souza, Post-Doc
A. Saito, Post-Doc
Z. He, Graduate Student
C. Jung, Graduate Student
O. Marinescu, Graduate Student
A. Joshi, Graduate Student
N. Shah, Graduate Student

4.2 Cumulative List of Journal Publications Resulting from the Research

The following journal publications resulted from this research:

- (1) C. Jung, A. Saito, and B. I. Epureanu: "Detection of Cracks in Mistuned Bladed Disks using Reduced Order Models and Vibration Data", *Journal of Vibration and Acoustics*, submitted, 2011.
- (2) A. Joshi and B. I. Epureanu: "Reduced Order Models for Blade-to-Blade Damping Variability in Mistuned Blisks", *Journal of Vibration and Acoustics*, submitted, 2011.
- (3) O. Marinescu, B. I. Epureanu, and M. Banu: "Reduced-Order Models of Mistuned Cracked Bladed Disk", *Journal of Vibration and Acoustics*, to appear, 2011.
- (4) A. Saito and B. I. Epureanu: "Bilinear Modal Representations for Reduced-Order Modeling of Localized Piecewise-linear Oscillators", *Journal of Sound and Vibration*, to appear, 2011.
- (5) K. D'Souza, A. Saito, and B. I. Epureanu: "Reduced Order Modeling for Nonlinear Analysis of Cracked Mistuned Multi-Stage Bladed Disk Systems", *AIAA Journal*, submitted, 2010.
- (6) K. D'Souza and B. I. Epureanu: "A Statistical Characterization of the Effects of Mistuning in Multi-Stage Bladed Disks", *Journal of Turbomachinery*, submitted, 2010.
- (7) A. Saito, B. I. Epureanu, M. P. Castanier, and C. Pierre: "Node Sampling for Nonlinear Vibration Analysis of Structures with Intermittent Contact", *AIAA Journal*, Vol. 48(9), pp. 1903-1915, 2010.
- (8) A. Saito, M. P. Castanier, and C. Pierre, "Estimation and Veering Analysis of Nonlinear Resonant Frequencies of Cracked Plate", *Journal of Sound and Vibration*, Vol. 326(3-5), pp.725-739, 2009.
- (9) Z. He, B. I. Epureanu, and C. Pierre: "Convergence Predictions for Aeroelastic Calculations of Tuned and Mistuned Tuned Bladed Disk", *Journal of Fluids and Structures*, Vol. 24(5), pp. 732-749, 2008.

REFERENCES

- [1] Tobias, S. A. and Arnold, R. N., "The Influence of Dynamical Imperfection on the Vibration of Rotating Disks," *Proceedings of the Institution of Mechanical Engineers*, Vol. 171, 1957, pp. 669–690.
- [2] Wei, S.-T. and Pierre, C., "Localization Phenomena in Mistuned Assemblies with Cyclic Symmetry Part I: Free Vibrations," *ASME Journal of Vibration, Acoustics, Stress, and Reliability in Design*, Vol. 110, 1988, pp. 429–438.
- [3] Wei, S.-T. and Pierre, C., "Localization Phenomena in Mistuned Assemblies with Cyclic Symmetry Part II: Forced Vibrations," *ASME Journal of Vibration, Acoustics, Stress, and Reliability in Design*, Vol. 110, 1988, pp. 439–449.
- [4] Griffin, J. H. and Hoosac, T. M., "Model Development and Statistical Investigation of Turbine Blade Mistuning," *ASME Journal of Vibration, Acoustics, Stress, and Reliability in Design*, Vol. 106, No. 2, 1984, pp. 204–210.
- [5] Castanier, M. P., Óttarsson, G., and Pierre, C., "A Reduced Order Modeling Technique for Mistuned Bladed Disks," *Journal of Vibration and Acoustics*, Vol. 119, No. 3, 1997, pp. 439–447.
- [6] Bladh, R., Castanier, M. P., and Pierre, C., "Component-Mode-Based Reduced Order Modeling Techniques for Mistuned Bladed Disks - Part I: Theoretical Models," *Journal of Engineering for Gas Turbines and Power - Transactions of the ASME*, Vol. 123, No. 1, 2001, pp. 89–99.
- [7] Bladh, R., Castanier, M. P., and Pierre, C., "Component-Mode-Based Reduced Order Modeling Techniques for Mistuned Bladed Disks - Part II: Application," *Journal of Engineering for Gas Turbines and Power - Transactions of the ASME*, Vol. 123, 2001, pp. 100–108.
- [8] Lim, S.-H., Bladh, R., Castanier, M. P., and Pierre, C., "A Compact, Generalized Component Mode Mistuning Representation for Modeling Bladed Disk Vibration," *Proceedings of the 44th AIAA/ASME/ASCE/AHS/ASC Structures, Structural Dynamics, and Materials Conference and Exhibit*, Norfolk, VA, April 2003.
- [9] Yang, M. T. and Griffin, J. H., "A Normalized Modal Eigenvalue Approach for Resolving Modal Interaction," *ASME Journal of Engineering for Gas Turbines and Power*, Vol. 119, No. 3, 2001, pp. 647–650.
- [10] Yang, M. T. and Griffin, J. H., "A Reduced-Order Model of Mistuning Using a Subset of Nominal System Modes," *Journal of Engineering for Gas Turbines and Power - Transactions of the ASME*, Vol. 123, Oct. 2001, pp. 893–900.
- [11] Feiner, D. M. and Griffin, J. H., "A Fundamental Model of Mistuning for a Single Family of Modes," *Journal of Turbomachinery*, Vol. 124, 2002, pp. 597–605.
- [12] Petrov, E. P., Sanliturk, K. Y., and Ewins, D. J., "A New Method for Dynamic Analysis of Mistuned Bladed Disks Based on the Exact Relationship Between Tuned and Mistuned Systems," *Journal of Engineering for Gas Turbines and Power - Transactions of the ASME*, Vol. 124, Jul 2002, pp. 586–597.
- [13] Hall, K. C., "Deforming Grid Variational Principle for Unsteady Small Disturbance Flows in Cascades," *AIAA Journal*, Vol. 31, No. 5, 1993, pp. 891–900.

- [14] Hall, K. C. and Lorence, C. B., “Calculation of Three-Dimensional Unsteady Flows in Turbomachinery Using the Linearized Harmonic Euler Equations,” *Journal of Turbomachinery*, Vol. 115, No. 4, 1993, pp. 800–809.
- [15] Chaviaropoulos, P. K. and Hansen, M. O. L., “Investigating Three-Dimensional and Rotational Effects on Wind Turbine Blades by Means of a Quasi-3D Navier-Stokes Solver,” *Journal of Fluids Engineering*, Vol. 122, No. 2, 2000, pp. 330–336.
- [16] Fransson, T. H., Jöcker, M., Bölcs, A., and Ott, P., “Viscous and Inviscid Linear/Nonlinear Calculations Versus Quasi-Three-Dimensional Experimental Cascade Data for a New Aeroelastic Turbine Standard Configuration,” *Journal of Turbomachinery*, Vol. 121, No. 4, 1999, pp. 717–725.
- [17] Bell, D. L. and He, L., “Three-Dimensional Unsteady Flow for an Oscillating Turbine Blade and the Influence of Tip Leakage,” *Journal of Turbomachinery*, Vol. 122, No. 1, 2000, pp. 93–101.
- [18] Kaza, K. R. V. and Kielb, R. E., “Flutter of Turbofan Rotors With Mistuned Blades,” *AIAA Journal*, Vol. 22, No. 11, 1984, pp. 1618–1625.
- [19] Kaza, K. R. V. and Kielb, R. E., “Vibration and Flutter of Mistuned Bladed-Disk Assemblies,” *AIAA Journal of Propulsion and Power*, Vol. 1, No. 5, 1985, pp. 336–344.
- [20] Pierre, C. and Murthy, D., “Aeroelastic Model Characteristics of Mistuned Blade Assemblies: Mode Localization and Loss of Eigenstructure,” *AIAA Journal*, Vol. 30, No. 10, 1992, pp. 2483–2496.
- [21] Pierre, C., Smith, T. E., and Murthy, D., “Localization of Aeroelastic Modes in Mistuned High-Energy Turbines,” *Journal of Propulsion and Power*, Vol. 10, No. 3, 1994, pp. 318–328.
- [22] Sadeghi, M. and Liu, F., “Computation of Mistuning Effects on Cascade Flutter,” *AIAA Journal*, Vol. 39, No. 1, 2001, pp. 22–28.
- [23] Gerolymos, G. A., “Coupled Three-Dimensional Aeroelastic Stability Analysis of Bladed Disks,” *Journal of Turbomachinery*, Vol. 115, No. 4, 1993, pp. 791–799.
- [24] Moyroud, F. and Fransson, T., “A Modal Coupling for Fluid and Structure Analyses of Turbomachine Flutter: Application to a Fan Stage,” *Proceedings of ASME Turbo Expo*, 1996, pp. 1–10.
- [25] Seinturier, E., Dupont, C., Berthillier, M., and Dumas, M., “A New Aeroelastic Model for Mistuned Bladed Disks,” *Proceedings of the 43rd AIAA/ASME/ASCE/AHS/ASC Structures, Structural Dynamics, and Materials Conference*, Vol. 4, 2002, pp. 2628–2638.
- [26] Kielb, R. E., Feiner, D. M., Griffin, J. H., and Miyakozawa, T., “Probabilistic Analysis of Mistuned Bladed Disks and Blisks with Aerodynamic and FMM Structural Coupling,” *Proceedings of the 9th National Turbine Engine HCF Conference*, 2004, pp. 1–10.
- [27] Kielb, R. E., Feiner, D. M., Griffin, J. H., and Miyakozawa, T., “Flutter of Mistuned Bladed Disks and Blisks with Aerodynamic and FMM Structural Coupling,” *Proceedings of ASME Turbo Expo*, Vol. 6, 2004, pp. 573–579.
- [28] Cedar, R. D. and Stow, P., “The Addition of Quasi-Three-Dimensional Terms into a Finite Element Method for Transonic Turbomachinery Blade-to-Blade Flows,” *International Journal for Numerical Methods in Fluids*, Vol. 5, No. 2, 1985, pp. 101–114.

- [29] Bateman, H., “Irrotational Motion of A Compressible Fluid,” *Proceedings of the National Academy of Science*, Vol. 16, 1930, pp. 816–825.
- [30] Horn, R. and Johnson, C., *Topics in Matrix Analysis*, Cambridge University Press, 1991.
- [31] Fransson, T. H. and Verdon, J. M., “Updated Report on Standard Configurations for Unsteady Flow Through Vibrating Axial-Flow Turbomachine Cascades: Status as of July 1991,” Tech. rep., Royal Institute of Technology, Stockholm, Sweden and United Technologies Research Center, East Hartford, Connecticut, USA., 1992.
- [32] Epureanu, B. I., Dowell, E. H., and Hall, K. C., “Mach Number Influence on Reduced Order Models of Inviscid Potential Flows in Turbomachinery,” *Journal of Fluids Engineering*, Vol. 124, No. 4, 2002, pp. 977–987.
- [33] Allemang, R. J., “The Modal Assurance Criterion - Twenty Years of Use and Abuse,” *Journal of Sound and Vibration*, Vol. 37, No. 8, 2003, pp. 14–23.
- [34] Anderson, P. W., “Absence of Diffusion in Certain Random Lattices,” *Physical Review*, Vol. 109, No. 5, 1958, pp. 1492–1505.
- [35] Tobias, S. A. and Arnold, R. N., “The Influence of Dynamical Imperfection on the Vibration of Rotating Disks,” *Proceedings of the Institution of Mechanical Engineers*, Vol. 171, 1957, pp. 669–690.
- [36] Bladh, R., *Efficient Predictions of the Vibratory Response of Mistuned Bladed Disks by Reduced Order Modeling*, PhD Thesis, Mechanical Engineering Department, University of Michigan, 2001.
- [37] Bladh, R., Castanier, M. P., and Pierre, C., “Component-Mode-Based Reduced Order Modeling Techniques for Mistuned Bladed Disks, Part II: Application,” *ASME Journal of Engineering for Gas Turbines and Power*, Vol. 123, No. 1, 2001, pp. 100–108.
- [38] Lim, S., Bladh, R., Castanier, M. P., and Pierre, C., “A Compact, Generalized Component Mode Mistuning Representation for Modeling Bladed Disk Vibrations,” AIAA Paper 2003-1545, *Proceedings of the 44th AIAA/ASME/ASCE/AMS Structures, Structural Dynamics and Material Conference*, Norfolk, VA, 2003.
- [39] Yang, M. T. and Griffin, J. H., “A Normalized Modal Eigenvalue Approach for Resolving Modal Interaction,” *ASME Journal of Engineering for Gas Turbines and Power*, Vol. 119, No. 3, 2001, pp. 647–650.
- [40] Yang, M. T. and Griffin, J. H., “A Reduced-Order Model of Mistuning Using a Subset of Nominal System Modes,” *ASME Journal of Engineering for Gas Turbines and Power*, Vol. 123, No. 4, 2001, pp. 893–900.
- [41] Feiner, D. M. and Griffin, G. H., “A Fundamental Model of Mistuning for a Single Family of Modes,” *ASME Journal of Turbomachinery*, Vol. 124, No. 4, 2002, pp. 597–605.
- [42] Petrov, E. P., Sanliturk, K. Y., and Ewins, D. J., “A New Method for Dynamic Analysis of Mistuned Bladed Disks Based on the Exact Relationship Between Tuned and Mistuned Systems,” *ASME Journal of Engineering for Gas Turbines and Power*, Vol. 124, No. 3, 2002, pp. 586–597.
- [43] Kaza, K. R. V. and Kielb, R. E., “Flutter of Turbofan Rotors With Mistuned Blades,” *AIAA Journal*, Vol. 22, No. 11, 1984, pp. 1618–1625.

- [44] Kaza, K. R. V. and Kielb, R. E., "Vibration and Flutter of Mistuned Bladed-Disk Assemblies," *AIAA Journal of Propulsion and Power*, Vol. 1, No. 5, 1985, pp. 336–344.
- [45] Crawley, E. F. and Hall, K. C., "Optimization and Mechanisms of Mistuning in Cascades," *ASME Journal of Engineering for Gas Turbines and Power*, Vol. 107, No. 2, 1985, pp. 418–426.
- [46] Khader, N. and Loewy, R., "Shaft Flexibility Effects on Aeroelastic Stability of a Rotating Bladed Disk," *AIAA Journal of Propulsion and Power*, Vol. 5, No. 6, 1989, pp. 718–726.
- [47] Chaviaropoulos, P. K. and Hansen, M. O. L., "Investigating Three-Dimensional and Rotational Effects on Wind Turbine Blades by Means of a Quasi-3D Navier-Stokes Solver," *ASME Journal of Fluids Engineering*, Vol. 122, No. 2, 2000, pp. 330–336.
- [48] Fransson, T. H., Jöcker, M., Böls, A., and Ott, P., "Viscous and Inviscid Linear/Nonlinear Calculations Versus Quasi-Three-Dimensional Experimental Cascade Data for a New Aeroelastic Turbine Standard Configuration," *ASME Journal of Turbomachinery*, Vol. 121, No. 4, 1999, pp. 717–725.
- [49] Bell, D. L. and He, L., "Three-Dimensional Unsteady Flow for an Oscillating Turbine Blade and the Influence of Tip Leakage," *ASME Journal of Turbomachinery*, Vol. 122, No. 1, 2000, pp. 93–101.
- [50] He, Z., Epureanu, B. I., and Pierre, C., "Effects of Unsteady Aerodynamics on the Dynamic Response of Mistuned Bladed Disks," *Proceedings of the 3rd MIT Conference on Computational Fluid and Solid Mechanics*, Boston, MA, 2005.
- [51] Seinturier, E., Dupont, C., Berthillier, M., and Dumas, M., "A New Aeroelastic Model for Mistuned Bladed Disks," AIAA Paper 2002-1533, *Proceedings of the 43rd AIAA/ASME/ASCE/AHS/ASC Structures, Structural Dynamics, and Materials Conference*, 2002.
- [52] Gerolymos, G. A., "Coupled Three-Dimensional Aeroelastic Stability Analysis of Bladed Disks," *ASME Journal of Turbomachinery*, Vol. 115, No. 4, 1993, pp. 791–799.
- [53] Moyroud, F., Jacquet-Richardet, G., and Fransson, T., "A Modal Coupling for Fluid and Structure Analyses of Turbomachine Flutter. Application to a Fan Stage," ASME Paper 96-GT-335, *Proceedings of ASME Turbo Expo 1996*, 1996.
- [54] He, Z., Epureanu, B. I., and Pierre, C., "Influence of Aerodynamic Coupling on the Dynamics of Mistuned Bladed Disks," *Proceedings of the 10th National Turbine Engine High Cycle Fatigue Conference*, , New Orleans, LA, 2005.
- [55] He, Z., Epureanu, B. I., and Pierre, C., "A Novel Hybrid Method to Predict the Convergence History of Aeroelastic Calculations of Mistuned/Tuned Bladed Disks," *Proceedings of the ASME Pressure Vessels and Piping 2006 Conference (Accepted)*, 2006.
- [56] Bladh, J. R., *Efficient Predictions of the Vibratory Response of Mistuned Bladed Disks by Reduced Order Modeling*, PhD Thesis, The University of Michigan, Ann Arbor, MI, 2001.
- [57] Hall, K. C., Lorence, B. C., and Clark, W. S., "Nonreflecting Boundary Conditions for Linearized Unsteady Aerodynamic Calculations," AIAA Paper 1993-882, *Proceedings of the 31st Aerospace Sciences Meeting and Exhibit*, Reno, NV, 1993.
- [58] Bury, K. V., *Statistical Models in Applied Science*, John Wiley & Sons, New York, NY, 1975, pp. 118–121.

- [59] Dimarogonas, A. D., “Vibration of Cracked Structures: A State of the Art Review,” *Engineering Fracture Mechanics*, Vol. 55, No. 5, 1996, pp. 831–857.
- [60] Saito, A., Castanier, M. P., and Pierre, C., “Effects of a Cracked Blade on Mistuned Turbine Engine Rotor Vibration,” *Proceedings of IDETC 2007*, Las Vegas, Nevada, USA, September 2007, DETC2007-35663.
- [61] Kuttler, J. R. and Sigillito, V. G., “On Curve Veering,” *Journal of Sound and Vibration*, Vol. 75, No. 4, 1981, pp. 585–588.
- [62] Leissa, A. W., “On a Curve Veering Aberration,” *Zeitschrift für Angewandte Mathematik und Physik (ZAMP)*, Vol. 25, No. 1, 1974, pp. 99–111.
- [63] Perkins, N. C. and Mote, C. D., “Comments on Curve Veering in Eigenvalue Problems,” *Journal of Sound and Vibration*, Vol. 106, No. 3, 1986, pp. 451–463.
- [64] Pierre, C. and Dowell, E. H., “Localization of Vibrations by Structural Irregularity,” *Journal of Sound and Vibration*, Vol. 114, No. 3, 1987, pp. 549–564.
- [65] Pierre, C., “Mode Localization and Eigenvalue Loci Veering Phenomena in Disordered Structures,” *Journal of Sound and Vibration*, Vol. 126, No. 3, 1988, pp. 485–502.
- [66] Triantafyllou, M. S. and Triantafyllou, G. S., “Frequency Coalescence and Mode Localization Phenomena: A Geometric Theory,” *Journal of Sound and Vibration*, Vol. 150, No. 3, 1991, pp. 485–500.
- [67] Vidoli, S. and Vestroni, F., “Veering Phenomena in Systems with Gyroscopic Coupling,” *Journal of Applied Mechanics*, Vol. 72, No. 5, 2005, pp. 641–647.
- [68] Challamel, N., Lanos, C., and Casandjian, C., “Localization in the Buckling or in the Vibration of a Two-Span Weakened Column,” *Engineering Structures*, Vol. 28, No. 5, 2006, pp. 776–782.
- [69] Lepidi, M., Gattulli, V., and Vestroni, F., “Static and Dynamic Response of Elastic Suspended Cables with Damage,” *International Journal of Solids and Structures*, Vol. 44, No. 25-26, 2007, pp. 8194–8212.
- [70] Lynn, P. P. and Kumbasar, N., “Free Vibrations of Thin Rectangular Plates Having Narrow Cracks with Simply Supported Edges,” *Development in Mechanics*, Vol. 4, 1967, pp. 911–928.
- [71] Petyt, M., “The Vibration Characteristics of a Tensioned Plate Containing a Fatigue Crack,” *Journal of Sound and Vibration*, Vol. 8, No. 3, 1968, pp. 377–389.
- [72] Stahl, B. and Keer, L. M., “Vibration and Stability of Cracked Rectangular Plates,” *International Journal of Solids and Structures*, Vol. 8, No. 1, 1972, pp. 69–91.
- [73] Hirano, Y. and Okazaki, K., “Vibration of Cracked Rectangular-Plates,” *Bulletin of the JSME-Japan Society of Mechanical Engineers*, Vol. 23, 1980, pp. 732–740.
- [74] Solecki, R., “Bending Vibration of a Simply Supported Rectangular Plate with a Crack Parallel to One Edge,” *Engineering Fracture Mechanics*, Vol. 18, No. 6, 1983, pp. 1111–1118.
- [75] Yuan, J. and Dickinson, S. M., “The Flexural Vibration of Rectangular Plate Systems Approached by Using Artificial Springs in the Rayleigh-Ritz Method,” *Journal of Sound and Vibration*, Vol. 159, No. 1, 1992, pp. 39–55.
- [76] Liew, K. M., Hung, K. C., and Lim, M. K., “A Solution Method for Analysis of Cracked Plates Under Vibration,” *Engineering Fracture Mechanics*, Vol. 48, No. 3, 1994, pp. 393–404.

- [77] Ma, C. C. and Huang, C. H., “Experimental and Numerical Analysis of Vibrating Cracked Plates at Resonant Frequencies,” *Experimental Mechanics*, Vol. 41, No. 1, 2001, pp. 8–18.
- [78] Christides, S. and Barr, A. D. S., “One-Dimensional Theory of Cracked Bernoulli-Euler Beams,” *International Journal of Mechanical Sciences*, Vol. 26, No. 11-12, 1984, pp. 639–648.
- [79] Shen, M.-H. H. and Pierre, C., “Natural Modes of Bernoulli-Euler Beams with Symmetric Cracks,” *Journal of Sound and Vibration*, Vol. 138, No. 1, 1990, pp. 115–134.
- [80] Shen, M.-H. H. and Pierre, C., “Free Vibrations of Beams with a Single-Edge Crack,” *Journal of Sound and Vibration*, Vol. 170, No. 2, 1994, pp. 237–259.
- [81] Chondros, T. G., Dimarogonas, A. D., and Yao, J., “A Continuous Cracked Beam Vibration Theory,” *Journal of Sound and Vibration*, Vol. 215, No. 1, 1998, pp. 17–34.
- [82] Gudmundson, P., “The Dynamic Behavior of Slender Structures with Cross-Sectional Cracks,” *Journal of the Mechanics and Physics of Solids*, Vol. 31, No. 4, 1983, pp. 329–345.
- [83] Pugno, N., Surace, C., and Ruotolo, R., “Evaluation of the Non-linear Dynamic Response to Harmonic Excitation of a Beam with Several Breathing Cracks,” *Journal of Sound and Vibration*, Vol. 235, No. 5, 2000, pp. 749–762.
- [84] Bovsunovsky, A. P. and Surace, C., “Consideration Regarding Superharmonic Vibrations of a Cracked Beam and the Variation in Damping Caused by the Presence of the Crack,” *Journal of Sound and Vibration*, Vol. 288, No. 4-5, 2005, pp. 865–886.
- [85] Carpinteri, A. and Pugno, N., “Towards Chaos in Vibrating Damaged Structures—Part I: Theory and Period Doubling Cascade,” *Journal of Applied Mechanics*, Vol. 72, No. 4, 2005, pp. 511–518.
- [86] Andreaus, U., Casini, P., and Vestroni, F., “Non-Linear Dynamics of a Cracked Cantilever Beam under Harmonic Excitation,” *International Journal of Non-Linear Mechanics*, Vol. 42, No. 3, 2007, pp. 566–575.
- [87] Shaw, S. W. and Holmes, P. J., “A Periodically Forced Piecewise Linear Oscillator,” *Journal of Sound and Vibration*, Vol. 90, No. 1, 1983, pp. 129–155.
- [88] Butcher, E. A., “Clearance Effects on Bilinear Normal Mode Frequencies,” *Journal of Sound and Vibration*, Vol. 224, No. 2, 1999, pp. 305–328.
- [89] Shen, M.-H. H. and Chu, Y. C., “Vibrations of Beams with a Fatigue Crack,” *Computers and Structures*, Vol. 45, No. 1, 1992, pp. 79–93.
- [90] Chondros, T. G., Dimarogonas, A. D., and Yao, J., “Vibration of a Beam with a Breathing Crack,” *Journal of Sound and Vibration*, Vol. 239, No. 1, Jan 2001, pp. 57–67.
- [91] Chati, M., Rand, R., and Mukherjee, S., “Modal Analysis of a Cracked Beam,” *Journal of Sound and Vibration*, Vol. 207, No. 2, Oct 1997, pp. 249–270.
- [92] Kisa, M. and Brandon, J., “The Effects of Closure of Cracks on the Dynamics of a Cracked Cantilever Beam,” *Journal of Sound and Vibration*, Vol. 238, No. 1, Nov 2000, pp. 1–18.
- [93] Zuo, L. and Curnier, A., “Nonlinear Real and Complex-Modes of Conewise Linear-Systems,” *Journal of Sound and Vibration*, Vol. 174, No. 3, Jul 1994, pp. 289–313.

- [94] Jiang, D., Pierre, C., and Shaw, S. W., “Large-Amplitude Non-Linear Normal Modes of Piecewise Linear Systems,” *Journal of Sound and Vibration*, Vol. 272, No. 3-5, 2004, pp. 869–891.
- [95] Chen, S. L. and Shaw, S. W., “Normal Modes for Piecewise Linear Vibratory Systems,” *Nonlinear Dynamics*, Vol. 10, No. 2, Jun 1996, pp. 135–164.
- [96] Lacarbonara, W., Arafat, H. N., and Nayfeh, A. H., “Non-Linear Interactions in Imperfect Beams at Veering,” *International Journal of Non-Linear Mechanics*, Vol. 40, No. 7, 2005, pp. 987–1003.
- [97] ANSYS, Inc., Pittsburgh, PA, *ANSYS Release 10.0 Documentation*, 2005.
- [98] Hintz, R. M., “Analytical Methods in Component Modal Synthesis,” *AIAA Journal*, Vol. 13, No. 8, 1975, pp. 1007–1016.
- [99] Herting, D. N., “A General Purpose, Multi-Stage, Component Modal Synthesis Method,” *Finite Elements in Analysis and Design*, Vol. 1, No. 2, 1985, pp. 153–164.
- [100] Poudou, O., *Modeling and Analysis of the Dynamics of Dry-Friction-Damped Structural Systems*, Ph.D. thesis, The University of Michigan, 2007.
- [101] Petrov, E. P. and Ewins, D. J., “Effects of Damping and Varying Contact Area at Blade-Disk Joints in Forced Response Analysis of Bladed Disk Assemblies,” *Journal of Turbomachinery - Transactions of the ASME*, Vol. 128, Apr 2006, pp. 403–410.
- [102] Nacivet, S., Pierre, C., Thouverez, F., and Jezequel, L., “A Dynamic Lagrangian Frequency-Time Method for the Vibration of Dry-Friction-Damped Systems,” *Journal of Sound and Vibration*, Vol. 265, No. 1, Jul 2003, pp. 201–219.
- [103] Ji, L., Mace, B. R., and Pinnington, R. J., “A Mode-Based Approach for the Mid-Frequency Vibration Analysis of Coupled Long- and Short-Wavelength Structures,” *Journal of Sound and Vibration*, Vol. 289, No. 1-2, 2006, pp. 148–170.
- [104] Saito, A., Castanier, M. P., and Pierre, C., “Vibration Analysis of Cracked Cantilevered Plates Near Natural Frequency Veerings,” *Proceedings of the 49th AIAA/ASME/ASCE/AHS/ASC Structures, Structural Dynamics, and Materials Conference*, AIAA, Reston, VA, 2008, AIAA 2008-1872.
- [105] Craig, R. R., *Structural Dynamics: An Introduction to Computer Methods*, John Wiley & Sons, New York, 1981.
- [106] Cameron, T. and Griffin, J., “An Alternating Frequency/Time Domain Method for Calculating the Steady-State Response of Nonlinear Dynamic Systems,” *Journal of Applied Mechanics*, Vol. 56, 1989, pp. 149–154.
- [107] Nayfeh, A. and Mook, D., *Nonlinear Oscillations*, John Wiley & Sons, 1979.
- [108] Pierre, C., Ferri, A. A., and Dowell, E. H., “Multi-Harmonic Analysis of Dry Friction Damped Systems Using an Incremental Harmonic Balance Method,” *Journal of Applied Mechanics*, Vol. 52, No. 4, 1985, pp. 958–964.
- [109] Laxalde, D., Thouverez, F., Sinou, J. J., and Lombard, J. P., “Qualitative Analysis of Forced Response of Blisks with Friction Ring Dampers,” *European Journal of Mechanics - A/Solids*, Vol. 26, No. 4, 2007, pp. 676–687.

- [110] Sinou, J. J. and Lees, A. W., “A Non-Linear Study of a Cracked Rotor,” *European Journal of Mechanics A/Solids*, Vol. 26, No. 1, Jan 2007, pp. 152–170.
- [111] Poudou, O., Pierre, C., and Reisser, B., “A New Hybrid Frequency-Time Domain Method for the Forced Vibration of Elastic Structures With Friction and Intermittent Contact,” *Proceedings of the 10th International Symposium on Transport Phenomena and Dynamics of Rotating Machinery, paper ISROMAC10-2004-068*, Honolulu, Hawaii, March 2004.
- [112] Poudou, O. and Pierre, C., “A New Method for the Analysis of the Nonlinear Dynamics of Structures With Cracks,” *Proceedings of NOVEM 2005*, Saint-Raphaël, France, April 2005.
- [113] Powell, M. J. D., “A Hybrid Method for Nonlinear Equations,” *Numerical Methods for Nonlinear Algebraic Equations*, edited by P. Rabinowitz, Gordon and Breach Science Publishers, London, 1970.
- [114] Butcher, E. and Lu, R., “Order Reduction of Structural Dynamic Systems with Static Piecewise Linear Nonlinearities,” *Nonlinear Dynamics*, Vol. 49, No. 3, 2007, pp. 375–399.
- [115] Vakakis, A. F., Manevitch, L. I., Mikhlin, Y. V., Pilipchuk, V. N., and Zevin, A. A., *Normal Modes and Localization in Nonlinear Systems*, John Wiley & Sons, Inc., New York, 1996.
- [116] Oden, J. T. and Pires, E. B., “Algorithms and Numerical Results for Finite-Element Approximations of Contact Problems with Non-Classical Friction Laws,” *Computers & Structures*, Vol. 19, 1984, pp. 137–147.
- [117] Simo, J. C. and Laursen, T. A., “An Augmented Lagrangian Treatment of Contact Problems Involving Friction,” *Computers & Structures*, Vol. 42, Jan 1992, pp. 97–116.
- [118] Craig, R. R. and Bampton, M. C. C., “Coupling of Substructures for Dynamic Analyses,” *AIAA Journal*, Vol. 6, No. 7, 1968, pp. 1313–1319.
- [119] Guyan, R. J., “Reduction of Stiffness and Mass Matrices,” *AIAA Journal*, Vol. 3, No. 2, 1965, pp. 380.
- [120] Brahmi, K., Bouhaddi, N., and Fillod, R., “Reduction of Junction Degrees of Freedom Before Assembly in Dynamic Substructuring,” *Proceedings of the ASME Design Engineering Technical Conference*, Vol. 3, 1995, pp. 699–708.
- [121] Balmés, E., “Use of Generalized Interface Degrees of Freedom in Component Mode Synthesis,” *Proceedings of International Modal Analysis Conference*, Society for Experimental Mechanics, Bethel, CT, 1996, pp. 204–210.
- [122] Castanier, M. P., Tan, Y. C., and Pierre, C., “Characteristic Constraint Modes for Component Mode Synthesis,” *AIAA Journal*, Vol. 39, No. 6, 2001, pp. 1182–1187.
- [123] Henshell, R. D. and Ong, J. H., “Automatic Masters for Eigenvalue Economization,” *Earthquake Engineering & Structural Dynamics*, Vol. 3, No. 4, 1975, pp. 375–383.
- [124] Shah, V. N. and Raymund, M., “Analytical Selection of Masters for the Reduced Eigenvalue Problem,” *International Journal for Numerical Methods in Engineering*, Vol. 18, No. 1, 1982, pp. 89–98.
- [125] Kidder, R. L., “Reduction of Structural Frequency Equations,” *AIAA Journal*, Vol. 11, 1973, pp. 892–892.
- [126] Flax, A. H., “Comment on ”Reduction of Structural Frequency Equations”, ” *AIAA Journal*, Vol. 13, 1975, pp. 701–702.

- [127] Kidder, R. L., “Reply by Author to A. H. Flax,” *AIAA Journal*, Vol. 13, 1975, pp. 702–703.
- [128] Grinenko, N. I. and Mokeev, V. V., “Problems of Studying Vibrations of Structures by the Finite-Element Method,” *International Applied Mechanics*, Vol. 21, No. 3, 1985, pp. 231–235.
- [129] Matta, K. W., “Selection of Degrees of Freedom for Dynamic Analysis,” *Journal of Pressure Vessel Technology - Transactions of the ASME*, Vol. 109, 1987, pp. 65–69.
- [130] Bouhaddi, N. and Fillod, R., “A Method for Selecting Master DOF in Dynamic Substructuring using the Guyan Condensation Method,” *Computers & Structures*, Vol. 45, No. 5-6, 1992, pp. 941–946.
- [131] Hitziger, T., Mackens, W., and Voss, H., “A Condensation-Projection Method for Generalized Eigenvalue Problems,” *High Performance Computing 1*, edited by H. Power and C. A. Brebbia, Elsevier Applied Science, London, 1995, pp. 239–282.
- [132] Kim, K. O. and Choi, Y. J., “Energy Method for Selection of Degrees of Freedom in Condensation,” *AIAA Journal*, Vol. 38, 2000, pp. 1253–1259.
- [133] Cho, M. and Kim, H., “Element-Based Node Selection Method for Reduction of Eigenvalue Problems,” *AIAA Journal*, Vol. 42, 2004, pp. 1677–1684.
- [134] Kim, H. and Cho, M., “Two-Level Scheme for Selection of Primary Degrees of Freedom and Semi-Analytic Sensitivity Based on the Reduced System,” *Computer Methods in Applied Mechanics and Engineering*, Vol. 195, 2006, pp. 4244–4268.
- [135] O’Callahan, J., “A Procedure for an Improved Reduced System (IRS) Model,” *Proceedings of the 7th International Modal Analysis Conference*, Las Vegas, NV, January 1989, pp. 17–21.
- [136] Li, W., “A Degree Selection Method of Matrix Condensations for Eigenvalue Problems,” *Journal of Sound and Vibration*, Vol. 259, No. 2, 2003, pp. 409–425.
- [137] Oh, D. and Park, Y., “Order Reduction Based on Singular Values of a Modal matrix,” *Mechanical Systems and Signal Processing*, Vol. 8, No. 1, 1994, pp. 63–79.
- [138] Udawadia, F. E., “Methodology for Optimum Sensor Locations for Parameter Identification in Dynamic Systems,” *Journal of Engineering Mechanics*, Vol. 120, No. 2, 1994, pp. 368–390.
- [139] Penny, J. E. T., Friswell, M. I., and Garvey, S. D., “Automatic Choice of Measurement Locations for Dynamic Testing,” *AIAA Journal*, Vol. 32, 1994, pp. 407–414.
- [140] Kammer, D. C., “Sensor Placement for On-Orbit Modal Identification and Correlation of Large Space Structures,” *Journal of Guidance Control and Dynamics*, Vol. 14, No. 2, 1991, pp. 251–259.
- [141] Zhu, J. and Zhang, W., “Maximization of Structural Natural Frequency with Optimal Support Layout,” *Structural and Multidisciplinary Optimization*, Vol. 31, 2006, pp. 462–469.
- [142] ÅKesson, B. and Olhoff, N., “Minimum Stiffness of Optimally Located Supports for Maximum Value of Beam Eigenfrequencies,” *Journal of Sound and Vibration*, Vol. 120, No. 3, 1988, pp. 457–463.
- [143] Szelag, D. and Mroz, Z., “Optimal Design of Vibrating Beams with Unspecified Support Reactions,” *Computer Methods in Applied Mechanics and Engineering*, Vol. 19, No. 3, 1979, pp. 333–349.

- [144] Won, K. M. and Park, Y. S., “Optimal Support Positions for a Structure to Maximize its Fundamental Natural Frequency,” *Journal of Sound and Vibration*, Vol. 213, No. 5, 1998, pp. 801–812.
- [145] O’Callahan, J., Avitabile, P., and Riemer, R., “System Equivalent Reduction Expansion Process (SEREP),” *Proceedings of the 7th International Modal Analysis Conference*, Las Vegas, NV, January 1989, pp. 29–37.
- [146] Friswell, M. I., Garvey, S. D., and Penny, J. E. T., “Model-Reduction using Dynamic and Iterated IRS Techniques,” *Journal of Sound and Vibration*, Vol. 186, 1995, pp. 311–323.
- [147] Friswell, M. I., Garvey, S. D., and Penny, J. E. T., “The Convergence of the Iterated IRS Method,” *Journal of Sound and Vibration*, Vol. 211, 1998, pp. 123–132.
- [148] Friswell, M. I., Penny, J. E. T., and Garvey, S. D., “Using Linear Model Reduction to Investigate the Dynamics of Structures with Local Non-Linearities,” *Mechanical Systems and Signal Processing*, Vol. 9, No. 3, 1995, pp. 317–328.
- [149] Poudou, O. and Pierre, C., “Hybrid Frequency-Time Domain Methods for the Analysis of Complex Structural Systems with Dry Friction Damping,” *Proceedings of of the 44th AIAA/ASME/ASCE/AHS/ASC Structures, Structural Dynamics, and Materials Conference*, Vol. 1, Apr 2003, pp. 111–124.
- [150] Voss, H., “An Error Bound for Eigenvalue Analysis by Nodal Condensation,” *Numerical Treatment of Eigenvalue Problems*, edited by J. Albrecht, L. Collatz, and W. Velete, Vol. 3, Birkhäuser Verlag, Stuttgart, 1983, pp. 205–214.
- [151] Thomas, D. L., “Errors in Natural Frequency Calculations Using Eigenvalue Economization,” *International Journal for Numerical Methods in Engineering*, Vol. 18, 1982, pp. 1521–1527.
- [152] Mackens, W. and Voss, H., “Nonnodal Condensation of Eigenvalue Problems,” *Zeitschrift für Angewandte Mathematik und Mechanik (ZAMM)*, Vol. 79, No. 4, 1999, pp. 243–255.
- [153] Saito, A., Castanier, M. P., Pierre, C., and Poudou, O., “Efficient Nonlinear Vibration Analysis of the Forced Response of Rotating Cracked Blades,” *Journal of Computational and Nonlinear Dynamics - Transactions of the ASME*, Vol. 4, No. 1, 2009, pp. 011005.
- [154] Saito, A., Castanier, M. P., and Pierre, C., “Estimation and Veering Analysis of Nonlinear Resonant Frequencies of Cracked Plates,” *Journal of Sound and Vibration*, Vol. 326, No. 3-5, 2009, pp. 725–739.
- [155] Carter, B. J., Wawrzynek, P. A., and Ingraffea, A. R., “Automated 3-D Crack Growth Simulation,” *International Journal for Numerical Methods in Engineering*, Vol. 47, No. 1-3, 2000, pp. 229–253.
- [156] Friswell, M. I., Penny, J. E. T., and Garvey, S. D., “The Application of the IRS and Balanced Realization Methods to Obtain Reduced Models of Structures with Local Non-Linearities,” *Journal of Sound and Vibration*, Vol. 196, No. 4, 1996, pp. 453–468.
- [157] Irons, B., “Structural Eigenvalue Problems: Elimination of Unwanted Variables,” *AIAA Journal*, Vol. 3, No. 5, 1965, pp. 961–962.
- [158] Segalman, D. J., “Model Reduction of Systems with Localized Nonlinearities,” *Journal of Computational and Nonlinear Dynamics*, Vol. 2, No. 3, 2007, pp. 249–266.
- [159] Burton, T. and Rhee, W., “On the Reduction of Nonlinear Structural Dynamics Models,” *Journal of Vibration and Control*, Vol. 6, No. 4, 2000, pp. 531–556.

- [160] Bennighof, J. K. and Lehoucq, R. B., “An Automated Multilevel Substructuring Method for Eigenspace Computation in Linear Elastodynamics,” *SIAM Journal on Scientific Computing*, Vol. 25, No. 6, 2004, pp. 2084–2106.
- [161] Theodosiou, C. and Natsiavas, S., “Dynamics of Finite Element Structural Models with Multiple Unilateral Constraints,” *International Journal of Non-Linear Mechanics*, Vol. 44, No. 4, 2009, pp. 371–382.
- [162] Papalukopoulos, C. and Natsiavas, S., “Dynamics of Large Scale Mechanical Models Using Multilevel Substructuring,” *Journal of Computational and Nonlinear Dynamics*, Vol. 2, No. 1, 2007, pp. 40–51.
- [163] Pesheck, E. and Pierre, C., “A New Galerkin-Based Approach for Accurate Non-Linear Normal Modes Through Invariant Manifolds,” *Journal of Sound and Vibration*, Vol. 249, No. 5, 2002, pp. 971–993.
- [164] Apiwattanalungarn, P., Shaw, S. W., and Pierre, C., “Component Mode Synthesis Using Nonlinear Normal Modes,” *Nonlinear Dynamics*, Vol. 41, No. 1-3, Aug 2005, pp. 17–46.
- [165] Feeny, B. F. and Kappagantu, R., “On the Physical Interpretation of Proper Orthogonal Modes in Vibrations,” *Journal of Sound and Vibration*, Vol. 211, No. 4, 1998, pp. 607–616.
- [166] Cusumano, J. and Bai, B.-Y., “Period-Infinity Periodic Motions, Chaos, and Spatial Coherence in a 10 Degree of Freedom Impact Oscillator,” *Chaos, Solitons & Fractals*, Vol. 3, No. 5, 1993, pp. 515–535.
- [167] Kappagantu, R. and Feeny, B. F., “An ”Optimal” Modal Reduction of a System with Frictional Excitation,” *Journal of Sound and Vibration*, Vol. 224, No. 5, 7 1999, pp. 863–877.
- [168] Kerschen, G., Golinval, J.-C., Vakakis, A. F., and Bergman, L. A., “The Method of Proper Orthogonal Decomposition for Dynamical Characterization and Order Reduction of Mechanical Systems: An Overview,” *Nonlinear Dynamics*, Vol. 41, No. 1, 2005, pp. 147–169.
- [169] Weaver, W., Timoshenko, S. P., and Young, D. H., *Vibration Problems in Engineering*, chap. 2, Wiley-IEEE, 5th ed., Jan 1990.
- [170] Della, C. N. and Shu, D., “Vibration of Delaminated Composite Laminates: A Review,” *Applied Mechanics Reviews*, Vol. 60, No. 1, 2007, pp. 1–20.
- [171] Wang, J., Liu, Y., and Gibby, J., “Vibrations of Split Beams,” *Journal of Sound and Vibration*, Vol. 84, No. 4, 1982, pp. 491–502.
- [172] Mujumdar, P. and Suryanarayan, S., “Flexural Vibrations of Beams with Delaminations,” *Journal of Sound and Vibration*, Vol. 125, No. 3, 1988, pp. 441–461.
- [173] Burlayenko, V. N. and Sadowski, T., “Influence of Skin/Core Debonding on Free Vibration Behavior of Foam and Honeycomb Cored Sandwich Plates,” *International Journal of Non-Linear Mechanics*, 2009.
- [174] Żak, A., Krawczuk, M., and Ostachowicz, W., “Vibration of a Laminated Composite Plate with Closing Delamination,” *Journal of Intelligent Material Systems and Structures*, Vol. 12, No. 8, 2001, pp. 545–551.
- [175] Kwon, Y. W. and Lannamann, D. L., “Dynamic Numerical Modeling and Simulation of Interfacial Cracks in Sandwich Structures for Damage Detection,” *Journal of Sandwich Structures and Materials*, Vol. 4, No. 2, 4 2002, pp. 175–199.

- [176] Kikuchi, N. and Oden, J. T., *Contact Problems in Elasticity: A Study of Variational Inequalities and Finite Element Methods*, chap. 6, SIAM, Philadelphia, 1988.
- [177] Holmes, P., Lumley, J. L., and Berkooz, G., *Turbulence, Coherent Structures, Dynamical Systems and Symmetry*, Cambridge University Press, New York, 1996.
- [178] Sirovich, L., “Turbulence and the Dynamics of Coherent Structures Part I: Coherent Structures,” *Quarterly of Applied Mathematics*, Vol. 45, No. 3, OCT 1987, pp. 561–571.
- [179] Saito, A., Epureanu, B. I., Castanier, M. P., and Pierre, C., “Node Sampling for Nonlinear Vibration Analysis of Structures with Intermittent Contact,” *AIAA Journal*, Vol. 48, No. 9, 2010, pp. 1903–1915.
- [180] Song, S. H., *Vibration Analysis and System Identification of Mistuned Multistage Turbine Engine Rotors*, Ph.D. thesis, The University of Michigan, 2007.
- [181] Castanier, M. P. and Pierre, C., “Modeling and Analysis of Mistuned Bladed Disk Vibration: Status and Emerging Directions,” *Journal of Propulsion and Power*, Vol. 22, March 2006, pp. 384–396.
- [182] Bladh, R., Castanier, M. P., and Pierre, C., “Effects of Multistage Coupling and Disk Flexibility on Mistuned Bladed Disk Dynamics,” *Journal of Engineering for Gas Turbines and Power - Transactions of the ASME*, Vol. 125, No. 1, 2003, pp. 121–130.
- [183] Song, S. H., Castanier, M. P., and Pierre, C., “Multi-Stage Modeling of Turbine Engine Rotor Vibration,” *Proceedings of the ASME 2005 Design Engineering Technical Conference and Computers and Information in Engineering Conference*, Long Beach, CA, USA, September 2005, DETC2005-85740.
- [184] Song, S. H., Castanier, M. P., and Pierre, C., “Multi-Stage Modeling of Mistuned Turbine Engine Rotor Vibration,” *Proceedings of the NATO AVT-121 Symposium on Evaluation, Control and Prevention of High Cycle Fatigue in Gas Turbine Engines for Land, Sea, and Air*, Granada, Spain, October 2005, RTO-MP-AVT-121-P-06.
- [185] Lim, S.-H., Bladh, R., Castanier, M. P., and Pierre, C., “Compact, Generalized Component Mode Mistuning Representation for Modeling Bladed Disk Vibration,” *AIAA Journal*, Vol. 45, No. 9, 2007, pp. 2285–2298.
- [186] Song, S. H., Castanier, M. P., and Pierre, C., “System Identification of Multistage Turbine Engine Rotors,” *Proceedings of GT2007 ASME Turbo Expo*, Montreal, Canada, May 2007, GT2007-28307.
- [187] Laxalde, D., Thouverez, F., and Lombard, J.-P., “Dynamical Analysis of Multi-Stage Cyclic Structures,” *Mechanics Research Communications*, Vol. 34, No. 4, 2007, pp. 379–384.
- [188] Laxalde, D., Lombard, J.-P., and Thouverez, F., “Dynamics of Multistage Bladed Disks Systems,” *Journal of Engineering for Gas Turbines and Power*, Vol. 129, No. 4, 2007, pp. 1058–1064.
- [189] Sternchüss, A., Balmès, E., Jean, P., and Lombard, J.-P., “Reduction of Multistage Disk Models: Application to an Industrial Rotor,” *Journal of Engineering for Gas Turbines and Power*, Vol. 131, No. 1, 2009, pp. 012502.
- [190] Sinha, A., “Reduced-Order Model of a Mistuned Multi-Stage Bladed Rotor,” *International Journal of Turbo and Jet Engines*, Vol. 25, No. 3, 2008, pp. 145–153.

- [191] Chatelet, E., D'Ambrosio, F., and Jacquet-Richardet, G., "Toward Global Modeling Approaches for Dynamic Analyses of Rotating Assemblies of Turbomachines," *Journal of Sound and Vibration*, Vol. 282, No. 1-2, 2005, pp. 163–178.
- [192] Turhan, O. and Bulut, G., "Linearly Coupled Shaft-Torsional and Blade-Bending Vibrations in Multi-Stage Rotor-Blade Systems," *Journal of Sound and Vibration*, Vol. 296, No. 1-2, 2006, pp. 292–318.
- [193] Rzadkowski, R. and Sokolowski, J., "Coupling Effects Between the Shaft and Two Bladed-Discs," *Advances in Vibration Engineering*, Vol. 4, No. 3, 2005, pp. 249–266.
- [194] Rzadkowski, R. and Drewczynski, M., "Coupling of Vibration of Several Bladed Discs on the Shaft, Part I: Free Vibration Analysis," *Advances in Vibration Engineering*, Vol. 8, No. 2, 2009, pp. 125–137.
- [195] Segù, B. and Casanova, E., "Application of a Reduced Order Modeling Technique for Mistuned Bladed Disk-Shaft Assemblies," *Proceedings of GT2007 ASME Turbo Expo*, May 2007, GT2007-27594.
- [196] Boulton, L. A. and Casanova, E., "Reduced Order Model for a Two Stage Gas Turbine including Mistuned Bladed Disks and Shaft Interaction," *Proceedings of the GT2009 ASME Turbo Expo*, Jun 2009, GT2009-59335.
- [197] Laxalde, D. and Thouverez, F., "Non-Linear Vibrations of Multi-Stage Bladed Disks Systems with Friction Ring Dampers," *Proceedings of the ASME International Design Engineering Technical Conferences and Computers and Information in Engineering Conference 2007, Paper DETC2007-34473*, ASME, Las Vegas, Nevada, USA, September 2007.
- [198] Saito, A., Castanier, M. P., and Pierre, C., "Effects of a Cracked Blade on Mistuned Turbine Engine Rotor Vibration," *Journal of Vibration and Acoustics - Transactions of the ASME*, Vol. 131, No. 6, 2009, pp. 061006.
- [199] Kharyton, V., Laine, J.-P., Thouverez, F., and Kucher, O., "Cracked Blade Detection from Bladed Disk Forced Response," *Proceedings of the GT2009 ASME Turbo Expo*, 2009, GT2009-59598.
- [200] Ewins, D. J., "The Effects of Detuning Upon the Forced Vibrations of Bladed Disks," *Journal of Sound and Vibration*, Vol. 9, No. 1, 1969, pp. 65–79.
- [201] Dye, R. C. F. and Henry, T. A., "Vibration Amplitudes of Compressor Blades Resulting From Scatter in Blade Natural Frequencies," *ASME Journal of Engineering for Power*, Vol. 91, No. 3, 1969, pp. 182–188.
- [202] Hurty, W. C., "Dynamic Analysis of Structural Systems Using Component Modes," *AIAA Journal*, Vol. 3, No. 4, 1965, pp. 678–685.
- [203] Craig, R. R. and Chang, C.-J., "Free-Interface Methods of Substructure Coupling for Dynamic Analysis," *AIAA Journal*, Vol. 14, No. 11, 1976, pp. 1633–1635.
- [204] Irretier, H., "Spectral Analysis of Mistuned Bladed Disk Assemblies by Component Mode Synthesis," *Vibrations of Bladed Disk Assemblies*, edited by D. J. Ewins and A. V. Srinivasan, American Society of Mechanical Engineers, New York, 1983, pp. 115–125.
- [205] Zheng, Z.-C. and Wang, F.-R., "Dynamic Analysis of Blade Groups Using Component Mode Synthesis," *Vibrations of Blades and Bladed Disk Assemblies*, edited by R. E. Kielb and N. F. Rieger, American Society of Mechanical Engineers, New York, 1985, pp. 97–103.

- [206] D'Souza, K., Saito, A., and Epureanu, B. I., "Reduced-Order-Modeling for Nonlinear Analysis of Cracked Mistuned Multi-Stage Bladed Disk Systems," *AIAA Journal*, Vol. submitted, 2010.

APPENDICES

**5 FLUID-STRUCTURAL COUPLING EFFECTS ON THE DYNAMICS OF
MISTUNED BLADED DISKS**

Reducing vibrations, and in particular the resonant forced response of bladed disks, is an important concern for the turbomachinery industry. Cyclic symmetry is a convenient assumption for the analysis of (tuned) bladed disks. However, cyclic symmetry does not hold for mistuned disks which exhibit small differences among sectors. Mistuning is unavoidable in practice due to manufacturing tolerances and in-service wear and tear, and can cause a drastic increase of the forced response. Hence, the effects of mistuning on the vibration of turbomachinery rotors have been extensively investigated (e.g. Tobias and Arnold¹).

In early work, simplified models with only several degrees of freedom (DOF) were used to study the dynamics of mistuned bladed disks.²⁻⁴ While such simplified models, like lumped parameter models, are convenient and insightful to investigate the effects of major system parameters (such as mistuning, structural and aerodynamic coupling), they are not accurate enough to study real/practical bladed disks. Models based on the finite element method (FEM) can represent the actual bladed disks accurately. However, the large number of DOF (usually several millions) of the FEM models makes the computation time practically not affordable. Hence, different reduced order models (ROM) have been developed.⁵⁻¹² Current high fidelity structural models reduce the computation time greatly compared to the original FEM model. Moreover, various fluid dynamic models have been developed to calculate with high speed the unsteady pressure on the blades¹³⁻¹⁷ by (usually) assuming linearity of the unsteady pressure with respect to the displacements of the blades.

Severe mode localization and excessive vibration amplitude of bladed disks are major detrimental effects of mistuning. Previous work has shown that interblade structural coupling is a critical factor affecting the dynamics of mistuned bladed disks. In operating conditions, bladed disks are always interacting with flows, and hence, bladed disks exhibit both structural and aerodynamical coupling. Thus, *aeroelastic* calculations are necessary for accurate predictions. Although compact and accurate structural reduced order models have been developed, only a few studies of the dynamics of mistuned bladed disks have been conducted with considerations of aerodynamic forces. Traditionally, the aerodynamic stiffness matrix was calculated using the blade normal modes with/without constraint modes. For example, Kaza and Kielb^{18,19} used a beam structural model and a two-dimensional aerodynamic model to study the vibrations and flutter of mistuned bladed disks. Pierre and Murthy²⁰ and Pierre *et al.*²¹ developed a perturbation method to investigate the aeroelastic mode localization and eigenstructure transformations. Sadeghi and Liu²² studied the phase mistuning and frequency mistuning effects on two-dimensional cascade flutter. Gerolymos²³ calculated the tuned aeroelastic modes using an iterative process over frequency dependent unsteady aerodynamic forces for a shroud-less bladed disk. Moyroud *et al.*²⁴ developed a similar iteration process using different structural and aerodynamic computer codes, and calculated the aeroelastic tuned eigenvalues for bladed disks with and without shrouds. In these latter two methods,^{23,24} the aerodynamic code used the tuned system modes to calculate the unsteady aerodynamic forces. During the iterative process, Gerolymos²³ used a mode modification technique to update the new eigenvalues and eigenvectors, and Moyroud *et al.*²⁴ solved the eigenvalue problem directly. Seinturier *et al.*²⁵ adopted the structural model developed by Bladh *et al.*^{6,7} to calculate the forced response of mistuned bladed disks. Because that structural model is sub-structured into blade and disk components, cantilever-blade normal modes and constraint modes were used to calculate the unsteady aerodynamic forces.²⁵ The constraint modes are obtained by enforcing unit displacements on interface DOF successively. Kielb *et al.*^{26,27} used the fundamental mistuning model (FMM) developed by Feiner and

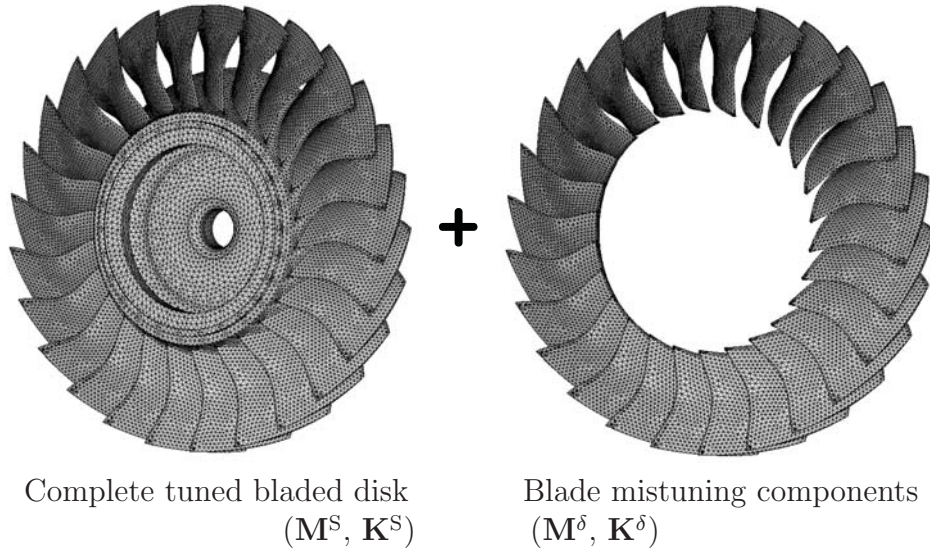


Fig. 1. Sub-structuring of a mistuned bladed disk.

Griffin¹¹ to investigate the flutter and forced response problems of mistuned bladed disks. Although FMM uses the tuned system modes as the modal basis, cantilever-blade normal modes are still used to calculate the unsteady aerodynamic forces.^{26,27} Distinct from these previous studies, the current paper discusses a new method to incorporate the aerodynamic coupling into a high fidelity structural reduced order model by using the tuned system modes directly to calculate the unsteady aerodynamic stiffness matrix, and by employing iterations over the eigenvalues of the system to obtain accurate results. A new fluid-structure coupling method in the modal space is developed to incorporate the aerodynamic effects into a compact and accurate ROM. The component mode mistuning (CMM) method⁸ is used for the structural model, and a quasi-3D unsteady aerodynamic code is employed to calculate the unsteady aerodynamic forces. Traditionally, the cantilever-blade normal modes (and the constraint modes) have been used to calculate the aerodynamic stiffness matrix.^{20,21,25–27} However, in the CMM model, the tuned system modes are used as the modal basis. Herein, the tuned system modes are used to calculate the aerodynamic stiffness matrix iteratively over the eigenvalues of the system. The results using the traditional method and the new method are compared. It is found that, for the case studied, there are notable differences between the results using the new model and the traditional method with cantilever-blade normal modes only. To achieve accurate results, constraint modes are necessary. However, the inclusion of constraint modes in the aerodynamic calculation increases significantly the computation time compared to using the tuned system modes directly.

This paper is organized as follows. In the next two sections, the CMM structural model and the quasi-3D aerodynamic model are introduced. The methods to incorporate the aerodynamic coupling into the CMM model using the cantilever-blade normal modes and the tuned system modes are presented in the following section. The two methods are applied to an industrial rotor. Results and discussions are presented in the following section. Finally, the last section summarizes the conclusions of this work.

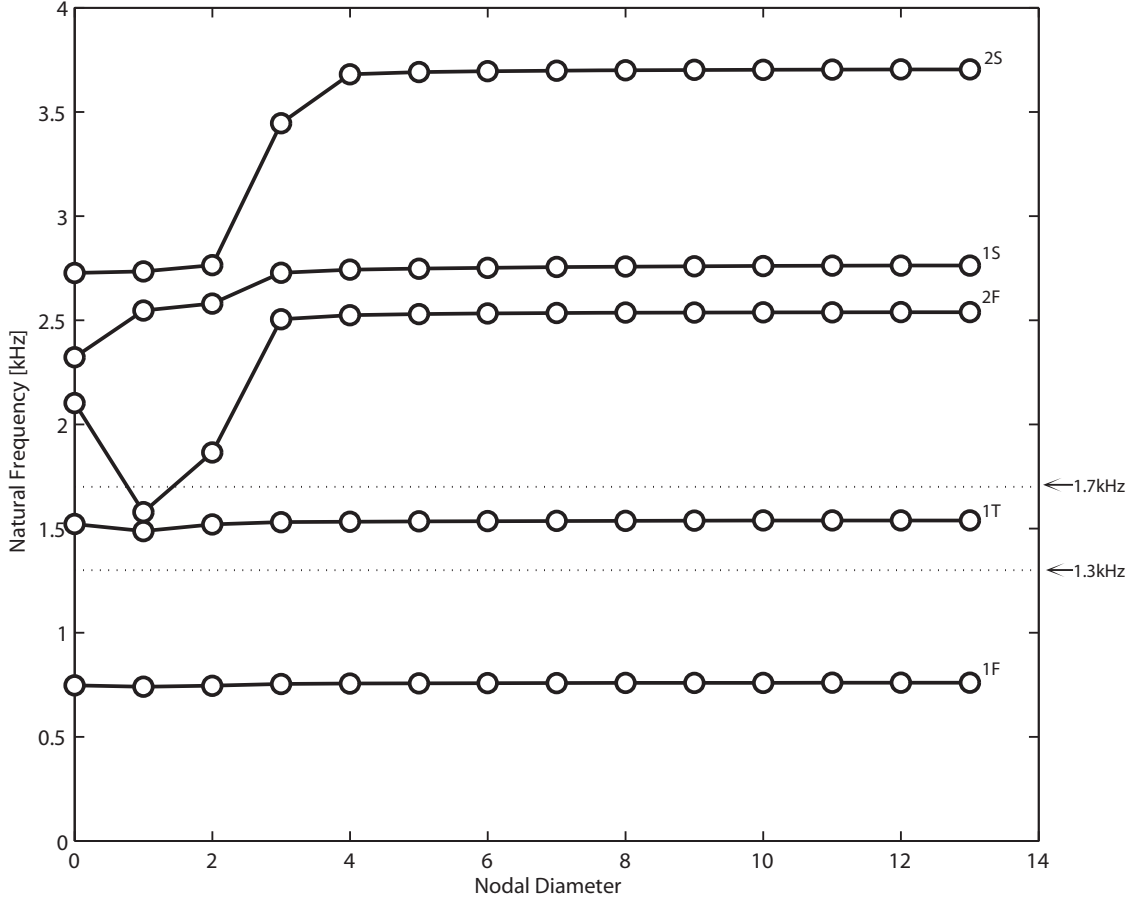


Fig. 2. Natural frequencies versus nodal diameter numbers for the tuned bladed disk.

5.1 Structural Reduced Order Model

The common method for bladed disks is to conduct FEM analysis for only one sector based on cyclic symmetry. However, when the cyclic symmetry is destroyed by mistuning, the analysis of the whole model is needed if FEM method is employed. Herein, an efficient and precise reduced order modeling method developed by Lim *et al.*⁸ for mistuned bladed disks is used. A group of tuned system modes are used as the modal space of the whole (mistuned) system. The major advantage of this reduced order model is the projection of the deviation of cantilever blade stiffness onto the tuned system modal space. For brevity, only the synthesized equations in the reduced modal space are presented here. The details of the reduced order model can be found in the original paper (by Lim *et al.*⁸). The hybrid-interface component mode synthesis (CMS) method is employed in this model. As shown in Fig. 1, the mistuned bladed disk is partitioned into two components: a free-interface component (the tuned bladed disk) and a fixed-interface component (the blade mistuning). The fixed-interface component is a virtual component instead of a physical component because it is the difference between the mistuned system and the nominal tuned system. Under the assumption that the mistuned modes for a system with small mistuning can be captured by the tuned system modes alone when the tuned system modes have close frequencies (within

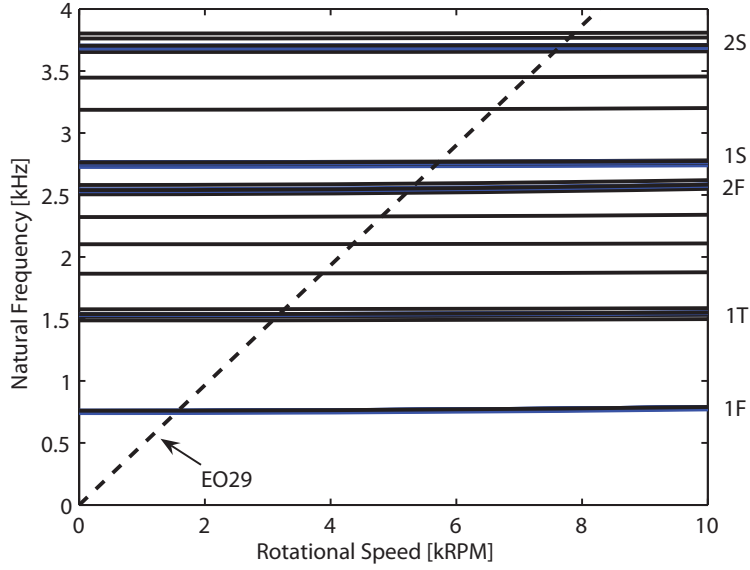


Fig. 3. The Campbell diagram for the tuned bladed disk. EO stands for Engine Order.

a small range⁸⁻¹⁰), the ROM can be constructed by using only the tuned system modes (which are obtained by conducting cyclic symmetry analysis of one sector). The synthesized equations for the eigenvalue problem and (separately) the forced response problem can be expressed as⁸

$$\left[(1 + j\gamma)\mathbf{K}^{\text{syn}} + \mathbf{K}^{\text{a}} - \omega^2\mathbf{M}^{\text{syn}} \right] \mathbf{q}_\phi^{\text{S}} = \mathbf{0}, \quad (1)$$

$$\left[(1 + j\gamma)\mathbf{K}^{\text{syn}} + \mathbf{K}^{\text{a}} - \omega^2\mathbf{M}^{\text{syn}} \right] \mathbf{q}_\phi^{\text{S}} = \Phi_\Gamma^{\text{S},0*} \mathbf{f}, \quad (2)$$

where matrices \mathbf{M}^{syn} and \mathbf{K}^{syn} are given by

$$\mathbf{M}^{\text{syn}} = \mathbf{I} + \Phi_\Gamma^{\text{S},0*} \delta\mathbf{M} \Phi_\Gamma^{\text{S},0},$$

$$\mathbf{K}^{\text{syn}} = \mathbf{\Lambda} + \Phi_\Gamma^{\text{S},0*} \delta\mathbf{K} \Phi_\Gamma^{\text{S},0},$$

with $\delta\mathbf{M}$ and $\delta\mathbf{K}$ denoting the physical mistuned mass and stiffness matrices.

5.2 Frequency Domain Unsteady Aerodynamic Model

A quasi-three dimensional model of a cascade operating in an inviscid, irrotational and isentropic flow is employed based on the full-potential equation using a Galerkin formulation¹³ and by considering the variation of stream tube heights.²⁸ Consider the flow between two neighboring stream surfaces. The velocity vector may be expressed as the gradient of the scalar velocity potential $\hat{\phi}$. The conservation of mass can be expressed as

$$\frac{\partial(\hat{\rho}h)}{\partial t} + \nabla \cdot (\hat{\rho}\nabla\hat{\phi}h) = 0, \quad (3)$$

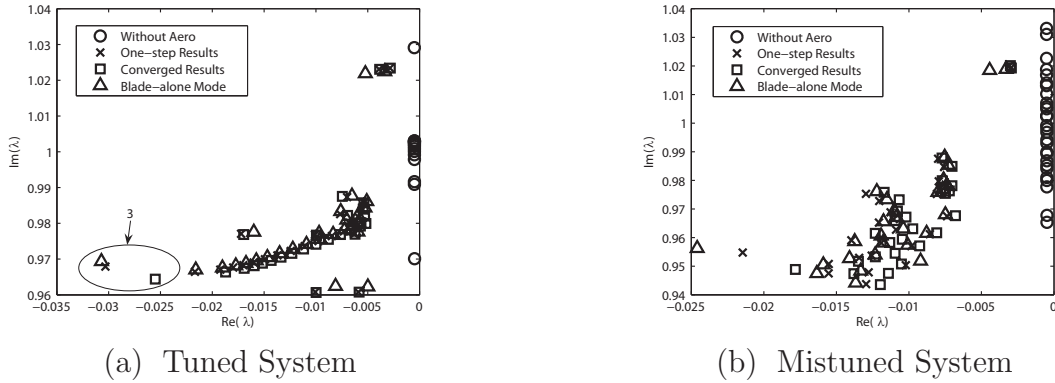


Fig. 4. Eigenvalues of the 1T system modes with structural damping γ of 0.001. The eigenvalue λ is related to ω by $\lambda = j\omega$.

where $\hat{\rho}$ denotes the full solution, including steady and unsteady components, $\hat{\rho}$ is the density of the fluid, and h is the height of the stream tube. For an isentropic flow, the density and the pressure can be expressed as

$$\hat{\rho} = \rho_T \left\{ 1 - \frac{\gamma_c - 1}{C_T^2} \left[\frac{1}{2} (\nabla \hat{\phi})^2 + \frac{\partial \hat{\phi}}{\partial t} \right] \right\}^{\frac{1}{\gamma_c - 1}},$$

$$\hat{p} = p_T \left\{ 1 - \frac{\gamma_c - 1}{C_T^2} \left[\frac{1}{2} (\nabla \hat{\phi})^2 + \frac{\partial \hat{\phi}}{\partial t} \right] \right\}^{\frac{\gamma_c}{\gamma_c - 1}},$$

where \hat{p} is the (complete steady and unsteady) pressure. Eq. (3) can be transformed by applying a variational principle.^{13,29} Namely, the velocity potential, which satisfies Eq. (3) in a simple-connected domain D , renders extremum of the functional Π given by

$$\Pi = \frac{1}{T} \int_T \int \int_D \hat{p} h dx dy dt + \frac{1}{T} \int_T \oint \hat{Q} \hat{\phi} h ds dt,$$

where \hat{Q} is the prescribed mass flux on the boundary.

The steady flow in each stream tube is calculated first. Then, the unsteady flow is linearized about the steady flow under the assumption that the unsteady flow induced by the motion of the blades is a small perturbation to the steady flow. Only one passage between two neighboring blades is solved by assuming that the flow is periodic along the circumferential direction. Hence, the velocity potential can be expressed as the sum of a steady potential Φ and the real part of an unsteady periodic potential ϕ , i.e. $\hat{\phi}(x, y, t) = \Phi(x, y) + \Re[\phi(x, y)e^{j\omega t}]$, with $\phi \ll \Phi$ and \Re denoting the real part.

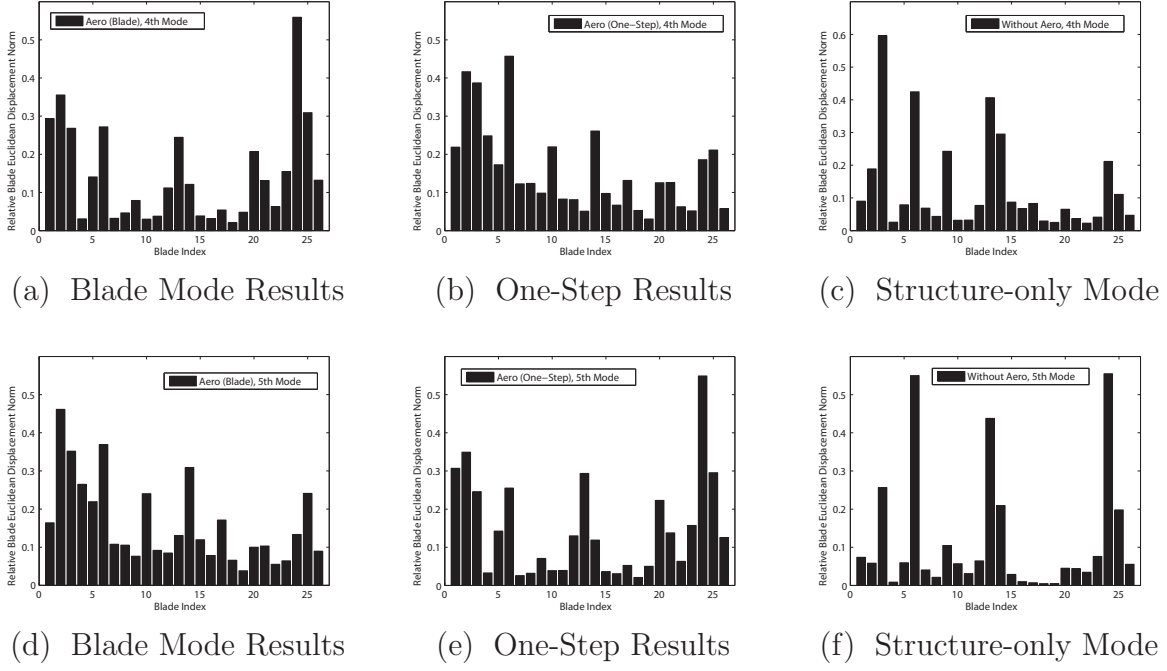


Fig. 5. 4-th and 5-th mistuned mode shape amplitudes in the 1T frequency range for mistuning pattern δ_n^e .

5.3 Fluid-Structure Coupling Models

5.3.1 Fluid-Structure Coupling Using Blade Modes

In previous work (Lim *et al.*⁸), the stiffness mistuning projection is implemented by using the following modal transformation

$$\Phi_{\Gamma}^{S,0} = \mathbf{I} \otimes [\Phi^{\text{CB}} \Psi^{\text{CB}}] \begin{bmatrix} \mathbf{q}_{\phi}^{\text{CB}} \\ \mathbf{q}_{\psi}^{\text{CB}} \end{bmatrix} = (\mathbf{I} \otimes \mathbf{U}^{\text{CB}}) \mathbf{q}^{\text{CB}}, \quad (4)$$

where \otimes denotes the Kronecker product,³⁰ and

$$\mathbf{U}^{\text{CB}} = \begin{bmatrix} \Phi^{\text{CB}} & \Psi^{\text{CB}} \end{bmatrix},$$

$$(\mathbf{q}^{\text{CB}})^* = \begin{bmatrix} (\mathbf{q}_{\phi}^{\text{CB}})^* & (\mathbf{q}_{\psi}^{\text{CB}})^* \end{bmatrix}.$$

The constraint modes are obtained by enforcing unit displacements on each DOF at the interface successively, while keeping other DOFs at the interface free. The purpose of Ψ^{CB} is to describe the displacements at the boundaries between components of the bladed disk, such as blade-disk boundary and shroud-to-shroud boundary.

The projection used in Eq. (4) can be used to calculate the aerodynamic stiffness matrix \mathbf{K}^a also. First, the aerodynamic stiffness coupling coefficients in the complex cyclic constraint and cantilever-blade normal modal coordinates $\tilde{\mathbf{A}}$ are calculated. The modal transformation between $\tilde{\mathbf{A}}$ and the aerodynamic stiffness coupling coefficients in the physical coordinates \mathbf{A}

can be expressed as⁸

$$\begin{aligned}\tilde{\mathbf{A}} &= (\mathbf{I} \otimes \mathbf{U}^{\text{CB}*}) (\mathbf{E}^* \otimes \mathbf{I}) \mathbf{A} (\mathbf{E} \otimes \mathbf{I}) (\mathbf{I} \otimes \mathbf{U}^{\text{CB}}) \\ &= (\mathbf{E}^* \otimes \mathbf{I}) (\mathbf{I} \otimes \mathbf{U}^{\text{CB}*}) \mathbf{A} (\mathbf{I} \otimes \mathbf{U}^{\text{CB}}) (\mathbf{E} \otimes \mathbf{I}).\end{aligned}\quad (5)$$

Therefore, the aerodynamic stiffness coupling matrix in the tuned structure-only system modal coordinates can be expressed (using Eqns. 4 and 5) in the following form

$$\begin{aligned}\mathbf{K}^a &= \Phi_{\Gamma}^{\text{S},0*} \mathbf{A} \Phi_{\Gamma}^{\text{S},0} \\ &= \mathbf{q}^{\text{CB}*} (\mathbf{I} \otimes \mathbf{U}^{\text{CB}*}) \mathbf{A} (\mathbf{I} \otimes \mathbf{U}^{\text{CB}}) \mathbf{q}^{\text{CB}} \\ &= \mathbf{q}^{\text{CB}*} (\mathbf{E} \otimes \mathbf{I}) \tilde{\mathbf{A}} (\mathbf{E}^* \otimes \mathbf{I}) \mathbf{q}^{\text{CB}}.\end{aligned}\quad (6)$$

For every mode shape \mathbf{U}_m^{CB} (i.e. for every column m of \mathbf{U}^{CB} , the unsteady pressure distribution on the blade $p_{m,i}^{\text{CB}}$ is calculated for every interblade phase angle σ_i of index i , which is given by $\sigma_i = 2\pi i/N_{\text{B}}$, (for $i = 0, 1, \dots, N_{\text{B}} - 1$), where N_{B} is the number of blades. Note that σ_i and $\sigma_{N_{\text{B}}+i}$ correspond to the same interblade phase angle. Hence, $\tilde{\mathbf{A}}$ is a block diagonal matrix where each block relates to a specific interblade phase angle index, and

$$\tilde{\mathbf{A}} = \begin{bmatrix} \tilde{\mathbf{A}}^0 & & & \\ & \tilde{\mathbf{A}}^1 & & \\ & & \ddots & \\ & & & \tilde{\mathbf{A}}^{N_{\text{B}}-1} \end{bmatrix}.\quad (7)$$

The elements $\tilde{\mathbf{A}}_{mn}^i$ of the diagonal block $\tilde{\mathbf{A}}^i$ can be obtained by integrating the dot product of the m -th mode \mathbf{U}_m^{CB} with the n -th corresponding force, in the direction of the local normal \mathbf{n} as follows

$$\tilde{\mathbf{A}}_{mn}^i = \int_A \mathbf{U}_m^{\text{CB}*} \cdot p_{n,i}^{\text{CB}} \mathbf{n} dA, \quad m, n = 1, 2, \dots, N_U, \quad (8)$$

where N_U is the number of modes in \mathbf{U}_m^{CB} . The number of constraint modes are usually much larger than the number of cantilever-blade normal modes retained in \mathbf{U}_m^{CB} . Hence, for bladed disks without shrouds, the constraint modes are usually neglected.⁸ In this scenario, the dimension of $\tilde{\mathbf{A}}_{mn}^i$ in Eq. (8) is the number of cantilevered-blade modes selected N_{CB} , and the modal transformations shown in Eqns. 4, 5 and 6 successively become⁸

$$\Phi_{\Gamma}^{\text{S},0} = (\mathbf{I} \otimes \Phi^{\text{CB}}) \mathbf{q}_{\phi}^{\text{CB}}, \quad (9)$$

$$\begin{aligned}\tilde{\mathbf{A}} &= (\mathbf{I} \otimes \Phi^{\text{CB}*}) (\mathbf{E}^* \otimes \mathbf{I}) \mathbf{A} (\mathbf{E} \otimes \mathbf{I}) (\mathbf{I} \otimes \Phi^{\text{CB}}) \\ &= (\mathbf{E}^* \otimes \mathbf{I}) (\mathbf{I} \otimes \Phi^{\text{CB}*}) \mathbf{A} (\mathbf{I} \otimes \Phi^{\text{CB}}) (\mathbf{E} \otimes \mathbf{I}),\end{aligned}\quad (10)$$

$$\begin{aligned}\mathbf{K}^a &= \Phi_{\Gamma}^{\text{S},0*} \mathbf{A} \Phi_{\Gamma}^{\text{S},0} \\ &= \mathbf{q}_{\phi}^{\text{CB}*} (\mathbf{I} \otimes \Phi^{\text{CB}*}) \mathbf{A} (\mathbf{I} \otimes \Phi^{\text{CB}}) \mathbf{q}_{\phi}^{\text{CB}} \\ &= \mathbf{q}_{\phi}^{\text{CB}*} (\mathbf{E} \otimes \mathbf{I}) \tilde{\mathbf{A}} (\mathbf{E}^* \otimes \mathbf{I}) \mathbf{q}_{\phi}^{\text{CB}}.\end{aligned}\quad (11)$$

Blade	δ_n^e [%]	Blade	δ_n^e [%]
1	5.06	14	2.93
2	2.68	15	-1.67
3	2.30	16	-0.60
4	-3.84	17	-3.65
5	4.27	18	-3.50
6	-2.74	19	0.03
7	-4.29	20	0.15
8	-1.71	21	3.27
9	0.81	22	2.76
10	0.65	23	-0.62
11	1.20	24	-2.06
12	-0.92	25	0.91
13	-3.17	26	-3.65

Table 1
Mistuning pattern in E for the case study rotor.

5.3.2 Fluid-Structure Coupling Using System Modes

A natural other choice for calculating the aerodynamic stiffness matrix is to employ the same projection as the one used for mistuning, i.e. by using the approach shown above. However, for the cases where the constraint modes are needed to calculate the aerodynamic stiffness matrix (e.g. bladed disks with shrouds), the computation time is likely to become formidable because the unsteady pressure distribution has to be calculated for every constraint mode and every interblade phase angle index. Moreover, the aerodynamic calculation is sensitive to the blade motion, and consequently the small errors caused by the modal projection (similar to the one shown in Eq. (9)) may lead to large errors in the resulting aerodynamic stiffness matrix (expressed in the structure-only tuned system modal coordinates). To overcome these difficulties, tuned (structure-only) system modes are used directly to calculate the aerodynamic stiffness matrix. Since these modes are structure-only modes, iterations over frequencies are needed because the aerodynamic stiffness matrix \mathbf{K}^a in Eq. (1) is dependent on the frequencies. From Eq. (1), the *aeroelastic* system modes can be expressed as

$$\Phi_{\Gamma,i}^{S,n} = \sum_{r=1}^{N_S} Q_{\phi,ri}^{S,n} \Phi_{\Gamma,r}^{S,0}, \quad i = 1, 2, \dots, N_S, \quad (12)$$

or in the matrix form as

$$\Phi_{\Gamma}^{S,n} = \Phi_{\Gamma}^{S,0} \mathbf{Q}_{\phi}^{S,n}, \quad (13)$$

where the superscript n denotes results after n steps of iteration, N_S is the number of tuned structure-only system modes used in the component mode mistuning model, and the matrix $\mathbf{Q}_{\phi}^{S,n}$ is given by

$$\mathbf{Q}_{\phi}^{S,n} = \begin{bmatrix} \mathbf{q}_{\phi,1}^{S,n} & \mathbf{q}_{\phi,2}^{S,n} & \dots & \mathbf{q}_{\phi,N_S}^{S,n} \end{bmatrix}. \quad (14)$$

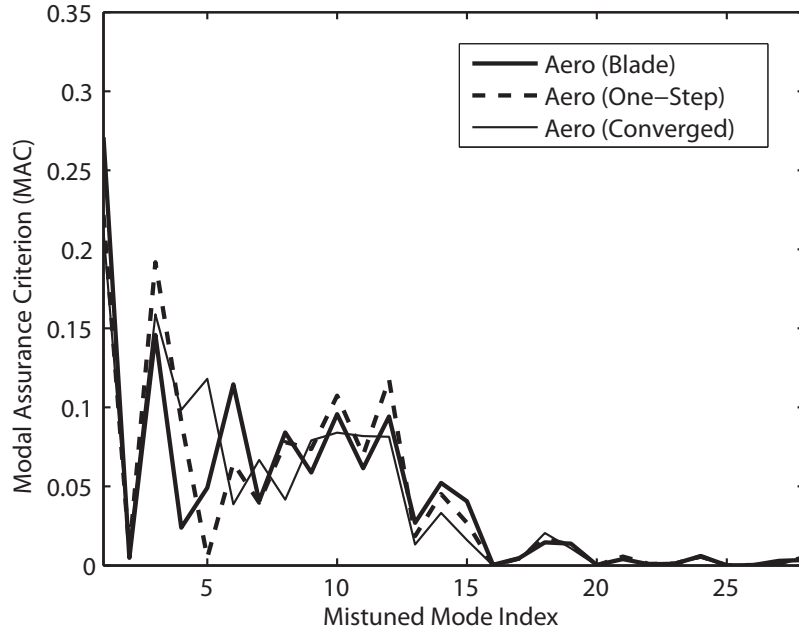


Fig. 6. MAC number between the 3-rd structure-only mistuned mode and the aeroelastic mistuned modes in the 1T system mode frequency region.

For a tuned system, the aeroelastic modes have constant interblade phase angles, while no constant interblade phase angle exists in the mistuned aeroelastic modes. However, the aerodynamic calculation requires periodic boundary conditions. To address this issue and calculate the converged aerodynamic stiffness matrix, two different methods are proposed: one for tuned systems and the other for mistuned systems. In the first step of both methods, structure-only mode shapes and (complex) eigenvalues ω^0 are computed. Then, at every iteration step n , the aerodynamic stiffness matrix (expressed in the tuned structure-only modal coordinates) $\mathbf{K}^{a,n}$ is obtained using the eigenvalues ω^{n-1} calculated in the previous iteration step, and new eigenvalues ω^n are computed using $\mathbf{K}^{a,n}$. Iterations are performed until convergence in the aerodynamic stiffness matrix is achieved. This is distinct from classical flutter calculations where, for example, iterations are needed to determine the flutter speed. Here, the aeroelastic eigenvalues and eigenmodes for a particular flow condition (which is before flutter) are of interest. The iterations needed are performed over the eigenvalues (of un-converged aeroelastic system) because the aerodynamic stiffness matrix is dependent on these eigenvalues.

5.3.3 Tuned Case

Because every tuned aeroelastic system mode has a specific interblade phase angle, the corresponding unsteady pressure distribution on a blade has the same interblade phase angle also. Hence, the aerodynamic stiffness matrix in the tuned aeroelastic system modal coordinates

$\hat{\mathbf{A}}^{T,n}$ may be expressed in the form of a block diagonal matrix as

$$\hat{\mathbf{A}}^{T,n} = \begin{bmatrix} \hat{\mathbf{A}}_0^{T,n} & & & \\ & \hat{\mathbf{A}}_1^{T,n} & & \\ & & \ddots & \\ & & & \hat{\mathbf{A}}_{N_B-1}^{T,n} \end{bmatrix}. \quad (15)$$

Unlike Eq. (7), the dimensions of the blocks $\hat{\mathbf{A}}_i^{T,n}$ in Eq. (15) can be different for different i , and depend on the number of tuned structure-only system modes used in the CMM model that relate to the i -th interblade phase angle σ_i . The aerodynamic stiffness matrix in the tuned structure-only system modal coordinates $\mathbf{K}^{a,n}$ can be calculated by using the modal transformation shown in Eq. (13). One obtains

$$\mathbf{K}^{a,n} = \mathbf{P}^{n*} \hat{\mathbf{A}}^{T,n} \mathbf{P}^n, \quad (16)$$

where $\mathbf{P}^n = (\mathbf{Q}_\phi^{S,n})^{-1}$ is the modal transformation from the tuned aeroelastic system modes to the tuned structure-only system modes.

5.3.4 Mistuned Case

Because of the linearity of the unsteady aerodynamic model, the unsteady aerodynamic forces exerted on the blade due to the i -th mistuned aeroelastic system mode $\Phi_{\Gamma,i}^{S,n}$ can be expressed as

$$\mathbf{F}_i^{S,n} = \sum_{r=1}^{N_S} Q_{\phi,ri}^{S,n} \mathbf{F}_{i,r}^{S,0}, \quad i = 1, 2, \dots, N_S. \quad (17)$$

Note that the mode $\Phi_{i,r}^{S,0}$ is vibrating with the i -th *mistuned* system natural frequency related to the force $\mathbf{F}_i^{S,n}$. Hence, the forces $\mathbf{F}_{i,r}^{S,0}$ are different for distinct $\mathbf{F}_i^{S,n}$. The elements of the aerodynamic stiffness matrix (in the mistuned aeroelastic system modal coordinates) $\hat{\mathbf{A}}^{M,n}$ can be obtained as

$$\begin{aligned} \hat{\mathbf{A}}_{ij}^{M,n} &= \Phi_{\Gamma,i}^{S,n*} \mathbf{F}_j^{S,n} \\ &= \left(\sum_{r=1}^{N_S} Q_{\phi,ri}^{S,n*} \Phi_{\Gamma,r}^{S,0*} \right) \left(\sum_{t=1}^{N_S} Q_{\phi,tj}^{S,n} \mathbf{F}_{j,t}^{S,0} \right) \\ &= \sum_{r=1}^{N_S} \sum_{t=1}^{N_S} Q_{\phi,ri}^{S,n*} \Phi_{\Gamma,r}^{S,0*} Q_{\phi,tj}^{S,n} \mathbf{F}_{j,t}^{S,0}. \end{aligned} \quad (18)$$

Due to the orthogonality of eigenvectors with different interblade phase angles, only terms in which $\Phi_{\Gamma,r}^{S,0}$ and $\mathbf{F}_{j,t}^{S,0}$ have the same interblade phase angle will be non-zero in Eq. (18). The aerodynamic stiffness matrix in the tuned structure-only system modal coordinates can be derived in the same way as Eq. (16). One obtains

$$\mathbf{K}^{a,n} = \mathbf{P}^{n*} \hat{\mathbf{A}}^{M,n} \mathbf{P}^n. \quad (19)$$

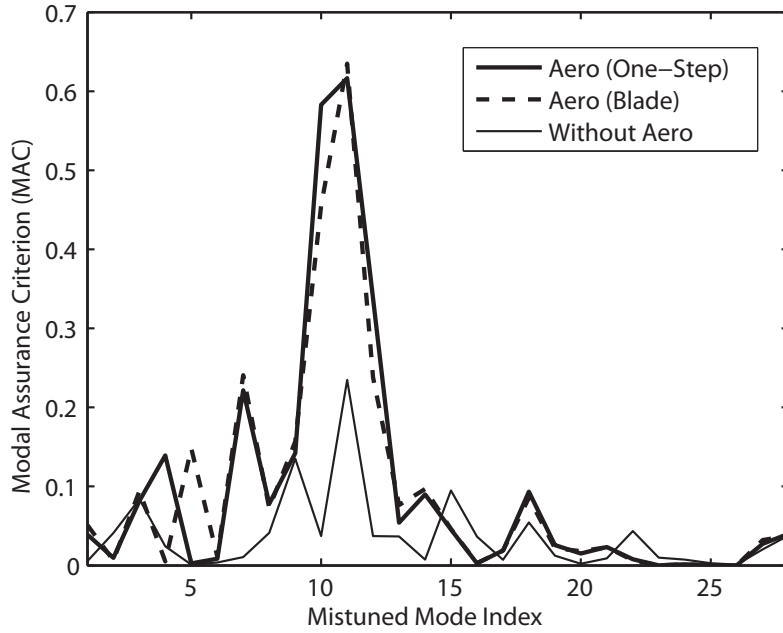
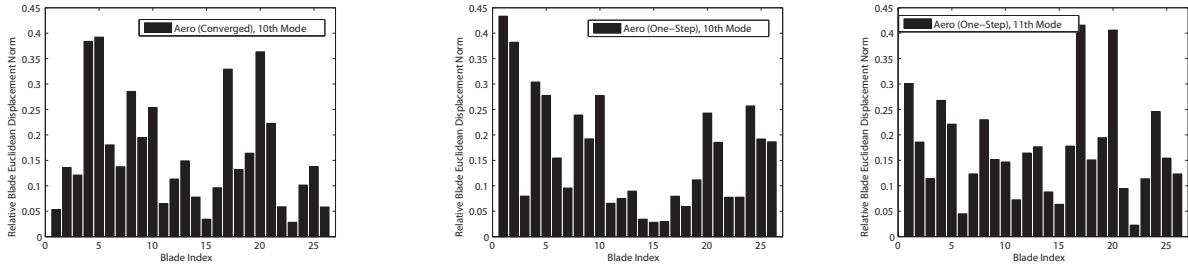


Fig. 7. MAC number between the 10-th converged aeroelastic mistuned mode the mistuned modes using other methods.

One may note that the tuned system can be calculated using the same method as for the mistuned system described above, by setting the mistuning to zero. However, each tuned mode shape $\Phi_{\Gamma,r}^{S,0}$ is related to N_S different frequencies (in Eq. (18)), while every tuned mode shape $\Phi_{\Gamma,i}^{S,n}$ is related to only one frequency in the method shown in Eqns. 15 and 16 for the tuned case. Thus, the method based on Eqns. 15 and 16 saves a large amount of computation time compared to the method above, but it is valid only for tuned cases.

5.4 Case Study

The structural ROM model has been validated by comparing the results with MSC-NASTRAN,⁸ and the aerodynamic code has been validated by comparing the results with several other unsteady CFD codes and experiment results^{16,31,32} for cascade flows. An industrial bladed disk with 26 sectors shown on the left in Fig. 1 was investigated. The complete FEM model has 1,306,500 DOF, and each blade has 21,582 DOF, with 990 DOF at the interface between the blade and the disk. The large number of interface DOF makes this case study challenging because the inclusion of the boundary constraint modes is practically impossible. Fig. 2 shows the natural frequencies versus nodal diameter numbers for the tuned system. The frequency range from 1300 Hz to 1700 Hz was studied. The frequency range investigated covers the second group (first torsion: 1T) of system modes. The rotation speed of interest is determined using the Campbell diagram shown in Fig. 3, and 15 layers are used for the aerodynamic calculations. The upstream far field steady Mach number near the hub is 0.4, and the reduced frequency (based on half chord and inlet velocity near the hub) is approximately 1.45 near the hub. For brevity, the method using the cantilever-blade normal modes is referred to as the blade mode method. The method using the system modes is referred to as the system mode method. Finally, the uncoupled and the coupled results using



(a) 10-th Converged Aeroelastic Mode (b) 10-th One-step Aeroelastic Mode (c) 11-th One-step Aeroelastic Mode

Fig. 8. Mistuned aeroelastic mode shape amplitudes.

the system mode method are referred to as one-step results and converged results. Small mistuning of Young’s modulus E of every blade is considered. Tab. 1 shows the employed mistuning patterns (δ_n^e) and the corresponding blades. The standard deviation of δ_n^e is 2.7% and the mean value is close to zero. The structural damping γ is 0.001. The number of DOF of the CMM model is 28. Finally, 5 cantilever-blade normal modes and 990 blade-disk boundary constraint modes are used for the mistuning projection, but only the corresponding cantilever-blade normal mode (1T) is used for the aeroelastic calculation in the blade mode method (where not stated otherwise). As discussed in the following, the bladed disk studied herein has relatively strong aerodynamic coupling, which may not be the case for a variety of other blisk operating conditions. Also, a strong sensitivity of aerodynamic forces to interblade phase angle is observed for the bladed disk studied.

5.4.1 Free Vibration Problem

Fig. 4 shows the tuned and mistuned eigenvalue locus of the 1T system modes of the system in the complex plane ($\lambda = j\omega$). The imaginary part of an eigenvalue represents frequency, and the real part represents damping. A positive real part indicates that the damping is negative and that the system is unstable for the corresponding mode shape. The aeroelastic eigenvalues are distinct from the structure-only eigenvalues. The aerodynamic coupling is strong for this case study, as indicated by the fact that the largest aerodynamic damping value is close to 0.03. Note that the regular pattern of the tuned aeroelastic eigenvalues is destroyed when mistuning is introduced. Compared to the tuned aeroelastic eigenvalues, the range of the real part of the mistuned aeroelastic eigenvalues narrows down, and the range of the imaginary part expands, which means that the mistuned frequencies spread out, and mistuning stabilizes the system. These results are in agreement with the well known beneficial effect of mistuning on flutter (Pierre and Murthy,²⁰ Pierre *et al.*²¹). For most of the tuned eigenvalues, the one-step results and converged results are almost identical for frequencies, but show notable differences in damping, which agrees with Gerolymos.²³ However, for the eigenvalue corresponding to the interblade phase angle index 3, the converged result and the one-step result exhibit significant differences in both frequency and damping (as shown in Fig. 4). This indicates that for this traveling wave, the dependence of the unsteady aerodynamic force on the eigenvalue is complex. For the mistuned eigenvalues, the one-step and converged results show similar differences. The results using the blade mode method are close to the one-step results, while some of the tuned and mistuned eigenvalues have notable differences. In the following, a tuned system mode with a positive interblade phase angle

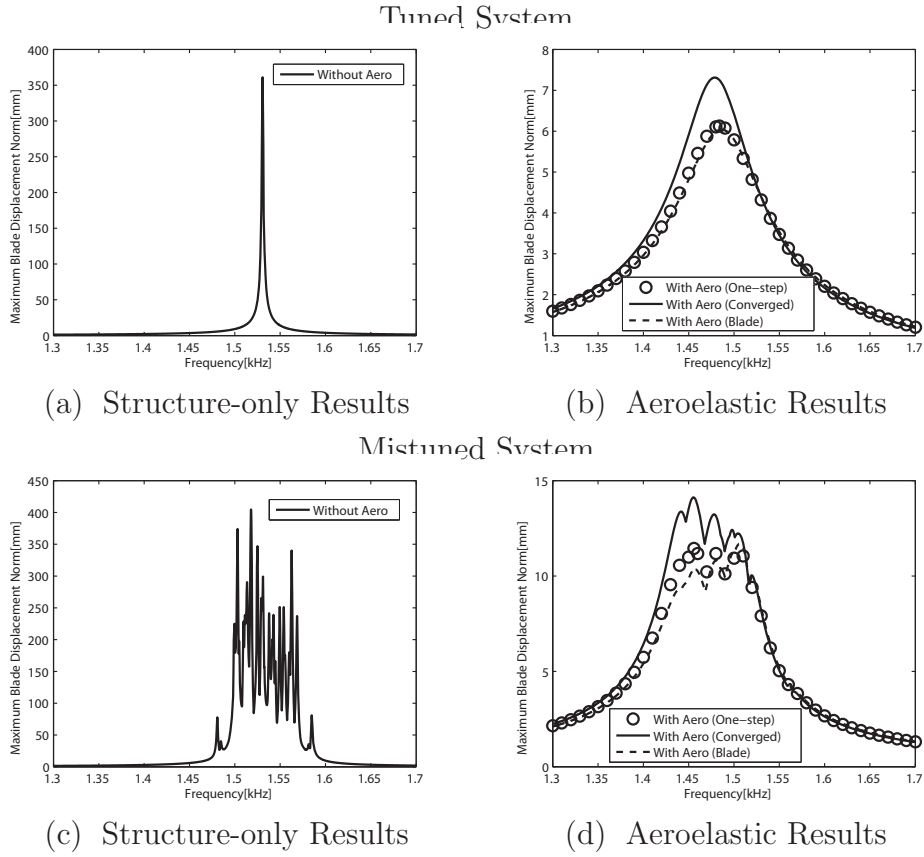
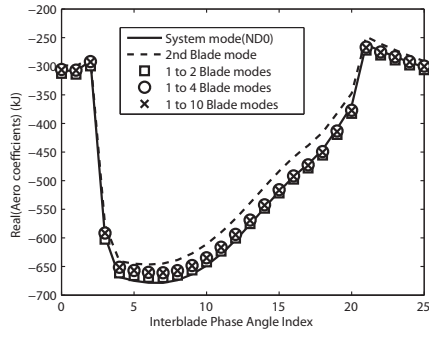


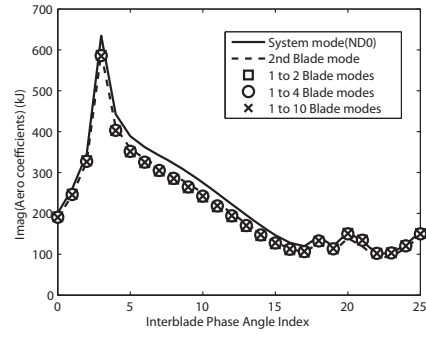
Fig. 9. Forced response for engine order 29 excitation in the 1T system mode frequency range with a structural damping γ of 0.001.

corresponds to a traveling wave in the same direction of rotation.

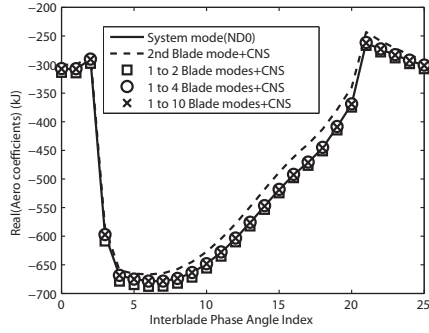
Pierre *et al.*²¹ showed that the aeroelastic mode shapes transit from constant interblade phase angle (or extended) modes to localized modes when mistuning increases. Also, there are numerous mode crossings in the transition region, which are caused by the frequency switching for different mistuned modes. This is demonstrated in Fig. 5, which shows the 4-th and 5-th mistuned aeroelastic modes. The modes on the left column are the results using the blade mode method. The modes on the middle column are the one-step results using the system mode method. The modes on the right are the structure-only modes. Interestingly, the 4-th mode on the left column is similar to the 5-th mode on the middle column. Also, the 5-th mode on the right column is similar to the 4-th mode on the middle column. This indicates that the mistuned aeroelastic mode crossings are very complex in the transition region. For these two sets of results, although the 4-th and 5-th mistuned modes are similar, the mistuned mode crossing patterns are different because the frequency orders of these two modes are switched. However, the mistuned structure-only modes are totally different from the mistuned aeroelastic modes. In fact, for some structure-only modes, *no similar modes* can be found in the aeroelastic modes. For example, Fig. 6 shows the modal assurance criterion (MAC) numbers between the 3-rd structure-only mistuned mode and the aeroelastic mistuned modes using the blade mode method and the system mode method. The MAC number MAC_{cd} shows the linear dependence of two different modes Ψ_c and Ψ_d ,



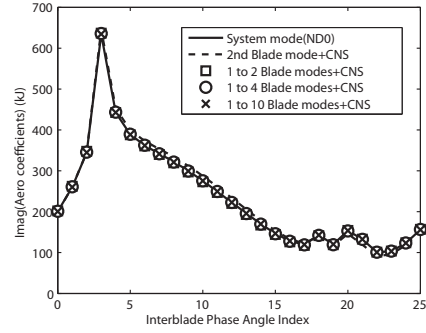
(a) Real Part (without constraint modes)



(b) Imaginary Part (without constraint modes)



(c) Real Part (with constraint modes)



(d) Imaginary Part (with constraint modes)

Fig. 10. Aerodynamic stiffness coefficients using the system mode and the combined cantilever-blade normal modes for the 1T system mode frequency range; CNS stands for constraint.

and is defined as³³

$$MAC_{cd} = \frac{\|(\Psi_c)^* \cdot (\Psi_d)\|_2^2}{\|\Psi_c\|_2^2 \cdot \|\Psi_d\|_2^2}. \quad (20)$$

The range of the MAC number is from 0 to 1, and a MAC number of 1 corresponds to two modes that are linearly dependent. As shown in Fig. 6, the highest MAC number is only about 0.3, which confirms the clear difference between structure-only and aeroelastic modes.

The aeroelastic mistuned modes are less localized compared to the structural mistuned modes. Wei and Pierre² showed that not only the mistuning level, but also the interblade coupling is important for a mistuned mode to be localized. In this case, the additional aerodynamic interblade coupling affects the severity of mode localization. For example, Fig. 7 shows the MAC numbers between the 10-th converged aeroelastic mistuned mode and the mistuned modes using other methods. The 10-th and 11-th one-step aeroelastic modes, as well as the 11-th mode using the blade mode method, have the largest MAC numbers close to 0.6 with this mode. Also, there is no similar structural mode for this aeroelastic mode. Fig. 8 shows the magnitude of this mode (subfigure 8(a)) and the 10-th (subfigure 8(b)) and 11-th (subfigure 8(c)) one-step aeroelastic modes. Although the MAC numbers between the 10-th mistuned converged mode and these two one-step modes are the largest ones, there are significant differences between the blade amplitude patterns of these three modes.

5.4.2 Forced Response

The tuned and mistuned forced responses of the system in the 1T system mode frequency range, subjected to an engine order 29 excitation, are shown in Fig. 9. The applied forces are unit loads on one of the nodes at the tip of each blade. The aeroelastic peak frequencies are smaller than the structure-only peak frequencies, which can be predicted from Fig. 4(a) since an engine order 29 excitation corresponds to the same interblade phase angle as interblade phase angle index 3. In general, the aerodynamic stiffness matrix should be recalculated for every excitation frequency, however, only one aerodynamic stiffness matrix, calculated for the eigenvalue problem, was used herein. The fluid-structure coupling introduces additional damping into the system, so that the tuned and mistuned aeroelastic peak forced response amplitudes are also smaller than those observed for the structure-only system. Also, the additional aerodynamic coupling leads to the disappearance of several mistuned forced response peaks. The results using the blade mode method are similar to the results using the system mode method. Nonetheless, it is interesting to note that the resonance frequency where the maximum mistuned aeroelastic forced response occurs is different for the results using the blade mode method and the system mode method.

The amplification factor, defined as the ratio between the mistuned and tuned peak values, is 1.12 for the structure only case, and it is 1.87, 1.93 and 1.94 for the one-step result, converged result and the result using the blade mode method. The large increase of the amplification factor due to the inclusion of aerodynamic coupling can be predicted from Fig. 4. As shown in Fig. 4(a), the tune mode corresponding to interblade phase angle index 3 has the largest aerodynamic damping. A mistuned aeroelastic mode can be viewed as a linear combination of tuned aeroelastic modes. Therefore, the damping of a mistuned aeroelastic mode can also be viewed as a linear combination of the damping of tuned aeroelastic modes. Hence, the beneficial effect of mistuning on flutter (as shown in Fig. 4(b)) is observed because the range of the mistuned aerodynamic damping is smaller than the range of the tuned aerodynamic damping. Thus, all the values of the mistuned aerodynamic damping are smaller than the tuned aerodynamic damping corresponding to the interblade phase angle index 3. Hence, the amplification factor is larger because the mistuned aerodynamic damping is smaller.

The 95 percentile response levels shown in Fig. 11 are calculated using Monte Carlo simulations to determine statistically the likely maximum forced response amplification factor due to mistuning. A number of 1,000 mistuning patterns are used for each mistuning level. Note that the Monte Carlo simulations here assume that the aerodynamic stiffness matrix is the same as the one obtained using the mistuning pattern shown in Tab. 1 (δ_n^e). In general, the aerodynamic stiffness matrix may be different for distinct mistuning patterns if the system mode method is used. As shown in Fig. 11, the aeroelastic 95 percentile response levels are smaller than the structure only response when the mistuning level is small. This indicates that the sensitivity of the amplification factor to mistuning is decreased by the aerodynamic coupling. When the mistuning level becomes larger, the aeroelastic 95 percentile response levels overpass the structure only response and increase to a larger value, around 3. This is consistent with Fig. 9. To demonstrate the effect of different damping values for different tuned system modes (as in the case of aerodynamic damping), two 95 percentile response levels are also plotted in Fig. 11. The first one is referred to as the *varied structural damping* case and the second one is referred to as the *very large structural damping* case. In the varied structural damping case, no aeroelastic coupling is considered and the structural damping γ

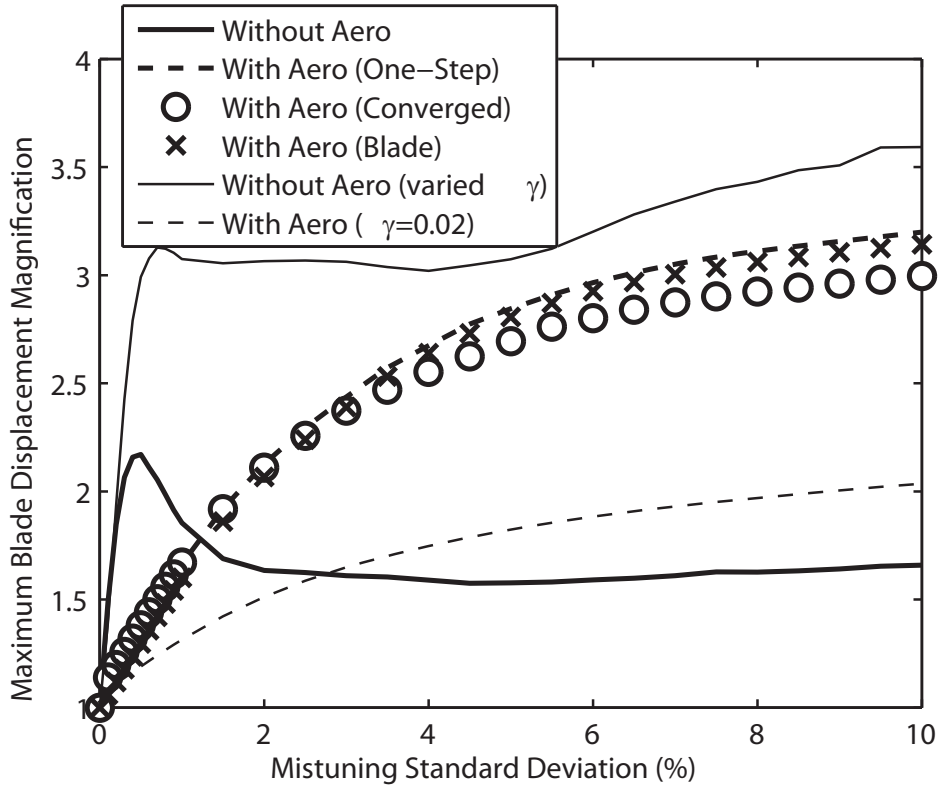


Fig. 11. 95 percentile response levels for the engine order 29 excitation in the 1T system mode frequency range.

related to nodal diameter 3 modes is 0.003 while the structural damping γ is 0.001 for the other modes. In the very large structural damping case, the aeroelastic coupling using the system mode method with converged results is included, and the structural damping γ is set to 0.02. Compared to the structure only result with fixed $\gamma = 0.001$, the sensitivity of the amplification factor to mistuning does not change significantly in the varied structural damping case. However, for this case, when the mistuning standard deviation becomes larger than 0.5%, the amplification factor becomes larger than 3. Compared to the aeroelastic results with $\gamma = 0.001$, the amplification factor is always smaller than 2 in the very large structural damping case because the very large structural damping decreases the relative difference between the mistuned aeroelastic damping and the tuned aeroelastic damping corresponding to the interblade phase angle index 3. Note that in the very large structural damping case, the sensitivity of the amplification factor to mistuning from the aeroelastic calculation is still smaller than the structure only results.

5.4.3 Accuracy of the Blade Mode Method

For brevity, the cantilever-blade normal modes are referred to as the blade modes in this section. As shown above, the results using the blade mode method has notable differences compared to the results using the system mode method. There are at least two possible reasons for these differences: one is the difference in the vibration frequencies used in the aerodynamic calculation (system natural frequencies are used in the system mode method, and natural frequencies of cantilever-blade normal modes are used in the blade mode method), the other is the difference in the mode shapes. To account for the difference in the vibra-

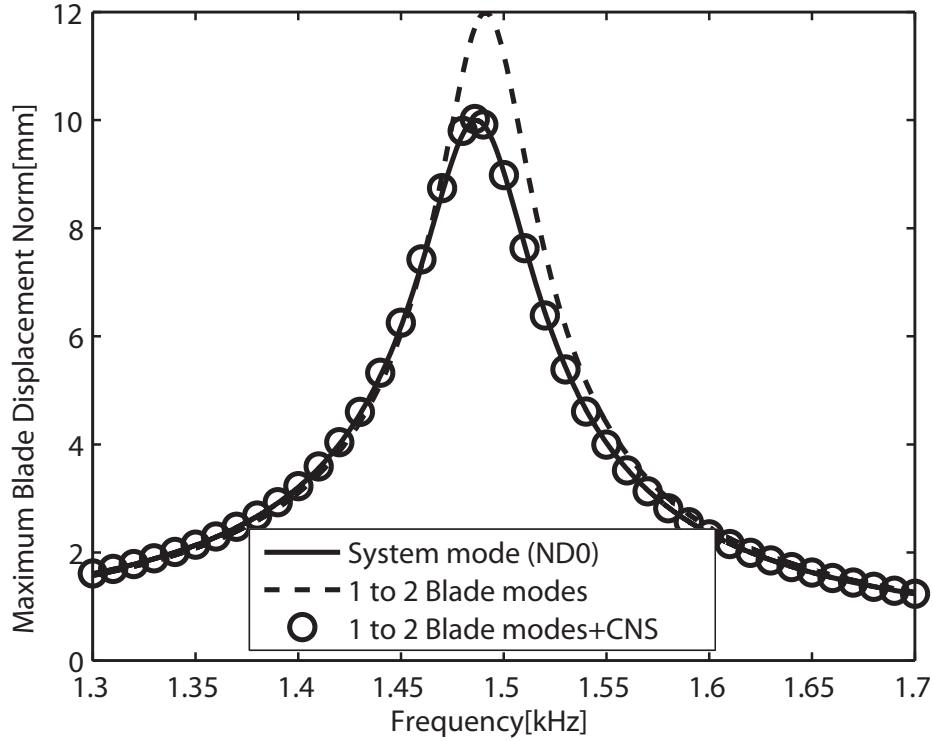


Fig. 12. Tuned forced responses to engine order 5 excitation with the aerodynamic stiffness matrix using the system mode, the second cantilever-blade normal mode with and without the constraint modes for the 1T system mode frequency range; CNS stands for constraint.

tion frequencies, a similar iterative process to the system mode method can be developed. To account for the difference in the mode shapes, the neglected constraint modes can be included. However, the inclusion of the constraint modes using the modal projection similar to Eq. (11) is practically formidable for the aerodynamic calculations because of the large number of constraint modes. For example, for this case study, the required computation time is about 4.7 seconds on a SunBlade-1000 machine for a single passage of a layer with respect to a specific mode shape and eigenvalue. Then, using the blade mode method with just one blade mode requires about 0.5 hours of computation time because there are 15 layers and 26 different interblade phase angle for every blade mode. Usually, the computational time for numerical simulations cannot be estimated using a simple multiplicative relation. However, here that is possible because the unsteady code used in this paper is a frequency domain code, and the computation time of the structural ROM code as well as the computation time of the steady aerodynamic calculation are negligible compared to the computation time of the unsteady aerodynamic calculation. Hence, using the blade mode method with one blade mode and 990 constraint modes would cost approximately 500 hours. Using the system mode method with 26 tuned system modes consumes about 0.5 hours per iteration step for the tuned system, while the required computation time is about 13 hours per iteration step for the mistuned system (because the unsteady calculation is needed for 26 different eigenvalues for every tuned system mode).

In order to investigate the effect of neglecting the constraint modes, some artificial blade modes are generated to calculate the aerodynamic stiffness shown in Eq. (7). These artificial blade modes are either the system mode related to the nodal diameter zero, or the corre-

sponding combined blade modes with or without the constraint modes (shown in Eqns. 4 and 9). For example, for the 1T system mode frequency range, these generated artificial blade modes replace the original 1T blade mode to conduct the aerodynamic calculation, and then use the modal projection shown in Eq. (11) to calculate the aerodynamic stiffness matrix. Fig. 10 shows the resulting aerodynamic stiffness coefficients (the diagonal elements of $\tilde{\mathbf{A}}$ in Eq. (7)) using these artificial modes generated from the system mode and using the second, the first two, the first four, and the first ten blade modes. The MAC number between the system mode and the corresponding 1T blade mode is 0.992, which means that they are very close to linearly dependent. However, the results using the second blade mode without the constraint modes are different from the results using the system mode. The inclusion of other blade modes changes the real part of the aerodynamic stiffness matrix, does not change the imaginary part. Nonetheless, the results with the constraint modes are in good agreement with the results using the system mode, especially when other blade modes are also included. Note that in Fig. 10, a strong sensitivity of aerodynamic stiffness coefficients on the interblade phase angle is observed, particularly for interblade phase angle index 3. It is believed that a fluid instability exists in this region for the case studied. The difference between the one-step and converged results shown in Fig. 4 can be caused by such a fluid instability which is sensitive to frequency. Fig. 12 shows the tuned forced responses to the engine order 5 excitation. The aerodynamic stiffness matrices are obtained using the artificial modes generated from the system mode and the first two blade modes (with and without the constraint modes). Significant differences in the peak forced response values and the resonance frequencies are observed between the results using the system mode and the first blade mode without the constraint modes. The inclusion of the constraint modes yields almost identical results with the results obtained using the system modes.

In principle, the blade mode method with *all* the constraint modes would be more accurate than the system mode method because the constraint modes represent all the physical coupling at the interface, while only the modal coupling between the select tuned system modes is considered in the system mode method. That would be the case only if all the constraint modal coordinates are kept in the final ROM modal space. However, the size of the final ROM modal space and the required time for the aerodynamic calculation would become extremely large. Hence, the system mode method combined with the CMM model is a very good compromise between accuracy and computation time.

**6 CONVERGENCE PREDICTIONS FOR AEROELASTIC CALCULATIONS
OF TUNED AND MISTUNED BLADED DISKS**

Mistuning, small differences between the sectors of bladed disks, can lead to drastic changes in the dynamics of such systems. The large increase in the forced response of the system due to mistuning has been observed and studied for a long time.^{34,35}

Recently, compact and accurate reduced order models (ROMs) have been developed.^{36–42} In particular, the fundamental mistuning model (FMM)⁴¹ and the component mode mistuning (CMM)³⁸ method have been proposed. These approaches use one group of tuned system modes as basis for model reduction. The results obtained without aerodynamic coupling and by using these ROMs have been shown to be as accurate as the results obtained using the finite element method (FEM).^{38,41} However, realistic bladed disks are coupled not only structurally, but also aerodynamically. Previous studies on lumped structural parameter models showed that interblade structural coupling and mistuning are two key factors affecting mistuned systems.^{2,3} Aerodynamic forces, which provide aerodynamic damping as well as blade-to-blade coupling, may change the dynamics of the system dramatically. Also, the flutter problem arises when aerodynamic forces are considered. Hence, the inclusion of aerodynamic coupling in current ROMs is necessary.

Early studies on the frequency domain aeroelastic problem of mistuned bladed disks used simple structural and aerodynamic models.^{43–46} In these simple models, the blades are usually represented by two dimensional airfoils or cantilevered beams, and they can only have rigid body mode shapes, e.g. pitch and plunge motions, which are far from the real three-dimensional elastic motion. Recently, the aerodynamic calculation of unsteady pressure induced by elastic blade motions has been studied intensely, and numerous models have been proposed.^{13,14,47–49} However, the applications of these aerodynamic models to aeroelastic calculations are limited. Kielb et al.^{26,27} incorporated a three-dimensional Reynolds averaged Navier-Stokes (RANS) CFD code into the FMM model.⁴¹ ⁵⁰ incorporated a quasi-three dimensional potential flow CFD code into the CMM model.³⁸ Both methods use the cantilever-blade normal modes (in the complex traveling wave coordinates) and their vibration frequencies to calculate the unsteady aerodynamic forces.⁵¹ used both cantilevered blade modes and constraint modes to calculate the unsteady aerodynamic forces.

Few studies have been conducted on the *true realistic* aeroelastic calculations.⁵² used a mode modification technique to solve the tuned aeroelastic eigenvalue problem.⁵³ proposed a direct iterative method to calculate the aeroelastic eigenvalue problem.⁵⁴ used the tuned structural system modes and the aeroelastic frequencies to calculate the aerodynamic forces with an iterative method. These studies have shown that the converged tuned and mistuned results have significant differences compared to the one-step results or the results using the blade normal modes.

In,⁵⁴ the aeroelastic calculation requires much less computational time for the tuned case compared to the mistuned case. The tuned cases require about 0.5 hour for one step on a SunBlade-1000 machine and up to 5 steps to converge. The mistuned cases require about 10 hours for one step, and usually require more steps to converge compared to the tuned cases. Such large amounts of computation time make it very important to be able to predict the number of iterations needed to get converged results. This paper proposes a new hybrid method to predict the convergence history. Several critical ratios are introduced to represent the properties of the system. This new technique is hybrid in that it uses both exact information from accurate models as well as randomly generated Monte Carlo models

which allow for stochastic predictions for general aeroelastic configurations.⁵⁵ The relation between the unsteady aerodynamic forces and the aeroelastic frequencies is approximated by a linear relation, which holds for many cases. For example, in many aeroelastic problems, the changes in frequency during the iterative process are small because structural stiffness dominates the aerodynamic stiffness. Hence, structural frequencies are good starting states for the iterative calculations (initial guesses). Also, good initial guesses may be available from previous calculations, as is the case for design optimization applications. Herein, the new hybrid technique is applied to a realistic bladed disk. The simulated convergence histories give good predictions for the actual convergence histories. Monte Carlo simulations using the new hybrid technique with varying critical ratios show that the magnitudes of aerodynamic matrices and their gradients with respect to the aeroelastic frequencies are two key factors affecting the convergence history.

6.1 Aeroelastic Model

This section summarizes the approach used to include aerodynamic effects within the CMM method by using the tuned structure-only system modes with iterations over natural frequencies and mode shapes. For a complete description of the aeroelastic models using the cantilever-blade normal modes and the tuned structure-only system modes, one may refer to.^{50,54} Note that the tuned aeroelastic calculation is not discussed separately here because it is similar to the mistuned aeroelastic calculation.

In the tuned system modal space (employed by FMM and CMM methods), the modal equations for the eigenvalue and forced response problems can be expressed as^{38,54}

$$[(1 + j\gamma)\mathbf{K}^{\text{syn}} + \mathbf{K}^{\text{a}} - \omega^2\mathbf{M}^{\text{syn}}]\mathbf{q}_\phi^{\text{S}} = \mathbf{0}, \quad (21)$$

and

$$[(1 + j\gamma)\mathbf{K}^{\text{syn}} + \mathbf{K}^{\text{a}} - \omega^2\mathbf{M}^{\text{syn}}]\mathbf{q}_\phi^{\text{S}} = \mathbf{\Phi}_\Gamma^{\text{S},0*} \mathbf{f}, \quad (22)$$

where $*$ denotes the Hermitian of a complex matrix, $j = \sqrt{-1}$, $\mathbf{\Phi}^{\text{S},0}$ is a truncated set of normal modes (in the frequency range of interest) of the tuned system with structural coupling only, subscript Γ denotes the blade DOFs, $\mathbf{q}_\phi^{\text{S}}$ are the corresponding modal coordinates, \mathbf{K}^{a} is the complex aerodynamic coupling (stiffness) matrix related to $\mathbf{\Phi}^{\text{S},0}$, γ is the modal structural damping, \mathbf{f} is the physical force acting on the blades, and the matrices \mathbf{M}^{syn} and \mathbf{K}^{syn} are the whole modal mass and stiffness matrices, including the structural stiffness and mass mistuning components. Note that only structural stiffness mistuning is considered in this paper, and the tuned structure-only system modes $\mathbf{\Phi}^{\text{S},0}$ are normalized with respect to the tuned mass matrix in the physical domain. Hence, $\mathbf{M}^{\text{syn}} = \mathbf{I}$. Also, note that $\mathbf{K}^{\text{a}}\mathbf{q}_\phi^{\text{S}}$ represents the modal aerodynamic forces. Therefore, linearity between the blade motion and the aerodynamic forces induced by the blade motion is assumed. Such linearity holds when the blade motions are small.^{13,14} However, the dependence of the aerodynamic forces on the complex vibration frequency is nonlinear,¹³ which requires iterative calculations for accurate aeroelastic results. Note that \mathbf{K}^{a} is a complex matrix.

Due to cyclic symmetry, the tuned structure-only modes can be expressed in a standing wave form or a traveling wave form.⁵⁶ In this paper, the traveling wave form is used. Hence, for

every tuned structure-only mode, a constant phase angle σ_i between adjacent sectors exists, which is referred to as the interblade phase angle

$$\sigma_i = \frac{2\pi i}{N_B}, \quad i = 0, 1, \dots, N_B - 1, \quad (23)$$

where N_B is the number of blades, and i is the traveling wave index associated with the tuned system mode. For $i = 0$ and $i = N_B/2$ (if N_B is even), the traveling wave and the standing wave are the same. For $i = 1$ to $i = (N_B - 2)/2$ (if N_B is even) or $i = (N_B - 1)/2$ (if N_B is odd), σ_i and σ_{N_B-i} correspond to the same nodal diameter i , but with opposite traveling directions. The undamped tuned structure-only system modes related to σ_i and σ_{N_B-i} are complex conjugates. Their real and imaginary parts are the corresponding standing wave modes. It is easy to show that traveling waves with different interblade phase angles are orthogonal to each other.⁵⁶

The aeroelastic system modes can be obtained from Eq. (21) as

$$\Phi_{\Gamma,i}^{S,n} = \sum_{r=1}^{N_S} Q_{\phi,ri}^{S,n} \Phi_{\Gamma,r}^{S,0}, \quad i = 1, 2, \dots, N_S, \quad (24)$$

or in the matrix form as

$$\Phi_{\Gamma}^{S,n} = \Phi_{\Gamma}^{S,0} \mathbf{Q}_{\phi}^{S,n}, \quad (25)$$

where the superscript n denotes results after n steps of iterative calculations, N_S is the number of tuned structure-only system modes used in Eq. (21), and the matrix $\mathbf{Q}_{\phi}^{S,n}$ is in the form of

$$\mathbf{Q}_{\phi}^{S,n} = \begin{bmatrix} \mathbf{q}_{\phi,1}^{S,n} & \mathbf{q}_{\phi,2}^{S,n} & \dots & \mathbf{q}_{\phi,N_S}^{S,n} \end{bmatrix}. \quad (26)$$

The unsteady aerodynamic forces (acting on a blade and) induced by the i -th aeroelastic system mode $\Phi_{\Gamma,i}^{S,n}$ can be obtained (using superposition) by the following linear relation

$$\mathbf{F}_i^{S,n} = \sum_{r=1}^{N_S} Q_{\phi,ri}^{S,n} \mathbf{F}_{i,r}^{S,0}, \quad i = 1, 2, \dots, N_S, \quad (27)$$

where $\mathbf{F}_i^{S,n}$ is the unsteady aerodynamic force induced by the mode shape $\Phi_{\Gamma,i}^{S,n}$, and $\mathbf{F}_{i,r}^{S,0}$ is the unsteady aerodynamic force induced by the r -th tuned structure-only system mode shape $\Phi_{\Gamma,r}^{S,0}$. Note that, at the n -th iteration step, the mode $\Phi_{\Gamma,i}^{S,0}$ vibrates with the i -th *mistuned* complex system natural frequency ω_i^n (where ω_i^n is complex; see Eq. (21)). Hence, $\mathbf{F}_{i,r}^{S,0}$ is also related to ω_i^n . The elements of the aerodynamic matrix (in the mistuned aeroelastic system modal coordinates) $\hat{\mathbf{A}}^{M,n}$ can be expressed as

$$\begin{aligned} \hat{\mathbf{A}}_{ij}^{M,n} &= \Phi_{\Gamma,i}^{S,n*} \mathbf{F}_j^{S,n} \\ &= \left(\sum_{r=1}^{N_S} Q_{\phi,ri}^{S,n*} \Phi_{\Gamma,r}^{S,0*} \right) \left(\sum_{t=1}^{N_S} Q_{\phi,tj}^{S,n} \mathbf{F}_{j,t}^{S,0} \right) \\ &= \sum_{r=1}^{N_S} \sum_{t=1}^{N_S} Q_{\phi,ri}^{S,n*} \Phi_{\Gamma,r}^{S,0*} Q_{\phi,tj}^{S,n} \mathbf{F}_{j,t}^{S,0}. \end{aligned} \quad (28)$$

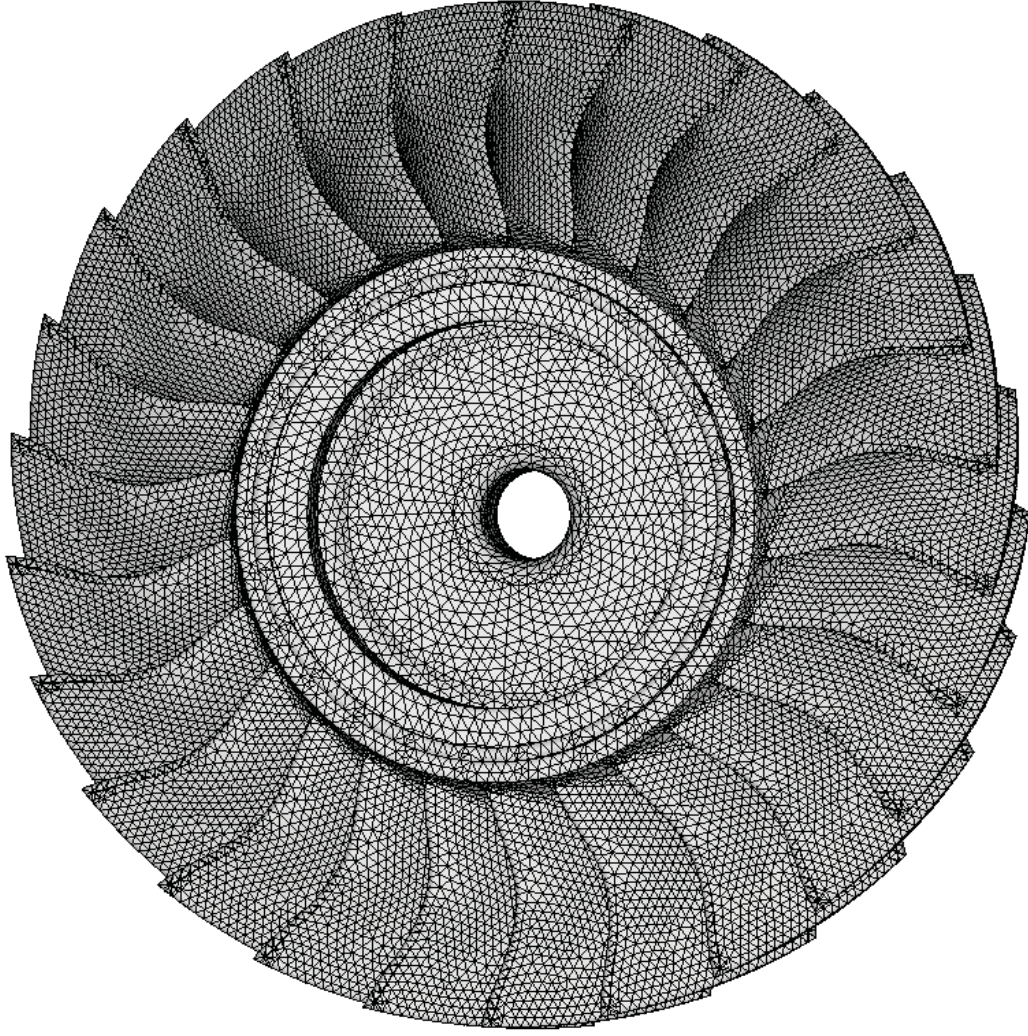


Fig. 13. Finite element model of an industrial bladed disk.

The calculations in Eq. (28) can be simplified using the orthogonality between $\Phi_{\Gamma,r}^{S,0}$ and $\mathbf{F}_{j,t}^{S,0}$ with different interblade phase angles. The aerodynamic matrix in the tuned structure-only system modal coordinates can be derived by using the modal transformation shown in Eq. (25). One obtains

$$\mathbf{K}^{a,n} = \mathbf{P}^{n*} \hat{\mathbf{A}}^{M,n} \mathbf{P}^n, \quad (29)$$

where $\mathbf{P}^n = (\mathbf{Q}_\phi^{S,n})^{-1}$ is the modal transformation from the mistuned aeroelastic system modes to the tuned structure-only system modes.

After each iteration n , the matrix $\mathbf{K}^{a,n}$ is compared to $\mathbf{K}^{a,n-1}$ and the iterative process continues until their values are converged. An aerodynamic matrix with zero elements is used for the first step of iteration.

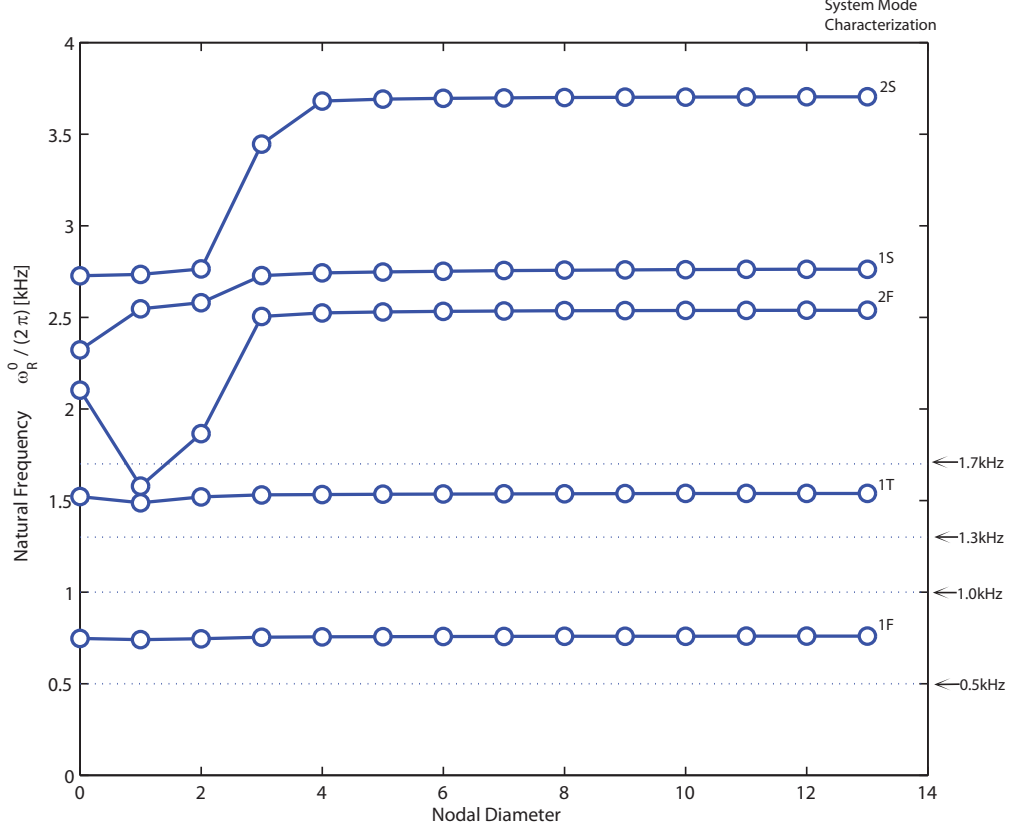


Fig. 14. Natural frequencies versus nodal diameter numbers for the tuned bladed disk assembly.

6.2 Hybrid Technique: General Case

In this section, for clarity, $\mathbf{F}(\omega_i^n, \Phi_{\Gamma,r}^{S,n})$ is used to replace $\mathbf{F}_i^{S,n}$ and $\mathbf{F}(\omega_i^n, \Phi_{\Gamma,r}^{S,0})$ is used to replace $\mathbf{F}_{i,r}^{S,0}$ in Eq. (27). Hence, Eq. (27) can be rewritten as

$$\mathbf{F}(\omega_i^n, \Phi_{\Gamma,r}^{S,n}) = \sum_{r=1}^{N_S} Q_{\phi,ri}^{S,n} \mathbf{F}(\omega_i^n, \Phi_{\Gamma,r}^{S,0}), \quad i = 1, 2, \dots, N_S. \quad (30)$$

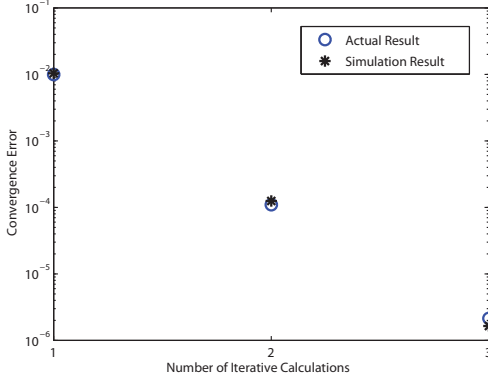
From Eqs. 25, 28 and 29, $\mathbf{K}^{a,n}$ can be expressed as

$$\begin{aligned} \mathbf{K}^{a,n} &= \mathbf{P}^{n*} \hat{\mathbf{A}}^{M,n} \mathbf{P}^n \\ &= \mathbf{P}^{n*} \mathbf{Q}_{\phi}^{S,n*} \hat{\mathbf{A}}_0^{M,n} \mathbf{P}^n \\ &= \hat{\mathbf{A}}_0^{M,n} \mathbf{P}^n, \end{aligned} \quad (31)$$

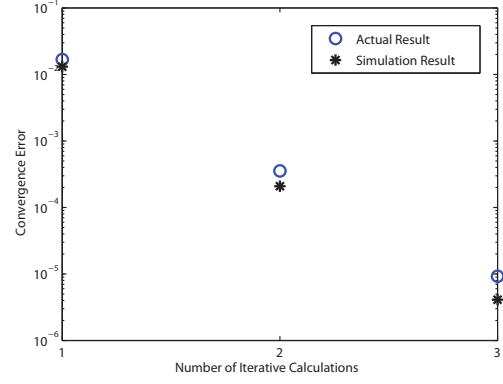
where the elements of matrix $\hat{\mathbf{A}}_0^{M,n}$ can be obtained using Eq. (30) as follows

$$\begin{aligned} \hat{\mathbf{A}}_{0,ij}^{M,n} &= \Phi_{\Gamma,i}^{S,0*} \mathbf{F}(\omega_j^n, \Phi_{\Gamma,r}^{S,n}) \\ &= \sum_{r=1}^{N_S} Q_{\phi,rj}^{S,n} \Phi_{\Gamma,i}^{S,0*} \mathbf{F}(\omega_j^n, \Phi_{\Gamma,r}^{S,0}). \end{aligned} \quad (32)$$

1F Mode group

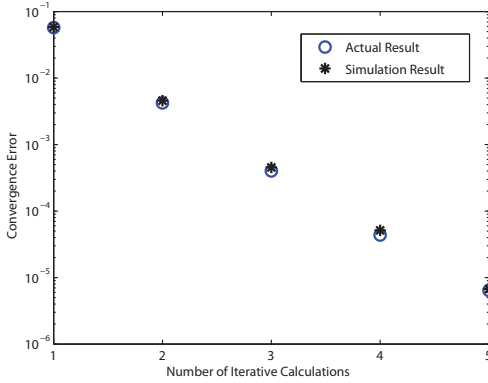


(a) Tuned case

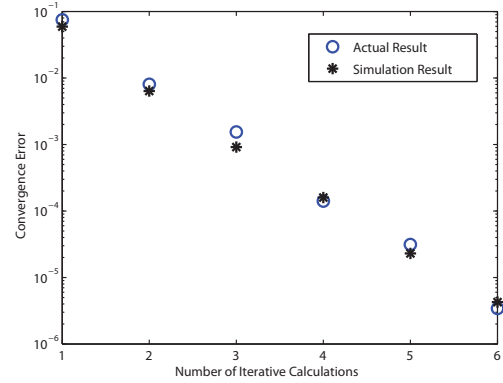


(b) Mistuned case

1T Mode group



(c) Tuned case



(d) Mistuned case

Fig. 15. Convergence errors of the actual calculation and the hybrid technique using the actual matrices.

Usually, the aerodynamic calculation to obtain each term $\Phi_{\Gamma,i}^{S,0*} \mathbf{F}(\omega_j^n, \Phi_{\Gamma,r}^{S,0})$ in Eq. (32) is very time consuming because of the large dimension of the overall problem as well as the eigenvalue analysis required for the far field nonreflective boundary conditions.⁵⁷ Hence, parametric studies for the convergence history are formidably expensive computationally. To overcome this difficulty, changes in aerodynamic forces $\mathbf{F}(\omega_j^n, \Phi_{\Gamma,r}^{S,0})$ due to changes in aeroelastic frequencies are approximated by assuming a linear dependence of aerodynamic forces on vibration frequencies. Fig. 14 shows a typical variation of the natural frequency $\omega_{R,j}^0$ (i.e. real part of ω_j^0) as a function of nodal diameter diagram, where each nodal diameter represents an interblade phase angle of a tuned system mode. The horizontal lines correspond to blade dominant modes, while the slant lines correspond to disk dominant modes. Usually, the frequency range covering only one group of blade dominant system modes is considered, so the differences between the aeroelastic frequencies are small. Although the actual dependence of aerodynamic forces on the frequencies is nonlinear, their linear approximation can give reasonable predictions about the convergence history. Also, the real and imaginary parts of the complex aeroelastic frequency are assumed to be two independent variables because the gradient of the aerodynamic forces with respect to these two variables can be distinct. Under this assumption, $\mathbf{F}(\omega_j^n, \Phi_{\Gamma,r}^{S,0})$ can be expressed as

$$\begin{aligned}
\mathbf{F}(\omega_j^n, \Phi_{\Gamma,r}^{S,0}) &\approx \mathbf{F}(\omega_r^0, \Phi_{\Gamma,r}^{S,0}) \\
&+ \mathbf{D}_R(\omega_r^0, \Phi_{\Gamma,r}^{S,0}) \frac{\omega_{R,j}^n - \omega_{R,r}^0}{\omega_{\text{ref}}} \\
&+ \mathbf{D}_I(\omega_r^0, \Phi_{\Gamma,r}^{S,0}) \frac{\omega_{I,j}^n - \omega_{I,r}^0}{\omega_{\text{ref}}},
\end{aligned} \tag{33}$$

where a subscript R denotes the real part of the complex frequency, and a subscript I denotes the imaginary part of the complex frequency, $\mathbf{D}(\omega_r^0, \Phi_{\Gamma,r}^{S,0})$ is the linear coefficient of the aerodynamic force to the relative changes of natural frequencies, ω_r^0 is the r -th structure-only complex frequency, and ω_{ref} is a reference frequency. Because only one group of blade dominant modes is considered, the mean value of the corresponding frequencies for these modes is used as ω_{ref} in this paper, except in the case of a tuned case, as discussed in Sec. 6.3. Note that the unit for ω is rad/s instead of Hz here. Therefore, one can rewrite Eq. (32) as

$$\begin{aligned}
\hat{\mathbf{A}}_{0,ij}^{M,n} &\approx \sum_{r=1}^{N_S} Q_{\phi,rj}^{S,n} \Phi_{\Gamma,i}^{S,0*} \left[\mathbf{F}(\omega_r^0, \Phi_{\Gamma,r}^{S,0}) \right. \\
&\quad + \mathbf{D}_R(\omega_r^0, \Phi_{\Gamma,r}^{S,0}) \frac{\omega_{R,j}^n - \omega_{R,r}^0}{\omega_{\text{ref}}} \\
&\quad \left. + \mathbf{D}_I(\omega_r^0, \Phi_{\Gamma,r}^{S,0}) \frac{\omega_{I,j}^n - \omega_{I,r}^0}{\omega_{\text{ref}}} \right]
\end{aligned} \tag{34}$$

or

$$\begin{aligned}
\hat{\mathbf{A}}_{0,ij}^{M,n} &\approx \sum_{r=1}^{N_S} \left[\Phi_{\Gamma,i}^{S,0*} \mathbf{F}(\omega_r^0, \Phi_{\Gamma,r}^{S,0}) Q_{\phi,rj}^{S,n} \right. \\
&\quad + \Phi_{\Gamma,i}^{S,0*} \mathbf{D}_R(\omega_r^0, \Phi_{\Gamma,r}^{S,0}) \left(Q_{\phi,rj}^{S,n} \frac{\omega_{R,j}^n - \omega_{R,r}^0}{\omega_{\text{ref}}} \right) \\
&\quad \left. + \Phi_{\Gamma,i}^{S,0*} \mathbf{D}_I(\omega_r^0, \Phi_{\Gamma,r}^{S,0}) \left(Q_{\phi,rj}^{S,n} \frac{\omega_{I,j}^n - \omega_{I,r}^0}{\omega_{\text{ref}}} \right) \right].
\end{aligned} \tag{35}$$

By examining Eq. (35), five matrices are defined as

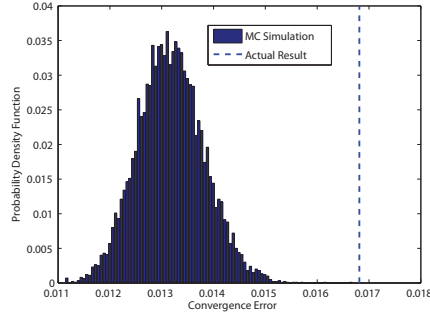
$$\mathbf{A}_{0,ij} = \Phi_{\Gamma,i}^{S,0*} \mathbf{F}(\omega_j^0, \Phi_{\Gamma,j}^{S,0}), \tag{36}$$

$$\mathbf{G}_{0,ij}^R = \Phi_{\Gamma,i}^{S,0*} \mathbf{D}_R(\omega_j^0, \Phi_{\Gamma,j}^{S,0}), \tag{37}$$

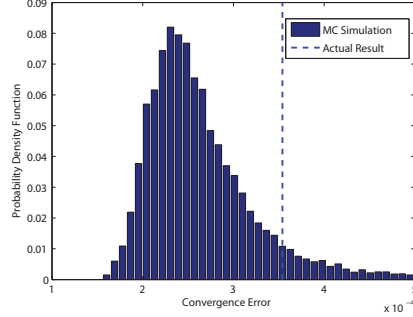
$$\mathbf{G}_{0,ij}^I = \Phi_{\Gamma,i}^{S,0*} \mathbf{D}_I(\omega_j^0, \Phi_{\Gamma,j}^{S,0}), \tag{38}$$

$$\mathbf{T}_{R,ij}^n = Q_{\phi,ij}^{S,n} \frac{\omega_{R,j}^n - \omega_{R,i}^0}{\omega_{\text{ref}}}, \tag{39}$$

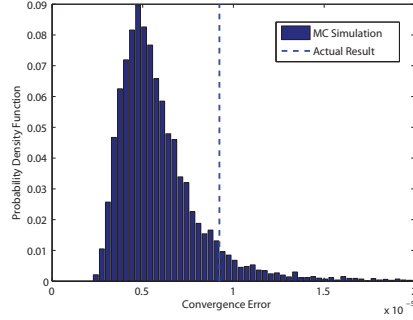
$$\mathbf{T}_{I,ij}^n = Q_{\phi,ij}^{S,n} \frac{\omega_{I,j}^n - \omega_{I,i}^0}{\omega_{\text{ref}}}. \tag{40}$$



(a) First step



(b) Second step



(c) Third step

Fig. 16. Probability density function of results using the perturbed matrices for the mistuned case in the 1F frequency range.

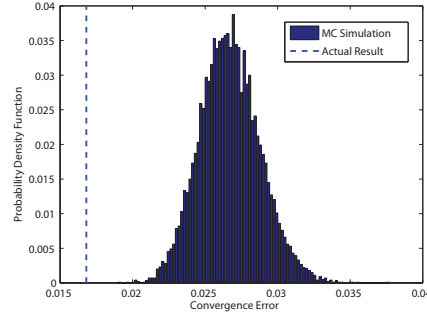
Hence, Eq. (35) can be rewritten in a matrix form

$$\hat{\mathbf{A}}_0^{M,n} = \mathbf{A}_0 \mathbf{Q}_\phi^{S,n} + \mathbf{G}_0^R \mathbf{T}_R^n + \mathbf{G}_0^I \mathbf{T}_I^n. \quad (41)$$

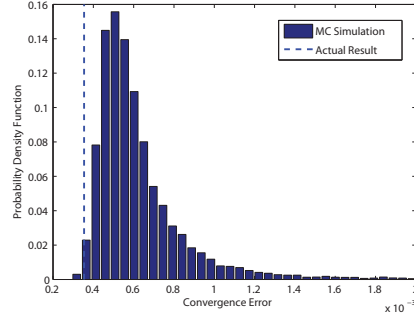
Finally, the aerodynamic matrix in the tuned structure-only system modal space $\mathbf{K}^{a,n}$ can be obtained as

$$\mathbf{K}^{a,n} = \mathbf{A}_0 + \mathbf{G}_0^R \mathbf{T}_R^n \mathbf{P}^n + \mathbf{G}_0^I \mathbf{T}_I^n \mathbf{P}^n. \quad (42)$$

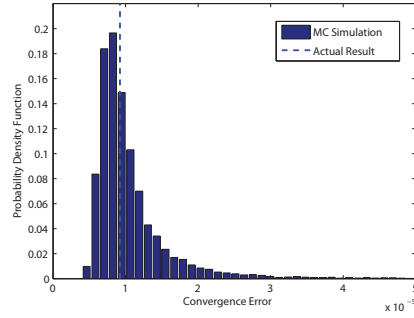
The linear dependence of $\mathbf{K}^{a,n}$ on \mathbf{T}_R^n and \mathbf{T}_I^n reflects the linear approximation of in Eq. (33). Due to the orthogonality of vectors with different interblade phase angles, \mathbf{A}_0 and \mathbf{G}_0 are block diagonal matrices in which every block corresponds to one interblade phase angle. Moreover, \mathbf{A}_0 is precisely the tuned aerodynamic matrix after the first step in the iterative calculation. In fact, during the first step calculation, an aerodynamic matrix with zero entries is used. Hence, the aeroelastic eigenvalues and eigenvectors are the structure-only ones. Thus,



(a) First step



(b) Second step



(c) Third step

Fig. 17. Probability density function of results using the totally random matrices for the mistuned case in the 1F frequency range.

both \mathbf{P}^n and $\mathbf{Q}_\phi^{S,n}$ are identity matrices, and $\omega_j^n - \omega_i^0 = 0$ when $j = i$. This results in $\mathbf{T}_R^n = \mathbf{0}$, $\mathbf{T}_I^n = \mathbf{0}$ and $\mathbf{K}^{a,n} = \mathbf{A}_0$. \mathbf{A}_0 is referred to as the aerodynamic (coefficient) matrix. \mathbf{G}_0^R and \mathbf{G}_0^I represent ratios between the change of every entry in \mathbf{A}_0 and the change of the corresponding complex natural frequency. \mathbf{G}_0^R and \mathbf{G}_0^I are referred to as the frequency gradient matrices and they can be estimated easily by changing the real and imaginary parts of the eigenvalues and recalculating the tuned aerodynamic matrix. \mathbf{T}_R^n and \mathbf{T}_I^n account for the effect of the complex frequency changes into the modal transform matrix between the aeroelastic and structure-only modal spaces. Note that \mathbf{A}_0 , \mathbf{G}_0^R and \mathbf{G}_0^I are constant during the iterative calculations, which provides very important computational savings.

To investigate the effects of various factors on the iterative process, several ratios are defined as follows

$$r_A = \frac{\|\mathbf{A}_0\|}{\omega_{\text{ref}}^2}, \quad (43)$$

$$r_G = \frac{\sqrt{\|\mathbf{G}_0^R\|^2 + \|\mathbf{G}_0^I\|^2}}{\|\mathbf{A}_0\|}, \quad (44)$$

$$r_F = \frac{\sigma(\omega_s^0)}{\omega_{\text{ref}}}, \quad (45)$$

$$r_V = \frac{\omega_D - \omega_B}{\omega_{\text{ref}}}, \quad (46)$$

$$r_M = \frac{\|\mathbf{K}_M^{\text{syn}}\|}{\omega_{\text{ref}}^2}, \quad (47)$$

where $\|\mathbf{A}_0\|$ denotes the Euclidean norm of \mathbf{A}_0 , $\sigma(\omega_s^0)$ is the standard deviation of the structural natural frequencies of the blade dominant system modes, ω_D and ω_B are the frequencies in the frequency veering region corresponding to the disk and blade dominant modes, and $\mathbf{K}_M^{\text{syn}}$ is the mistuned part of the structural stiffness matrix \mathbf{K}^{syn} . If there is no frequency veering region, $r_V = 0$. r_A , referred to as the aero ratio, denotes the strength of aerodynamic coupling. r_G , referred to as the gradient ratio, denotes the sensitivity of the aerodynamic coupling to natural frequencies. Note that only one gradient ratio is defined because the magnitudes of \mathbf{G}_0^R and \mathbf{G}_0^I are usually very similar. r_F , referred to as the frequency ratio, denotes the spread of the frequencies of the investigated group of blade dominant system modes. r_F is also an indicator of the strength of the structural coupling through the disk. A larger r_F indicates stronger structural coupling. r_V , referred to as the veering ratio, denotes the strength of the frequency veering phenomenon. Note, only one frequency veering region is considered in the current study, although multiple frequency veering regions are easy to implement. r_M , referred to as the mistuning ratio, denotes the strength of the structural mistuning. The assumption of a linear relationship between the aerodynamic forces and frequency is most likely to be violated when the fluid system is near an instability such as an acoustic resonance or shedding. Predicting the frequency of these fluid instabilities is more complicated and an alternate method, such as a quadratic approximation may be needed.

6.3 Hybrid Technique: Tuned Case

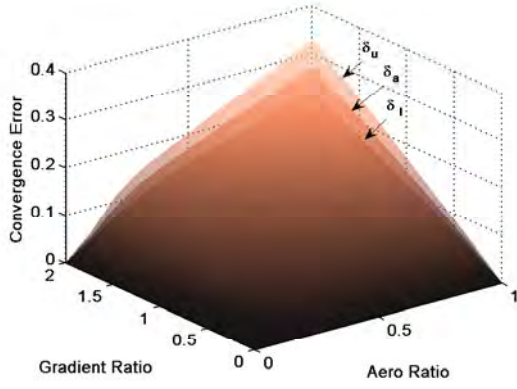
When a bladed disk is perfectly tuned, no coupling is present between the tuned structure-only system modes with different interblade phase angles. Therefore, a tuned aeroelastic mode can only be a linear combination of the tuned structure-only system modes with the same interblade phase angle. Hence, $\mathbf{Q}_\phi^{S,n}$, \mathbf{P}^n and then \mathbf{T}^n are block diagonal matrices, each block corresponding to an interblade phase angle. From Eq. (42), the aerodynamic matrix $\mathbf{K}^{a,n}$ is also a block diagonal matrix. In this case, the whole aeroelastic problem can be decomposed into N_B degraded aeroelastic problems. Therefore, Eq. (21) and Eq. (42) can be simplified as

$$[(1 + j\gamma)\mathbf{\Lambda}_i + \mathbf{K}_i^a - \omega^2\mathbf{I}]\mathbf{q}_{\phi,i}^S = \mathbf{0}, \quad (48)$$

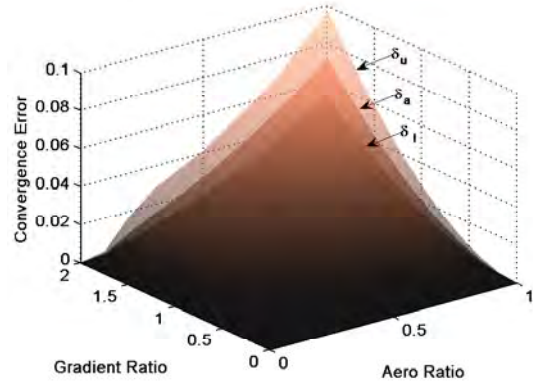
and

$$\mathbf{K}_i^{a,n} = \mathbf{A}_{0,i} + \mathbf{G}_{0,i}^R \mathbf{T}_{R,i}^n \mathbf{P}_i^n + \mathbf{G}_{0,i}^I \mathbf{T}_{I,i}^n \mathbf{P}_i^n, \quad (49)$$

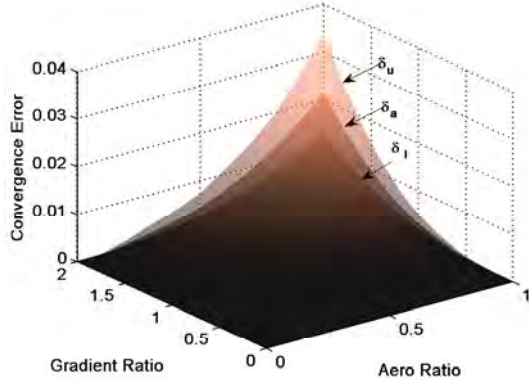
where $i = 0, 1, \dots, N_B$ is the interblade phase angle index, and $\mathbf{\Lambda}$ is the undamped tuned structural stiffness matrix. The dimension of each aeroelastic problem is the number of



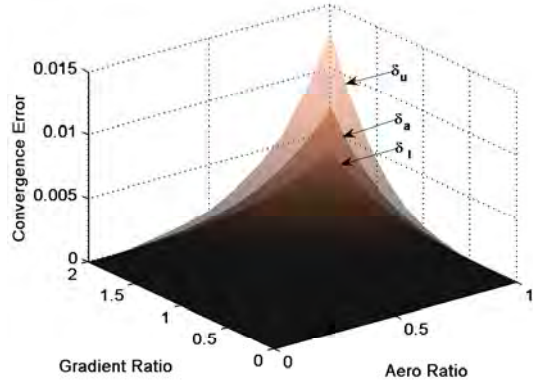
(a) First step



(b) Second step



(c) Third step



(d) Fourth step

Fig. 18. Monte Carlo simulation results (mean error δ_a and error limits δ_u and δ_l of 90 % confidence level) for a mistuned system with changing r_A and r_G .

tuned structure-only system modes related to the corresponding interblade phase angle σ_i . Compared to the general case, the dimension of the problem is one order of magnitude smaller. Hence, the computation time saving is very important, especially when parametric studies are desired, such as is the case for the Monte Carlo simulations.

In this paper, only two aeroelastic modes are considered in the simplified tuned case study. Although more aeroelastic modes can be included easily in the computation, in most of practical calculations (like the case of a frequency veering region), it is enough to consider just two modes. For simplicity, the index i is dropped from Eq. (48) and Eq. (49), and a superscript or a subscript T is used to denote the simplified tuned case. For example,

$$\mathbf{\Lambda}_i = \mathbf{\Lambda}^T = \text{Diag}(\omega_{01}^2, \omega_{02}^2), \quad (50)$$

$$\mathbf{K}_i^a = \mathbf{K}_T^a, \quad (51)$$

$$\mathbf{A}_{0,i} = \mathbf{A}_0^T, \quad (52)$$

$$\mathbf{G}_{0,i}^R = \mathbf{G}_0^{TR}, \quad (53)$$

$$\mathbf{G}_{0,i}^I = \mathbf{G}_0^{TI}, \quad (54)$$

where Diag denotes a diagonal matrix, and ω_{01} , ω_{02} are the two undamped tuned struc-

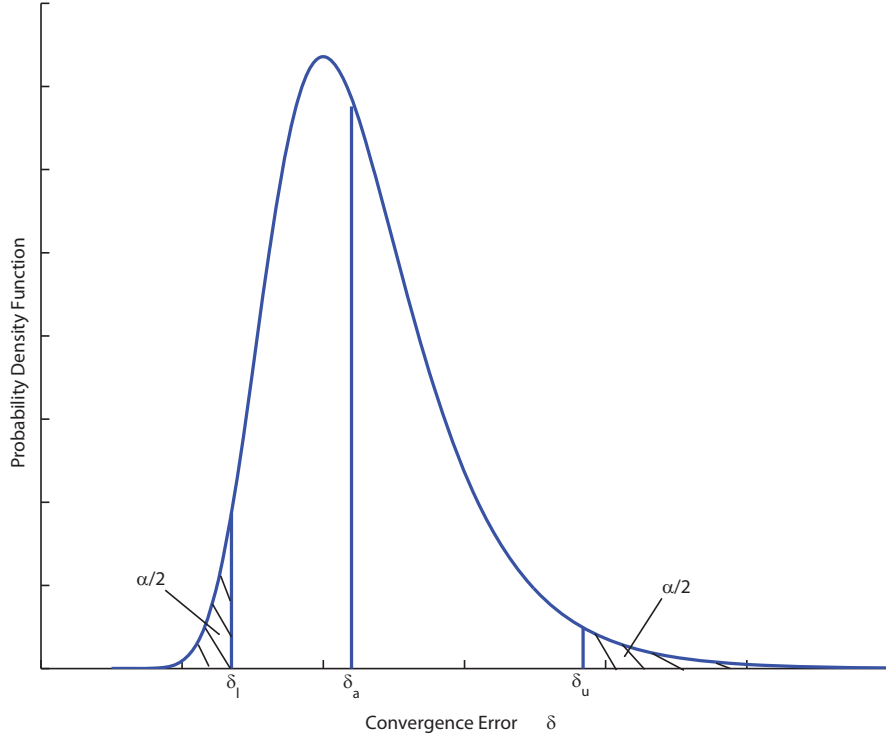


Fig. 19. Illustration of confidence levels with confidence $1 - \alpha$.

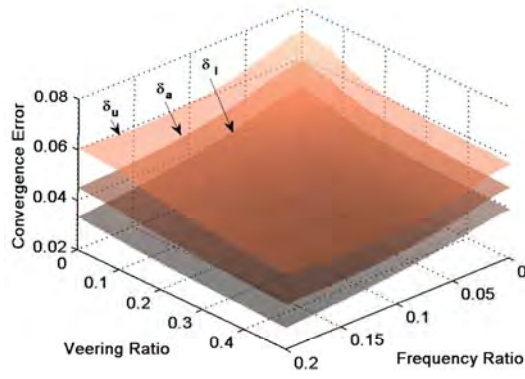
tural frequencies in the veering region. The frequency ratio r_F and mistuning ratio r_M are disregarded in this case, and the veering ratio r_V^T is redefined as

$$r_V^T = \frac{\omega_{02} - \omega_{01}}{\omega_{01}}. \quad (55)$$

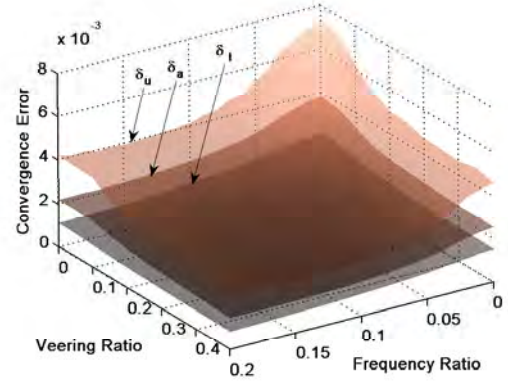
6.4 Results and Discussion

6.4.1 Case Study for an Actual Bladed Disk

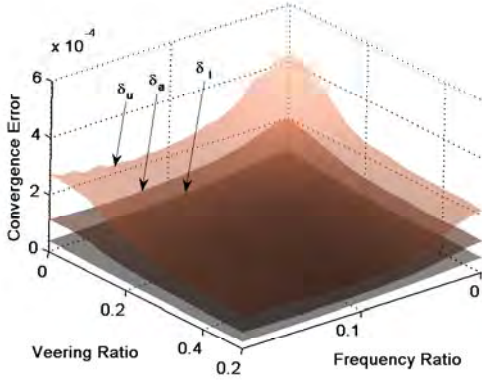
In this section, the convergence histories of the aeroelastic calculations for an industrial bladed disk from previous studies⁵⁴ are reproduced using the hybrid technique. The 26-bladed disk shown in Fig. 13 represents a stage of an industrial turbine. Fig. 14 shows the structural natural frequencies versus nodal diameter numbers for the tuned system. Two frequency ranges were studied in.⁵⁴ The first one features the first group of system modes (first flexural: 1F), ranging from 500 Hz to 1000 Hz. The other one features the second group of system modes (first torsion: 1T). Because there is a frequency veering region in the 1T frequency range, the dimension for this frequency range is 28. The blade stiffness mistuning pattern considered in this paper has a standard deviation of 0.027 and a mean value of zero. The structural damping used for aeroelastic calculation is 0.001. The mass ratio μ of the airfoil is 310, where $\mu = m/(\rho\pi b^2)$ with m denoting the mass of the airfoil per unit span, ρ denoting the steady flow density and b denoting half of the chord length. One step



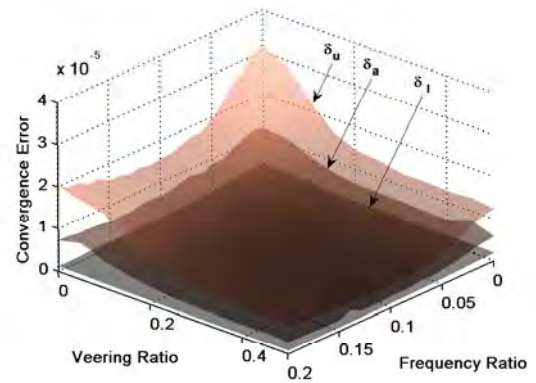
(a) First step



(b) Second step



(c) Third step



(d) Fourth step

Fig. 20. Monte Carlo simulation results (mean error δ_a and error limits δ_u and δ_l of 90 % confidence level) for a mistuned system with changing r_F and r_V .

in the iterative calculation consumes about 40 minutes for the tuned case and 7 hours for the mistuned case on a SunBlade-1000 machine. The tuned and mistuned structural modal stiffness matrices can be obtained directly from the CMM computer code *Turbo-Reduce 2002*.³⁸ The aerodynamic coefficient matrix \mathbf{A}_0 can be obtained after one step of calculation for the tuned system. The frequency gradient matrices \mathbf{G}_0^R and \mathbf{G}_0^I can be calculated as discussed in Sec. 6.2. The sensitivity matrices \mathbf{D}^R and \mathbf{D}^I are calculated by using a finite difference approach, i.e., by perturbing the real and imaginary parts of the complex frequency and calculating the changes in aerodynamic forces. Tab. 2 shows the reference frequency and the actual ratios for these two frequency ranges. The bladed disk considered here has relatively weak structural coupling and relatively strong aerodynamic damping. For real turbomachinery bladed disks, the frequency variation of structural-only system modes can be as high as 80% for some blisks and the aerodynamic damping is within the range of 1% for most turbomachinery blading. Fig. 15 shows the simulated and actual convergence errors versus numbers of calculation step for the tuned and mistuned systems in the 1F and 1T frequency ranges. The convergence error is defined as

$$\delta^n = \frac{|\mathbf{K}_{n+1}^a - \mathbf{K}_n^a|}{|\mathbf{K}_{n+1}^a|}, \quad (56)$$

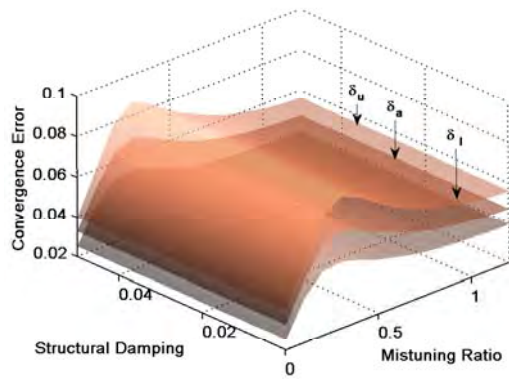
where $|\mathbf{K}_n^a|$ denotes the sum of absolute values of all the entries in the aerodynamic matrix \mathbf{K}^a after n -th step of calculation. Because $\mathbf{K}_0^a = \mathbf{0}$ is used, δ^0 is always equal to 1, and hence it is not shown. The actual iteration stops when $\delta^n \leq 10^{-5}$. The simulated results match very well the actual results. For the mistuned case, in the 1F frequency range, the differences between the simulated and actual results are slightly larger than those in other cases. These differences are likely caused by the nonlinear relation between the aerodynamic forces and the aeroelastic natural frequencies. Hence, the predictions made for convergence histories are less accurate for cases of strong nonlinear dependence of aerodynamic forces on frequency. Nonetheless, for many cases this dependence is approximately linear. For example, in many aeroelastic problems, the changes in frequency during the iterative process are small because good starting states for the iterative calculations (initial guesses) are available (e.g. from structural frequencies, or from previous calculations, as is the case for design optimization applications). To address general aeroelastic configurations, perturbed matrices are used. For example, for the matrix \mathbf{A}_0 , a perturbed matrix \mathbf{A}_0^P is generated by perturbing every entry of \mathbf{A}_0 with a random percentage within a certain range. If that certain range is ϵ_A , an element of \mathbf{A}_0^P can be obtained as

$$\mathbf{A}_{0,ij}^P = (1 + \epsilon_{A,ij}) \cdot \mathbf{A}_{0,ij}, \quad i, j = 1, 2, \dots, N_S, \quad (57)$$

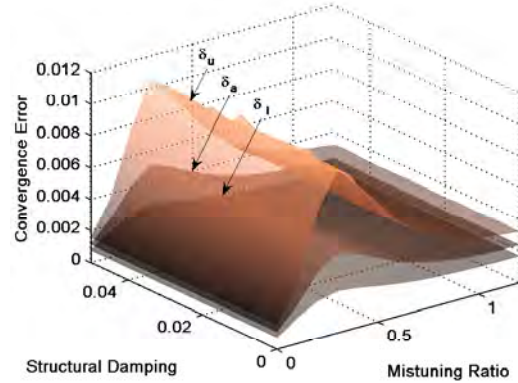
where $\epsilon_{A,ij}$ is a random number, and $\epsilon_{A,ij} \in [-\epsilon_A, \epsilon_A]$. Fig. 16 shows the probability density function (PDF) of the convergence errors using the randomly perturbed matrices for the mistuned 1F case. 10,000 samples are used and the percentage ranges are 0.3 for \mathbf{A}_0 , \mathbf{G}_0^R and \mathbf{G}_0^I , and 0 for others. The actual results are also plotted on Fig. 16. Although the calculation of aerodynamic forces is still linear, the actual results are in the ranges of the PDF or close. Note that in this case, the numerical simulation requires only about 3 minutes for each iteration step with 10,000 samples.

Also, one can generate all the matrices randomly using the acquired ratios defined in Sec. 6.2. For example, the reference frequency can be set to be the average of the structural frequencies of the blade dominant modes. Next, every entry of \mathbf{A}_0 can be generated randomly first, and then the Euclidean norm of \mathbf{A}_0 is forced to match the actual aero ratio r_A . Fig. 17 shows the PDF of the convergence errors using the totally random matrices for the mistuned 1F case. As shown in Fig. 17, the hybrid technique using totally random numbers with fixed ratios predicts the actual results with good accuracy. One may observe that the ranges of the PDF in Fig. 16 are larger than those in Fig. 17. This is because the sampled space of totally random systems includes the space of slightly perturbed systems. Hence, the actual convergence errors are closer to the broader ranges of the Monte Carlo predictions (i.e. Fig. 16). Also, the first step results in Fig. 16 and Fig. 17 are less accurate than the results after more iterations. For the results after more iterations, the changes in the complex frequencies (compared with results of the last iterative step) become smaller. Therefore, the assumption of linearity between aerodynamic forces and complex frequencies is more closely satisfied, and the hybrid approach is more accurate.

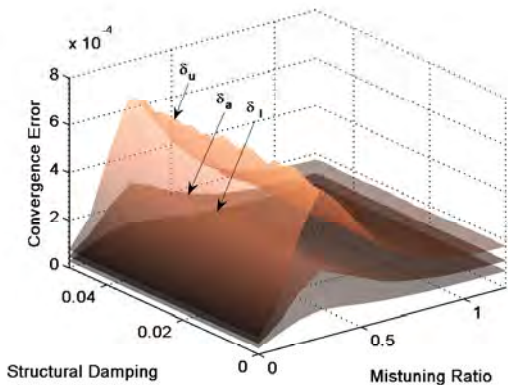
Tab. 3 shows the relative errors of the converged results using the hybrid method compared with the actual converged results. For the 1F frequency range, the errors are small (although above 10^{-5}). For the 1T frequency range, the errors are larger. This is likely caused by the fact that, having a veering region, the eigenvalues in the 1T frequency range have a broader range than those in the 1F frequency range. Hence, the errors become larger. However, the purpose



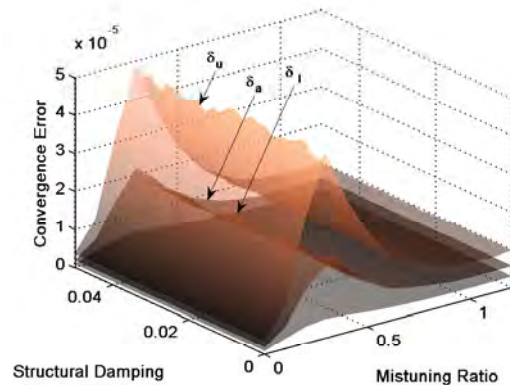
(a) First step



(b) Second step



(c) Third step



(d) Fourth step

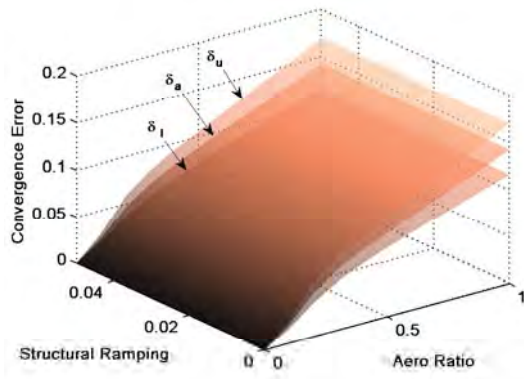
Fig. 21. Monte Carlo simulation results (mean error δ_a and error limits δ_u and δ_l of 90 % confidence level) for a mistuned system with changing r_M and γ .

of the hybrid technique is to predict the *convergence history* of the aeroelastic calculation correctly and quickly, and not to predict the actual aeroelastic results.

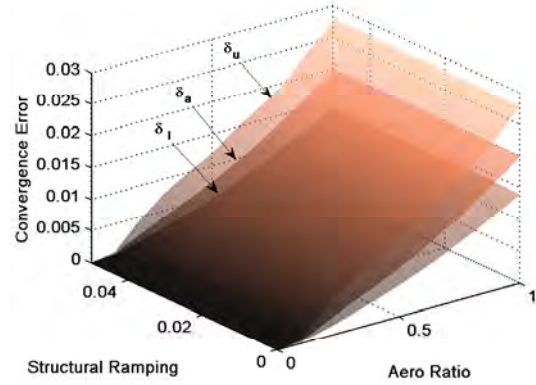
6.4.2 General Monte Carlo Simulation

To investigate the effects of various factors on the iteration convergence, a Monte Carlo simulation is performed by changing two ratios while other ratios are kept constant. For every combination of these ratios, all the matrices are determined randomly by matching the ratios and the predefined reference frequency. Actually, under this formulation, the results will hold irrespective of the reference frequency. The dimension of the system is 10 for normal cases and 12 for cases with a frequency veering region. Usually, actual systems have larger dimensions. However, a 10-dimension system is considered large enough to study the effects of critical factors. 10,000 samples are used for every combination of the ratios. The nominal values of the ratios are 0.3 for r_A , 1.0 for r_G , 0.01 for r_F , 0 for r_V , 0.2 for r_M and 0.001 for γ .

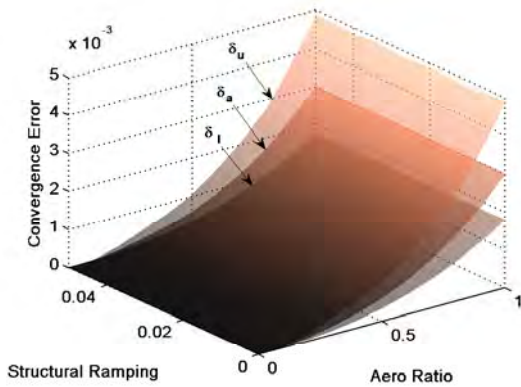
Fig. 18 shows the convergence error with changing r_A and r_G . The mean error, as well as the 90% confidence levels are plotted. As shown in Fig. 19, for a confidence $1-\alpha$, a $\alpha/2$ portion of all the samples fall below the lower confidence level δ_l and fall beyond the upper confidence



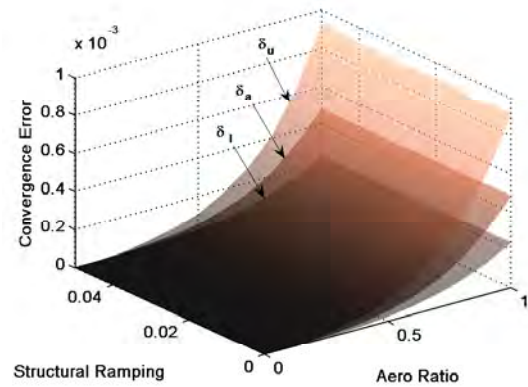
(a) First step



(b) Second step



(c) Third step



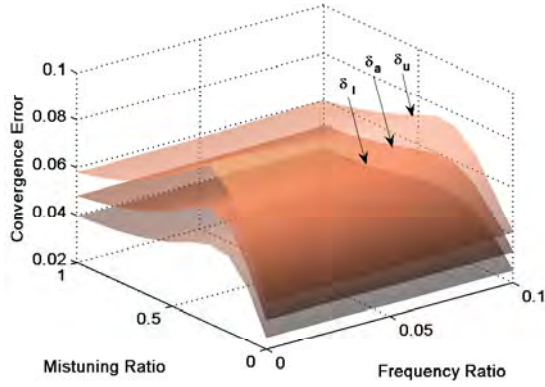
(d) Fourth step

Fig. 22. Monte Carlo simulation results (mean error δ_a and error limits δ_u and δ_l of 90 % confidence level) for a mistuned system with changing r_A and γ .

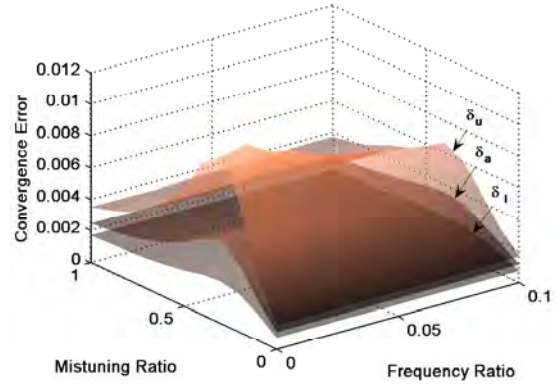
level δ_u .⁵⁸ Also shown in Fig. 19 is the average (mean) error δ_a . When $r_A = 0$ or $r_G = 0$, which represents no aerodynamic influence or no aerodynamic matrix dependence on the complex frequency, the convergence error is 0. The convergence error becomes larger when r_A or r_G grows. If both r_A and r_G are very large, convergence cannot be achieved. This phenomenon is not shown in Fig. 18 because the iterative calculation fails in such a situation. A large r_A indicates that the system has a large aerodynamic matrix, which can change the complex aeroelastic frequency significantly. A large r_G makes this aerodynamic matrix sensitive to the change of aeroelastic natural frequencies. Hence, the iterative process fails to converge when r_A and r_G are both large. Note that the computation time for one iteration step in this case is about 70 minutes with 10,000 samples.

Fig. 20 shows the convergence error with changing r_F and r_V . The basic trend is that the system converges slower when r_F or r_V becomes smaller. However, the effect is relatively small, and there is no case in which convergence cannot be achieved.

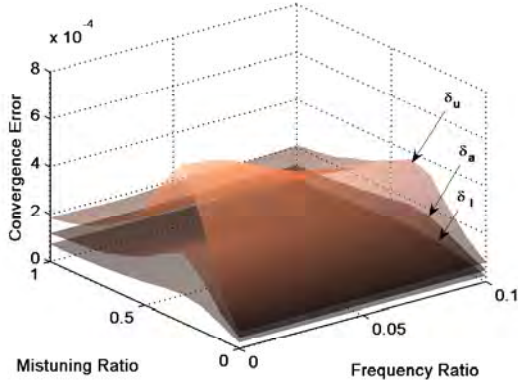
The convergence error with changing r_M and γ is shown in Fig. 21. The structural damping γ has no significant effect on the convergence error. When the mistuning ratio r_M becomes larger, the convergence error first grows rapidly, then drops, and finally approaches a constant value. The mistuned system converges always slower than the tuned one. There are



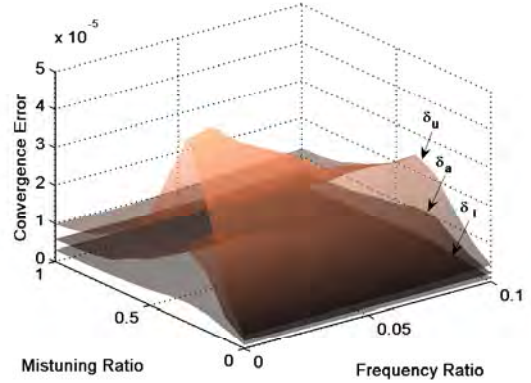
(a) First step



(b) Second step



(c) Third step



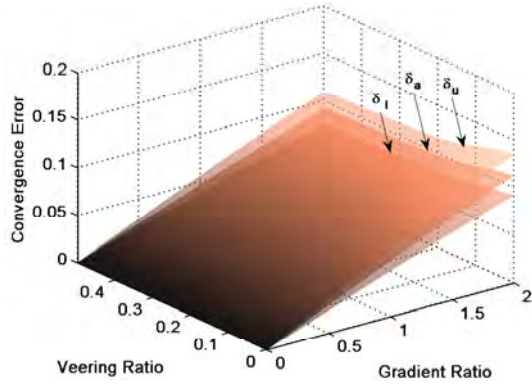
(d) Fourth step

Fig. 23. Monte Carlo simulation results (mean error δ_a and error limits δ_u and δ_l of 90 % confidence level) for a mistuned system with changing r_F and r_M .

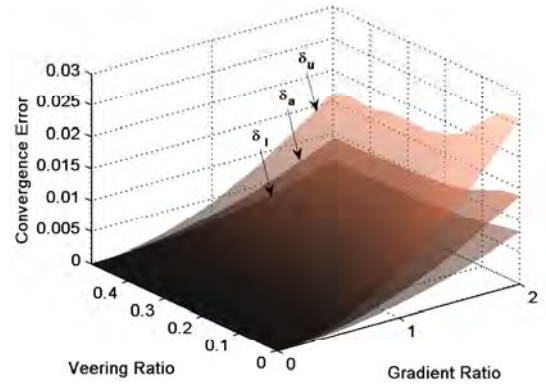
two major consequences of the growth of r_M . First, the differences between the tuned and mistuned structural frequencies become larger. Second, the off-diagonal terms in $\mathbf{Q}_\phi^{S,n}$ become larger. Note that when the system is tuned, $\mathbf{Q}_\phi^{S,n}$ is a block diagonal matrix. Both factors make the matrices \mathbf{T}^R and \mathbf{T}^I in Eq. (41) have larger variations during the iterations. When the mistuning level is relatively small, this effect dominates, and the system converges harder. However, when the mistuning level is very large, the combined (tuned and mistuned) structural stiffness matrix becomes larger, which makes the relative effect of the aerodynamic matrix smaller. Then, the system exhibits a slow reduction in the convergence error. Also, overall, the effect of r_M on the convergence is small compared to r_A and r_G .

As shown in Fig. 15, the convergence error is larger for a mistuned system than a tuned system, which can be predicted from Fig. 21. Also, the convergence error is larger for the 1T frequency range than for the 1F frequency range. From Tab. 2, the major differences between the critical ratios for these two frequency ranges are r_G and r_V . Because the effect of r_V is not very significant, the larger value of r_G for the 1T range is the major reason for the slower convergence in this frequency range.

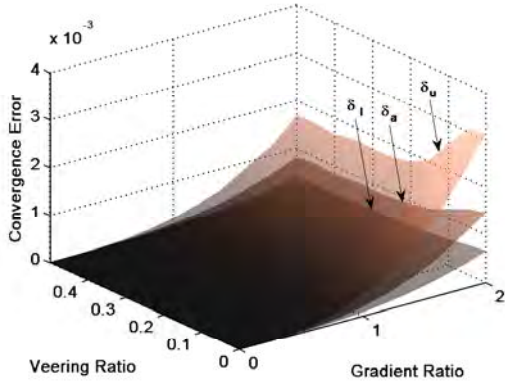
Fig. 22 shows the convergence error with changing r_A and γ . The structural damping has no significant effect on the convergence error. The convergence error increases quickly when the



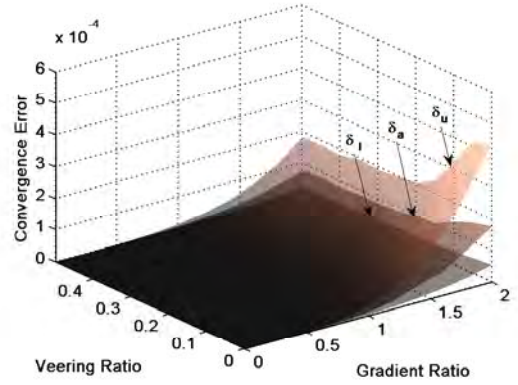
(a) First step



(b) Second step



(c) Third step



(d) Fourth step

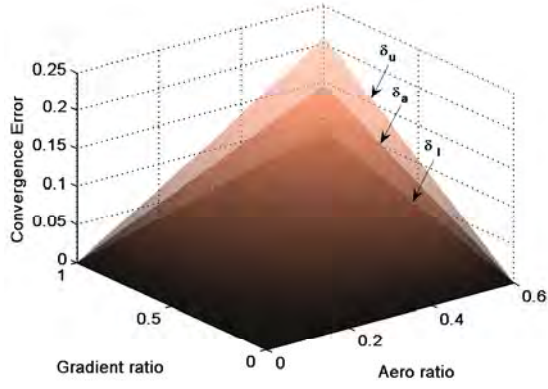
Fig. 24. Monte Carlo simulation results (mean error δ_a and error limits δ_u and δ_l of 90 % confidence level) for a mistuned system with changing r_G and r_V .

aero ratio r_A becomes larger. Fig. 23 shows the convergence error for various ratios r_F and r_M . The effect of the frequency ratio r_F on the convergence error is small. When the mistuning ratio r_M increases (from 0), the convergence error increases rapidly first, and then decreases smoothly. Fig. 24 shows the convergence error for various r_G and r_V . A larger gradient ratio r_G makes the aeroelastic iterations harder to converge, while a larger veering ratio r_V makes the iterations easier to converge. However, the effect of r_G is much more significant than r_V .

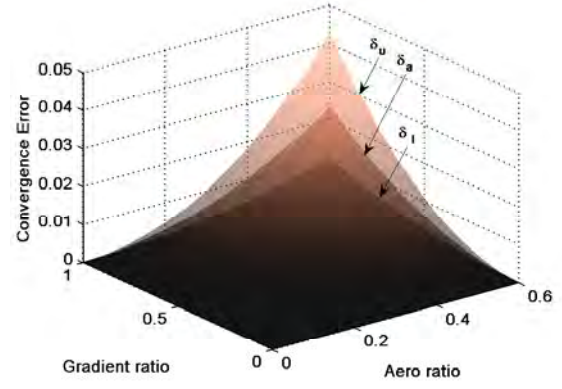
6.4.3 Monte Carlo Simulation: Tuned System

A tuned system described in Sec. 6.3 is studied. The only critical ratios considered here are r_A^T , r_G^T and r_V^T . 10,000 samples for every combination of these ratios are used for the Monte Carlo simulation. The smallest one of the tuned undamped structural natural frequencies is used as a reference frequency. For this case, the largest relative error in the aerodynamic damping with one-step calculation is 20% compared to the converged result.

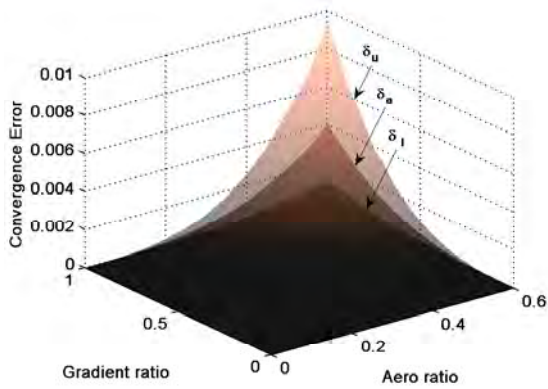
Fig. 25 shows the convergence error with changing r_A^T and r_G^T . The veering ratio r_V^T is 0. Similar to Fig. 18, larger r_A^T and r_G^T make the aeroelastic calculation harder to converge. This is consistent with,⁵³ where Moyroud et al. state that tuned bladed disks made of composites



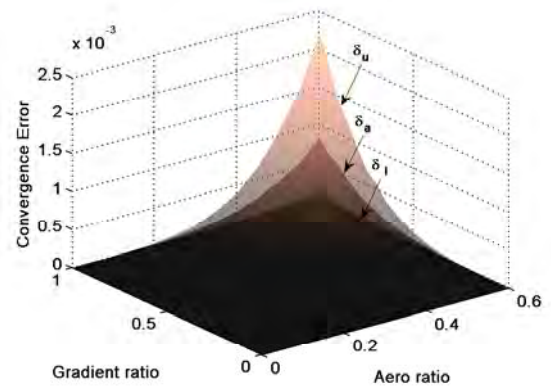
(a) First step



(b) Second step



(c) Third step



(d) Fourth step

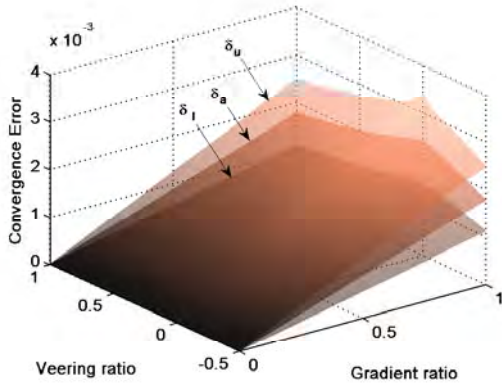
Fig. 25. Monte Carlo simulation results (mean error δ_a and error limits δ_u and δ_l of 90 % confidence level) for a tuned system with changing r_A^T and r_G^T .

Table 2

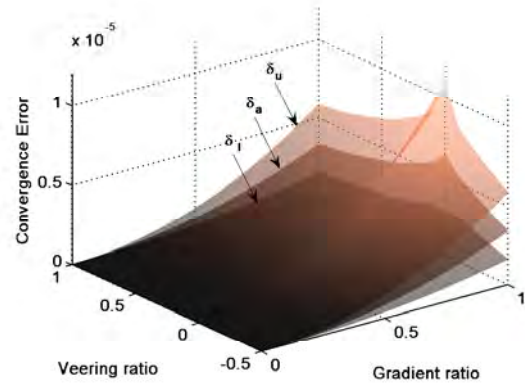
Reference frequency and actual ratios for the 1F and 1T frequency ranges of the industrial bladed disk.

Frequency range	1F	1T
ω_{ref} (rad/s)	4745	9616
r_A	0.237	0.289
r_G	0.625	2.415
r_F	7.96×10^{-3}	8.94×10^{-3}
r_V	0.0	5.92×10^{-2}
r_M	0.131	0.0134
γ	0.006	0.001

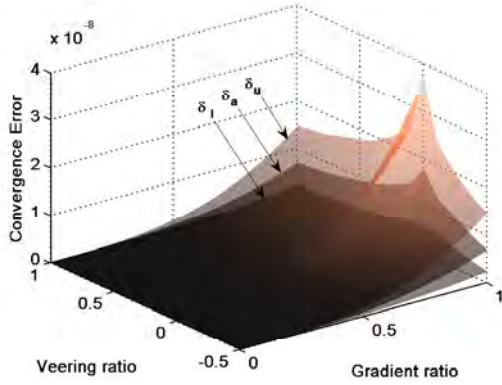
are harder to converge than the tuned bladed disks made of metallic alloys. This is explained herein by the fact that, for composite bladed disks, the ratios r_A^T and r_G^T are smaller than those of metallic bladed disks under the same operation point and with the same geometry. Actually, from Sec. 6.4.2, this conclusion also holds for the mistuned case. The convergence



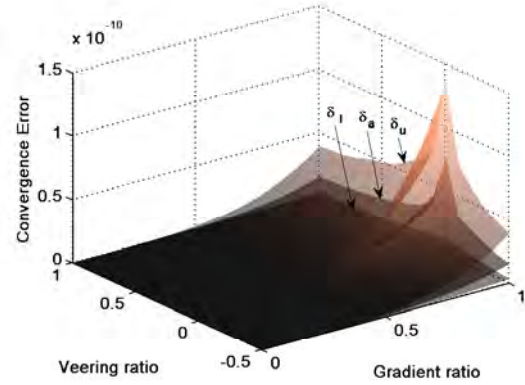
(a) First step



(b) Second step



(c) Third step



(d) Fourth step

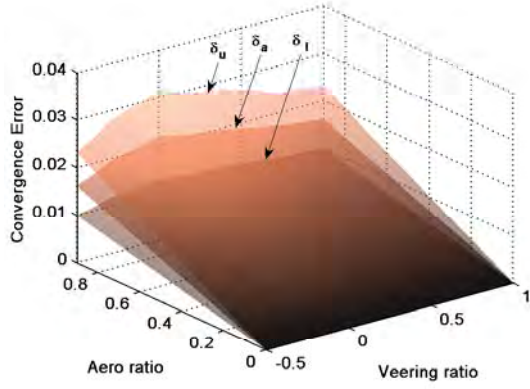
Fig. 26. Monte Carlo simulation results (mean error δ_a and error limits δ_u and δ_l of 90 % confidence level) for a tuned system with changing r_G^T and r_V^T .

Table 3

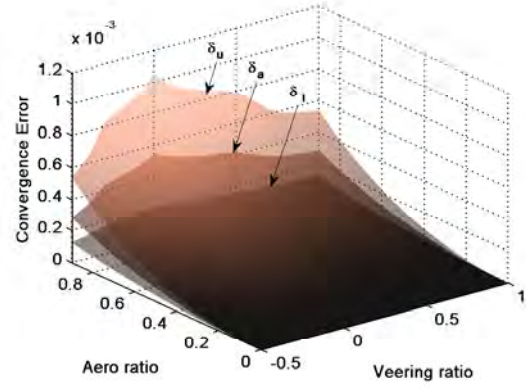
Relative errors between simulated converged results and actual converged results.

System	1F Tuned	1F Mistuned	1T Tuned	1T Mistuned
Error	8.35×10^{-5}	6.55×10^{-4}	4.36×10^{-3}	1.77×10^{-2}

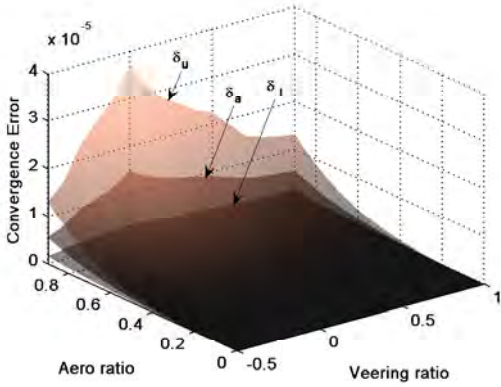
error with changing r_G^T and r_V^T is shown in Fig. 26. The aero ratio r_A^T is 0.01. Similar to Fig. 20, when the frequencies ω_{01} and ω_{02} (in Eq. (50)) are closer, the aeroelastic calculation becomes harder to converge. This result is particularly useful to be compared with the discussions of⁵² who states that for a tuned system, the stability of the iterations requires that the eigenfrequencies are well separated. Note that in Fig. 25, a system with a zero value of r_V^T can converge fast if r_A^T and r_G^T are both small. Also, note that Fig. 26 and Fig. 20 show a relatively small effect of r_V^T on the convergence error. This seems somewhat contrary to.⁵² However, in,⁵² the iteration is formulated using a mode-modification technique, which calculates the tuned aeroelastic eigenvalues and eigenvectors separately for every aeroelastic mode. The aeroelastic calculations shown here in Sec. 6.2 and Sec. 6.3 are formulated by solving the aeroelastic eigenvalue problem directly. Although this method requires more computation time for finding eigenvalues and eigenvectors, it is shown that it is better than the mode-modification technique in the sense of convergence. Fig. 27 shows the convergence



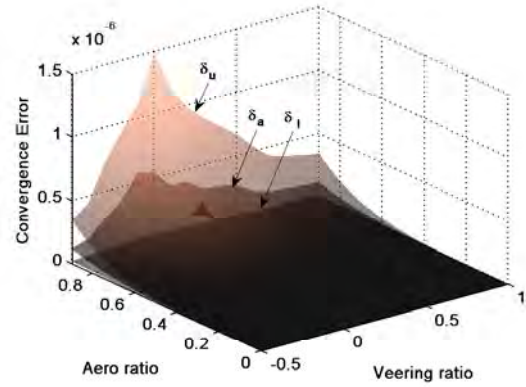
(a) First step



(b) Second step



(c) Third step



(d) Fourth step

Fig. 27. Monte Carlo simulation results (mean error δ_a and error limits δ_u and δ_l of 90 % confidence level) for a tuned system with changing r_V^T and r_A^T .

error for various r_V^T and r_A^T . The convergence error increases quickly with increasing r_A^T , and the aeroelastic iterations become harder to converge when r_V^T approaches 0.

**7 ESTIMATION AND VEERING ANALYSIS OF NONLINEAR RESONANT
FREQUENCIES OF CRACKED PLATES**

It is well known that the natural frequencies of cracked elastic structures differ from their healthy counterparts. A comprehensive literature survey of research activities regarding the vibration problems of various structures with cracks is found in the work by Dimarogonas.⁵⁹ In this paper, linear and nonlinear vibration of a cantilevered rectangular plate with a crack is investigated. The primary focus of this study is the vibration response near the *eigenvalue loci veerings* and *crossings* that occur as the crack length or location is varied. This work was motivated by an observation of closely-spaced nonlinear resonant frequencies with similar mode shapes, in the nonlinear frequency response of a turbine engine rotor with a cracked blade.⁶⁰

Eigenvalue loci veerings, also known as avoided crossings, or eigenvalue avoidance, are observed in plots of eigenvalues versus a system parameter. In particular, a veering refers to a region in which two eigenvalue loci approach each other and almost cross as the system parameter is changed, but instead of crossing they appear to veer away from each other, with each locus then following the previous path of the other.⁶¹ Although this phenomenon was initially regarded as an “aberration” caused by approximation methods applied to the original infinite-dimensional eigenvalue problems,⁶² it was shown by Perkins and Mote⁶³ that the phenomenon can be observed for continuous systems. Since then, several researchers have noted and investigated the relation between veerings and mode localization phenomena.^{64–66} In conjunction with the localization, it is known that the veerings are associated with coupling between the modes, which is typically seen as the mixed mode shapes near the veering regions. There can also be a mixing between modes in different physical domains, such as electrical and mechanical domains.⁶⁷ These phenomena have also been investigated for the damaged structures, such as two-span weakened column,⁶⁸ and cables with damage.⁶⁹

For vibration problems of cracked rectangular plates, variations in natural frequencies and mode shapes due to crack length variations have been known for a long time. The initial contribution to the study of vibration problems of cracked rectangular plates was made by Lynn and Kumbasar,⁷⁰ who calculated the vibration frequency drop of plates due to cracking by numerically solving the Fredholm integral equation of the first kind. Petyt⁷¹ also investigated the variation of frequency of fundamental mode due to crack length by experiments and a finite element method. Those contributions were followed by a number of investigations based on plate vibration theory, including those by Stahl and Keer,⁷² Hirano and Okazaki,⁷³ Solecki,⁷⁴ and Yuan and Dickinson.⁷⁵ Although the trajectories of frequencies versus crack length appear in these articles, the veering regions and associated dynamics of the cracked plates near those regions were not highlighted. Liew *et al.*⁷⁶ applied a domain decomposition method to obtain the out-of-plane vibration frequencies of cracked plates, and they not only confirmed the results found by Stahl and Keer⁷² and Hirano and Okazaki⁷³ but also considered a wider range of crack length ratio. It is noted that they examined a plate with a centrally-located internal crack and reported *frequency crossings* instead of veerings. In other words, for this case they observed that two approaching eigenvalue loci would intersect as crack length increased, which is also known as *crossover*. More recently, Ma and Huang⁷⁷ also reported variations in natural frequencies and associated mode shapes due to changes in crack length for a square plate with an edge crack, based on experiments and finite element analysis. As was mentioned by many others, Ma and Huang stated that the nonlinearity due to the *crack closing effect* has to be considered for the in-plane bending case, but crack closing was neglected in their study because their work focused on the out-of-plane bending vibration.

In the studies of cracked rectangular plate vibrations reviewed above, the in-plane bending vibration was not considered and thus the crack closing effect was not examined. In contrast, the issue of crack closing effect naturally arose in the studies of vibration problems of cracked beams, for which in-plane bending vibration is typically of primary research interest. For the study of cracked Bernoulli-Euler beams, a pioneering contribution was made by Christides and Barr in their application of the Hu-Washizu-Barr variational principle to the cracked beam problem.⁷⁸ Further extension was made by Shen and Pierre for Bernoulli-Euler beams with symmetric cracks⁷⁹ and single-edge cracks.⁸⁰ A generalization to the theory was made by Chondros *et al.*⁸¹ However, in these studies, the nonlinear effect was not considered. Gudmundson⁸² pointed out that measured natural frequencies of a beam with a fatigue crack differ from those calculated without considering the crack closing effect. He also addressed the significance of the crack closing effect for accurately predicting the frequency shifts due to cracking. The crack closing effect is also known to cause phenomena that appear only in nonlinear response cases, such as superharmonic and subharmonic resonances^{83,84} and period doubling bifurcations.^{85,86}

One of the methods to estimate the (primary) resonant frequencies of the cracked beams is the application of the *bilinear frequency* approximation. This was initially introduced for calculating the effective resonant frequencies of piecewise linear oscillators (e.g., Shaw and Holmes⁸⁷), and it has been used for approximating the effective vibration frequency of multi-DOF piecewise linear systems (e.g., Butcher⁸⁸). It has also been used for estimating the natural frequency of cracked beams.^{86,89,90} Chati *et al.*⁹¹ extended the concept of the bilinear frequency to study the vibration of a cracked beam using a multi-DOF oscillator model. They assumed that if the crack is sufficiently shallow, the actual and bilinear mode shapes are close to each other, and thus the frequency can be approximated by the bilinear frequency. Most of the methods reviewed above assume that the crack has only two states—closed or open. This assumption is accurate when the relative motion of the crack surfaces is simple, such as the in-plane bending vibration of cantilevered beams. However, in general, the motion of crack surfaces is more complicated, and there may be more than two states. For example, crack closing may proceed gradually and/or occur at different regions on the crack surfaces at different times.

The closing crack was also modeled by equivalent linear model by Kisa and Brandon,⁹² with the assumption that the stiffness change due to a crack can be expressed as a linear combination of the stiffness matrix of uncracked beam and that due to cracking and contact. An emerging approach for dealing with this issue is the application of Nonlinear Normal Modes.^{93–95} However, the applicability of this approach is still limited to simple structures or simplified vibration problems, due mostly to its computational costs for constructing the nonlinear normal modes.

With regard to the veering phenomena for nonlinear structural systems, very little is known about how the nonlinearities influence the response near the veering regions. Lacarbonara *et al.*⁹⁶ investigated nonlinear modal interactions of an imperfect beam near veering regions, the nonlinearities of which are quadratic and cubic nonlinearities due to large-amplitude vibration, through perturbation and bifurcation analyses. They observed distinguishing features in the response, such as mode localization due to nonlinear coupling and frequency-island generation, which illustrates the richness of the dynamics in veering regions for nonlinear structural systems.

In this paper, the vibration of cracked cantilevered plates in frequency veering regions is investigated. As reviewed above, veering phenomena have not been studied thoroughly for cracked structures, in either the linear or nonlinear dynamics regime. Regarding the vibration of cantilevered cracked plates, the research reviewed above focused only on the out-of-plane vibration, and crack closing effects were intentionally neglected. On the other hand, studies of cracked beams have focused on in-plane bending in most cases. Thus, the crack closing effect on the vibration response has been investigated in many studies of cracked beams. However, veering and modal interaction phenomena between in-plane and out-of-plane vibration modes have not been studied in this context. Moreover, in general, the veering phenomena in nonlinear structural systems have not been studied well. Therefore, in this paper, first the eigenvalue loci veering due to cracking is examined using a cracked cantilevered plate example without considering the crack closing effect. The crack closing effect is then included and associated nonlinear resonant frequencies are identified. A novel method for accurately estimating the nonlinear resonant frequencies is then introduced, by generalizing the concept of bilinear frequency approximation that utilizes the results of linear eigenvalue analyses of the system. The method is validated by comparing the results with those calculated by the nonlinear forced response analysis. Furthermore, the applicability of the method near the veering regions is discussed, and the effects of the crack closing on the resonant frequencies are discussed in detail for some specific veering regions.

This paper is organized as follows. In section 7.1, the cracked plate vibration problem and the finite element model are introduced. In section 7.2, the linear free response of a cracked plate is considered using a finite element model of a three-dimensional cantilevered plate with a planar surface-breaking crack that runs parallel to the cantilevered edge, and the associated frequency veering and crossing phenomena are shown. In section 7.3, a solution technique for the nonlinear forced response analysis, called the hybrid frequency/time (HFT) method, is briefly reviewed. The nonlinear forced response calculation is then carried out and the effects of nonlinearity to the response in the neighborhood of representative veering regions are discussed in detail. In section 7.4, the method for estimating the nonlinear resonant frequency is introduced as a generalization to the bilinear frequency approximation.

7.1 Cracked Plate Model

In this paper, the vibration of a cantilevered rectangular plate comprised of linear isotropic elastic material is considered. The plate is discretized with a standard finite element method (FEM), and the deformation is assumed to be infinitesimally small. In this study, nonlinearities other than the one due to intermittent contact at the crack surfaces are not considered. Namely, the governing equation of the cracked plate is

$$\mathbf{M}\ddot{\mathbf{u}}(t) + \mathbf{C}\dot{\mathbf{u}}(t) + \mathbf{K}\mathbf{u}(t) = \mathbf{b}(t) + \mathbf{f}(\mathbf{u}); \quad \mathbf{M}, \mathbf{C}, \mathbf{K} \in \mathbb{R}^{n \times n}, \mathbf{u}, \mathbf{b}, \mathbf{f} \in \mathbb{R}^n \quad (58)$$

where \mathbf{u} is the displacement vector, \mathbf{M} , \mathbf{C} and \mathbf{K} denote the mass, damping, and stiffness matrices, $\mathbf{b}(t)$ denotes the time-dependent external force, and $\mathbf{f}(\mathbf{u})$ denotes the nonlinear force caused by the intermittent contact at the crack.

A finite element (FE) model of a cantilevered plate with a transverse crack is shown in Fig. 28, where $h = 1.5 \times 10^{-1}\text{m}$, $l = 6.0 \times 10^{-2}\text{m}$, $t = 3.0 \times 10^{-3}\text{m}$. The material model is steel

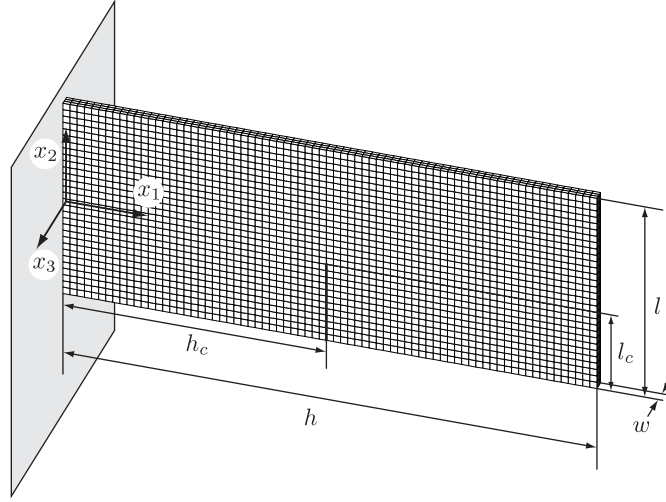


Fig. 28. Finite element model of the cracked plate

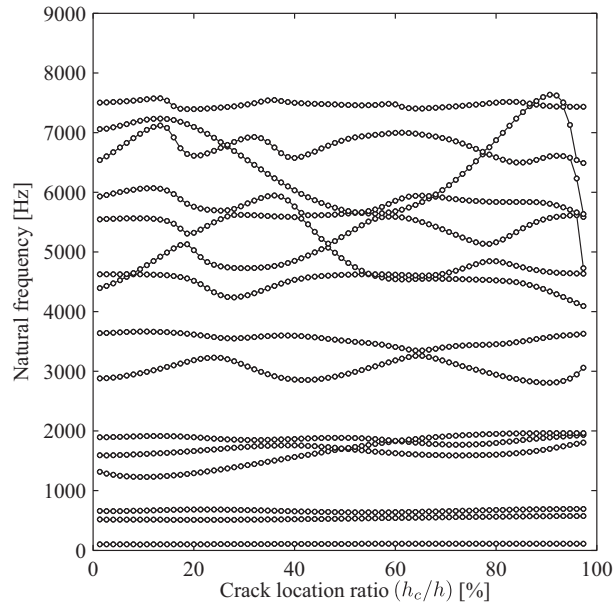
with Young's modulus $E = 200\text{GPa}$, density $\rho = 7800\text{kg/m}^3$, and Poisson's ratio $\nu = 0.3$. The FE model is composed of 6,750 brick linear elements and has approximately 28,000 DOF. This FE model is used for all the numerical results in this paper, and the generation of the FE model as well as component mode synthesis were performed with the commercial code ANSYS.⁹⁷

7.2 Linear Free Response Analysis

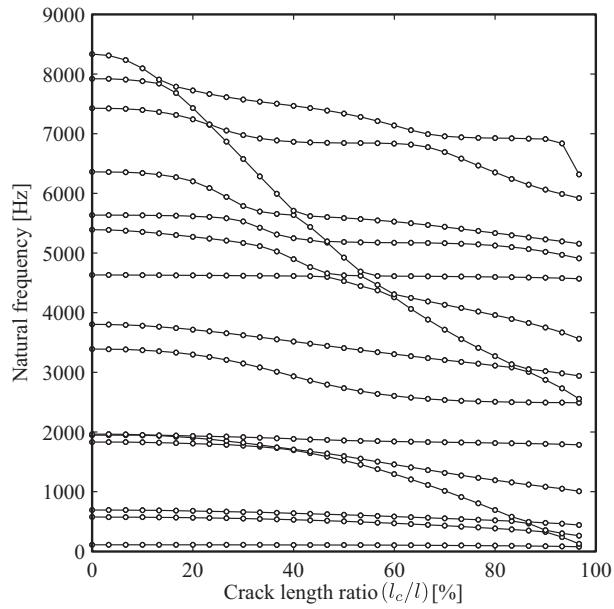
7.2.1 Natural frequency variation due to variations in crack location and length

First, in order to visualize the variations in the natural frequencies for crack parameter variations, which are closely related to the variations in the nonlinear resonant frequencies, the underlying linear system is studied in this section. Namely, the nonlinear contact force $\mathbf{f}(\mathbf{u})$ in the Eq. (58) is ignored, and for the FE model shown in Fig. 28, eigenvalue analysis was performed for various values of l_c/l and h_c/h . The results for the first 15 natural frequencies for two representative cases are shown in Fig. 29.

First, Fig. 29(a) shows the results where the crack length was fixed at $l_c/l = 40\%$, and the crack location was varied as $1.33 \leq h_c/h \leq 97.3\%$. As can be seen, the changes in the natural frequencies due to the variation in h_c/h are quite complicated, and multiple loci veerings and crossings are observed. In order to examine the individual veering regions, some cases with realistic crack length ratio, $l_c/l < 60\%$, are discussed below. For example in Fig. 29(a), starting around $h_c/h = 15\%$, modes 10 and 11 approach each other, but rather than crossing they veer away near $h_c/h = 19\%$ with high curvature. Second, the crack location was fixed at $h_c/h = 50\%$, and the crack length was varied, the results of which are shown in Fig. 29(b). The most notable distinction from the case in Fig. 29(a) is that the natural frequency variation due to crack length change is monotonic, i.e., as l_c/l increases, all natural frequencies tend to decrease. Although the amount of frequency drop is dependent on the mode of interest, this is due to the fact that the stiffness of the plate decreases monotonically for all modes as the crack length increases.



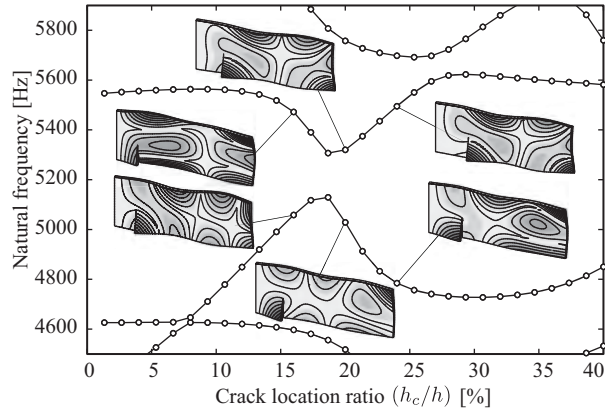
(a)



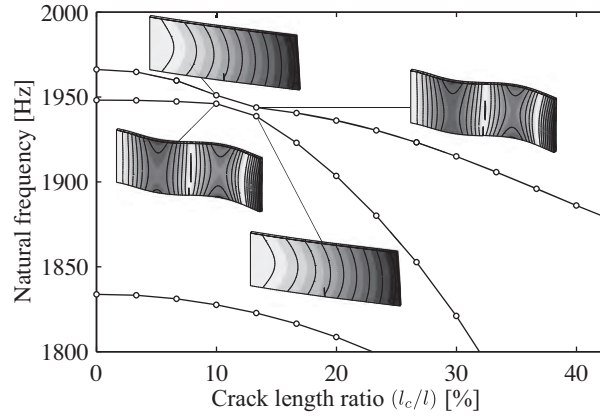
(b)

Fig. 29. First 15 natural frequencies versus (a) crack location ratio h_c/h for $l_c/l = 0.40$, (b) crack length ratio l_c/l for $h_c/h = 0.50$

7.2.2 Mode shape variation due to variations in crack location and length



(a)



(b)

Fig. 30. Magnified veering/crossing regions and associated mode shapes: (a) 10th and 11th modes for $l_c/l = 0.40$; (b) fifth and sixth modes for $h_c/h = 0.50$.

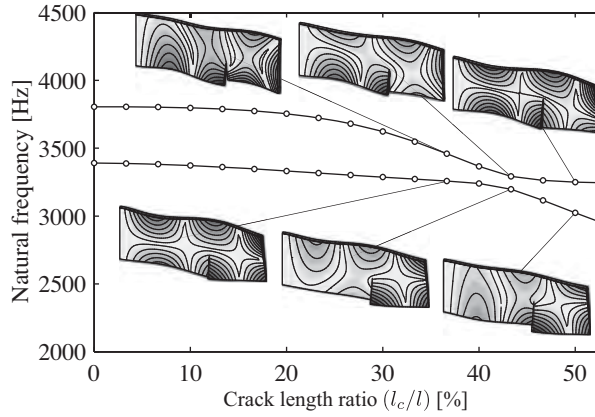


Fig. 31. Magnified veering between modes seven and eight for $h_c/h = 0.63$

In order to see the veering regions more closely, and to see the variations in the mode shapes, representative cases are shown in Figs. 30 and 31. Figure 30(a) shows the veering between the modes 10 and 11 for $l_c/l = 40\%$, where $1.33 \leq h_c/h \leq 40\%$. An important characteristic of the loci veering is the mode shapes associated with the natural frequencies on each locus before veering are interchanged during the veering in a continuous manner.⁶³ This is illustrated in Fig. 30(a), which shows that mode shapes 10 and 11 become mixed and then appear to begin switching as the crack location ratio is increased through the veering region. On the other hand in Fig. 30(b), the region for the mode shape switching between modes five and six is narrow, and it appears to be a loci crossing. This can be explained by considering that mode five (before switching) corresponds to the second out-of-plane bending mode whereas mode six (before switching) corresponds to the first in-plane bending mode, and there is little or no coupling between these modes due to their geometric dissimilarity. Fig. 31 shows another veering region due to crack length variation, for modes seven and eight with crack location $h_c/h = 0.63$. For this case, both mode mixing and switching can be observed in a more continuous manner than the cases observed in Fig. 30.

7.3 Nonlinear Forced Response Analysis

In the previous section, the interchanging of modes as well as mode coupling were observed in frequency veering and crossing regions. However, only natural frequencies of the linear system were considered. The nonlinearity due to contact of the crack surfaces was neglected. In this section, a method to calculate the nonlinear resonant frequencies of the cracked plate is described. The method is then applied to the calculation of nonlinear resonant frequencies in veering/crossing regions, and their characteristics are discussed.

7.3.1 Component Mode Synthesis

In order to generate a reduced-order model, the plate is separated into two components (substructures) Ω_1 and Ω_2 along the crack path, as shown in Fig. 32, and a hybrid-interface method of component mode synthesis (CMS)^{98,99} is employed. The CMS methods have been widely used for the vibration analysis of systems such as friction-damped systems,^{100–102} build-up structures,¹⁰³ and cracked structures.^{92,104} This process is advantageous over the

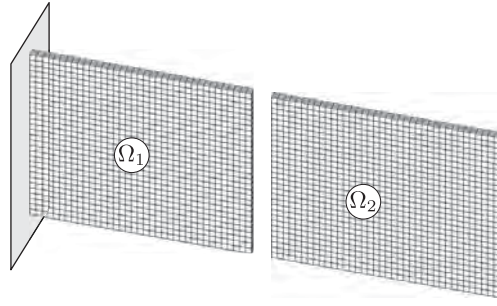


Fig. 32. Plate divided into two substructures

direct application of FE analysis because it provides improved computational efficiency while maintaining direct access to the dynamics of the crack-surface DOF. Furthermore, it has good accuracy relative to the original FE model over the frequency range of interest. The accessibility to the nodes on the crack surfaces is essential to the proper calculation of the boundary condition at the crack surfaces, which is modeled as contact/impact forces in the formulation described in 7.3.2. Namely, the dynamics of the FE degrees of freedom are projected onto constraint modes Ψ_c , inertia relief attachment modes Ψ_a (if rigid-body motion exists), and a truncated set of free-interface normal modes Φ_k . Interested readers may consult, e.g., Craig,¹⁰⁵ for the detailed formulation of each mode set.

Let the displacement vector \mathbf{u} be partitioned into boundary DOF, \mathbf{u}_b , and interior DOF \mathbf{u}_i . By denoting the inertia relief attachment coordinates and a truncated set of free-interface modal coordinates as \mathbf{q}_a and \mathbf{q}_k , the linear projection is expressed as,

$$\begin{bmatrix} \mathbf{u}_b \\ \mathbf{u}_i \end{bmatrix} = \begin{pmatrix} \mathbf{I} & \mathbf{0} & \mathbf{0} \\ \Psi_{ic} & \hat{\Psi}_a & \hat{\Psi}_k \end{pmatrix} \begin{bmatrix} \mathbf{u}_b \\ \mathbf{q}_a \\ \mathbf{q}_k \end{bmatrix} \quad (59)$$

where $\hat{\Psi}_a = \Psi_{ia} - \Psi_{ic}\Psi_{ba}$, $\hat{\Psi}_k = \Phi_{ik} - \Psi_{ic}\Phi_{bk}$, \mathbf{I} is the identity matrix, Ψ_{ic} is the boundary partition of Ψ_c , Ψ_{ia} and Ψ_{ba} denote the interior and the boundary partitions of Ψ_a , and Φ_{ik} and Φ_{bk} denote the interior and the boundary partitions of Φ_k . Denoting Eq. (59) with a compact notation, $\mathbf{u} = \Psi\mathbf{q}$, the application of Eq. (59) to Eq. (58) yields a smaller number of equations, i.e.,

$$\mathbf{M}'\ddot{\mathbf{q}} + \mathbf{C}'\dot{\mathbf{q}} + \mathbf{K}'\mathbf{q} = \mathbf{b}' + \mathbf{f}'(\mathbf{q}) \quad (60)$$

where $\mathbf{M}' = \Psi^T\mathbf{M}\Psi$, $\mathbf{C}' = \Psi^T\mathbf{C}\Psi$, $\mathbf{K}' = \Psi^T\mathbf{K}\Psi$, $\mathbf{b}' = \Psi^T\mathbf{b}$, and $\mathbf{f}' = \Psi^T\mathbf{f}$. The superscript “ \prime ” is omitted for convenience in the subsequent formulations.

7.3.2 Hybrid frequency/time domain method

For the calculation of steady-state response to harmonic excitation, an extension to the alternating frequency/time-domain method,¹⁰⁶ which is based on the concept of the method of harmonic balance,¹⁰⁷ is employed in this study. Because of its computational efficiency and accuracy, this type of method has been developed and applied to forced response problems for various nonlinear systems, such as friction damped systems^{101, 102, 108, 109} and cracked shafts.¹¹⁰ In particular, the hybrid frequency/time-domain (HFT) method developed by Poudou *et*

al.^{100,111,112} and the authors¹⁰⁴ is applied in this paper. Namely, the method assumes that the steady-state vibration response of \mathbf{q} in Eq. (60), as well as the external force \mathbf{b} and the nonlinear force due to intermittent contact \mathbf{f} are approximated as truncated Fourier series, i.e.,

$$\mathbf{q} = \text{Re} \left(\sum_{k=0}^{n_h} (\mathbf{Q}_k^c - j\mathbf{Q}_k^s) e^{jk\omega t} \right) \quad (61)$$

$$\mathbf{b} = \text{Re} \left(\sum_{k=0}^{n_h} (\mathbf{B}_k^c - j\mathbf{B}_k^s) e^{jk\omega t} \right) \quad (62)$$

$$\mathbf{f} = \text{Re} \left(\sum_{k=0}^{n_h} (\mathbf{F}_k^c - j\mathbf{F}_k^s) e^{jk\omega t} \right) \quad (63)$$

where $2\pi/\omega$ is the fundamental frequency, n_h is the number of non-zero harmonics and $j = \sqrt{-1}$. Note that \mathbf{Q}_k^c and $-\mathbf{Q}_k^s$ are the vectors of real and imaginary parts of k th Fourier coefficients of \mathbf{q} , where superscripts c and s denote cosine and sine components of the vibration respectively. The same notation is applied to \mathbf{B}_k^c , \mathbf{B}_k^s , \mathbf{F}_k^c , and \mathbf{F}_k^s . Substituting Eqs. (61) through (63) into Eq. (60) and considering the orthogonality of harmonic functions, it results in a nonlinear algebraic equation with respect to the Fourier coefficients for k th harmonic number, i.e.,

$$\mathbf{\Lambda}_k \mathbf{Q}_k = \mathbf{B}_k + \mathbf{F}_k(\mathbf{Q}) \quad (64)$$

where $\mathbf{Q}_0 = \mathbf{Q}_0^c$, $\mathbf{B}_0 = \mathbf{B}_0^c$, $\mathbf{F}_0 = \mathbf{F}_0^c$, $\mathbf{\Lambda}_0 = \mathbf{K}$, $\mathbf{Q}_k = [(\mathbf{Q}_k^c)^T, (\mathbf{Q}_k^s)^T]^T$, $\mathbf{B}_k = [(\mathbf{B}_k^c)^T, (\mathbf{B}_k^s)^T]^T$, $\mathbf{F}_k = [(\mathbf{F}_k^c)^T, (\mathbf{F}_k^s)^T]^T$, and

$$\mathbf{\Lambda}_k = \begin{pmatrix} -(k\omega)^2 \mathbf{M} + \mathbf{K} & (k\omega) \mathbf{C} \\ -(k\omega) \mathbf{C} & -(k\omega)^2 \mathbf{M} + \mathbf{K} \end{pmatrix} \quad (65)$$

for $k = 1, \dots, n_h$. Assembling Eq. (65) for all $k = 0, 1, \dots, n_h$,

$$\mathbf{\Lambda} \mathbf{Q} = \mathbf{B} + \mathbf{F}(\mathbf{Q}) \quad (66)$$

where $\mathbf{\Lambda}$ is a pseudo-block diagonal matrix with $\mathbf{\Lambda}_k$ on its diagonal blocks for $k = 0, \dots, n_h$, $\mathbf{Q} = [\mathbf{Q}_0^T, \dots, \mathbf{Q}_{n_h}^T]^T$, $\mathbf{B} = [\mathbf{B}_0^T, \dots, \mathbf{B}_{n_h}^T]^T$, and $\mathbf{F} = [\mathbf{F}_0^T, \dots, \mathbf{F}_{n_h}^T]^T$. Eq. (66) can then be solved with nonlinear algebraic equation solvers. For the numerical examples shown in this paper, the Hybrid Powell method¹¹³ was employed.

7.3.3 Results of forced response analysis

In this subsection, the result of nonlinear forced response analysis for the cantilevered cracked plate is presented, with the methods described in 7.3.1 and 7.3.2. The damping was chosen to be $\mathbf{C} = \alpha \mathbf{M} + \beta \mathbf{K}$ where $\alpha = 1.22$ and $\beta = 8.16 \times 10^{-9}$, which result in damping that is approximately equivalent to modal (structural) damping ratio $\zeta = 1.00 \times 10^{-4}$ ($\gamma = 2.00 \times 10^{-4}$) within the frequency range of $1900 \leq f \leq 2000$ Hz. Vectors of harmonic forcing, the resultant of which is equal to 1N, is applied to the nodes on the tip face of the plate to excite the modes of interest. The number of harmonics was chosen as $n_h = 9$, which showed convergence in the resonant frequency predicted in the frequency response for the modes of

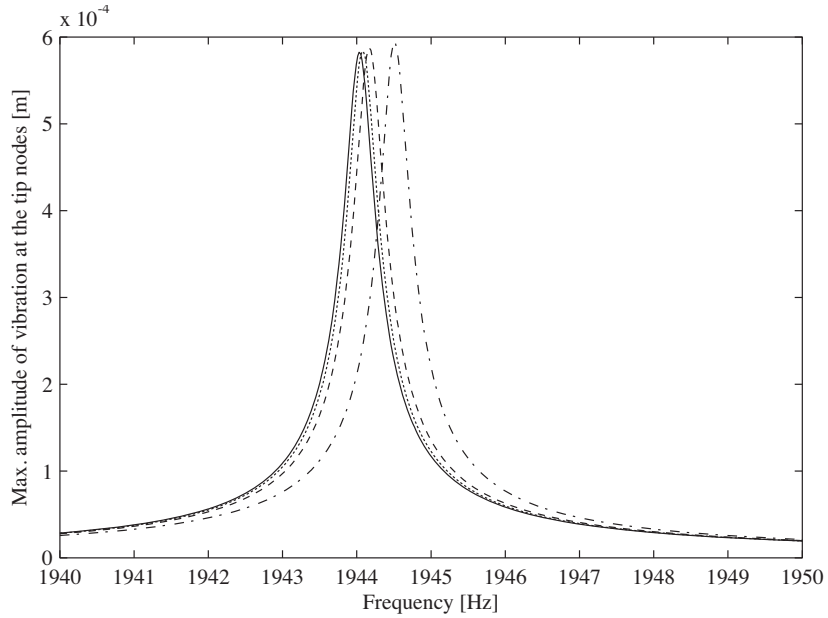


Fig. 33. Convergence on the forced response results of the sixth mode (in-plane bending) for $h_c/h = 0.5$ and $l_c/l = 0.167$; —, $n_h = 9$, ----, $n_h = 7$, - · - ·, $n_h = 5$, · · · ·, $n_h = 3$.

interest. A representative result of a convergence study in terms of the number of harmonic numbers is shown in Fig. 33 for the sixth mode with $h_c/h = 0.5$ and $l_c/l = 0.167$. For the case shown in Fig. 33, the predicted resonant frequency converged within 0.003% relative error. Representative results are shown in Fig. 34 where $h_c/h = 0.5$, $l_c/l = 0.167$ for Fig. 34(a), and $l_c/l = 0.2$ for Fig. 34(b). Fig. 34(a) shows the resonant peaks corresponding to modes five and six, which correspond to the third out-of-plane bending and the first in-plane bending modes, respectively, whereas the order of the modes is interchanged in Fig. 34(b).

7.4 Bilinear Frequency Approximation

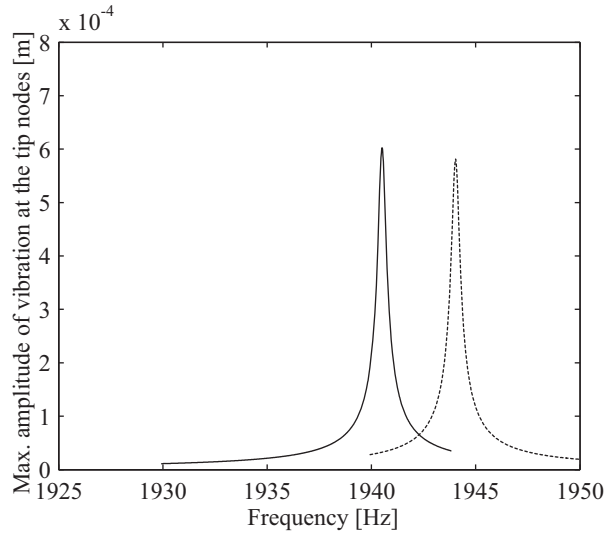
7.4.1 Formulation

As an alternative way of predicting the nonlinear vibration frequencies, the bilinear frequency approximation is generalized for the analysis of three-dimensional cracked structures, and an analysis framework based on reduced-order modeling as well as prediction of mode switching during the veering regions is proposed in this section. The resonant peaks predicted by the forced response to harmonic excitation is then compared with those calculated by the bilinear frequency approximations.

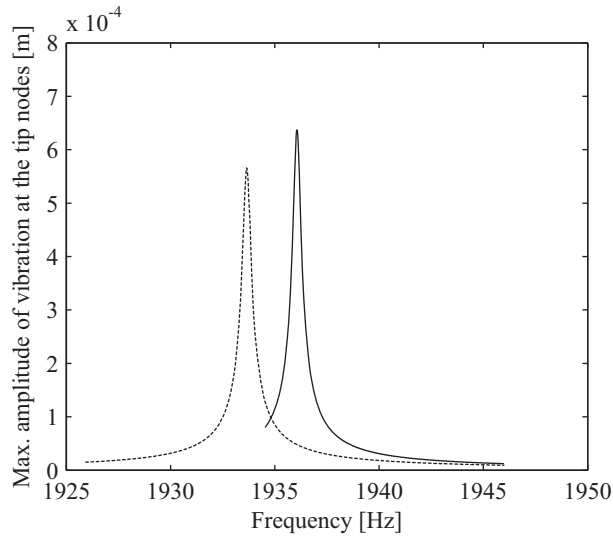
The bilinear frequency was originally introduced as the effective vibration frequency of a piecewise linear, single-DOF system and defined as (e.g., Ref.⁸⁷),

$$\omega_b = \frac{2\omega_1\omega_2}{\omega_1 + \omega_2} \quad (67)$$

where ω_b is the bilinear frequency, ω_1 is the natural frequency of one of the linear systems associated with the piecewise linear system, and ω_2 is that of the other linear system of the piecewise linear system. This expression is the exact solution, for the frequency of free



(a)



(b)

Fig. 34. Results of nonlinear harmonic response analysis for $h_c/h = 0.5$: (a) $l_c/l = 0.167$, —, fifth mode (out-of-plane bending), ----, sixth mode (in-plane bending); (b) $l_c/l = 0.200$, ----, fifth mode (in-plane bending), —, sixth mode (out-of-plane bending).

oscillation of the piecewise linear single-DOF oscillator with vanishing clearance/gap at the equilibrium. The application of Eq. (67) to a multi-DOF piecewise linear system is rather straightforward if there is only one pair of linear systems. However in the cases of cracked plates formulated with multiple DOF on crack surfaces, it involves multiple piecewise linear systems, or a *conewise* linear systems.⁹³ Hence an assumption has to be made such that the cracked system has only two linear systems corresponding to two states, i.e., the crack is open or closed. These are designated as states 1 and 2, respectively, in the following formulation. The definition of the states 1 and 2 is a natural extension to that proposed by Chati *et al.*,⁹¹ which was applied to the analysis of in-plane bending vibrations of a cracked beam. Namely, with the assumption of the open state, there is no connection between the nodes on one crack surface and the nodes on the other surface (Fig. 35(a)), allowing the inter-penetration of the crack surfaces. On the other hand with the closed state, the relative DOF along the direction that is perpendicular to the crack surfaces are fixed to be zero, whereas the other

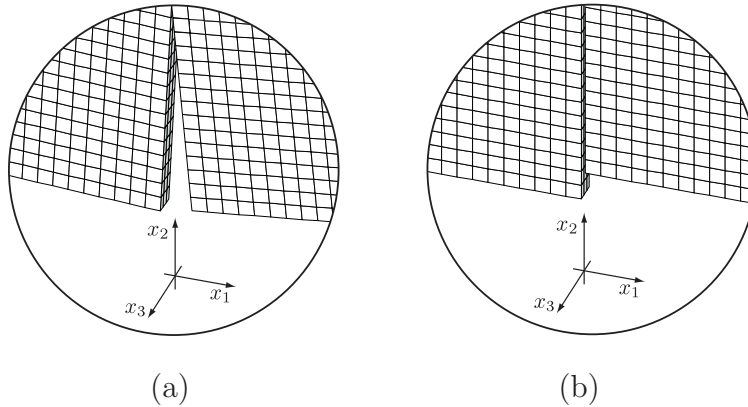


Fig. 35. Constraints for bilinear frequency calculation: (a) Open (no constraints); (b) Closed (sliding).

two DOF of each node are allowed to move freely in the plane tangent to the constrained direction (Fig. 35(b)). In other words, the crack surfaces are allowed to slide with respect to each other, which is consistent with the assumption employed in the formulation in 7.3.2. Associated mathematical formulation is given as follows.

For a given crack length, eigenvalues of Eq. (58) for undamped case with open crack assumption are obtained as

$$\mathbf{K}\phi = \omega_1^2 \mathbf{M}\phi \quad (68)$$

where ϕ is the eigenvector and ω_1^2 is the associated eigenvalue. On the other hand, the eigenvalues and eigenvectors for the other case, namely the case with allowing sliding of crack surfaces, are obtained by imposing appropriate constraints on Eq. (68) as follows. Let A and B denote the crack surfaces facing each other, by assuming that the amplitude of vibration is much smaller than the finite element mesh size on the crack surfaces, it is possible to identify the finite element nodes that may be in contact during the vibration cycle. Hence such pairs of nodes are numbered and a set C_{cp} is defined where all numbers that denote the contact pairs are included. Defining g_n as the *gap* between the nodes on the surfaces A and B for the n th contact pair, the constraints to be imposed on the nodes of n th contact pair are expressed as

$$g_n = (u_n)_A - (u_n)_B = 0, \quad n \in C_{cp} \quad (69)$$

where $(u_n)_A$ and $(u_n)_B$ denote the displacements of the nodes on the surface A and B , projected onto the normal direction pointing outward from the surface A or B . It is noted that appropriate coordinate transformation must be applied to the displacement vector based on the normal vector at each node, in order to correctly calculate g_n . It should also be noted that the motion of the nodes in tangential plane that is perpendicular to the normal direction, is not constrained at all by Eq. (69), i.e., the nodes are free to slide with each other on the tangential plane. This also indicates that the crack surfaces are assumed to be frictionless, which is widely-employed assumption for the vibration problem of cracked beams and plates. Applying the constraints Eq. (69) to the eigenvalue problem Eq. (68), a

constrained eigenvalue problem is obtained as

$$\begin{bmatrix} \mathbf{K} & \mathbf{N}^T \\ \mathbf{N} & \mathbf{0} \end{bmatrix} \begin{bmatrix} \boldsymbol{\phi} \\ \boldsymbol{\lambda} \end{bmatrix} = \omega_2^2 \begin{bmatrix} \mathbf{M} & \mathbf{0} \\ \mathbf{0} & \mathbf{0} \end{bmatrix} \begin{bmatrix} \boldsymbol{\phi} \\ \boldsymbol{\lambda} \end{bmatrix} \quad (70)$$

where \mathbf{N} is the matrix of coefficients that are associated with Eq. (69) and the appropriate transformation matrix, and $\boldsymbol{\lambda}$ is the vector of Lagrange multipliers of size $|C_{cp}|$. One method to solve this indefinite eigenvalue problem is to use an eigenvalue solver for indefinite systems. Another method is to first eliminate the redundant equations due to the constraint equations Eq. (69), and the resulting positive definite eigenvalue problem is then solved by an eigenvalue solver for definite systems. It should be noted that this methodology can easily be incorporated with the reduced-order modeling framework described in 7.3.1 as the motion of the nodes on the crack surfaces in the three-dimensional space can be captured with the reduced-order model.

With the eigenvalue problems Eqs. (69) and (70), the i th bilinear resonant frequency ω_{bi} of the cracked plate is approximated based on Eq. (67):

$$\omega_{bi} = \frac{2\omega_{1i}\omega_{2i}}{\omega_{1i} + \omega_{2i}} \quad (71)$$

where ω_{1i} and ω_{2i} denote the frequencies of the i th mode of the states 1 and 2. It is emphasized that the index i does not denote the index of eigenvalues, but it denotes the index of the eigenvectors of the *non-cracked* plate. Namely, the eigenvectors of the non-cracked plate are indexed based on their natural frequencies, i.e., for non-cracked plate, the eigenvalues are ordered as $\omega_1 \leq \omega_2 \leq \dots \leq \omega_{N-1} \leq \omega_N$ where N is the size of the non-cracked plate model, and corresponding eigenvectors are labeled as $[\boldsymbol{\phi}_1, \boldsymbol{\phi}_2, \dots, \boldsymbol{\phi}_{N-1}, \boldsymbol{\phi}_N]$. The reason for introducing this ordering will become apparent shortly. The bilinear frequency ω_{bi} for a given crack length is calculated by using the natural frequencies of the corresponding i th mode of the states 1 and 2.

The advantage of this method is that the frequency of the nonlinear response is obtained without calculating the associated response shapes, thus it only involves eigenvalue extraction of two linear systems. However, as mentioned, this method is known to be accurate for systems with a relatively short crack. In addition, a drawback of this method is that the choice of proper pairs of ω_{1i} and ω_{2i} is not apparent with the presence of a veering or crossing, because the mode shapes associated with the natural frequencies switch their orders. A way to overcome the latter problem is to track each mode by observing the correlation between the modes during the variation of crack length or crack location. In this paper, the modal assurance criterion³³ (MAC) is employed as the measure of correlation.

Denoting the crack length as p ($= l_c$), it is noted that \mathbf{N} and $\boldsymbol{\lambda}$ are dependent on p . That is, $\mathbf{N} = \mathbf{N}(p)$ and $\boldsymbol{\lambda} = \boldsymbol{\lambda}(p)$. The eigenvector is also dependent on p , or $\boldsymbol{\phi} = \boldsymbol{\phi}(p)$, and the correlation between the i th mode shape of the system with $p = p_0$ and the j th mode shape with the perturbed crack length $p = p_0 + \Delta p$ can be characterized by

$$MAC_{ij}^k = \frac{|\boldsymbol{\phi}_i^k(p_0)^T \boldsymbol{\phi}_j^k(p_0 + \Delta p)|^2}{\|\boldsymbol{\phi}_i^k(p_0)\|^2 \|\boldsymbol{\phi}_j^k(p_0 + \Delta p)\|^2}, \quad k = 1, 2 \quad (72)$$

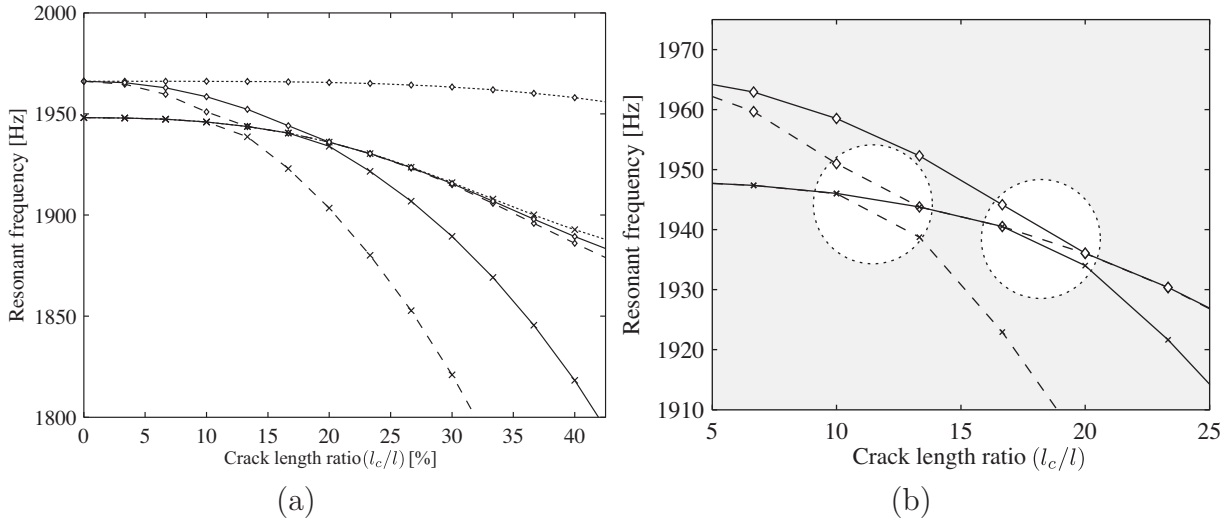


Fig. 36. Comparison between natural frequencies with open and sliding B.C.'s., and bilinear frequencies for the system with $h_c/h = 0.50$: (a) The fifth and sixth natural frequencies of the system with sliding and open B.C.s, and bilinear frequencies: --- \diamond ---, sixth mode with sliding B.C.; --- \times ---, fifth mode with sliding B.C.; -- \diamond --, sixth natural frequency with open B.C.; -- \times --, fifth natural frequency with open B.C.; — \diamond —, sixth bilinear frequency; — \times —, fifth bilinear frequency; (b) Close-up view of the veering region for natural frequencies with open B.C. and bilinear frequencies: -- \diamond --, sixth natural frequency with open B.C.; -- \times --, fifth natural frequency with open B.C.; — \diamond —, sixth bilinear frequency; — \times —, fifth bilinear frequency.

where ϕ is the eigenvector of the system defined by Eq. (70), the subscripts i and j denote the indices for modes, the superscript k indicates the state, and MAC_{ij}^k takes the value between 0 and 1, which respectively correspond to no correlation, and consistent correlation between $\phi_i(p_0)$ and $\phi_j(p_0 + \Delta p)$. Namely, the i th eigenvector is tracked based on the value of MAC throughout the variation of the crack length (p), such that the correct natural frequencies for the i th eigenvector in Eq. (71) can be calculated.

In order to better clarify the behavior of the natural frequencies of the system with open and sliding boundary conditions, as well as the bilinear frequencies, the above mentioned analysis framework was applied to the reduced-order model of the cracked plate with $h_c/h = 0.50$. As an example, the veering region between the fifth and sixth modes are shown in Fig. 36. As was shown in 7.2.2, the modes of interest are the in-plane and out-of-plane bending modes. In Fig. 36, two significant insights into the behavior of the frequencies are shown. The first is that the existence and location vary between the cases with open and sliding boundary conditions, and bilinear frequency. For the case with sliding boundary condition, the veering between fifth and sixth modes does *not* exist. On the other hand for the open boundary condition case, the loci of fifth and sixth modes approach and veer away where $10 \leq l_c/l \leq 15\%$. Therefore the bilinear frequency also has the veering region due to that for the open boundary condition, but slightly shifted toward larger crack length ratio because of the absence of the veering for the sliding boundary condition case (Fig. 36(b)). The second is that the bilinear frequency is *always* bounded by the frequencies corresponding to the cases with sliding and open boundary conditions, which are respectively the upper and lower bounds (Fig. 36(a)). This can also be easily verified from Eq. (71), i.e., if $\omega_{1i} \leq \omega_{2i}$, then $\omega_{1i} \leq \omega_{bi}$ and $\omega_{bi} \leq \omega_{2i}$. Furthermore, it is noted that the width between the upper and lower bounds indicates the strength of the effect of contact nonlinearity on the resonant frequency.

For instance, for the fifth bilinear frequency that corresponds to the in-plane bending mode, the width between the bounds is much larger than that for the sixth bilinear frequency, which corresponds to the out-of-plane bending mode. This is due to the fact that the motion of the in-plane bending mode is greatly influenced by the existence of the contact force at the crack surfaces, whereas the out-of-plane bending modes is not so much affected by the contact force considering that the motion of the crack surfaces is almost perpendicular to the crack surfaces.

It is noted that there have been other approaches for obtaining approximate bilinear frequencies for multi-DOF systems, such as the one presented in Refs.,^{88,92,93,114} which is based on the construction of an equivalent linear stiffness matrix. The current implementation of the proposed method is not compatible with the equivalent stiffness matrix method, as the linear subregions, which are the systems with the sliding B.C. and the one with the open B.C., are realized by the application of constraints at the discontinuities. It means that the subregions have different number of DOFs, and the resulting stiffness matrices are not the same size. This issue could be solved by first applying the modal decomposition to the matrices for both subregions, and construct the equivalent stiffness matrix in the modal space, by adjusting the modal stiffness matrix size by mode truncation such that size of the modal matrices of the subregions is identical. However, the resulting equivalent modal stiffness matrix is a diagonal matrix with bilinear frequencies on its diagonal, hence this method produces the same bilinear frequencies as the one produced by the proposed method. It is noted that even with the equivalent stiffness method, the matching of correct modes is still necessary to calculate the bilinear frequencies, as the natural frequencies on the diagonal terms of modal stiffness matrices do not necessarily represent the same mode.

7.4.2 Comparison with the results of forced response analysis

Using the bilinear frequency approximation described above, the nonlinear vibration frequencies of the cracked plate are calculated, and they are compared with those obtained by the HFT method. It is noted that the comparison between the resonant frequencies obtained by forced response analysis, and the bilinear frequencies, namely the vibration frequencies of *unforced* system, has been made based on the assumption that the resonant frequencies reside in the vicinity of the frequencies associated with the nonlinear normal modes.¹¹⁵ Furthermore, the resonant frequencies are assumed to be independent of the amplitude of forcing, based on the fact that the resonant frequencies of piecewise linear systems with the vanishing gap at the equilibrium are not dependent on vibration amplitude.^{87,104}

It is also noted that the HFT method is capable of calculating the *gradual opening and closing* of crack faces during a vibration cycle, by considering the three-dimensional time trajectory of nodes on crack faces at the steady-state. A detailed formulation can be found in Ref.,¹⁰⁴ and its accuracy was validated by a comparison with the results of time integration of a FE model. The role of the HFT method here is to find the accurate frequency response results without any assumption on the number of linear subregions, as opposed to the assumption that there are two linear subregions for the bilinear frequency approximations.

Three representative veering regions are considered, which are the cases where (a) the interaction between the loci is weak and the corresponding modes are: (1) in-plane and out-of-plane

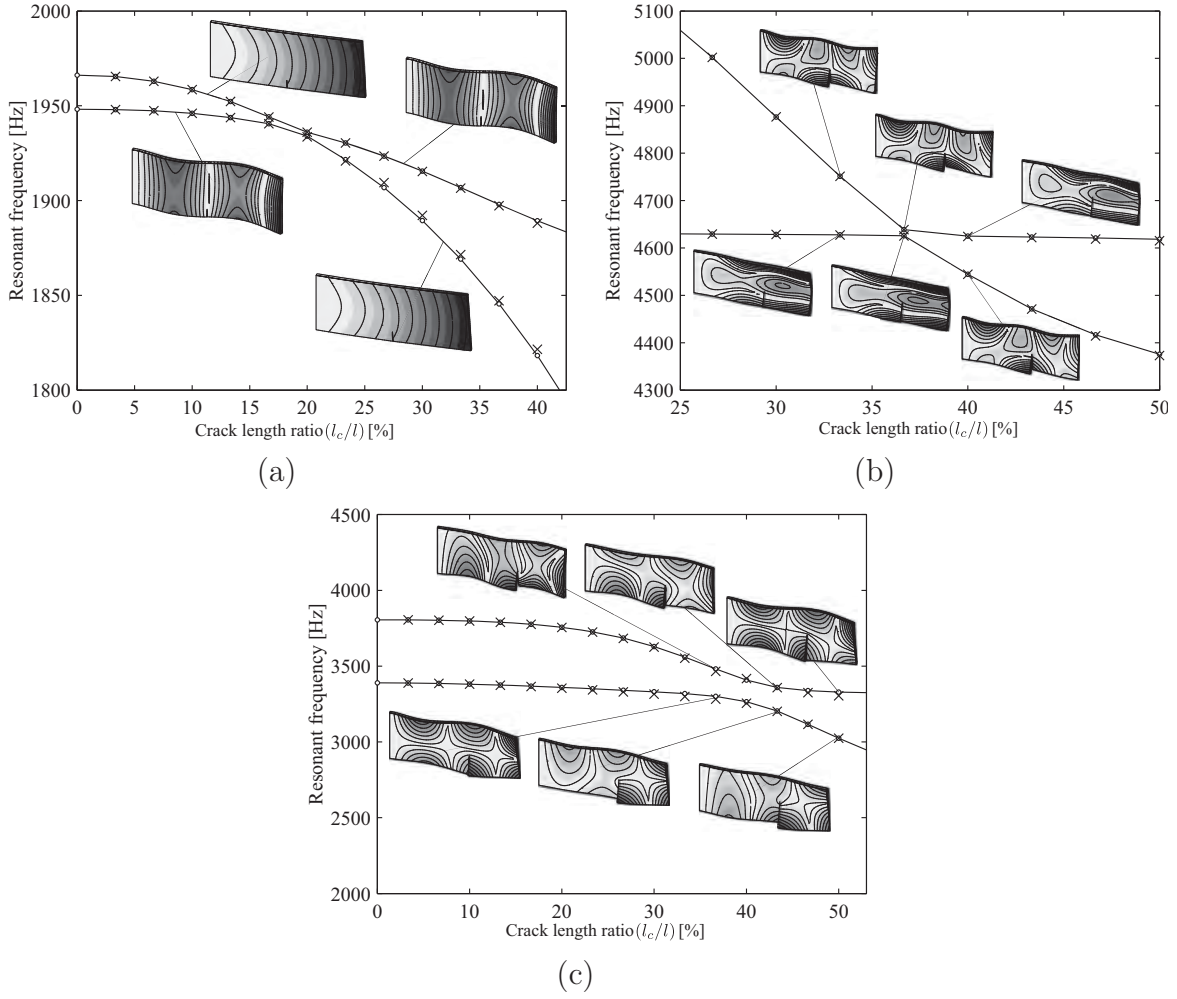


Fig. 37. Comparison between bilinear frequency assumption and HFT method, and corresponding mode shapes with open B.C. : (a) $h_c/h = 0.50$, $-o-$, bilinear frequency, 'x', HFT method; (b) $h_c/h = 0.60$, $-o-$, bilinear frequency, 'x', HFT method; (c) $h_c/h = 0.63$, $-o-$, bilinear frequency, 'x', HFT method.

bending modes, and (2) both out-of-plane bending modes, and (b) the interaction between the loci is strong and veering occurs in a continuous way and the associated modes are both out-of-plane bending modes.

First, the veering between an in-plane bending mode and an out-of-plane bending mode is considered, using the modes five and six, for $h_c/h = 0.50$, as shown in Fig. 30(b). The results of forced response analysis as well as the calculation based on bilinear frequency assumption are shown in Fig. 37(a). As can be seen, the order-switching of modes can be observed even for this nonlinear system. The most notable distinction from the linear assumption, i.e., Fig. 30(b), is that the veering occurs with longer crack length at around 20% in Fig. 37(a), than the one at around 10% with the linear assumption in Fig. 30(b). This is due to the *stiffening* effect because of the contact/impact of crack surfaces during the vibration cycle, which represents the dynamics of the cracked plates appropriately. Regarding the bilinear frequency approximation, a notable result has been observed: the bilinear frequency assumption predicts the resonant frequency calculated by HFT method quite well even for relatively large crack length ratio ($l_c/l \leq 40\%$).

Second, the veering between two out-of-plane bending modes is considered, using the modes nine and ten for $h_c/h = 0.60$, and the calculation results are shown in Fig. 37(b). This result also shows that bilinear frequency approximates the resonant frequencies quite well for the case of veering between out-of-plane bending modes, with relatively large crack length. Even though the effect of nonlinearity on the vibration frequency is smaller than that on the in-plane bending modes, as it does not involve much contact/impact between crack surfaces, this clearly indicates that the bilinear frequency approximation can also be used for the prediction of nonlinear vibration frequencies of out-of-plane bending modes.

Third, the veering between the torsion and out-of-plane bending modes are examined, using the modes seven and eight for $h_c/h = 0.63$ and results are shown in Fig. 37(c). This veering region features a switching of modes in a continuous way, or in other words, the mode shapes gradually change as the crack length is varied. This result shows that the bilinear frequency approximation predicts the nonlinear vibration frequency quite well even for the modes that exhibit complicated geometry due to coupling between modes. Moreover, the results show that the approximation is accurate even for large cracks.

Lastly, it is restated here that the possibility of a non-vanishing gap at the crack faces at the equilibrium, which is known to change the nonlinear resonant frequency, is ignored in the above formulations. Detailed discussions on the effects of gap for the piecewise linear oscillators can be found in Refs.,^{88,93,94} and bilinear frequency expression for piecewise linear oscillators with a gap can be found in Refs..^{88,114} Furthermore, the discussion on the effects of a gap at the equilibrium for the forced vibration problems of a cracked structure was done by the authors in Ref.,¹⁰⁴ by the use of the HFT method. It was shown that as the amplitude of vibration increases, the nonlinear resonant frequency monotonically increases after the amplitude of vibration exceeds a threshold, and converges to a certain value, as can be seen in Ref..⁹⁴ Such behavior of the nonlinear resonant frequency might be captured by the extension of the amplitude-dependent bilinear frequency expression for piecewise linear oscillators, to the system with multiple discontinuities. However, such discussions and formulations are beyond the scope of this paper.

8 AN EFFICIENT REDUCED ORDER MODELING TECHNIQUE FOR NON-LINEAR VIBRATION ANALYSIS OF STRUCTURES WITH INTERMITTENT CONTACT

Vibration problems of structures with intermittent contact have been studied extensively for several decades. These problems have practical importance and feature theoretical complexity due to their nonlinear nature. A numerical modeling procedure of such problems based on the finite element (FE) method is presented in this paper. This work is motivated by a need for developing a model-based crack detection algorithm of elastic structures based on their spectral properties, such as resonant frequencies and response shapes. In order to properly predict the resonant frequencies of such structures, one has to consider the nonlinearity caused by intermittent contact at the cracks, the so-called closing crack or breathing crack effect. This has hindered analysts from accurately calculating the resonant frequencies of cracked structures, because they cannot be calculated from classical linear modal analysis. As some sophisticated contact algorithms have been developed, such as the penalty method¹¹⁶ and the augmented Lagrangian method,¹¹⁷ the accuracy of the results of time transient simulation with FE models involving intermittent contact has been improved. Furthermore, studying vibration problems of such structures with an FE model with a realistic complexity is becoming feasible with the aid of high-performance computers. However, in turn, due to the advancement of these technologies, analysts tend to create models with a large number of degrees of freedom (DOF). This is based on the expectation that, as the model becomes more realistic and the results become more accurate, the problem can still be solved in a reasonable amount of time. However, at some point the number of DOF will overwhelm even the most advanced hardware and software. In fact, as the model complexity increases, the cost of solving contact problems increases dramatically, even when the potential contact areas are known a priori. This occurs even if one uses reduced order modeling techniques, such as the Craig-Bampton method.¹¹⁸ For forced response vibration problems of such structures, one can use accurate and efficient semi-analytical methods such as the ones based on the harmonic balance method (e.g., Ref.¹⁰⁷), by representing the steady-state dynamic response of the model with a truncated Fourier series. However, such methods still suffer from the increase of computational cost as it requires a fair number of harmonics to be included for the Fourier transform, in order to obtain an accurate result. Therefore, the goal of this paper is to propose an efficient reduced order modeling framework for vibration problems of elastic structures involving intermittent contact, with particular attention to modeling nonlinear vibration of cracked structures. The focus is placed upon reducing the number of DOF involved in the contact regions, in an automatic manner.

This paper is organized as follows. In section 8.1, a literature survey over the related fields is provided. In section 8.2, the proposed modeling framework is presented, including the reduced order modeling approach and contact DOF selection method. As applications of the method, a case study is shown in section 8.3, using an FE model of a cantilevered cracked plate.

8.1 Background

The issues of reducing and selecting DOF of FE models have been extensively studied by various methods and perspectives, such as the reduction of the interface DOF between sub-structures, selection of master DOF for Guyan reduction,¹¹⁹ optimal sensor placement, and optimal constraint locations. However, many of the available methods share to some extent similar goals and related to each other as described later.

Firstly, the issue of *reducing the number of interface DOF* between the components has been studied by several researchers. Brahmi *et al.*¹²⁰ proposed a method for reducing the number of interface DOF before the assembly of substructures, where basis vectors are chosen based on the combination of secondary modal analysis of the interface DOF partitions of the matrices, and the truncation of modes based on the singular value decomposition. Balmés¹²¹ introduced the framework for generalizing interface DOF such as constraint modes, by considering the new basis representing the actual interface displacements. Castanier *et al.*¹²² also proposed a technique for reducing the number of interface DOF by applying the modal analysis and mode truncation to the constraint mode partition of the matrices produced by the Component Mode Synthesis (CMS),¹¹⁸ the resulting modes of which are called the characteristic constraint modes after being transformed back into the finite element coordinates. All of these methods achieve the order reduction of the DOF at the interface. However, they do not provide any criteria as to *how* the interface DOF need be selected for accurately enforcing the boundary conditions.

Secondly, the *selection of master DOF* has been a crucial factor for determining the spectral property of the reduced order model for Guyan reduction-based reduction techniques, and many algorithms for the selection of the master DOF have been developed. As it shall be discussed later, this class of methods produces the results that tend to solve the optimization problem for the problems studied in this study, thus it is very relevant to our objective. An automatic master DOF selection algorithm was first proposed by Henshell and Ong,¹²³ in which the master DOF are chosen where the inertia is high and the stiffness is low, whereas the slave DOF are chosen where the inertia is low and the stiffness is high. This process can be automated by examining the radian frequency ω_s defined by fixing all DOF except the DOF index s . Namely, $\omega_s \triangleq \sqrt{k_{ss}/m_{ss}}$, for $s = 1, \dots, n$, where k_{ij} and m_{ij} are the entries at the i th row and j th column in FE stiffness and mass matrices of size n . The index s with the largest ω_s is identified at each iteration step, and the DOF is eliminated by an application of Guyan reduction with s being the slave DOF and all the other DOF being the master DOF. This process can be repeated until the number of master DOF reaches the desired number. An approach similar to this algorithm was proposed by Shah and Raymund¹²⁴ based on the discussion of Kidder and Flax,¹²⁵⁻¹²⁷ where the number of master DOF is controlled by iteratively eliminating the DOF whose ω_s is larger than the pre-defined cut-off frequency ω_c that is chosen to be approximately three times the highest significant frequency in the frequency range of interest. Independently from the work by Henshell and Ong, Grinenko and Mokeev developed an order reduction technique named frequency-dynamic condensation,¹²⁸ which also proposed a criterion to select master DOF. Although their criterion was legitimate, the implementation of the selection algorithm still suffers from tedious exhaustive-search calculation for selecting the DOF. The selection method proposed by Matta¹²⁹ also uses the ratio k_{ss}/m_{ss} with the similar criterion to that proposed by Henshell and Ong.¹²³ It was addressed that the method can be applied not only to the Guyan reduction but also to the CMS, where both static and vibration modes are used as basis vectors, onto which the system dynamics are projected. A method proposed by Bouhaddi and Fillod¹³⁰ used a different concept where if a DOF a is a *node* of an eigenmode, then fixing the DOF a results in $\hat{\lambda}_i = \lambda_i$ where λ_i is the i th eigenvalue of the non-fixed system, and $\hat{\lambda}_i$ is the eigenvalue of the system with DOF a being fixed. This concept may be understood using a vibration problem of a string with both ends fixed. That is, the lowest natural frequency of the string with a single support becomes the highest, if the support is placed at the node of the second mode

of vibration.¹³¹ This is because the first mode with the constraint then becomes identical to the second mode of the unconstrained string, which has the eigenvalue as the feasible upper bound of the first eigenvalue with a single constraint. It is noteworthy that Bouhaddi and Fillod explicitly aimed for *maximizing the minimum eigenvalue of the system where all the master DOF fixed*. This concept will be revisited in 8.2.3. The methods for the node selection reviewed so far are based on Henshell and Ong method to some extent. Another class of methods is that based on the concept of modal energy. The method proposed by Kim and Choi¹³² uses the energy distribution among the DOF for each mode, and by taking the partial sum over the rows of what they call energy distribution matrix, primary DOF set can be chosen. On the other hand the method proposed by Cho and Kim¹³³ utilizes the energy estimation in element-level by the Rayleigh quotient value of each element. Kim and Cho then proposed a selection method consisting of two steps;¹³⁴ model order reduction by Improved Reduced System (IRS)¹³⁵ using the master DOF selected via a method based on energy estimation of each element,¹³³ and subsequent sequential elimination method¹²³ with an iterative IRS. Another automatic DOF selection method named modal energy selection method proposed by Li¹³⁶ uses metric called index of classification, based on the approximate modal energy associated with each DOF. The method was successfully applied to an FE model of a cantilever beam problem. Oh and Park¹³⁷ also proposed a criterion for selecting the master DOF based on singular values of the modal matrix, however, it suffers from the computational cost due to exhaustive search over the possible master DOF sets, and depends on engineer's knowledge and intuition.

Thirdly, a similar but slightly different issue is the *selection of measurement locations* for vibration testing. For example, one may need to measure vibration displacements of a structure to determine vibration modes, typically with a limited number of sensors or the locations where the sensors can be placed. Thus, one may like to maximize the information one can obtain as much as possible, with the limited number of sensors or locations. However the question arises as to *how* the sensors need to be located, since the optimal configuration of sensors for such objective cannot be easily determined. There have been many methods developed to date for achieving this goal with various approaches. In particular, one of the successful approaches are based on information theory, which determine the sensor locations by optimizing a norm of the Fisher information matrix.¹³⁸ Among them, one of the most widely used techniques is the effective independence vector method, or the EIDV¹³⁹ method developed by Kammer.¹⁴⁰ The method determines the placement of sensors within the candidate locations while maintaining as much independent information as possible, i.e., maintaining the measured mode shapes as independent as possible. Therefore, it is natural to hypothesize that the application of the nonlinear boundary conditions to the optimum sensor locations would also well represent the real boundary conditions where the boundary conditions are applied to all locations in the region. This method is hereby considered in this study and the formulation is discussed in detail in 8.2.3.

Lastly, the issue of finding the optimal *constraint locations* to *maximize the fundamental natural frequency* of a structure is considered. This issue has an important relationship with the optimal master DOF selection. For instance, suppose there is a structure that can vibrate, and one may want to increase the lowest natural frequency as much as possible, by allocating a finite number of supports or kinematical constraints to the structure. However, the problem of finding the optimal number and the locations of such supports is not as easy as it appears. Therefore, it may be necessary to apply mathematically expensive optimization algorithms

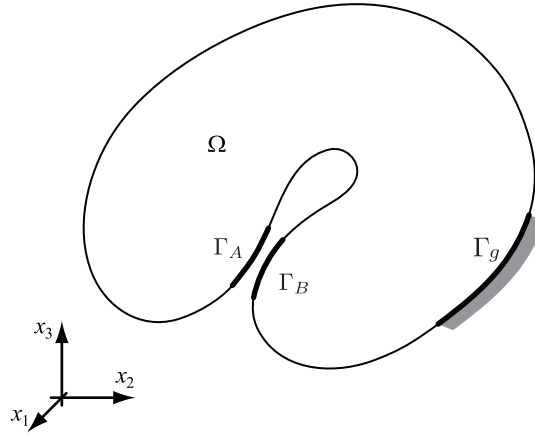


Fig. 38. An elastic structure with potentially contacting boundaries

to obtain such support locations, such as done in the work by Zhu and Zhang.¹⁴¹ On the other hand, Åkesson and Olhoff¹⁴² studied the problem by applying the Courant's maximum-minimum principle. Namely if there is a discrete dynamical system of size n and there are r ($< n$) kinematical constraints applied to the system, all the eigenvalues of the structure increase, and the increased eigenvalues are bounded by the following formula:

$$\lambda_i^0 \leq \lambda_i \leq \lambda_{i+r}^0, \quad i \in \{1, 2, \dots, n\} \quad (73)$$

where λ_i^0 and λ_{i+r}^0 denote the i th and $(i+r)$ th eigenvalues of the structure without the constraints, and λ_i is the i th eigenvalue of the constrained structure. Also based on the same principle and the findings of Ref.,¹⁴³ Won and Park¹⁴⁴ applied minimization method to obtain the optimal support location to achieve the maximum fundamental natural frequency of a cantilevered plate. They showed that the optimal support locations should be on the nodal lines of the $(r+1)$ th mode of the unconstrained structure. It is noted that this result conforms to the vibration problem of a fixed string mentioned above. This method was successfully applied to their specific examples, but the method can be applied only to special cases if the potentially-constrained region is the entire region of the structure, where the points on the nodal lines can be selected. Namely, if the regions to which the constraints are applied are limited to some specific regions of the structure, then the nodal lines may not exist in such regions, and the minimization problem becomes more complicated.

It is interesting to note that the idea of constraining the nodal lines was used to optimally select the master DOF for Guyan reduction by Bouhaddi and Fillod,¹³⁰ but they were not aware of the applicability of their method to optimally select the support positions, while Won and Park were not aware of the applicability of their method to optimally select the master DOF locations for Guyan reduction. In this paper, we take advantage of this similarity between the optimal master DOF selections and the constraint locations, in order to achieve the optimal selection of the DOF where the nonlinear boundary conditions are applied.

8.2 Mathematical Formulation

Consider small vibration problems of an elastic structure represented as Ω with a fixed boundary Γ_g , where the structure may or may not involve intermittent contact at Γ_A and Γ_B during the vibration cycles, such as shown in Fig. 38. Namely the boundaries open and close, thus the vibration problem is nonlinear because the condition for the the boundaries to be in contact is dependent on the displacement field itself. That is, the boundary conditions at Γ_A and Γ_B are nonlinear. It is well known that the system eigenvectors and eigen-frequencies are different from the actual response shapes and resonant frequencies of this nonlinear problem. In this paper, they are respectively referred to as the nonlinear normal modes (NNMs) and NNM frequencies.

Now, if the structure is discretized with a method such as finite element method, the non-linearity associated with the contact is *localized*, in the sense that the nonlinearity is caused only by a small portion of the entire structure. In the following formulations, a set of indices of DOF in such region is denoted as B (boundary), whereas a set of indices of the DOF in the rest of the regions is denoted as I (internal), and partitions of vectors and matrices associated with these sets are designated with subscripts of the associated lower-case italic letters, i.e., b and i . The sizes of the sets are denoted as $|B| = n_B$ and $|I| = n_I$. All the other DOF sets defined hereinafter follow the same notation.

If the finite element mass and stiffness matrices are denoted as $\mathbf{M} \in \mathbb{R}^{n \times n}$ and $\mathbf{K} \in \mathbb{R}^{n \times n}$ and the nodal displacement vector is given as $\mathbf{x} \in \mathbb{R}^n$, the governing equations of the vibration problem with the absence of external forcing and damping may be written in a partitioned matrix-vector form as follows:

$$\begin{pmatrix} \mathbf{M}_{bb} & \mathbf{M}_{bi} \\ \mathbf{M}_{ib} & \mathbf{M}_{ii} \end{pmatrix} \begin{bmatrix} \ddot{\mathbf{x}}_b \\ \ddot{\mathbf{x}}_i \end{bmatrix} + \begin{pmatrix} \mathbf{K}_{bb} & \mathbf{K}_{bi} \\ \mathbf{K}_{ib} & \mathbf{K}_{ii} \end{pmatrix} \begin{bmatrix} \mathbf{x}_b \\ \mathbf{x}_i \end{bmatrix} = \begin{bmatrix} \mathbf{f}_b(\mathbf{x}_b) \\ \mathbf{0} \end{bmatrix} \quad (74)$$

where a dot (\cdot) denotes a time derivative, and $\mathbf{f}_b \in \mathbb{R}^{n_B}$ denotes the nonlinear force associated with the intermittent contact. When dealing with this type of nonlinear vibration problems, one can apply linear reduced order modeling techniques, such as Guyan reduction,¹¹⁹ system equivalent reduction expansion process (SEREP),¹⁴⁵ iterated improved reduced system (IIRS),^{146,147} or Component mode synthesis (CMS).¹¹⁸ With such methods, one can obtain smaller system matrices by reducing the size of \mathbf{x}_i by means of Rayleigh-Ritz coordinate transformation comprising of various basis vectors such as static deformations and vibration modes, yet keeping the accessibility to the physical coordinates of \mathbf{x}_b . For instance, with the help of CMS, one can obtain a system with desired spectral properties *and* accessibility to \mathbf{x}_b , the size of which is as small as n_B DOF plus the number of linear normal modes whose frequencies lie in the frequency ranges of interest. The use of such linear reduced order modeling methods greatly helps ones to analyze the dynamic response of systems with localized nonlinearities, such as transient dynamic analysis,¹⁴⁸ and nonlinear harmonic response analysis.¹⁰⁴ However, even with these reduced order modeling methods, if the number of DOF involved in the b partition becomes large, especially the cases with very fine mesh in the contacting regions, one cannot take advantage of the linear reduced order modeling techniques, as the computational cost associated with the nonlinear dynamic analysis typically grows as the number of DOF in the b partition increases. Furthermore, if

one simply attempts to eliminate some of the DOF in the b partition, it results in inaccurate, or even wrong results, in comparison to the results obtained with a full set of DOF in the b partition. Therefore, in order to obtain accurate computational results, such as those of nonlinear forced response, one needs to keep as many boundary DOF as possible, which could easily result in prohibitively costly calculations. Typically as a “workaround” to avoid the inaccurate results due to the lack of sufficient DOF considered and at the same time to obtain efficient computational model, one has to select the DOF in a heuristic way, which greatly depends on the system characteristics and analyst’s experience and intuition. Moreover, if the model is developed in such ways, the error contained in the following analysis results cannot be estimated a priori. Our aim here is to develop an automatic way to select the DOF in B for a desired number of DOF to be selected.

8.2.1 Primary Model Reduction

In order to reduce the number of DOF included in I to make the subsequent development more efficient, first a model reduction is applied to Eq. (74). Namely, I is further divided into two sets, i.e., $I = O \cup D$ where O is a set of DOF indices associated with the nodes to be used in the following analysis, such as observing the behavior of the system or applying external loading, and D is the rest of DOF indices in I , which is to be apparently deleted from the system by the reduction methods. In addition, a set of DOF indices to be used as the *master* DOF is defined as active DOF, designated as A , and $A = B \cup O$. Now consider an eigenvalue problem of the system Eq. (74), where the eigenvalue λ and the corresponding eigenvector ϕ must satisfy the following:

$$\begin{pmatrix} \mathbf{K}_{aa} & \mathbf{K}_{ad} \\ \mathbf{K}_{da} & \mathbf{K}_{dd} \end{pmatrix} \begin{bmatrix} \phi_a \\ \phi_d \end{bmatrix} = \lambda \begin{pmatrix} \mathbf{M}_{aa} & \mathbf{M}_{ad} \\ \mathbf{M}_{da} & \mathbf{M}_{dd} \end{pmatrix} \begin{bmatrix} \phi_a \\ \phi_d \end{bmatrix} \quad (75)$$

where $\phi = [\phi_a^T, \phi_d^T]^T$. In this study, a mixed-boundary CMS of Hintz-Herting^{98,99} is chosen for the primary model reduction. Namely, without the presence of rigid body modes, the coordinate transformation is defined as

$$\begin{bmatrix} \mathbf{x}_a \\ \mathbf{x}_d \end{bmatrix} = \mathbf{H}\boldsymbol{\eta} = \begin{pmatrix} \boldsymbol{\Psi} & \hat{\boldsymbol{\Phi}} \end{pmatrix} \begin{bmatrix} \boldsymbol{\eta}_a \\ \boldsymbol{\eta}_m \end{bmatrix} \quad (76)$$

where $\mathbf{x}_a = \boldsymbol{\eta}_a$, $\boldsymbol{\eta}_m$ is a vector of modal coordinates, $\boldsymbol{\Psi}$ and $\hat{\boldsymbol{\Phi}}$ are so-called constraint modes and truncated free-interface normal modes in a modified form, which are respectively defined as

$$\boldsymbol{\Psi} = \begin{pmatrix} \mathbf{I} \\ -\mathbf{K}_{dd}^{-1}\mathbf{K}_{da} \end{pmatrix} \quad (77)$$

$$\hat{\boldsymbol{\Phi}} = \begin{pmatrix} \mathbf{0} \\ \boldsymbol{\Phi}_d + \mathbf{K}_{dd}^{-1}\mathbf{K}_{da}\boldsymbol{\Phi}_a \end{pmatrix} \quad (78)$$

and $\boldsymbol{\Phi} = [\phi_{(1)}, \phi_{(2)}, \dots, \phi_{(k)}]$, $k < n$, each subscript in parentheses denoting the corresponding mode number. Using the transformation defined as Eq. (76), the projected eigenvalue problem

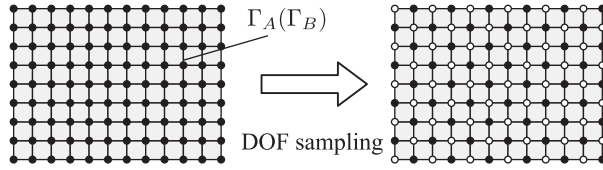


Fig. 39. Schematic of the node sampling: \bullet , selected node (N)

is obtained as

$$\mathbf{K}_H \boldsymbol{\eta} = \mu \mathbf{M}_H \boldsymbol{\eta} \quad (79)$$

where $\mathbf{M}_H = \mathbf{H}^T \mathbf{M} \mathbf{H}$ and $\mathbf{K}_H = \mathbf{H}^T \mathbf{K} \mathbf{H}$. It should be noted that the projected eigenvalue problem Eq. (79) possesses at least the same eigenvalues of the original systems, i.e., $\lambda_{(1)}, \lambda_{(2)}, \dots, \lambda_{(k)}$ (the indices may be different from the ones for the projected system.) This is because the subspace spanned by the columns of $(\boldsymbol{\Psi}, \hat{\boldsymbol{\Phi}})$ contains the eigenvectors of Eq. (75), i.e., $\boldsymbol{\phi}_{(j)} \in \text{span}(\boldsymbol{\Psi}, \hat{\boldsymbol{\Phi}})$ for $j = 1, \dots, k$, as $\text{span}(\boldsymbol{\Psi}, \hat{\boldsymbol{\Phi}}) = \text{span}(\boldsymbol{\Psi}, \boldsymbol{\Phi})$, and hence the projected eigenvalue problem has the same eigenvalues as the original ones. It means that, the eigenvalues of the projected system Eq. (79) does *not* contain any error in the eigenvalues and eigenvectors, with respect to those of the original eigenvalue problem of the finite element. Although this advantage comes with the expense of calculating the eigenvalues and eigenvectors of the finite element model, it is not a major drawback considering that the computational cost involved in the nonlinear computations with the original finite element would be more prohibitively expensive, than calculating a few normal modes of the finite element model.

8.2.2 Nonlinear DOF sampling

With the reduced order model obtained in 8.2.1, the next step is to select the DOF in B such that the nonlinear characteristics of the system can be well approximated by applying the nonlinear boundary conditions *only* on the selected DOF.

As mentioned, accurately calculating the NNM frequencies is of primary interest of this study. The NNM frequencies of the system can be obtained in several ways, such as time integration of Eq. (74) for harmonic loading, or harmonic-balance-based frequency/time domain analysis.^{104, 149} It was shown by the authors that the NNM frequencies for cracked plates obtained by the nonlinear harmonic response analysis can be well approximated by the application of bilinear frequency approximation even when the crack surfaces involve multiple DOF.¹⁰⁴ Therefore, as a measure to evaluate the results obtained with the selected DOF, bilinear frequency is used in the following development. Namely, the i th NNM frequency ω_{ni} can be approximated by a bilinear frequency ω_{bi} defined as

$$\omega_{bi} = \frac{2\omega_o\omega_s}{\omega_o + \omega_s} \quad (80)$$

where ω_o and ω_s are the natural frequencies of the corresponding linear systems, which can

be respectively obtained by solving the following eigenvalue problems:

$$\mathbf{K}_H \boldsymbol{\eta} = (\omega_o^2) \mathbf{M}_H \boldsymbol{\eta}, \quad \text{subject to } \textit{open} \text{ B.C.'s} \quad (81)$$

$$\mathbf{K}_H \boldsymbol{\eta} = (\omega_s^2) \mathbf{M}_H \boldsymbol{\eta}, \quad \text{subject to } \textit{sliding} \text{ B.C.'s} \quad (82)$$

The open B.C. is a boundary condition where no constraint is imposed on the nodes on Γ_A and Γ_B , or the DOF in B . Thus in fact Eq. (81) is identical to Eq. (79). On the other hand for the sliding B.C., it is assumed that Γ_A can freely slide with respect to Γ_B but cannot separate along the normal directions, as described as follows.

Here a contact pair is defined as a pair of nodes on Γ_A and Γ_B , which may or may not be in contact during the vibration, and a set of numbers denoting all the contact pairs is defined as C_{cp} . For the j th contact pair in C_{cp} , three mutually perpendicular normal vectors at a node on Γ_A are defined as \mathbf{n}_1^j , \mathbf{n}_2^j , and \mathbf{n}_3^j where \mathbf{n}_1^j is the normal vector pointing outward from the surface, \mathbf{n}_2^j and \mathbf{n}_3^j are unit vectors that are tangent to the surface and perpendicular to each other. Using these vectors, a coordinate transformation matrix $\mathbf{P}_A^j = (\mathbf{n}_1^j, \mathbf{n}_2^j, \mathbf{n}_3^j)$ is defined for each contact pair, with the assumption that a nodal displacement vector contains only translational DOF, such that the x_1 component of the displacement vector of the node is aligned with \mathbf{n}_1^j , and pointing outward from the surface. For the other node of the j th contact pair on Γ_B , the corresponding coordinate transformation matrix that aligns the x_1 component of the nodal displacement vector with the normal vector is defined as $\mathbf{P}_B^j = -\mathbf{P}_A^j$. Now assembling \mathbf{P}_A^j and \mathbf{P}_B^j for all $j \in C_{cp}$, a coordinate transformation is defined as

$$\mathbf{P} = \begin{pmatrix} \mathbf{P}_b & \mathbf{0} & \mathbf{0} \\ \mathbf{0} & \mathbf{I}_o & \mathbf{0} \\ \mathbf{0} & \mathbf{0} & \mathbf{I}_m \end{pmatrix}, \quad \text{where } \mathbf{P}_b = \overset{n_{C_{cp}}}{\mathbf{A}} (\mathbf{P}_A^j, \mathbf{P}_B^j) \quad (83)$$

and \mathbf{A} is an assembly operator, $\mathbf{P}_b \in \mathbb{R}^{n_B \times n_B}$, $\mathbf{I}_o \in \mathbb{R}^{n_o \times n_o}$, and $\mathbf{I}_m \in \mathbb{R}^{n_M \times n_M}$. Next, for the j th contact pair, the x_1 components of the nodal displacement vectors, which are denoted as η_A^j and η_B^j , are transformed to a relative displacement $w^j \triangleq (\eta_A^j + \eta_B^j)/\sqrt{2}$ and a displacement $v^j \triangleq (\eta_A^j - \eta_B^j)/\sqrt{2}$. Namely, denoting the set of DOF corresponding to u_A^j and u_B^j for all j th contact pair,

$$\begin{bmatrix} w^j \\ v^j \end{bmatrix} = \frac{1}{\sqrt{2}} \begin{pmatrix} 1 & 1 \\ 1 & -1 \end{pmatrix} \begin{bmatrix} \eta_A^j \\ \eta_B^j \end{bmatrix} \quad (84)$$

Now defining sets X , Y , and Z ($X \cup Y \cup Z = B$ and $n_X = n_Y = n_Z = n_{C_{cp}}$) that respectively contain sets of indices of the DOF corresponding to x_1 , x_2 , and x_3 for all $j \in C_{cp}$, and denoting the coefficient matrix in the Eq. (84) as \mathbf{R}^j , one can define a transformation matrix \mathbf{R} by assembling \mathbf{R}^j for $j \in C_{cp}$ as follows

$$\mathbf{R} = \begin{pmatrix} \mathbf{R}_x & \mathbf{0} \\ \mathbf{0} & \mathbf{I} \end{pmatrix}, \quad \text{where } \mathbf{R}_x = \overset{n_{C_{cp}}}{\mathbf{A}} (\mathbf{R}^j) \quad (85)$$

and $\mathbf{R}_x \in \mathbb{R}^{n_X \times n_X}$. Considering that $\mathbf{P}^{-1} = \mathbf{P}^T$ and $\mathbf{R}^{-1} = \mathbf{R}^T$, the eigenvalue problem Eq. (79) can be transformed to

$$K \mathbf{q} = (\omega_o^2) M \mathbf{q} \quad (86)$$

where $\boldsymbol{\eta} = \mathbf{PR}\mathbf{q}$, $M = (\mathbf{PR})^T \mathbf{M}_H \mathbf{PR}$, and $K = (\mathbf{PR})^T \mathbf{K}_H \mathbf{PR}$. Now noting that \mathbf{q} can be partitioned into $\mathbf{q} = [\mathbf{q}_r, \mathbf{q}_g]$ where \mathbf{q}_r is the vector of relative DOF, or $u^j, \forall j \in C_{cp}$, and \mathbf{q}_g is the generalized internal DOF containing $v^j, \forall j \in C_{cp}$, x_2 and x_3 components of the nodal displacement vectors of the nodes of the contact pairs, displacement vectors of the observer nodes, and modal coordinates. That is, Eq. (86) can be written as

$$\begin{pmatrix} K_{rr} & K_{rg} \\ K_{gr} & K_{gg} \end{pmatrix} \begin{bmatrix} \mathbf{q}_r \\ \mathbf{q}_g \end{bmatrix} = (\omega_o^2) \begin{pmatrix} M_{rr} & M_{rg} \\ M_{gr} & M_{gg} \end{pmatrix} \begin{bmatrix} \mathbf{q}_r \\ \mathbf{q}_g \end{bmatrix} \quad (87)$$

where $R \subset X$ and $G = (A \setminus R) \cup M$.

The best approximation to the NNM frequency can be obtained when the sliding boundary conditions are imposed on all of the nodes on the surface Γ_A and Γ_B . Namely the associated eigenvalue problem with the sliding boundary conditions can be obtained by constraining *all* the relative DOF, or $\mathbf{q}_r = \mathbf{0}$, i.e.,

$$K_{gg} \mathbf{q}_g = (\omega_s^2) M_{gg} \mathbf{q}_g \quad (88)$$

Now, we assume that we do *not* like to consider all nodes in R for the subsequent forced response analysis due to the large number of DOF involved in R . In other words, the nodes where the nonlinear boundary conditions are applied should be sampled such as illustrated in Fig. 39. The selected DOF is designated as nonlinear DOF, and a set of indices of the nonlinear DOF is denoted as N , where $N \subset R$. The rest of DOF in R is designated as linear DOF, and associated set is denoted as L where $N \cup L = R$. Therefore, the bilinear frequency should be calculated with ω_s such that the sliding B.C. is applied only on the DOF in N , or $\mathbf{q}_n = \mathbf{0}$, i.e.,

$$\begin{pmatrix} K_{ll} & K_{lg} \\ K_{gl} & K_{gg} \end{pmatrix} \begin{bmatrix} \mathbf{q}_l \\ \mathbf{q}_g \end{bmatrix} = (\omega_s^2) \begin{pmatrix} M_{ll} & M_{lg} \\ M_{gl} & M_{gg} \end{pmatrix} \begin{bmatrix} \mathbf{q}_l \\ \mathbf{q}_g \end{bmatrix} \quad (89)$$

Considering that the value of the natural frequency of the system with the open boundary conditions, ω_o , is independent on neither the number nor the pattern of the selected DOF (recalling that $\text{span}(\boldsymbol{\Psi}_c, \hat{\boldsymbol{\Phi}})$ contains the chosen eigenvectors), one can see from Eq. (80) that ω_{bi} is dependent only on ω_s for a fixed ω_o . Now considering the Rayleigh's theorem of constraints defined by Eq. (73), it is known that all the system's eigenvalues increase if a single constraint is imposed on a system. Therefore, as the number of constraints on Eq. (79) to calculate ω_s increases, ω_s increases. Furthermore, considering that ω_{bi} is a monotonically increasing function of ω_s for a fixed ω_o , or $\partial \omega_{bi} / \partial \omega_s = 2\omega_o^2 / (\omega_o + \omega_s)^2 \geq 0$, one can state that the best approximation of ω_{bi} for a given number of n_N can be obtained when the maximum ω_s is achieved. Thus a corresponding maximization problem is stated as follows:

$$\begin{aligned} & \max_{N \subset R} \omega_s(N) \\ & \text{subject to } |N| = n_N \end{aligned} \quad (90)$$

This maximization problem may be solved by mathematical programming methods, such as integer programming or topology optimization methods as was done in Ref.¹⁴¹ As it shall be discussed next, this maximization problem can in fact be treated in a more efficient way

by the use of Guyan reduction and some methods to choose the *master DOF* for reduced order modeling techniques.

8.2.3 Automatic master DOF selection

The methods for automatically selecting the master DOF for the Guyan reduction have been previously developed, such as in Refs.^{123,124,130} In particular, the method proposed by Henshell and Ong¹²³ appears to be the most successful approach. Although it has been known to be computationally expensive due to the nature of eliminating a single DOF per iteration and successive application of Guyan reduction, this can be alleviated by the application of the primary model reduction by the CMS as developed in 8.2.1. As was mentioned by Bouhaddi and Fillod,¹³⁰ and Shah and Raymund,¹²⁴ the master DOF of Guyan reduction should be chosen such that the valid eigenvalue range of the reduced order model is maximized. In general, it has been known that the eigenvalue range of validity is “bounded” by the lowest eigenvalue of the system with all the master DOF fixed. Here this concept is applied to the problem of finding the optimal N that solves Eq. (90). Namely, the corresponding eigenvalue problem is Eq. (89) by regarding \mathbf{q}_n as the master DOF. As was discussed in the Ref.,¹⁵⁰ the error bounds in the i th eigenvalue of the reduced model produced by the Guyan reduction can be obtained a priori by the following relationship

$$0 \leq \varepsilon_i \leq \frac{\lambda_i}{\lambda_{s,min} - \lambda_i} \quad (91)$$

where $\varepsilon_i \triangleq (\bar{\lambda}_i - \lambda_i)/\lambda_i$ is the relative error in the i th eigenvalue, $\bar{\lambda}_i$ is the i th eigenvalue of the reduced order model, λ_i is the i th eigenvalue of the original finite element model, and $\lambda_{s,min}$ is the smallest eigenvalue of the system with *all the master DOF fixed*. For $\lambda_i/\lambda_{s,min} \ll 1$, the upper bound asymptotically converges to the following value,¹⁵¹

$$0 \leq \varepsilon_i \leq \lambda_i/\lambda_{s,min} \quad (92)$$

Therefore, it is apparent that maximizing $\lambda_{s,min}$ results in minimizing the upper bound of the error for all the eigenvalues of the reduced order model. Hence this gives us a guideline for selecting the master DOF for Guyan reduction such that the errors in the eigenvalues of the resulting reduced order model are minimized.

By observing this fact from another point of view, one may see that if a certain set of master DOF can achieve the maximum $\lambda_{s,min}$, we can obtain not only an accurate reduced order model that can well approximate the first few lowest eigenvalues of the original system, but also as a “byproduct”, a good estimate on the *optimal constraint locations that maximize the fundamental frequency*. Recasting this to our original problem of selecting the optimal set N , the error bounds Eq. (92) associated with the eigenvalue problem Eq. (89) are written as

$$0 \leq \varepsilon_i \leq \frac{(\omega_o^2)_i}{(\omega_s^2)_1 - (\omega_o^2)_i} \quad (93)$$

where $\varepsilon_i \triangleq [(\bar{\omega}_o^2)_i - (\omega_o^2)_i]/(\omega_o^2)_i$, $(\bar{\omega}_o^2)_i$ is the i th eigenvalue of a reduced order model, $(\omega_s)_1$ is the lowest natural frequency of Eq. (89). The corresponding maximization problem is Eq. (90), and by solving this problem for the lowest eigenvalue, $(\omega_s)_1$, one can expect that the chosen nodes pattern is at least sub-optimal.

[1] $i = 1$ to $i = n_R - n_N$ Calculate $\sqrt{k_{jj}/m_{jj}}$ for $j \in R$ Find q_1 such that $\sqrt{k_{q_1 q_1}/m_{q_1 q_1}} = \max_{j \in R} \sqrt{k_{jj}/m_{jj}}$
 $L \leftarrow \{q_1, \dots, q_{n_k}\}$ where q 's are the DOF associated with the k th contact pair ($k \in C_{cp}$) and n_k is the number of DOF in k th contact pair $N \leftarrow R \setminus L$ $R \leftarrow N$ Calculate constraint modes Eq. (94) Apply Guyan reduction to the system matrices: $M \leftarrow \Psi^T M \Psi$, $K \leftarrow \Psi^T K \Psi$

Algorithm 1. DOF selection based on Henshell and Ong method

[1] Calculate Φ_k $i = 1$ to $i = n_R - n_N$ $\mathbf{A} \leftarrow \Phi_k^T \Phi_k$ $\mathbf{E} \leftarrow \Phi_k \mathbf{A}^{-1} \Phi_k^T$ Find q_1 such that $e_{q_1 q_1} = \min_{j \in R} e_{jj}$
 $L \leftarrow \{q_1, \dots, q_{n_k}\}$ where q 's are the DOF associated with the k th contact pair ($k \in C_{cp}$) and n_k is the number of DOF in k th contact pair $N \leftarrow R \setminus L$ $R \leftarrow N$ Delete rows of Φ_k corresponding to the DOF in L

Algorithm 2. DOF selection based on EIDV method

According to Refs.,^{151,152} the sequential elimination method by Henshell and Ong¹²³ tends to keep $\lambda_{s,min}$ high, as it eliminates the DOF associated with the highest constrained frequency at each iteration as the slave DOF. Namely after the elimination procedure, if the chosen master DOF are all fixed, the system is left with the DOF that were chosen as the slave DOF that were identified to have the highest constrained frequency at each elimination process. Thus the resulting system with all the master DOF fixed tends to have a larger $\lambda_{s,min}$ than that calculated with systems with other possible combinations of master DOF fixed. The Henshell and Ong's method that is adapted specifically for this problem is shown in Algorithm 1. First, at each iteration, the ratios of the diagonal terms of the stiffness matrix k_{jj} to the diagonal terms of the mass matrix m_{jj} are calculated for $\forall j \in R$, and the index q_1 that gives the maximum ratio among $j \in R$ is obtained. Next, the set L is updated such that it contains q_1 , and all the other DOF that are associated with the contact pair $k \in C_{cp}$ to which the q_1 th DOF belongs, e.g., the DOF that are perpendicular to the normal direction. The set N is then updated such that it excludes the selected DOF of L from R , and the set R is re-defined as N . A constraint mode is calculated by solving a problem where a unit displacement is applied to a DOF in N whereas all the other DOF in N being fixed. This is repeated for all DOF in N , resulting in the following matrix:

$$\Psi = \begin{pmatrix} \mathbf{I} \\ -(K_{ll})^{-1} K_{ln} \end{pmatrix} \quad (94)$$

where Ψ is the matrix of constraint modes for all DOF in N . The Guyan reduction is then applied to the mass and stiffness matrices. The iteration continues until the number of DOF in N reaches the specified value of n_N using Ψ .

In order to clarify the appropriateness of the algorithm in Algorithm 1 to this problem, another algorithm for selecting DOF is shown here for comparison. The method of effective independence vector, or the EIDV method developed by Kammer,¹⁴⁰ is a method to choose the sensor placement locations for the vibration measurement of large scale structures. The method aims to make the measured eigenvectors as linearly independent as possible. According to Penny *et al.*,¹³⁹ many of the criteria for choosing the master DOF for model order reduction have similar criteria for choosing measurement locations in a way such that

the *lower frequency modes can be captured accurately*. In fact, as examined by Penny *et al.*, both the Henshell and Ong method and the EIDV method produce acceptable selections in most cases, in a sub-optimal manner. The DOF selection algorithm based on the EIDV method is shown as Algorithm 2. First, the eigenvalue problem Eq. (88) is solved for the first k modes, and the associated modal matrix is designated as $\Phi_k = (\phi_1, \phi_2, \dots, \phi_k)$, or $K\Phi_k = M\Phi_k\Lambda_k$ where $\Lambda_k = \text{diag}_{j=1, \dots, k}((\omega_o^2)_j)$. The Fisher information matrix \mathbf{A} is then calculated as $\mathbf{A} = \Phi_k^T \Phi_k$, and an idempotent matrix \mathbf{E} is computed as $\mathbf{E} = \Phi_k \mathbf{A}^{-1} \Phi_k^T$, the diagonal of which is called the independence distribution vector (see Ref.¹⁴⁰ for detailed formulations.) The least contributing DOF to the independence of the modes among the ones in R is identified as the one with the smallest diagonal element in \mathbf{E} . The associated DOF are also identified and stored in L , and both N and R are updated as in the Henshell and Ong method. Finally the rows of Ψ_k corresponding to the DOF in L are deleted. The iteration continues until the size of N reaches the desired number n_N .

Although the EIDV method shares similar objective for choosing DOF with the Henshell and Ong method, the objective of the EIDV method is not exactly the maximization problem of Eq. (90). Therefore it is expected that the Henshell and Ong method returns better solutions to the given maximization problem than the EIDV method, as it is shown in the next section.

8.3 Case study

In section 8.2, the method to select the nonlinear DOF has been introduced. In this section, the validity and applicability of the method are discussed by applying the algorithm to an example problem. With the case study, the validity of the proposed method is discussed in terms of the bilinear frequencies and forced response. Furthermore a metric to assess their accuracy is introduced and examined.

8.3.1 Simple cracked plate model

Problem description A cantilevered cracked plate model was constructed with Young's modulus $E = 2.0 \times 10^{11}$ Pa, Poisson's ratio $\nu = 0.3$, and density $\rho = 7800$ kg/m³, and its geometry is shown as Fig. 40(a) where $w = 6.0 \times 10^{-3}$ m, $l = 6.0 \times 10^{-2}$ m, $h = 1.5 \times 10^{-1}$ m, $l_c/l = 0.625$, and $h_c/h = 0.475$. The model was discretized with 5,120 linear solid elements and resulted in mass and stiffness matrices with 18,630 DOF. On the crack surfaces as shown in Fig. 40(b), there are 180 nodes, or 90 contact pairs on the surfaces hence the number of the associated DOF is 540. The CMS method shown in the section 8.2.1 was then applied to the FE model, and it resulted in the 681 DOF (3.6% of the original size) system consisting of 621 physical DOF and 60 modal coordinates corresponding to the free-interface normal modes. With this reduced order model, both algorithms in Figs. 1 and 2 were applied for $n_N = 4, 8, 16, 32, 64$, and 128. For the EIDV method, the first four modes were considered.

In order to compare these results with an ‘‘intuitive’’ selection method, a selection criteria was also employed, where the nonlinear DOF were chosen based on the amount of *penetration* between the nodes in a contact pair for the modes of interest, which in this case is the fourth mode. Namely, it was hoped that penalizing the inter-penetration of the most penetrating

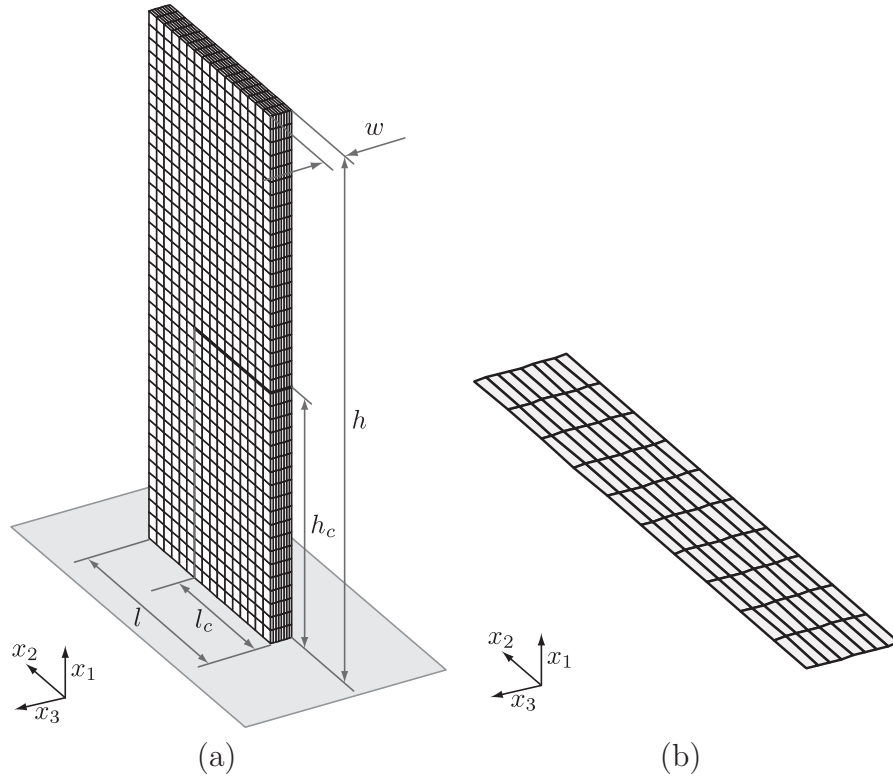


Fig. 40. Cantilevered cracked plate model: (a) FE model, (b) Magnified crack surface

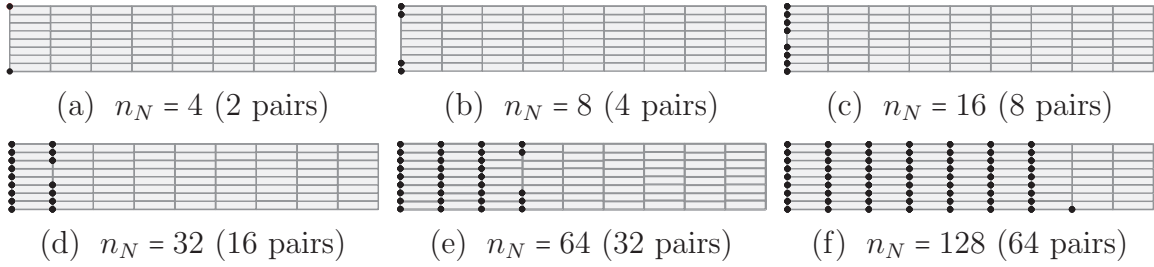


Fig. 41. Selected nodes by an intuitive approach (left edge open)

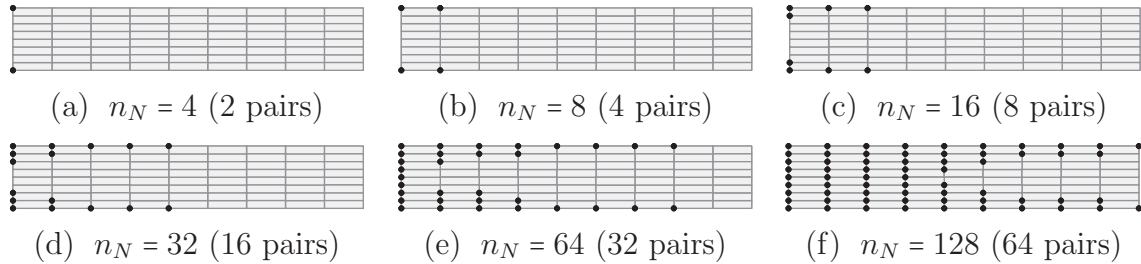


Fig. 42. Selected nodes by EIDV method (left edge open)

contact pairs would produce the “stiffest” system response. The selected node pattern with such criterion is shown as Fig. 41, and the results of the EIDV method and the Henshell and Ong method are shown as Figs. 42 and 43. As can be seen in Fig. 41, if the nodes are chosen based on the amount of penetration, the selection starts from the nodes near the crack edge (open side) for $n_N = 4$, and it then proceeds toward the tip of the crack (closed side) as n_N increases. It makes sense because the motion of the crack surfaces is significant near the open edge than that near the closed edge. On the other hand with the EIDV method, the method

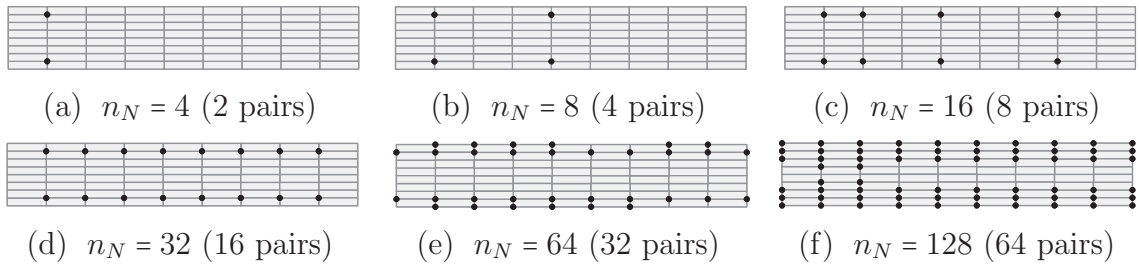
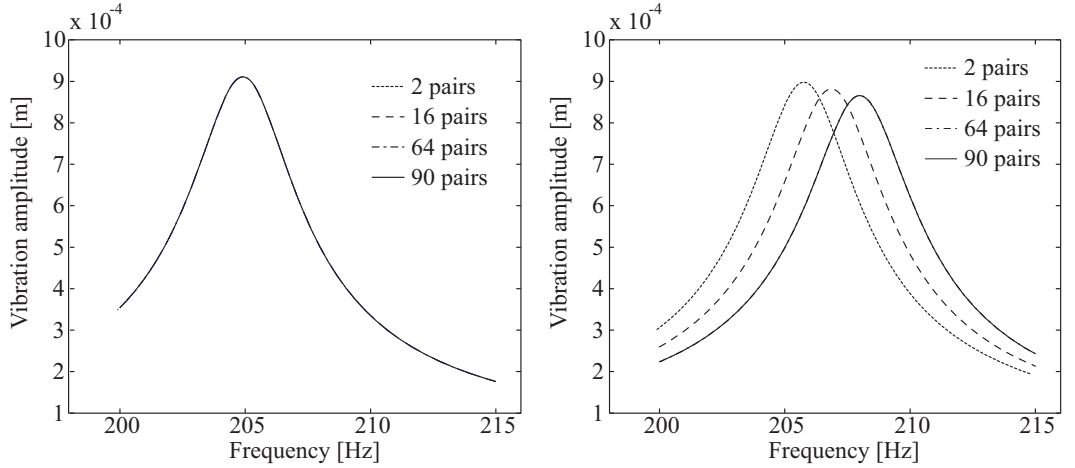
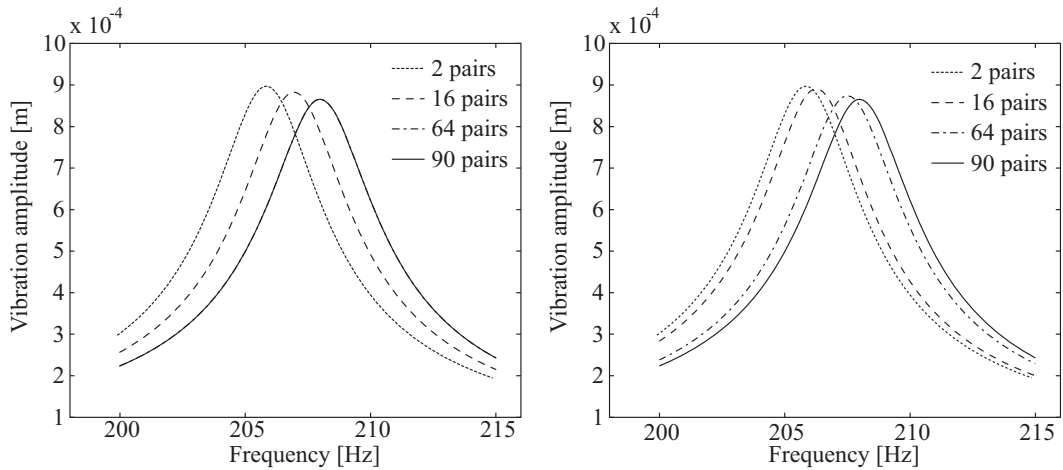


Fig. 43. Selected nodes by the modified Henshell and Ong method (left edge open)



(a) Henshell and Ong method (linear) (b) Henshell and Ong method (nonlinear)



(c) EIDV method (nonlinear) (d) Intuitive approach (nonlinear)

Fig. 44. Results of forced response analysis of the cracked plate

also starts to select the nodes near the crack edge, but it tends to choose more nodes on the crack rims than the nodes near the crack edge as shown in Fig. 42. Finally with the Henshell and Ong method, it also select the nodes near the crack edge first, for $n_N = 4$, but it then tends to select the nodes over the crack surface in a more distributed manner as can be seen in Fig. 43.

Forced Response Analysis Next, in order to see the influence of the application of the nonlinear B.C. onto the selected nodes on an NNM frequency, forced response analysis was carried

out by applying an external harmonic loading to the cracked plate. As one might notice, when the forced response of this structure with a crack is considered, the repetitive opening and closing of the crack faces must be treated appropriately with contact algorithms. As a result, the vibration is nonlinear and the steady-state response of the displacement may not be expressed as a harmonic function even if the external force is a harmonic function. Therefore in this study, the steady-state response was obtained by assuming that the displacement can be expressed as a truncated Fourier series, and the nonlinear boundary condition can be enforced by the penalty method.¹¹⁶ The method is called the hybrid frequency-time domain method,^{104,149} which is based on the concept of harmonic balance method.¹⁰⁷ Detailed formulation of the method is omitted in this paper.

It is noted that the system matrices were further reduced by the application of Eq. (76) to the reduced-order model before the forced response calculation, by keeping the selected node pairs as the active DOF and condensing out the other DOF including physical and modal coordinates. For example, with $n_N = 64$ (32 pairs), the system size was reduced down to 155 DOF, which is 0.83% of the original system size.

A harmonic forcing of magnitude 3 N was then applied at the tip of the plate, in order to excite the first vibration mode, which corresponds to the first out-of-plane bending mode. The forced response was calculated for both linear case, i.e., with the open B.C., and nonlinear case with the nonlinear boundary conditions imposed on N with the selections by the Henshell and Ong method. The results are shown in Figs. 44(a) and 44(b). As can be seen in Fig 44(a), the selection pattern does not alter the linear forced response. This is because the selection of the active DOF does not alter the eigenvalues of the reduced order model, and it was assumed that the system was completely linear when the forced response was calculated. On the other hand, the number of contact pairs greatly affects the results of nonlinear forced response as shown in Fig. 44(b). One may observe that the response with 64 contact pairs is almost identical to that with the full set of 90 contact pairs, which implies that for accurately calculating the nonlinear resonant frequencies, it may not be necessary to enforce nonlinear boundary conditions for all the contact pairs on the crack faces. The same forced response calculations were carried out with the node patterns selected by the EIDV method and the method based on the amount of penetration, and they are respectively shown in Figs. 44(c) and 44(d). As can be seen in Fig. 44(c), the results with the patterns chosen by the EIDV method are comparable with the ones produced by the Henshell and Ong method. On the other hand as can be seen in Fig. 44(d), the forced response with the node patterns chosen by the “intuitive” approach produced worse results than the other two methods, i.e., for a given number of n_N , the predicted resonant frequency by the approach is lower than that calculated by the other methods. This is the most visible in the results for $n_N = 64$, for which both the Henshell and Ong method and the EIDV methods produced results that are almost identical to the results for $n_N = 90$.

Bilinear Frequency Approximation Finally, the influence of the selected node pattern on the bilinear frequencies is discussed. The first four bilinear frequencies were calculated for the model with the selected node patterns with the three methods, and the results are shown in Fig. 45. The first four modes correspond to the first out-of-plane bending, the first torsion, the second out-of-plane bending, and the first in-plane bending modes respectively. The plots in Fig. 45 show the percentage errors in the bilinear frequency versus the number of contact pairs, where the error is defined as the ratio of the difference between the bilinear frequency

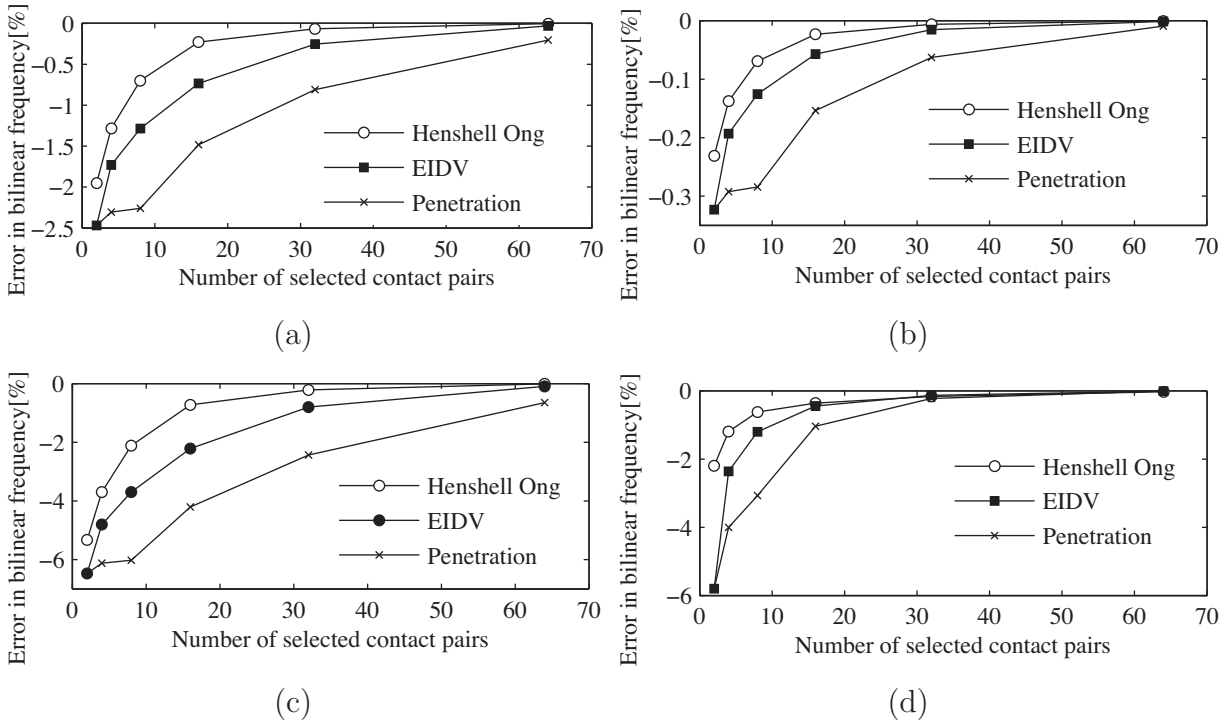


Fig. 45. Errors in the first four bilinear frequencies:(a) NNM 1, (b) NNM 2, (c) NNM 3, (d) NNM 4

with the sampled contact pairs and that with the full set of contact pairs, to that with the full set of contact pairs. As can be seen, the Henshell and Ong method consistently provides the best results among all the methods for the first four modes. Moreover, it shows the best convergence rate in terms of the number of contact pairs.

A posteriori accuracy assessment

As seen above, even though the intuitive approach chooses the contact pairs that show the most penetration, application of the nonlinear boundary conditions to these nodes does not result in the “stiffest” vibration response. To be specific, the Henshell and Ong method and the EIDV method produced the node patterns that yield the closer results to the reference results in terms of forced response and bilinear frequencies, than the patterns chosen by the intuitive approach. In particular, the Henshell and Ong method iteratively aims to solve the maximization problem Eq. (90) in a sub-optimal manner. Therefore the bilinear frequencies as well as the resonant frequencies were well approximated with the nodes chosen by the Henshell and Ong method. In order to better understand the governing factor for the accuracy of the results, a more physical interpretation of the results is provided here. Namely, the key effect for achieving the good approximation of the NNM frequency is to ensure, as much as possible, the non-penetrability condition on the contact pairs where the nonlinear B.C.s’ are *not* applied. The penetration should be evaluated during a vibration cycle, thus both the depth and the duration of the penetration should be taken into account. These quantities vary in space, and depend on the frequency of vibration. Hence as a metric to characterize not only the amount but also the duration of penetration over the entire crack surfaces for

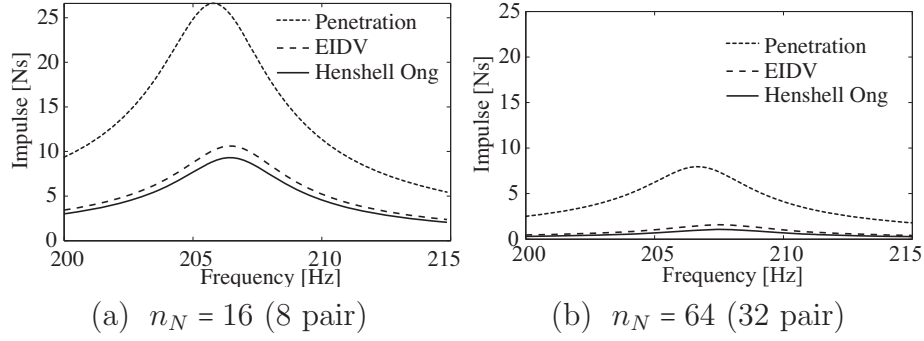


Fig. 46. Virtual impulse for a period of vibration for NNM 1

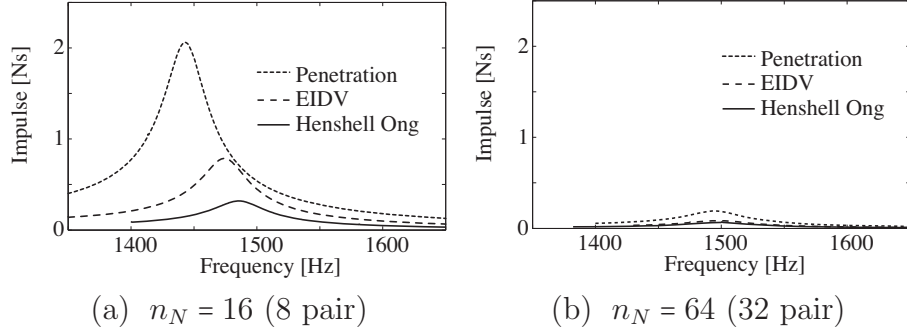


Fig. 47. Virtual impulse for a period of vibration for NNM 4

a given vibration frequency, the following quantity is introduced:

$$\hat{F} = \int_0^T \left(\int_{\Gamma_A(\Gamma_B)} k_e u_p(\mathbf{r}, t) d\Gamma \right) dt \quad (95)$$

where \hat{F} is a quantity with the dimension of impulse named “virtual impulse”, k_e is an equivalent spring constant per unit length determined by the ratio between the Young’s modulus multiplied by the characteristic area and the characteristic length, u_p is the amount of penetration along the surface normals, and T is the period of vibration associated with the NNM frequency. The quantity \hat{F} is calculated based on the calculated time trajectory of displacements of the nodes on the crack surfaces, and can be thought of as an impulse that does *not* contribute to the system response, as this impulse is not applied to the system when the response is calculated. In other words, the smaller the value of \hat{F} is, the stricter the boundary conditions are imposed on the nodes over the entire crack surfaces.

First, the forced response analysis was carried out, and the corresponding time history of u_p over the entire crack surface was recovered from the vibration response. The integrals in the Eq. (95) were then evaluated by a simple quadrature rule both in space and time. The metric was calculated for the first and the fourth modes for 8 and 32 pairs chosen by the methods, and the results are shown in Figs. 46 and 47. As can be seen in Figs. 46 and 47, the virtual impulse varies over the frequency range. In particular, when the frequency of excitation is close to the resonant frequency, or the NNM frequency, then the amount of penetration increases as well. However for all cases, the Henshell and Ong method consistently results in the smallest impulse over the frequency range among the three methods considered. It means that the nonlinear B.C. on the crack faces is the most strictly enforced by the node patterns chosen by the Henshell and Ong method.

9 NODE SAMPLING FOR NONLINEAR VIBRATION ANALYSIS OF STRUCTURES WITH INTERMITTENT CONTACT

Vibration problems of structures with intermittent contact have been studied extensively for several decades. These problems have practical importance and feature theoretical complexity due to their nonlinear nature. A numerical modeling procedure for such problems based on the finite element (FE) method is presented in this paper. This work is motivated by a need for developing a model-based crack detection algorithm of elastic structures based on their spectral properties, such as resonant frequencies and response shapes. In order to properly predict the resonant frequencies of such structures, one has to consider the nonlinearity caused by intermittent contact at the cracks; the so-called closing crack or breathing crack effect. This nonlinearity has hindered analysts from accurately calculating the resonant frequencies of cracked structures, because they cannot be calculated from classical linear modal analysis. Recently, sophisticated contact algorithms have been developed, such as the penalty method¹¹⁶ and the augmented Lagrangian method.¹¹⁷ Hence, the accuracy of the results of time transient simulations with FE models involving intermittent contact has been improved. Furthermore, studying vibration problems of such structures with an FE model with a realistic complexity is becoming feasible with the aid of high-performance computers. However, in turn, due to the advancement of these technologies, analysts tend to create models with increasingly larger number of degrees of freedom (DOF). This is based on the expectation that, as the models become more realistic and the results become more accurate, the problem can still be solved in a reasonable amount of time. However, the number of DOF required for high-fidelity predictions currently overwhelms even the most advanced hardware and software. That is because, as the model complexity increases, the cost of solving contact problems increases dramatically, even when the potential contact areas are known a priori. This occurs even if one uses reduced order modeling techniques, such as the Craig-Bampton method.¹¹⁸ For forced response vibration problems of such structures, one can use accurate and efficient semi-analytical methods such as the ones based on the harmonic balance method (e.g., Ref.¹⁰⁷), by representing the steady-state dynamic response of the model with a truncated Fourier series. However, such methods still suffer from the increase of computational cost as they require a fair number of harmonics to be included in the Fourier transform, to obtain an accurate result. Therefore, the goal of this paper is to present a new and efficient reduced order modeling framework for vibration problems of elastic structures involving intermittent contact, with particular attention to modeling nonlinear vibration of cracked structures. The reduced order model is constructed such that it can be used in conjunction with standard contact algorithms, such as Lagrange’s multipliers, penalty methods, and augmented Lagrangian methods. The focus is placed upon reducing the number of DOF involved in the contact regions, in an automatic manner.

This paper is organized as follows. In section 9.1, a literature survey over the related fields is provided. In section 9.2, the proposed modeling framework is presented, including the reduced order modeling approach and contact DOF selection method. As applications of the method, two case studies are shown in section 9.3, using FE models of a cantilevered cracked plate and an academic blade model.

9.1 Background

The issues of reducing and selecting DOF of FE models have been extensively studied by various methods and distinct perspectives, such as the reduction of the interface DOF between

substructures, selection of master DOF for Guyan reduction,¹¹⁹ optimal sensor placement, and optimal constraint locations. However, many of the available methods share similar goals and relate to each other (as described below).

Firstly, the issue of *reducing the number of interface DOF* between the components has been studied by several researchers. Brahmi *et al.*¹²⁰ proposed a method to be employed before the assembly of substructures in component-based modeling methods, where basis vectors are chosen based on the combination of secondary modal analysis of the interface DOF partitions of the matrices, and the truncation of modes based on the singular value decomposition. Balmés¹²¹ introduced the framework for generalizing interface DOF such as constraint modes, by considering the new basis representing the actual interface displacements. Castanier *et al.*¹²² also proposed a technique based on applying modal analysis and mode truncation to the constraint mode partition of the matrices produced by component mode synthesis (CMS).¹¹⁸ The resulting modes are transformed back into the FE coordinates and are called characteristic constraint modes. All of these methods achieve a reduction in the number of interface DOF. However, they do not provide any criteria as to *how* the interface DOF need be selected automatically (or even manually) for accurately enforcing the boundary conditions in the areas of intermittent contact.

Secondly, the *selection of master DOF* is a crucial factor for determining the spectral properties of reduced order models obtained by using Guyan reduction. Hence, many algorithms for the selection of the master DOF have been developed. These methods are relevant to our objective because they produce results that often solve the optimization problem considered in this study (as discussed in section 9.2). An automatic master DOF selection algorithm was first proposed by Henshell and Ong,¹²³ in which the master DOF are chosen where the inertia is high and the stiffness is low, whereas the slave DOF are chosen where the inertia is low and the stiffness is high. This process can be automated by examining the radian frequency ω_s defined by fixing all DOF except the DOF index s . Namely, $\omega_s \triangleq \sqrt{k_{ss}/m_{ss}}$, for $s = 1, \dots, n$, where k_{ij} and m_{ij} are the entries at the i th row and j th column in FE stiffness and mass matrices of size n . The index s with the largest ω_s is identified at each iteration step, and the DOF is eliminated by an application of Guyan reduction with s being the slave DOF and all the other DOF being the master DOF. This process can be repeated until the number of master DOF reaches the desired magnitude. An approach similar to this algorithm was proposed by Shah and Raymund¹²⁴ based on the discussion of Kidder and Flax,^{125–127} where the number of master DOF is controlled by iteratively eliminating the DOF whose ω_s is larger than a pre-defined cut-off frequency ω_c (that is chosen to be approximately three times the highest significant frequency in the frequency range of interest). Independently from the work by Henshell and Ong, Grinenko and Mokeev¹²⁸ developed an order reduction technique named frequency-dynamic condensation, which also uses a criterion to select master degree of freedom. Although their criterion was legitimate, the implementation of the selection algorithm still suffers from tedious exhaustive-search calculations for selecting the master DOF. The selection method proposed by Matta¹²⁹ also uses the ratio k_{ss}/m_{ss} with a criterion similar to that proposed by Henshell and Ong. This method can be applied not only to Guyan reduction but also to CMS, where both static and normal modes are used as basis vectors, onto which the system dynamics are projected. A method proposed by Bouhaddi and Fillod¹³⁰ uses a different concept, where if a DOF a is a *node* of the i th eigenmode, then fixing the DOF a results in $\hat{\lambda}_{i-1} = \lambda_i$, where λ_i is the i th eigenvalue of the non-fixed system, and $\hat{\lambda}_{i-1}$ is the eigenvalue of the system with the DOF a fixed. This concept may be

understood using a vibration problem of a string with both ends fixed. That is, the lowest natural frequency of the string with a single support becomes the highest if the support is placed at the node of the second mode of vibration.¹³¹ This is because the first mode with the constraint becomes identical to the second mode of the unconstrained string, which has the eigenvalue as the feasible upper bound of the first eigenvalue with a single constraint. It is noteworthy that Bouhaddi and Fillod explicitly aimed for *maximizing the minimum eigenvalue of the system where all the master DOF are fixed*. This concept will be revisited in section 9.2.3.

The methods for the node selection reviewed above are based on Henshell and Ong method to some extent. Another class of methods is based on the concept of modal energy. For example, the method proposed by Kim and Choi¹³² uses the energy distribution among the DOF for each mode, and chooses the set of primary DOF by taking the partial sum over the rows of the energy distribution matrix. The method proposed by Cho and Kim¹³³ utilizes energy estimation at discretization element level by the Rayleigh quotient value of each element. Kim and Cho then proposed a selection method consisting of two steps:¹³⁴ model order reduction by improved reduced system (IRS)¹³⁵ using the master DOF selected via the method based on energy estimation of each element,¹³³ and subsequent sequential elimination method¹²³ with an iterative IRS. Another automatic DOF selection method named modal energy selection method proposed by Li¹³⁶ uses a metric called index of classification, which is based on the approximate modal energy associated with each DOF. The method was successfully applied to an FE model of a cantilever beam. Oh and Park¹³⁷ also proposed a criterion for selecting the master DOF based on singular values of the modal matrix. However, that approach suffers from the computational cost due to exhaustive search over the possible master DOF sets, and depends on engineer's knowledge and intuition.

Thirdly, a similar but slightly different issue is the *selection of measurement locations* for vibration testing. For example, one may need to measure vibration displacements of a structure to determine vibration modes, typically with a limited number of sensors and limited locations where the sensors can be placed. Thus, one may like to maximize the information one can obtain with the limited number of sensors and locations. However the question arises as to *how* the sensors need to be located, since the optimal configuration of sensors for such objective cannot be easily determined. There have been many methods developed to date for achieving this goal. In particular, one class of approach is based on information theory. These approaches determine the sensor locations by optimizing the norm of the Fisher information matrix.¹³⁸ Among them, one of the most widely used techniques is the effective independence vector method, or the EIDV¹³⁹ method developed by Kammer.¹⁴⁰ The method determines the placement of sensors within the candidate locations while maintaining as much independent information as possible, i.e., maintaining the measured mode shapes as independent as possible. Therefore, it is natural to hypothesize that the application of the nonlinear boundary conditions to the optimum sensor locations would also well represent the full order model where the boundary conditions are applied at all locations in the intermittent contact region. This method is considered in this study and the associated formulation is discussed in detail in section 9.2.3.

Lastly, the issue of finding *the optimal constraint locations to maximize the fundamental natural frequency* of a structure is considered. This issue has an important relationship with the optimal master DOF selection. For instance, suppose one wants to increase as much as

possible the lowest natural frequency of a structure, by adding a finite number of supports or kinematical constraints to the structure. However, the problem of finding the optimal number and the locations of such supports is not as easy as it appears. Therefore, it may be necessary to apply computationally expensive optimization algorithms, such as done in the work by Zhu and Zhang.¹⁴¹ In contrast, Åkesson and Olhoff¹⁴² studied the problem by applying the Courant’s maximum-minimum principle. Namely, if there is a discrete dynamical system of size n , and there are r ($< n$) kinematical constraints applied to the system, then all the eigenvalues of the structure increase, and the increased eigenvalues are bounded by the following formula

$$\lambda_i^0 \leq \lambda_i \leq \lambda_{i+r}^0, \quad i \in \{1, 2, \dots, n\}, \quad (96)$$

where λ_i^0 and λ_{i+r}^0 denote the i th and $(i+r)$ th eigenvalues of the structure without the constraints, and λ_i is the i th eigenvalue of the constrained structure. Also based on the same principle and the findings of Szelag and Mroz,¹⁴³ Won and Park¹⁴⁴ applied a minimization method to obtain the optimal support location and achieve the maximum fundamental natural frequency of a cantilevered plate. They showed that the optimal support locations should be on the nodal lines of the $(r+1)$ th mode of the unconstrained structure. It is noted that this result conforms to the vibration problem of a fixed string mentioned above. This method was successfully applied to their specific examples, but the method can be applied only to special cases where the potentially-constrained region is the entire region of the structure and the points on the nodal lines can be selected. Namely, if the regions to which the constraints are applied are limited to some specific regions of the structure, then the nodal lines may not exist in such regions, and the minimization problem becomes more complicated.

It is interesting to note that the idea of constraining the nodal lines was used to optimally select the master DOF for Guyan reduction by Bouhaddi and Fillod,¹³⁰ but they were not aware of the applicability of their method to optimally select the support positions, while Won and Park¹⁴⁴ were not aware of the applicability of their method to optimally select the master DOF locations for Guyan reduction. In this paper, we take advantage of this similarity between the optimal master DOF selections and the constraint locations, in order to achieve the optimal selection of the DOF where the nonlinear boundary conditions are applied.

9.2 Mathematical Formulation

Consider the small vibrations of an elastic structure represented as Ω with a fixed boundary Γ_f , where the structure may involve intermittent contact at Γ_A and Γ_B during the vibration cycles, such as shown in Fig. 48. Namely the boundaries open and close. Thus, the vibration problem is nonlinear because the condition for the boundaries to be in contact is dependent on the displacement field itself. That is, the boundary conditions at Γ_A and Γ_B are nonlinear. It is well known that the system eigenvectors and eigen-frequencies are different from the actual response shapes and resonant frequencies of this nonlinear structure. In this paper, they are respectively referred to as the nonlinear normal modes (NNMs) and NNM frequencies, as was also done in Ref.¹¹⁴

If the structure is discretized with a method such as an FE method, the nonlinearity associated with the contact is *localized*, in the sense that the nonlinearity is caused only by a

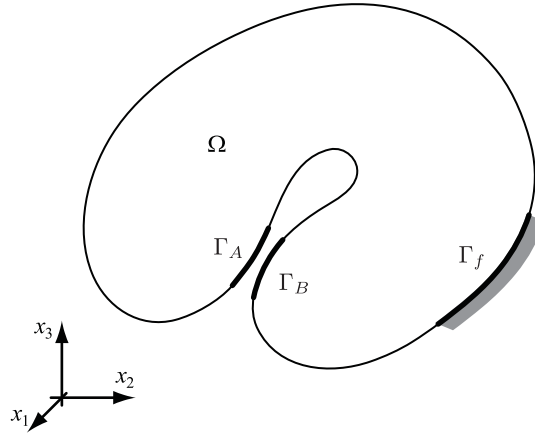


Fig. 48. An elastic structure with potentially contacting boundaries

small portion of the entire structure. In the following formulations, a set of indices of DOF in such region is denoted as B (boundary), whereas a set of indices of the DOF in the rest of the regions is denoted as I (internal), and partitions of vectors and matrices associated with these sets are designated with subscripts b and i . The sizes of the sets are denoted as $|B| = n_B$ and $|I| = n_I$. All the other DOF sets defined hereinafter follow the same notation.

Consider that the FE mass and stiffness matrices are denoted by $\mathbf{M} \in \mathbb{R}^{n \times n}$ and $\mathbf{K} \in \mathbb{R}^{n \times n}$, and the nodal displacement vector is given by $\mathbf{x} \in \mathbb{R}^n$. The governing equations of the vibration problem with the absence of external forcing and damping may be written in a partitioned matrix-vector form as follows

$$\begin{pmatrix} \mathbf{M}_{bb} & \mathbf{M}_{bi} \\ \mathbf{M}_{ib} & \mathbf{M}_{ii} \end{pmatrix} \begin{bmatrix} \ddot{\mathbf{x}}_b \\ \ddot{\mathbf{x}}_i \end{bmatrix} + \begin{pmatrix} \mathbf{K}_{bb} & \mathbf{K}_{bi} \\ \mathbf{K}_{ib} & \mathbf{K}_{ii} \end{pmatrix} \begin{bmatrix} \mathbf{x}_b \\ \mathbf{x}_i \end{bmatrix} = \begin{bmatrix} \mathbf{f}_b(\mathbf{x}_b) \\ \mathbf{0} \end{bmatrix}, \quad (97)$$

where $(\dot{\cdot})$ denotes a time derivative, and $\mathbf{f}_b \in \mathbb{R}^{n_B}$ denotes the nonlinear force associated with the intermittent contact.

When dealing with this type of nonlinear vibration problems, one can apply linear reduced order modeling techniques, such as Guyan reduction,¹¹⁹ system equivalent reduction expansion process (SEREP),¹⁴⁵ iterated improved reduced system (IIRS),^{146,147} or component mode synthesis (CMS).¹¹⁸ With such methods, one can obtain smaller system matrices by reducing the size of \mathbf{x}_i by means of Rayleigh-Ritz coordinate transformation comprising of various basis vectors such as static deformations and vibration modes, yet keeping the accessibility to the physical coordinates of \mathbf{x}_b . For instance, with the help of CMS, one can obtain a system with desired spectral properties *and* accessibility to \mathbf{x}_b , the size of which is as small as n_B DOF plus the number of linear normal modes whose frequencies lie in the frequency ranges of interest. The use of such linear reduced order modeling methods greatly helps analyze the dynamic response of systems with localized nonlinearities, such as transient dynamic analysis,¹⁴⁸ and nonlinear harmonic response analysis.¹⁵³ However, even with these reduced order modeling methods, if the number of DOF involved in the b partition becomes large (especially the cases with very fine mesh in the contacting regions) one cannot take advantage of the linear reduced order modeling techniques as the computational cost associated with the nonlinear dynamic analysis typically grows as the number of DOF in the

b partition increases. Furthermore, if one simply attempts to eliminate some of the DOF in the b partition, it results in inaccurate, or even wrong results. Therefore, to obtain accurate computational results, one needs to keep as many boundary DOF as possible. That can easily result in prohibitively costly calculations. Typically, as a workaround to avoid the inaccurate results due to the lack of sufficient DOF considered and at the same time to obtain efficient computational model, one has to select the DOF in a heuristic way, which greatly depends on the system characteristics and analyst's experience and intuition. Moreover, if the model is developed in such ways, the error in the analysis results cannot be estimated a priori. Our aim here is to develop an automatic way to select the DOF in B for a desired number of DOF to be selected.

Note that the major assumptions made in the proposed methodology are typical for such approaches, and can be summarized as follows.

- (1) The elastic structure is fixed in space, and the strain due to its vibration is infinitesimally small. Also, the nonlinearity comes purely from the intermittent contact at the contact surfaces, and it is localized. Other nonlinearities, such as large deformations or material nonlinearities are not considered.
- (2) Contact surfaces Γ_A and Γ_B are invariant in time, and meshed as needed to ensure enough accuracy. Hence, the computational mesh is very fine and the computational cost for solving the vibration problem involving the intermittent contact is prohibitively expensive. Therefore, the computational nodes have to be sampled, such that the resulting model has enough accuracy, yet the computational cost of using this model is as low as possible.

9.2.1 Primary Model Reduction

To reduce the number of DOF included in I and make the subsequent development more efficient, a model reduction is first applied to Eq. (97). Namely, I is divided into two sets, i.e., $I = O \cup D$, where O is a set of DOF indices associated with the nodes to be directly used in the structural analysis, and D is the rest of DOF indices in I , which is to be apparently deleted from the system by the reduction methods. In addition, a set of DOF indices to be used as the *master* DOF is defined as active DOF, designated as A , and $A = B \cup O$.

Next, consider an eigenvalue problem associated with Eq. (97), where the eigenvalue λ and the corresponding eigenvector ϕ must satisfy

$$\begin{pmatrix} \mathbf{K}_{aa} & \mathbf{K}_{ad} \\ \mathbf{K}_{da} & \mathbf{K}_{dd} \end{pmatrix} \begin{bmatrix} \phi_a \\ \phi_d \end{bmatrix} = \lambda \begin{pmatrix} \mathbf{M}_{aa} & \mathbf{M}_{ad} \\ \mathbf{M}_{da} & \mathbf{M}_{dd} \end{pmatrix} \begin{bmatrix} \phi_a \\ \phi_d \end{bmatrix}, \quad (98)$$

where $\phi = [\phi_a^T, \phi_d^T]^T$. In this study, a mixed-boundary CMS of Hintz-Herting^{98,99} is chosen for the primary model reduction. Namely, without the presence of rigid body modes, the coordinate transformation is defined as

$$\begin{bmatrix} \mathbf{x}_a \\ \mathbf{x}_d \end{bmatrix} = \mathbf{H}\boldsymbol{\eta} = \begin{pmatrix} \boldsymbol{\Psi} & \hat{\boldsymbol{\Phi}} \end{pmatrix} \begin{bmatrix} \boldsymbol{\eta}_a \\ \boldsymbol{\eta}_m \end{bmatrix}, \quad (99)$$

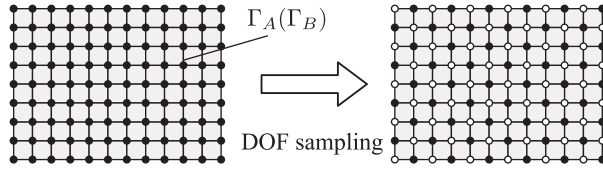


Fig. 49. Schematic of the node sampling: ●, selected node (N)

where $\mathbf{x}_a = \boldsymbol{\eta}_a$, $\boldsymbol{\eta}_m$ is a vector of modal coordinates, $\boldsymbol{\Psi}$ and $\hat{\boldsymbol{\Phi}}$ are so-called constraint modes and truncated free-interface normal modes in a modified form, which are respectively defined as

$$\boldsymbol{\Psi} = \begin{pmatrix} \mathbf{I} \\ -\mathbf{K}_{dd}^{-1}\mathbf{K}_{da} \end{pmatrix}, \quad (100)$$

$$\hat{\boldsymbol{\Phi}} = \begin{pmatrix} \mathbf{0} \\ \boldsymbol{\Phi}_d + \mathbf{K}_{dd}^{-1}\mathbf{K}_{da}\boldsymbol{\Phi}_a \end{pmatrix}, \quad (101)$$

and $\boldsymbol{\Phi} = [\boldsymbol{\phi}_{(1)}, \boldsymbol{\phi}_{(2)}, \dots, \boldsymbol{\phi}_{(k)}]$, $k < n$, each subscript in parentheses denoting the corresponding mode number. Using the transformation defined in Eq. (99), the projected eigenvalue problem is obtained as

$$\mathbf{K}_H \boldsymbol{\eta} = \mu \mathbf{M}_H \boldsymbol{\eta}, \quad (102)$$

where $\mathbf{M}_H = \mathbf{H}^T \mathbf{M} \mathbf{H}$ and $\mathbf{K}_H = \mathbf{H}^T \mathbf{K} \mathbf{H}$. It should be noted that the projected eigenvalue problem Eq. (102) possesses at least the same eigenvalues of the original systems, i.e., $\lambda_{(1)}, \lambda_{(2)}, \dots, \lambda_{(n_m)}$ although the indices may be different from the ones for the projected system. This is because the subspace spanned by the columns of $(\boldsymbol{\Psi}, \hat{\boldsymbol{\Phi}})$ contains the eigenvectors of Eq. (98), i.e., $\boldsymbol{\phi}_{(j)} \in \text{span}(\boldsymbol{\Psi}, \hat{\boldsymbol{\Phi}})$ for $j = 1, \dots, n_m$, as $\text{span}(\boldsymbol{\Psi}, \hat{\boldsymbol{\Phi}}) = \text{span}(\boldsymbol{\Psi}, \boldsymbol{\Phi})$. Hence, the projected eigenvalue problem has the same eigenvalues as the original ones. It means that, the eigenvalues of the projected system Eq. (102) does *not* contain any error in the eigenvalues and eigenvectors computed to those of the original eigenvalue problem of the FE model. Although this advantage comes with the expense of calculating the eigenvalues and eigenvectors of the full FE model, it is not a major drawback considering that the computational cost involved in the nonlinear computations with the original FE would be much more expensive than calculating a few normal modes of the full FE model.

9.2.2 Nonlinear DOF sampling

With the reduced order model obtained as discussed in section 9.2.1, the next step is to select the DOF in B such that the nonlinear characteristics of the system can be well approximated by applying the nonlinear boundary conditions *only* at the selected DOF.

As mentioned, accurately calculating the NNM frequencies is of primary interest of this study. The NNM frequencies of the system can be obtained in several ways, such as by time integration of Eq. (97) for harmonic loading, or by using harmonic-balance-based frequency/time domain analysis.^{149,153} It was shown by the authors that the NNM frequencies for cracked plates obtained by the nonlinear harmonic response analysis can be well approx-

imated by the application of bilinear frequency approximation even when the crack surfaces involve multiple DOF.¹⁵⁴ Therefore, as a measure to evaluate the results obtained with the selected DOF, bilinear frequency is used in the following development. Namely, the i th NNM frequency ω_{ni} can be approximated by a bilinear frequency ω_{bi} defined as

$$\omega_{bi} = \frac{2\omega_o\omega_s}{\omega_o + \omega_s} \quad (103)$$

where ω_o and ω_s are the natural frequencies of the corresponding linear systems, which can be respectively obtained by solving the following eigenvalue problems

$$\mathbf{K}_H\boldsymbol{\eta} = (\omega_o^2)\mathbf{M}_H\boldsymbol{\eta}, \quad \text{subject to } \textit{open} \text{ B.C.'s,} \quad (104)$$

$$\mathbf{K}_H\boldsymbol{\eta} = (\omega_s^2)\mathbf{M}_H\boldsymbol{\eta}, \quad \text{subject to } \textit{sliding} \text{ B.C.'s.} \quad (105)$$

The open B.C. is a boundary condition where no constraint is imposed on the nodes on Γ_A and Γ_B , or the DOF in B . Thus, in fact Eq. (104) is identical to Eq. (102). On the other hand for the sliding B.C., it is assumed that Γ_A can freely slide with respect to Γ_B but cannot separate along the local normal direction described as follows.

A contact pair is defined as a pair of nodes on Γ_A and Γ_B , which may be in contact during the vibration. A set of numbers denoting all the contact pairs is defined as C_{cp} . For the j th contact pair in C_{cp} , three mutually perpendicular normal vectors at a node on Γ_A are defined as \mathbf{n}_1^j , \mathbf{n}_2^j , and \mathbf{n}_3^j , where \mathbf{n}_1^j is the normal vector pointing outward from the surface, \mathbf{n}_2^j and \mathbf{n}_3^j are unit vectors that are tangent to the surface and perpendicular to each other. Using these vectors, a coordinate transformation matrix $\mathbf{P}_A^j = (\mathbf{n}_1^j, \mathbf{n}_2^j, \mathbf{n}_3^j)$ is defined for each contact pair with the assumption that a nodal displacement vector contains only translational DOF, such that the x_1 component of the displacement vector of the node is aligned with \mathbf{n}_1^i and points outward from the surface. For the other node of the j th contact pair on Γ_B , the corresponding coordinate transformation matrix that aligns the x_1 component of the nodal displacement vector with the normal vector is defined as $\mathbf{P}_B^j = -\mathbf{P}_A^j$. Assembling \mathbf{P}_A^j and \mathbf{P}_B^j for all $j \in C_{cp}$, a coordinate transformation is defined as

$$\mathbf{P} = \begin{pmatrix} \mathbf{P}_b & \mathbf{0} & \mathbf{0} \\ \mathbf{0} & \mathbf{I}_o & \mathbf{0} \\ \mathbf{0} & \mathbf{0} & \mathbf{I}_m \end{pmatrix}, \quad \text{where } \mathbf{P}_b = \underset{j=1}{\overset{n_{C_{cp}}}{\mathbf{A}}} (\mathbf{P}_A^j, \mathbf{P}_B^j), \quad (106)$$

and \mathbf{A} is an assembly operator, $\mathbf{P}_b \in \mathbb{R}^{n_B \times n_B}$, $\mathbf{I}_o \in \mathbb{R}^{n_o \times n_o}$, and $\mathbf{I}_m \in \mathbb{R}^{n_M \times n_M}$. Next, for the j th contact pair, the x_1 components of the nodal displacement vectors, which are denoted as η_A^j and η_B^j , are transformed to a relative displacement $u^j \triangleq (\eta_A^j + \eta_B^j)/\sqrt{2}$ and a displacement $v^j \triangleq (\eta_A^j - \eta_B^j)/\sqrt{2}$. Namely, denoting the set of DOF corresponding to u_A^j and u_B^j for all j th contact pair, one obtains

$$\begin{bmatrix} u^j \\ v^j \end{bmatrix} = \frac{1}{\sqrt{2}} \begin{pmatrix} 1 & 1 \\ 1 & -1 \end{pmatrix} \begin{bmatrix} \eta_A^j \\ \eta_B^j \end{bmatrix}. \quad (107)$$

Now by defining X , Y , and Z ($X \cup Y \cup Z = B$ and $n_X = n_Y = n_Z = n_{C_{cp}}$), the sets that respectively contain sets of indices of the DOF corresponding to x_1 , x_2 , and x_3 for all $j \in C_{cp}$, and denoting the coefficient matrix in the Eq. (107) as \mathbf{R}^j , one can define a transformation

matrix \mathbf{R} by assembling \mathbf{R}^j for $j \in C_{cp}$ as follows

$$\mathbf{R} = \begin{pmatrix} \mathbf{R}_x & \mathbf{0} \\ \mathbf{0} & \mathbf{I} \end{pmatrix}, \quad \text{where} \quad \mathbf{R}_x = \overset{n_{C_{cp}}}{\underset{j=1}{\mathbf{A}}} (\mathbf{R}^j), \quad (108)$$

and $\mathbf{R}_x \in \mathbb{R}^{n_x \times n_x}$. Since $\mathbf{P}^{-1} = \mathbf{P}^T$ and $\mathbf{R}^{-1} = \mathbf{R}^T$, the eigenvalue problem Eq. (102) can be transformed to

$$K\mathbf{q} = (\omega_o^2)M\mathbf{q}, \quad (109)$$

where $\boldsymbol{\eta} = \mathbf{P}\mathbf{R}\mathbf{q}$, $M = (\mathbf{P}\mathbf{R})^T \mathbf{M}_H \mathbf{P}\mathbf{R}$, and $K = (\mathbf{P}\mathbf{R})^T \mathbf{K}_H \mathbf{P}\mathbf{R}$. Next, note that \mathbf{q} can be partitioned into $\mathbf{q} = [\mathbf{q}_r, \mathbf{q}_g]$ where \mathbf{q}_r is the vector of relative DOF, or $u^j (\forall j \in C_{cp})$ and \mathbf{q}_g is the generalized internal DOF containing $v^j (\forall j \in C_{cp})$, the x_2 and x_3 components of the nodal displacement vectors of the nodes of the contact pairs, displacement vectors of the observer nodes, and the modal coordinates. That is, Eq. (109) can be written as

$$\begin{pmatrix} K_{rr} & K_{rg} \\ K_{gr} & K_{gg} \end{pmatrix} \begin{bmatrix} \mathbf{q}_r \\ \mathbf{q}_g \end{bmatrix} = (\omega_o^2) \begin{pmatrix} M_{rr} & M_{rg} \\ M_{gr} & M_{gg} \end{pmatrix} \begin{bmatrix} \mathbf{q}_r \\ \mathbf{q}_g \end{bmatrix}, \quad (110)$$

where $R \subset X$ and $G = (A \setminus R) \cup M$.

The best approximation to the NNM frequency can be obtained when the sliding boundary conditions are imposed on all of the nodes on the surfaces Γ_A and Γ_B . Namely, the associated eigenvalue problem with the sliding boundary conditions can be obtained by constraining *all* the relative DOF, or $\mathbf{q}_r = \mathbf{0}$, i.e.,

$$K_{gg}\mathbf{q}_g = (\omega_s^2)M_{gg}\mathbf{q}_g. \quad (111)$$

Next, we assume that we do *not* like to consider all nodes in R for the subsequent forced response analysis due to the large number of DOF involved in R . In other words, the nodes where the nonlinear boundary conditions are applied should be sampled, as illustrated in Fig. 49. The selected DOF are designated as nonlinear DOF, and a set of indices of the nonlinear DOF is denoted by N , where $N \subset R$. The rest of the DOF in R are designated as linear DOF, and the associated set is denoted by L , where $N \cup L = R$. Therefore, the bilinear frequency is calculated with ω_s such that the sliding B.C. is applied only on the DOF in N , or $\mathbf{q}_n = \mathbf{0}$, i.e.,

$$\begin{pmatrix} K_{ll} & K_{lg} \\ K_{gl} & K_{gg} \end{pmatrix} \begin{bmatrix} \mathbf{q}_l \\ \mathbf{q}_g \end{bmatrix} = (\omega_s^2) \begin{pmatrix} M_{ll} & M_{lg} \\ M_{gl} & M_{gg} \end{pmatrix} \begin{bmatrix} \mathbf{q}_l \\ \mathbf{q}_g \end{bmatrix}. \quad (112)$$

Considering that the natural frequencies of the system with the open boundary conditions, ω_o , are independent of both the number and the pattern of the selected DOF (recalling that $\text{span}(\boldsymbol{\Psi}_c, \hat{\boldsymbol{\Phi}})$ contains the chosen eigenvectors), one can see from Eq. (103) that ω_{bi} is dependent only on ω_s for a fixed ω_o .

Next, considering the Rayleigh's theorem of constraints defined by Eq. (96), it is known that the system's eigenvalues increase if a constraint is imposed on a system. Therefore, as the number of constraints on Eq. (102) increases, ω_s increases. Furthermore, ω_{bi} is a monotonically increasing function of ω_s for a fixed ω_o , because $\partial\omega_{bi}/\partial\omega_s = 2\omega_o^2/(\omega_o + \omega_s)^2 \geq 0$. Hence one can conclude that the best approximation of ω_{bi} for a given n_N is obtained when

the maximum ω_s is achieved. Thus, a corresponding maximization problem is stated as follows

$$\begin{aligned} & \max_{N \subset R} \omega_s(N), \\ & \text{subject to } |N| = n_N. \end{aligned} \quad (113)$$

This maximization problem may be solved by mathematical programming methods, such as integer programming or topology optimization methods as was done in Ref..¹⁴¹ As it shall be discussed next, this maximization problem can in fact be treated in a more efficient way by the use of Guyan reduction and methods to choose the *master DOF* for reduced order modeling techniques.

9.2.3 Automatic master DOF selection

The methods for automatically selecting the master DOF for Guyan reduction have been previously developed.^{123,124,130} In particular, the method proposed by Henshell and Ong¹²³ appears to be the most successful approach. Although it has been known to be computationally expensive due to the nature of eliminating a single DOF per iteration and the need for successive applications of Guyan reduction, this can be alleviated by the use of the primary model reduction by CMS as developed in section 9.2.1. As was mentioned by Bouhaddi and Fillod,¹³⁰ and Shah and Raymund,¹²⁴ the master DOF of Guyan reduction should be chosen such that the valid eigenvalue range of the reduced order model is maximized. In general, it has been known that the eigenvalue range of validity is bounded by the lowest eigenvalue of the system with all the master DOF fixed. Here, this concept is applied to the problem of finding the optimal N that solves Eq. (113). Namely, the corresponding eigenvalue problem is Eq. (112) where \mathbf{q}_n is regarded as the master DOF. As was discussed in Ref.,¹⁵⁰ the error bounds in the i th eigenvalue of the reduced model produced by the Guyan reduction can be obtained a priori by the following relationship

$$0 \leq \varepsilon_i \leq \frac{\lambda_i}{\lambda_{s,min} - \lambda_i}, \quad (114)$$

where $\varepsilon_i \triangleq (\bar{\lambda}_i - \lambda_i)/\lambda_i$ is the relative error in the i th eigenvalue, $\bar{\lambda}_i$ is the i th eigenvalue of the reduced order model, λ_i is the i th eigenvalue of the original finite element model, and $\lambda_{s,min}$ is the smallest eigenvalue of the system with *all the master DOF fixed*. For $\lambda_i/\lambda_{s,min} \ll 1$, the upper bound asymptotically converges to the following value¹⁵¹

$$0 \leq \varepsilon_i \leq \lambda_i/\lambda_{s,min}. \quad (115)$$

Therefore, it is apparent that maximizing $\lambda_{s,min}$ results in minimizing the upper bound of the error for all the eigenvalues of the reduced order model. Hence, this provides a guideline for selecting the master DOF for Guyan reduction such that the errors in the eigenvalues of the resulting reduced order model are minimized.

By observing this fact from another point of view, one may note that if a certain set of master DOF can achieve the maximum $\lambda_{s,min}$, one can obtain not only an accurate reduced order model that can well approximate the first few lowest eigenvalues of the original system, but also (as a byproduct) a good estimate on the *optimal constraint locations that maximize the fundamental frequency*. Recasting this to the original problem of selecting the optimal set N ,

[1] $i = 1$ to $i = n_R - n_N$ Calculate $\sqrt{k_{jj}/m_{jj}}$ for $j \in R$ Find q_1 such that $\sqrt{k_{q_1 q_1}/m_{q_1 q_1}} = \max_{j \in R} \sqrt{k_{jj}/m_{jj}}$
 $L \leftarrow \{q_1, \dots, q_{n_k}\}$ where q 's are the DOF associated with the k th contact pair ($k \in C_{cp}$) and n_k is the number of DOF in the k th contact pair $N \leftarrow R \setminus L$ $R \leftarrow N$ Calculate constraint modes using Eq. (117) Apply Guyan reduction to the system matrices: $M \leftarrow \Psi^T M \Psi$, $K \leftarrow \Psi^T K \Psi$

Algorithm 3. DOF selection based on Henshell and Ong method

the error bounds given in Eq. (115) and associated with the eigenvalue problem Eq. (112) are written as

$$0 \leq \varepsilon_i \leq \frac{(\omega_o^2)_i}{(\omega_s^2)_1 - (\omega_o^2)_i}, \quad (116)$$

where $\varepsilon_i \triangleq [(\bar{\omega}_o^2)_i - (\omega_o^2)_i]/(\omega_o^2)_i$, $(\bar{\omega}_o^2)_i$ is the i th eigenvalue of a reduced order model, $(\omega_s)_1$ is the lowest natural frequency of Eq. (112). The corresponding maximization problem is given by Eq. (113). Solving this problem for the lowest eigenvalue $(\omega_s)_1$, one can expect that the chosen nodes pattern is at least quasi-optimal.

According to Refs.,^{151,152} the sequential elimination method by Henshell and Ong¹²³ tends to keep $\lambda_{s,min}$ high, as it eliminates the DOF associated with the highest constrained frequency at each iteration as the slave DOF. Namely, after the elimination procedure, if the chosen master DOF are all fixed, the system is left with the (slave) DOF that were identified to have the highest constrained frequency at each elimination process. Thus, the resulting system with all the master DOF fixed tends to have a larger $\lambda_{s,min}$ than that calculated with systems with other possible combinations of master DOF fixed.

The Henshell and Ong's method that is adapted specifically for this problem is shown in Algorithm 3. First, at each iteration, the ratios of the diagonal terms of the stiffness matrix k_{jj} to the diagonal terms of the mass matrix m_{jj} are calculated for $\forall j \in R$. Next, the index q_1 that gives the maximum ratio among $j \in R$ is obtained. Next, the set L is updated such that it contains q_1 and all the other DOF that are associated with the contact pair $k \in C_{cp}$ to which the q_1 th DOF belongs (e.g., the DOF that are perpendicular to the normal direction). The set N is then updated such that it excludes the selected DOF of L from R , and the set R is re-defined as N . A constraint mode is calculated by solving a problem where a unit displacement is applied to a DOF in N whereas all the other DOF in N being fixed. This is repeated for all DOF in N , resulting in the following matrix

$$\Psi = \begin{pmatrix} \mathbf{I} \\ -(K_{ll})^{-1} K_{ln} \end{pmatrix}, \quad (117)$$

where Ψ is the matrix of constraint modes for all DOF in N . Guyan reduction is then applied to the mass and stiffness matrices. The iteration continues until the number of DOF in N reaches the desired value for n_N .

To demonstrate the performance of the proposed algorithm, another algorithm for selecting DOF is shown here for comparison. The method of effective independence vector, or the EIDV method developed by Kammer,¹⁴⁰ is a method to choose the sensor placement locations for the vibration measurement of large scale structures. The method aims to make the measured, or sampled/truncated eigenvectors as linearly independent as possible. According to Penny

[1] Calculate Φ_k $i = 1$ to $i = n_R - n_N$ $\mathbf{A} \leftarrow \Phi_k^T \Phi_k$ $\mathbf{E} \leftarrow \Phi_k \mathbf{A}^{-1} \Phi_k^T$ Find q_1 such that $e_{q_1 q_1} = \min_{j \in R} e_{jj}$
 $L \leftarrow \{q_1, \dots, q_{n_k}\}$ where q 's are the DOF associated with the k th contact pair ($k \in C_{cp}$) and n_k is the number of DOF in k th contact pair $N \leftarrow R \setminus L$ $R \leftarrow N$ Delete rows of Φ_k corresponding to the DOF in L

Algorithm 4. DOF selection based on EIDV method

et al.,¹³⁹ many of the criteria for choosing the master DOF for model order reduction are similar to choosing measurement locations in a way such that the *lower frequency modes can be captured accurately*. In fact, as examined by Penny *et al.*, both the Henshell and Ong method and the EIDV method produce acceptable selections in most cases (in a quasi-optimal manner). The DOF selection algorithm based on the EIDV method is shown as Algorithm 4. First, the eigenvalue problem in Eq. (111) is solved for the first k modes, and the associated modal matrix is denoted by $\Phi_k = (\phi_1, \phi_2, \dots, \phi_k)$. That is $K\Phi_k = M\Phi_k\Lambda_k$, where Λ_k is a diagonal matrix with diagonal entries being the square of the natural frequencies of the open B.C. linear system. The Fisher information matrix \mathbf{A} is then calculated as $\mathbf{A} = \Phi_k^T \Phi_k$, and an idempotent matrix \mathbf{E} is computed as $\mathbf{E} = \Phi_k \mathbf{A}^{-1} \Phi_k^T$. The diagonal of \mathbf{E} is called the independence distribution vector (see Ref.¹⁴⁰ for detailed formulations). The least contributing DOF to the independence of the modes among the ones in R is identified as the one with the smallest diagonal element in \mathbf{E} . The associated DOF are also identified and stored in L , and both N and R are updated as in the Henshell and Ong method. Finally, the rows of Ψ_k corresponding to the DOF in L are deleted. The iteration continues until the size of N reaches the desired n_N .

Although the EIDV method has a similar objective for choosing DOF as the Henshell and Ong method, the objective of the EIDV method is not exactly the maximization problem of Eq. (113). Therefore, it is expected that the Henshell and Ong method returns better solutions to the given maximization problem than the EIDV method, as it is shown in the next section.

9.3 Case studies

In section 9.2, the method to select the nonlinear DOF has been introduced. In this section, the performance and accuracy of the method are demonstrated by applying the algorithm to two example problems. In the first case study, the accuracy of the proposed method is discussed in terms of the bilinear frequencies and forced response. Furthermore, a metric to assess accuracy is introduced and examined. The second case study is provided to demonstrate the performance of the proposed method when applied to a system with a more realistic and complex FE model featuring a large number of DOF on the faces involving intermittent contact.

9.3.1 Simple cracked plate model

Problem description A cantilevered cracked plate model was constructed with Young's modulus $E = 2.0 \times 10^{11}$ Pa, Poisson's ratio $\nu = 0.3$, and density $\rho = 7800$ kg/m³, and geometry

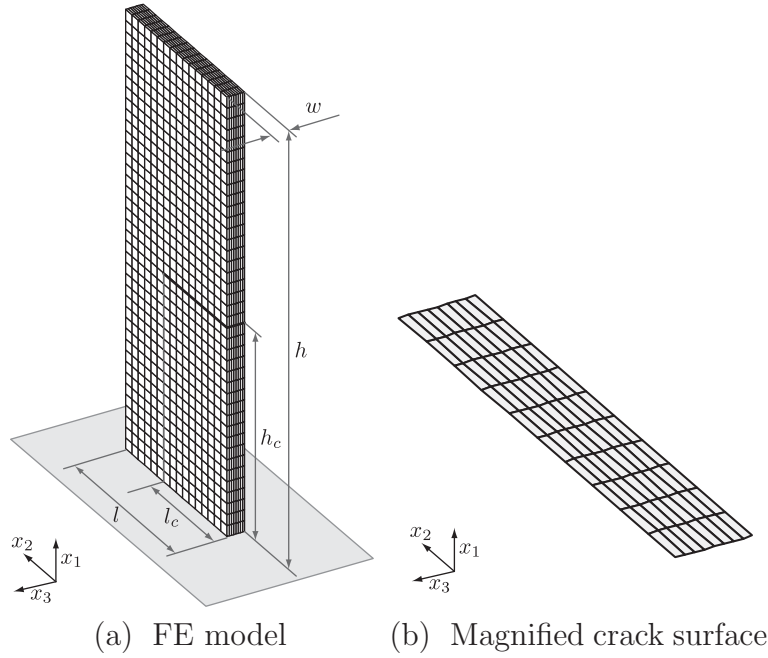


Fig. 50. Cantilevered cracked plate model

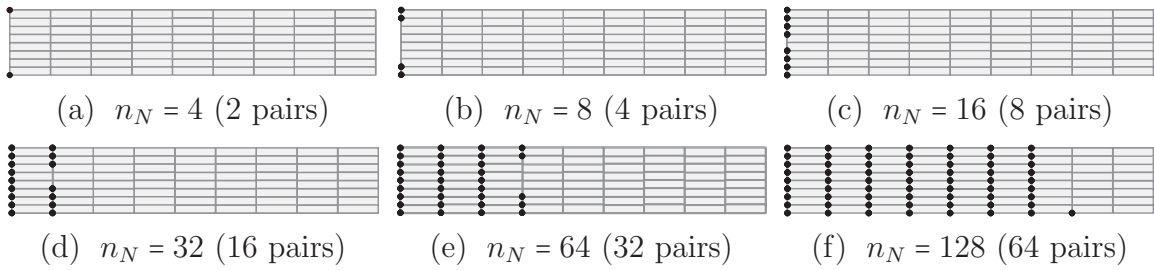


Fig. 51. Selected nodes by penetrating surface criterion (left edge open)

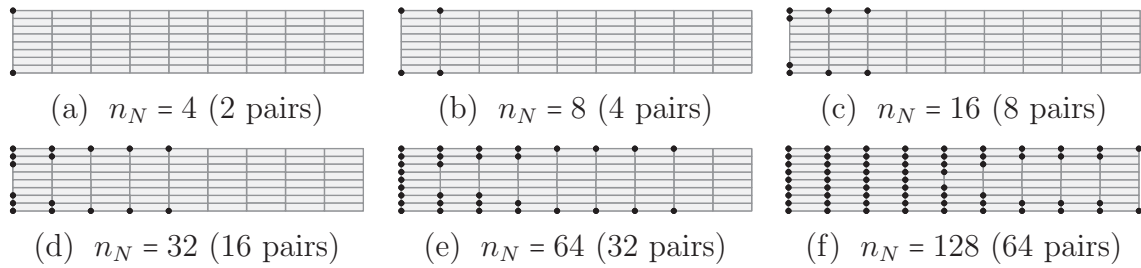


Fig. 52. Selected nodes by EIDV method (left edge open)

shown in Fig. 50(a), where $w = 6.0 \times 10^{-3}\text{m}$, $l = 6.0 \times 10^{-2}\text{m}$, $h = 1.5 \times 10^{-1}\text{m}$, $l_c/l = 0.625$, and $h_c/h = 0.475$. The model was discretized with 5,120 linear solid elements and resulted in mass and stiffness matrices with 18,630 DOF. On the crack surfaces shown in Fig. 50(b), there are 180 nodes, or 90 contact pairs on the surfaces. Hence, the number of associated DOF is 540. The CMS method shown in the section 9.2.1 was then applied to the FE model, and it resulted in a 681 DOF system (3.6% of the original size) consisting of 621 physical DOF and 60 modal coordinates corresponding to the free-interface normal modes. With this reduced order model, both algorithms in Algorithms 3 and 4 were applied for $n_N = 4, 8, 16, 32, 64$, and 128. For the EIDV algorithm, the first four modes were considered to construct the modal matrix.

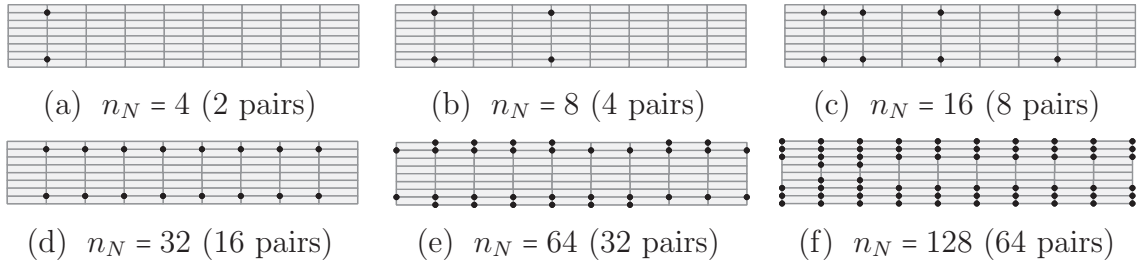


Fig. 53. Selected nodes by the Henshell and Ong method (left edge open)

Table 4

Average CPU times for generating node patterns over 100 trials, and typical CPU times to compute forced response for 256 steps within 200 to 215 Hz.

$3*n_N$	Penetrating surface criterion		EIDV		Henshell and Ong	
	Node selection [s]	Forced response [s]	Node selection [s]	Forced response [s]	Node selection [s]	Forced response [s]
2	6.15×10^{-1}	1.27	2.23	1.18	3.69	1.21
4	6.21×10^{-1}	5.64	2.26	3.99	3.68	3.23
8	6.18×10^{-1}	1.85×10^1	2.19	2.87×10^1	3.69	2.07×10^1
16	6.07×10^{-1}	5.00×10^1	2.20	1.07×10^2	3.65	9.35×10^1
32	6.09×10^{-1}	1.48×10^3	2.12	1.37×10^3	3.52	8.17×10^2
64	6.26×10^{-1}	1.08×10^4	1.93	9.86×10^3	2.66	1.03×10^4
90	N/A	2.62×10^4	N/A	2.62×10^4	N/A	2.62×10^4

In order to compare these results with an intuitive selection method, a selection criterion was also employed, where the nonlinear DOF were chosen based on the amount of *penetration* between the nodes in a contact pair for the modes of interest (the fourth mode), which is referred to as penetrating surface criterion. Namely, the penetrating surface criterion is based on the observation that penalizing the inter-penetration of the most penetrating contact pairs may produce the stiffest system response. The selected node pattern with such criterion is shown in Fig. 51, and the results of the EIDV method and the Henshell and Ong method are shown in Figs. 52 and 53. As can be seen in Fig. 51, if the nodes are chosen based on the penetrating surface criterion, the selection starts from the nodes near the crack edge (open side) for $n_N = 4$, and it then proceeds toward the tip of the crack (closed side) as n_N increases. This result is expected because the motion of the crack surfaces is more significant near the open edge than near the closed edge. In contrast, the EIDV method starts to select nodes near the crack edge, but it tends to choose more nodes on the crack rims than nodes near the crack edge, as shown in Fig. 52. Finally, the Henshell and Ong method selects the nodes near the crack edge first, for $n_N = 4$, but it then tends to select nodes over the crack surface in a more distributed manner, as can be seen in Fig. 53.

Forced Response Analysis Next, to evaluate the influence of the application of the nonlinear B.C. onto the selected nodes on an NNM frequency, forced response analysis was carried out by applying an external harmonic loading to the cracked plate. As one may note, the repetitive opening and closing of the crack faces must be treated appropriately with contact

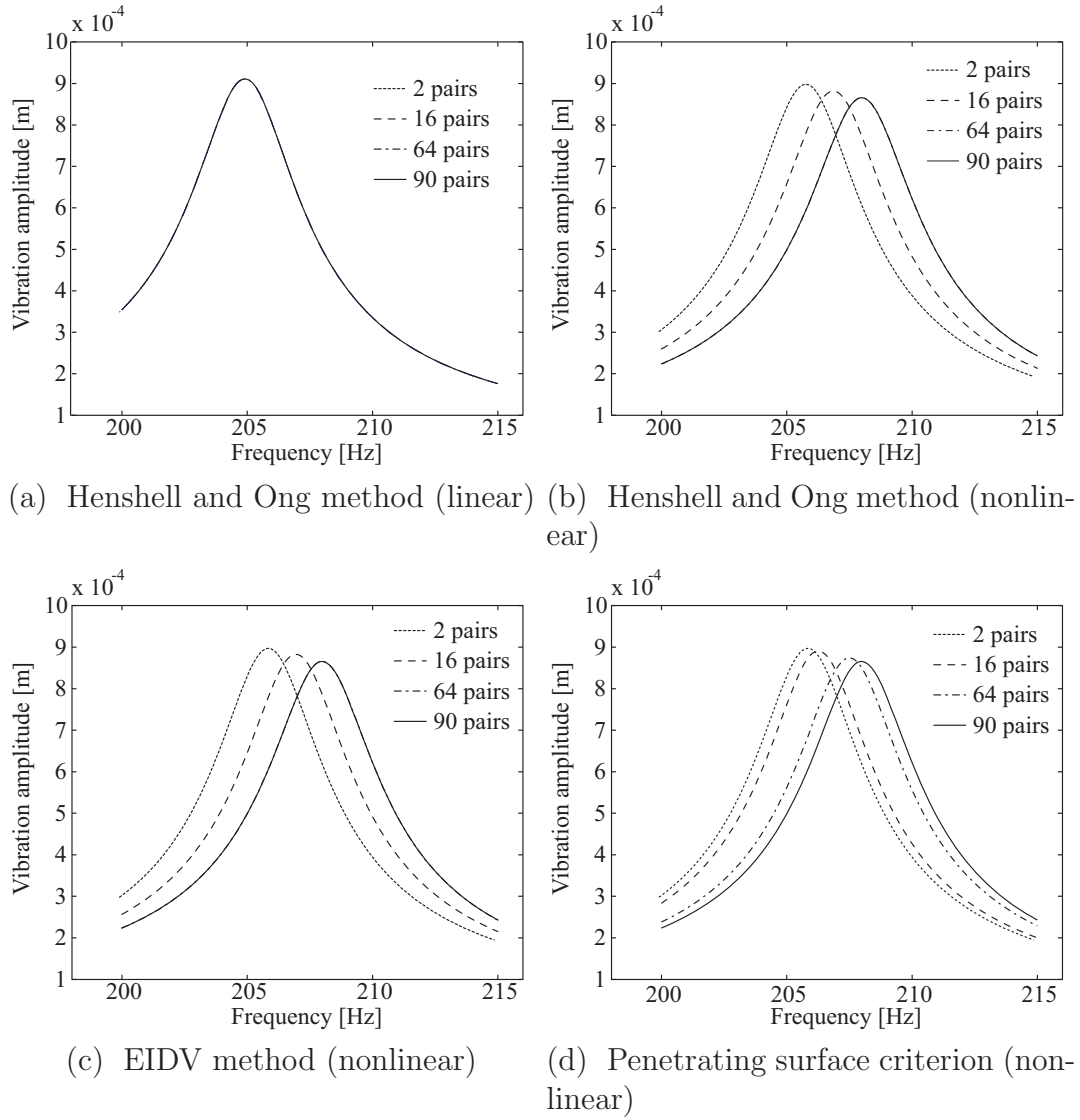


Fig. 54. Results of forced response analysis of the cracked plate

algorithms when the forced response of this cracked structure is considered. As a result, the vibration is nonlinear and the steady-state response may not be expressed as a harmonic function even if the external force is a harmonic function. Therefore, in this study the steady-state response was obtained by assuming that the displacement can be expressed as a truncated Fourier series, and the nonlinear boundary condition can be enforced by a penalty method.¹¹⁶ The solution method is also known as the hybrid frequency-time domain method,^{149,153} which is based on the concept of harmonic balance method.¹⁰⁷ The detailed formulation of the method is omitted in this paper for the sake of brevity.

It is noted that the system matrices were further reduced by the application of Eq. (99) to the reduced-order model before the forced response calculation was performed. That was done by keeping the selected node pairs as active DOF and condensing out the other DOF including physical and modal coordinates. For example, with $n_N = 64$ (32 pairs), the system size was reduced down to 155 DOF, which is 0.83% of the original system size.

A harmonic forcing of magnitude 3 N was then applied at the tip of the plate to excite the

first vibration mode, which is the first out-of-plane bending mode. The forced response was calculated for both the linear case (i.e., with open B.C.) and the nonlinear case (with the nonlinear boundary conditions imposed on N). The results are shown in Fig. 54. As can be seen in Fig 54(a), the selection pattern based on the Henshell and Ong method does not alter the *linear* forced response. This is because the selection of the active DOF does not alter the eigenvalues of the *linear* reduced order model. In contrast, the number of contact pairs greatly affects the results of nonlinear forced response as shown in Fig. 54(b). Also, one may observe that the response obtained with 64 contact pairs is almost identical to that obtained with the full set of 90 contact pairs. That implies that for accurately calculating the nonlinear resonant frequencies, it may not be necessary to enforce nonlinear boundary conditions for all the contact pairs on the crack faces. The same forced response calculations were carried out with the node patterns selected by the EIDV method and the penetrating surface criterion. The results obtained are shown in Figs. 54(c) and 54(d). As can be seen in Fig. 54(c), the results obtained with the patterns chosen by the EIDV method are comparable with the ones produced by the Henshell and Ong method. Also, as can be seen in Fig. 54(d), the forced response with the node patterns chosen by the penetrating surface criterion produced worse results than the other two methods, i.e., for a given number of n_N , the predicted resonant frequency by the approach is less accurate than that calculated by the other methods. This is the most visible in the results for $n_N = 64$, for which both the Henshell and Ong method and the EIDV method produced results that are almost identical to the results for the full model with $n_N = 90$.

Moreover, to evaluate the effects of n_N on the computational speed, the average CPU times for generating node patterns, as well as the ones required to obtain the steady-state forced response are shown in Table 4. The CPU time was measured on a computer with Intel Core 2 Duo 2.4GHz processor and 4.0GB of RAM. First, the CPU time for generating the node pattern with each algorithm was measured for 100 trials, and the average values are shown in Table 4. As can be seen, the node selection by Henshell and Ong method takes longer than the other two methods for all n_N , due mostly to the cost associated with the successive application of Guyan reduction. The other two methods are faster than the Henshell and Ong method. However, they sacrifice the accuracy in the resulting nonlinear forced response. Also note that the CPU time decreases as n_N increases for both EIDV and Henshell and Ong methods, because these methods eliminate the unnecessary DOF at each iteration, rather than choosing necessary DOF. Thus, the node pattern with larger n_N is generated with less CPU time. Second, the forced response was calculated at 256 points evenly-spaced in a frequency range from 200 Hz to 215 Hz for $n_N = 2, 4, 8, 16, 32,$ and 64 by the three methods considered, and for the case with $n_N = 90$, and the results are shown in Table 4. Although there is no significant CPU time difference among the selection algorithms, one can notice that the CPU time can be greatly reduced when the calculations are done with the sampled nodes, without sacrificing too much accuracy if the set of nodes were chosen by the proposed method. Also, note that the node selection has to be done only once for the entire frequency range of interest, and the cost is much smaller (e.g., only 0.03% for the Henshell and Ong method with $n_N = 64$) than that required for computing forced response with sufficiently large n_N . Bilinear Frequency Approximation Next, the influence of the selected node pattern on the bilinear frequencies is discussed. The first four bilinear frequencies were calculated for the model with the selected node patterns with the three node sampling methods, and the results are shown in Fig. 55 along with their linear vibration mode shapes. The first four

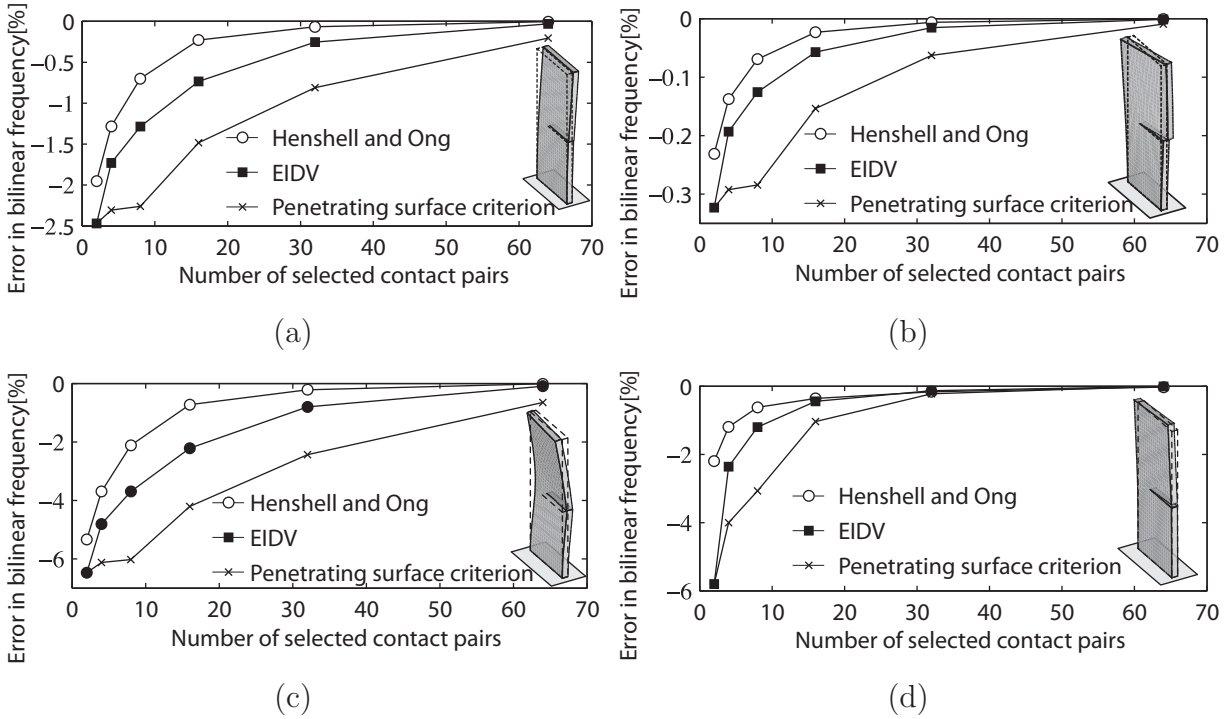


Fig. 55. Errors in the first four bilinear frequencies:(a) NNM 1, (b) NNM 2, (c) NNM 3, (d) NNM 4

modes correspond to the first out-of-plane bending, the first torsion, the second out-of-plane bending, and the first in-plane bending modes respectively. The plots in Fig. 55 show the percentage errors in the bilinear frequency versus the number of contact pairs, where the error is defined as the ratio of the difference between the bilinear frequency with the sampled contact pairs and the frequency obtained with the full set of contact pairs, to that with the full set of contact pairs. As can be seen in Fig. 55, the Henshell and Ong method consistently provides the best results among all the methods for the first four modes. Moreover, it shows the best convergence rate in terms of the number of contact pairs.

A posteriori accuracy assessment

Even though intuitive, the approach which chooses the contact pairs with the most penetration does not provide the best results because applying the nonlinear boundary conditions at these nodes does not result in the stiffest vibration response. In contrast, the Henshell and Ong method and the EIDV method produced node patterns that yield results closer to the reference results in terms of forced response and bilinear frequencies. In particular, the Henshell and Ong method iteratively aims to solve the maximization problem in Eq. (113) in a quasi-optimal manner. Therefore, the bilinear frequencies as well as the resonant frequencies were well approximated with the nodes chosen by the Henshell and Ong method.

To better understand the governing factor for the accuracy of the results, a more physical interpretation of the results is provided here. Namely, the key effect for achieving the good approximation of the NNM frequency is to ensure, as much as possible, the non-penetrability condition on the contact pairs where the nonlinear B.C.s' are *not* applied. Also, the penetration should be evaluated during a complete vibration cycle. Thus, both the depth and the duration of the penetration should be taken into account. These quantities vary in space, and

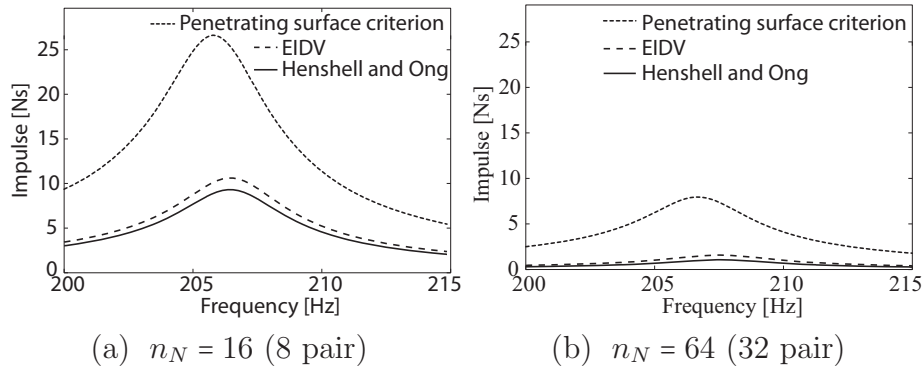


Fig. 56. Virtual impulse for a period of vibration for NNM 1

depend on the frequency of vibration. Hence as a metric to characterize not only the amount but also the duration of penetration over the entire crack surfaces for a given vibration frequency, the following quantity is introduced

$$\hat{F} = \int_0^T \left(\int_{\Gamma_A(\Gamma_B)} k_e u_p(\mathbf{r}, t) d\Gamma \right) dt, \quad (118)$$

where \hat{F} is a quantity with the dimension of impulse referred to as the virtual impulse, k_e is an equivalent spring constant per unit length determined by the ratio between the Young's modulus multiplied by the characteristic area and the characteristic length, u_p is the amount of penetration along the surface normals, and T is the period of vibration. The quantity \hat{F} is obtained based on the calculated time trajectory of displacements of the nodes on the crack surfaces, and can be thought of as an impulse that does *not* contribute to the system response. This impulse is not applied to the system when the response is calculated. In other words, the smaller the value of \hat{F} is, the stricter the boundary conditions are imposed on the nodes over the entire crack surfaces.

First, the forced response analysis was carried out, and the corresponding time history of u_p over the entire crack surface was recovered from the vibration response. The integrals in the Eq. (118) were then evaluated by a simple quadrature rule both in space and time. The metric was calculated for the first and the fourth modes for 8 and 32 pairs chosen by the node sampling methods, and the results are shown in Figs. 56 and 57. As can be seen in Figs. 56 and 57, the virtual impulse varies over the frequency range. In particular, when the frequency of excitation is close to the resonant frequency, the amount of penetration increases as well. However, for all cases, the Henshell and Ong method consistently results in the smallest impulse over the frequency range among the three methods considered. That means that the nonlinear B.C. on the crack faces is the most strictly enforced by the node patterns chosen by the Henshell and Ong method.

9.3.2 Large Scale Cracked Blade Model

In this subsection, the performance of the proposed method applied to a FE model of a cracked blade model with a large number of DOF is demonstrated. A blade model whose thickness is $2.5 \times 10^{-3} \text{m}$ and both chord and span lengths are approximately $5.0 \times 10^{-2} \text{m}$ was constructed, with the Young's modulus $E = 205 \text{GPa}$, density $\rho = 7832 \text{kg/m}^3$, and Poisson's ratio $\nu = 0.3$. The blade was discretized with linear and quadratic tetrahedral elements,

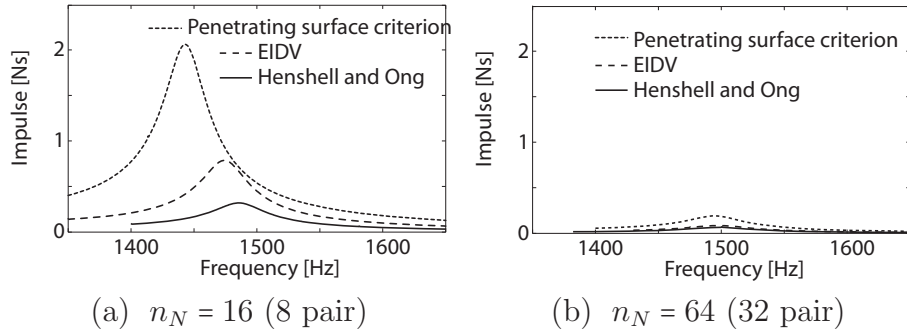


Fig. 57. Virtual impulse for a period of vibration for NNM 4

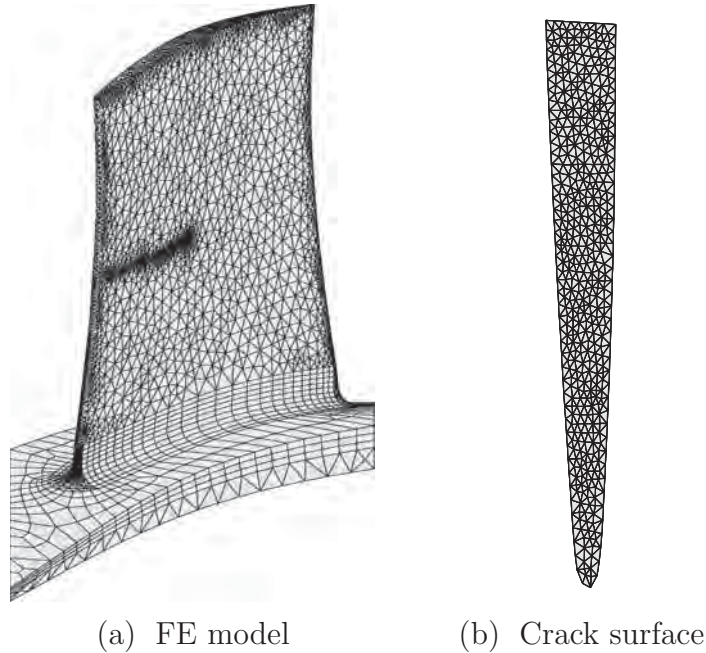


Fig. 58. A cracked blade model

resulting in a system with 392,361 DOF as shown in Fig. 58(a). The crack path as well as its surrounding FE mesh was generated by a fracture analysis code FRANC3D.¹⁵⁵ The crack surfaces consist of quadratic elements with 487 contact pairs at the edges of vertices of triangles, resulting in 2,922 DOF for both surfaces, as shown in Fig. 58(b). The size of the FE model was then reduced down to 2,949 DOF (0.75% of the original size) by the primary CMS method, which consists of 2,934 physical DOF (2,922 DOF on crack faces and 12 additional DOF for forcing) and 15 modal coordinates corresponding to the free-interface normal modes. The proposed method was then applied to the reduced order model, and the results are shown in Figs. 59 and 60. For the EIDV method, the first 15 modes were used for the calculations. As can be seen in Fig. 59, the EIDV method selects nodes along the rim of the crack faces, similar to the previous case study. In contrast, the Henshell and Ong method tends to choose the nodes slightly off the crack rim in a more distributed manner over the crack face, as in the previous example. With the selected node patterns, the first four bilinear frequencies were calculated. The first four modes correspond to the first out-of-plane bending, the first torsion, the second out-of-plane bending, and the first chord-wise bending mode respectively. The errors were then calculated as in the previous example and shown in Fig. 61 along with their linear vibration mode shapes. As can be seen in Fig. 61,

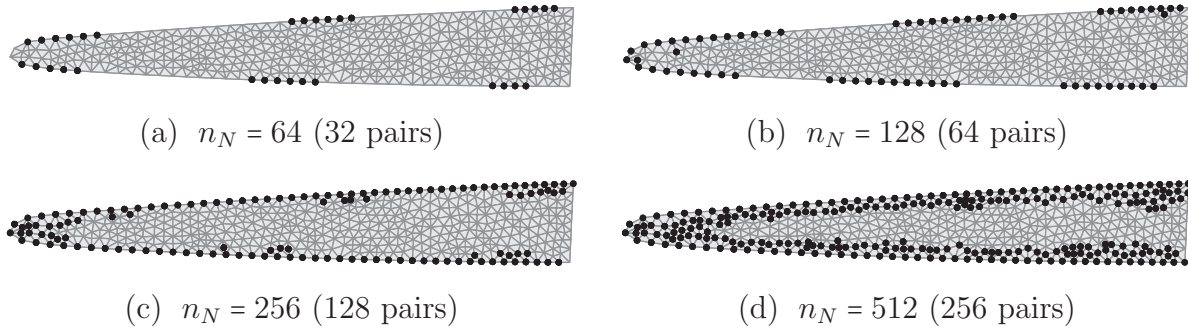


Fig. 59. Selected nodes by EIDV method for $n_B = 974$ (487pairs)

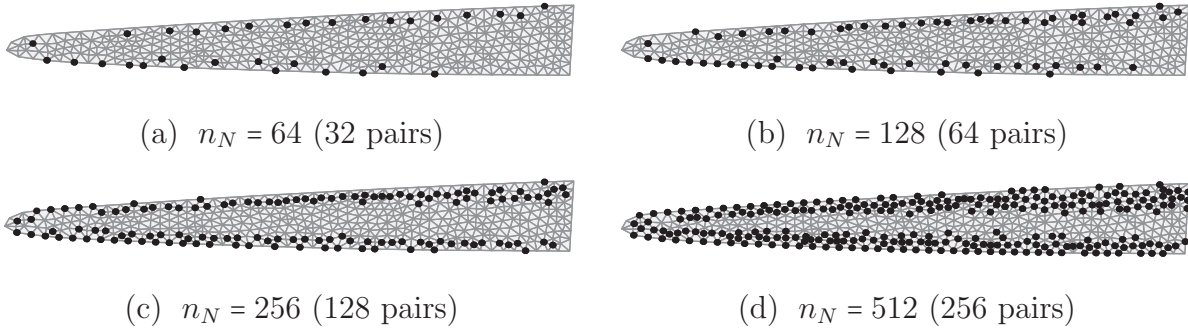


Fig. 60. Selected nodes by the Henshell and Ong method for $n_B = 974$ (487pairs)

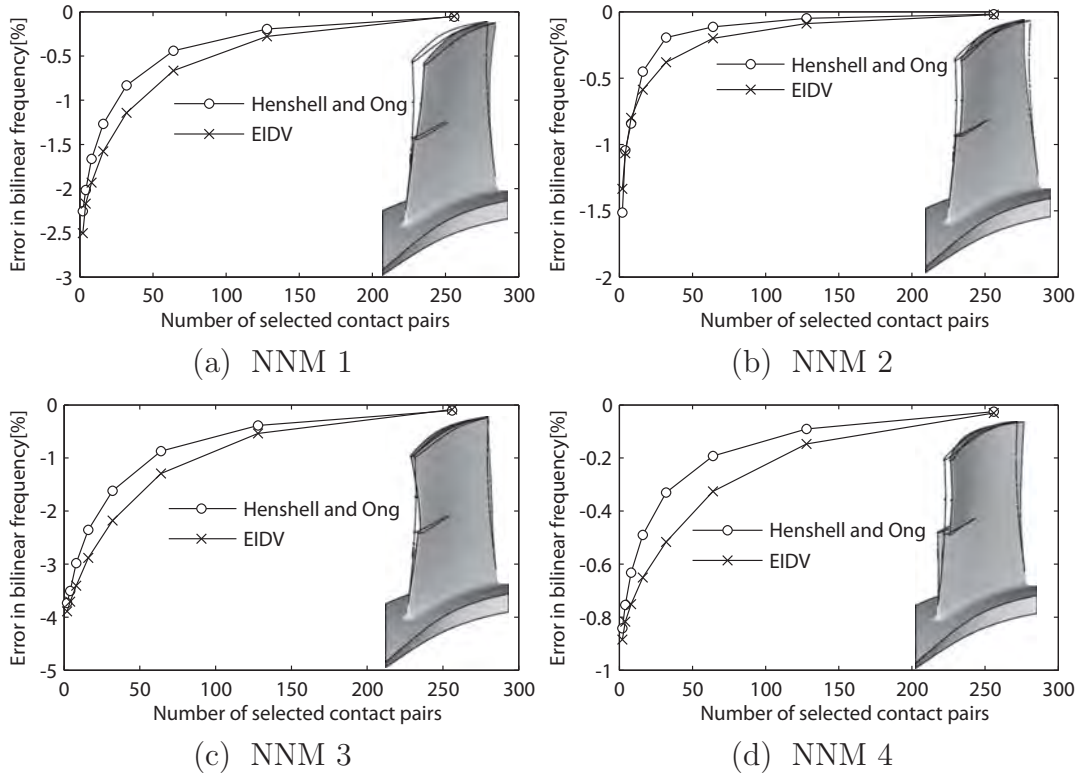


Fig. 61. Error in the bilinear frequency for the first four NNMs

the Henshell and Ong method consistently shows the better results than the results obtained by the EIDV method.

10 BILINEAR MODAL REPRESENTATIONS FOR REDUCED-ORDER MODELING OF LOCALIZED PIECEWISE-LINEAR OSCILLATORS

Dynamical systems with piecewise-linear nonlinearity appear in many disciplines where physical systems have discrete discontinuities. In this paper, a novel reduced order modeling method is proposed for piecewise-linear oscillators, with special attention to vibration problems of elastic media with contact nonlinearity. In particular, the piecewise-linear nonlinearity is assumed to be *localized*, in the sense that the nonlinearity appears only in a few regions, as opposed to globally distributed nonlinearities. Typical engineering examples of such systems can be found in many mechanical, aerospace, or civil structures involving gap nonlinearity caused by joints, interfaces between components, delamination, or cracks. In many cases, such nonlinearity is unavoidable for modeling, analyzing and controlling such structures. In addition, sometimes the dynamics of such structures (in certain operating conditions) cannot be reasonably well described without proper modeling of the nonlinearity. Moreover, due to the growing demand on the accuracy of the analysis of such structures, dealing with the complexity of such systems is increasingly challenging. Modeling such structures requires a careful treatment of the piecewise linear nonlinearity caused by discrete discontinuities. Hence, as the ratio of the number of discontinuities to the system dimensionality increases, the analysis of such system becomes more difficult. Therefore, an efficient reduced-order modeling methodology for accurately modeling such structures is greatly needed from both academic and practical standpoints.

Reduced order modeling has been an active research topic because it has high practical importance and because it provides a good understanding of the fundamental characteristics of a variety of dynamical systems. Many methods have been developed for various systems. Here, we shall restrict the discussion to the reduced order modeling of structural systems with localized and piecewise-linear nonlinearities. In terms of the properties of the dynamics of the system, reduced order modeling methods can be divided into methods based on linear transformations, and methods based on nonlinear normal modes (NNM).

Reduced order models based on linear transformations have been investigated by many researchers for solving nonlinear dynamic problems with localized nonlinearities. For example, Friswell *et al.*^{148, 156} developed methods such as the improved reduced system (IRS)¹³⁵ and the system equivalent expansion process (SEREP),¹⁴⁵ both of which are based on linear transformations similar to Irons-Guyan reduction^{119, 157} with improved dynamic characteristics. They concluded that these methods require that the DOF directly subjected to the nonlinearity be treated as master degrees of freedom (DOF) for the accurate prediction of the nonlinear dynamics. Segalman¹⁵⁸ proposed a model reduction technique for systems with localized nonlinearities (piecewise linear), by augmenting the set of linear normal modes with joint modes, which are basis functions with discontinuities at the locations where nonlinearities are present. The method is similar in nature to the method of component mode synthesis (CMS) and other reduced order modeling techniques based on linear transformations. However, the augmentation of conventional sets of basis functions with special modes yields a basis that effectively contains the configuration space for systems with local nonlinearities. A similar concept is applied in this paper.

Particular cases of piecewise nonlinearity are unilateral constraints. A large number of sophisticated methods have been proposed for systems with such nonlinearities. For example, the method proposed by Butcher and Lu¹¹⁴ is based on a linear approximation of the model reduction technique based on nonlinear master-slave relationship.¹⁵⁹ The transformation matrix of the method is produced by an iterative procedure and is similar to that of Irons-Guyan

reduction, where the DOF subjected to the piecewise-linear nonlinearity are retained in the reduced order model (ROM) as master DOF. The important characteristic of their method is that the ROM preserves the exact eigen-structure of (the linear part of) the original system. In particular, the method (named local equivalent linear stiffness method) was successfully applied to a system of four DOF lumped-mass piecewise-linear oscillators with two DOF being subjected to piecewise-linear nonlinearity.

Several attempts have been made to use also the concept of automated multi-level substructuring,¹⁶⁰ which was developed primarily for linear dynamics, for solving nonlinear dynamic problems with large dimensions and multiple discontinuities. For example, Theodosiou and Natsiavas¹⁶¹ proposed an analysis procedure for solving systems with multiple unilateral constraints using linear complementarity based contact algorithms in conjunction with a reduced order modeling method developed by Papalukopoulos and Natsiavas.¹⁶² There, the final ROM is obtained by automatically partitioning the structure into substructures and considering the DOF subjected to nonlinearity as master DOF.

In contrast, only a few attempts have been made to construct ROMs based on NNMs for piecewise linear systems. Chen and Shaw⁹⁵ proposed a method for constructing NNMs for multi-DOF piecewise linear systems by the invariant manifold approach (and an asymptotic expansion around the fixed point obtained in a Poincaré section). Jiang *et al.*⁹⁴ further generalized the method by the application of a Galerkin approximation of the invariant manifold.¹⁶³ A method based on NNMs was proposed by Apiwattanalungarn *et al.*¹⁶⁴ for general multi-DOF nonlinear structural systems by extending the concept of fixed-interface CMS (also known as Craig-Bampton method¹¹⁸) and using fixed-interface NNMs. Although the invariant manifold approach can produce the NNMs accurately, the application of the method to large dimensional models with multiple discontinuities is not yet effective mostly due to its computational cost.

Another class of order reduction methods is based on proper orthogonal decomposition (POD) and associated eigenvectors (proper orthogonal modes (POMs)), which can often be regarded as an optimal linear representation of the NNM in the sense of least squares.¹⁶⁵ POD has been applied to non-smooth system with impacts by Cusumano and Bai,¹⁶⁶ to relate the dimensionality and the spatial coherence of the system. Modal reduction using POMs for non-smooth system was then investigated by Kappagantu and Feeny¹⁶⁷ for a multi-DOF system with frictional excitation. Their study showed that the dominant POMs can preserve important characteristics of the system (such as bifurcations). Thus, the approach has been used for constructing reduced order models of various nonlinear systems in structural dynamics.¹⁶⁸ However, one of the most important difficulties in using POD is not avoided. Namely, the calculation of POMs requires solving the full nonlinear vibration problem.

Elastic structures with cracks are important engineering examples of system where intermittent contact plays a crucial role. There are a large number of publications regarding this issue. A comprehensive review can be found in Refs..^{59,154} In this paper, we hypothesize that the dynamics of the systems of interest with (localized) piecewise-linear nonlinearity can be approximated by a set of modes obtained for the system where certain special boundary conditions are applied on the crack surfaces. This hypothesis stems from the fact that the nonlinear resonant frequencies of piecewise linear systems derived from vibration problems of cracked structures can often be well captured by $f_b = 2f_o f_s / (f_o + f_s)$, where f_b is called

a *bilinear frequency*, while f_o and f_s are the natural frequencies of two linear systems with different boundary conditions. This concept was initially introduced as the exact natural frequency of a piecewise-linear oscillator with a single discontinuity,^{87,169} and was extended as a *bilinear frequency approximation* (BFA) of the nonlinear resonant frequencies for various systems with piecewise-linear nonlinearities, e.g., two dimensional cracked beams,⁹¹ piecewise linear oscillators with clearance,⁸⁸ and three dimensional cracked plates.¹⁵⁴ This concept is further exploited in this paper.

Another important engineering example of a system with potential intermittent contact appears in the vibration of *delaminated* composite laminates (such as delaminated beams and plates). A comprehensive literature review about this issue was provided by Della and Shu.¹⁷⁰ Many of the previous researchers did not consider the opening and closing of the delaminated interfaces. Instead, they assume that the delaminated interfaces do not touch during the vibration — which are referred to as *free modes*¹⁷¹ — or they assume that the interface is always closed with sliding of surfaces being permitted — which are sometimes referred to as *constrained modes*¹⁷² — or they avoided the interpenetration by adding spring elements between the layers, such as done by Burlayenko and Sadowski.¹⁷³ In contrast, an increasing number of investigations have considered the effects of contact. For example, vibration problems of a laminated plate with contact nonlinearity has been studied by Žak *et al.*,¹⁷⁴ where the contact forces are treated via a penalty method in the time domain. Kwon and Lannamann¹⁷⁵ also investigated the dynamic response of delaminated sandwich structures using finite element modeling in conjunction with impact nonlinearity at the delaminated surface. Žak *et al.* also considered the vibration problem of a delaminated composite beam, where beam finite elements were used in conjunction with impact conditions. However, reduced order modeling of such structures has not been studied.

In this paper, POD and POMs are first exploited for constructing ROMs of piecewise linear structures with multiple discontinuities. Next, a novel technique to approximate POMs by a set of linear normal modes with special boundary conditions is proposed. This technique is referred to as the bi-linear modal approximation and allows the construction of ROMs without having to find the POMs. Hence, the key drawback of using POMs (and POD) is overcome.

This paper is organized as follows. In Section 10.1, the mathematical formulation of the vibration of piecewise linear structures is briefly reviewed. In Section 10.2, POD is applied to a cracked plate, and the characteristics of the POMs are discussed. The bi-linear modal approximation of POMs is then proposed. The validity of the proposed method is further discussed in Section 10.4 using case studies of vibration problems for a cracked plate and a delaminated plate.

10.1 Mathematical formulation: Piecewise linear structures in a mapped subspace

Consider an N -dimensional (finite element) model of a structure. Denote the vector of generalized coordinates of the system by $\mathbf{x}(t) \in \mathbb{R}^N$, and associated kinetic and potential energies by $T(\dot{\mathbf{x}}) = (1/2)\dot{\mathbf{x}}^T \mathbf{M} \dot{\mathbf{x}}$ and $U(\mathbf{x}) = (1/2)\mathbf{x}^T \mathbf{K} \mathbf{x}$, where $\mathbf{M}, \mathbf{K} \in \mathbb{R}^{N \times N}$ are symmetric and positive-definite mass and stiffness matrices. Next, assume that the structure is subject to

unilateral inequality constraints of the form

$$g_i(\mathbf{x}) \geq 0, \quad i = 1, \dots, m, \quad (119)$$

where m is the number of constraints, and $m \ll N$. The gap function g_i designates the distance between the DOF of contact pairs at a crack. Hence, g_i can be expressed as

$$g_i(\mathbf{x}) = x_i^m - x_i^s - g_i^0, \quad i = 1, \dots, m, \quad (120)$$

where superscripts m and s indicate the DOF involved in the i th constraint, and g_i^0 is a constant initial gap. Note that herein g_i^0 is assumed to be zero for all i . It is known that non-vanishing clearances complicate the dynamics significantly.^{87,88} While those complications are intriguing, they are beyond the scope of this paper. Next, consider that the system is subject to non-conservative forces and other viscous forces. Then, the extended Hamilton's principle requires that in a time interval $[t_1, t_2]$

$$\int_{t_1}^{t_2} (\delta L_{\mathbf{x}}(\mathbf{x}, \dot{\mathbf{x}}) + \delta W_v + \delta W_{nc} + \delta W_{uc}) dt = 0, \quad (121)$$

where $L_{\mathbf{x}}(\mathbf{x}, \dot{\mathbf{x}}) = T(\dot{\mathbf{x}}) - U(\mathbf{x})$. δW_v is the virtual work of the viscous forces, and can be expressed as $\delta W_v = -\delta \mathbf{x}^T (\partial F / \partial \dot{\mathbf{x}})$ where $F(\dot{\mathbf{x}}) = (1/2) \dot{\mathbf{x}}^T \mathbf{C} \dot{\mathbf{x}}$, with $\mathbf{C} \in \mathbb{R}^{N \times N}$ being the damping matrix. δW_{nc} is the virtual work of the non-conservative forces $\mathbf{Q}(t) \in \mathbb{R}^N$, and can be expressed as $\delta W_{nc} = \delta \mathbf{x}^T \mathbf{Q}(t)$. δW_{uc} is the virtual work associated with the unilateral constraints in Eq. (119). In this paper, δW_{uc} is modeled by a penalty method.¹⁷⁶ The associated penalty functional P_x is a function of the physical coordinates $\mathbf{x}(t)$, and can be written as

$$P_x(\mathbf{x}) = \sum_{i=1}^m p_i(\mathbf{x}), \quad (122)$$

where $p_i(\mathbf{x})$ is a C^1 -continuous penalty functional for the i th constraint defined as $p_i(\mathbf{x}) = -(1/2)k_p \langle g_i(\mathbf{x}) \rangle^2$, where $k_p \in \mathbb{R}^+$ is a given penalty parameter, and $\langle \cdot \rangle$ denotes $\max(0, \cdot)$. The virtual work δW_{uc} can then be calculated by taking the functional derivative of P_x , or $\delta W_{uc} = \delta P_x(\mathbf{x})$.

We assume that $\mathbf{x}(t)$ undergoes a small amplitude vibration. Hence, the system may be subject to intermittent contact due to the constraints in Eq. (119). We further assume that one can find a subspace much smaller than N that captures $\mathbf{x}(t)$ well. Such a subspace is denoted here as $V = \text{span}(\phi_1, \phi_2, \dots, \phi_n)$, where $n \ll N$, and vectors ϕ_i are linearly independent vectors of length N . A transformation matrix associated with a linear map $V \mapsto \mathbb{R}^N$ is then formed as $\Phi = [\phi_1, \phi_2, \dots, \phi_n] \in \mathbb{R}^{N \times n}$ and applied to $\mathbf{x}(t)$, i.e., $\mathbf{x}(t) = \Phi \boldsymbol{\eta}(t)$ where $\boldsymbol{\eta}(t)$ is a vector of generalized coordinates containing $\eta_j(t)$ for $j = 1, \dots, n$. The penalty functional P_x is then evaluated in the $\boldsymbol{\eta}$ coordinates as

$$P_{\boldsymbol{\eta}}(\boldsymbol{\eta}) = - \sum_{i=1}^m \frac{1}{2} k_p \langle (\phi_c^i)^T \boldsymbol{\eta} - g_i^0 \rangle^2, \quad (123)$$

where ϕ_c^i denotes the transpose of a row of Φ corresponding to the contact DOF of the i th contact pair. Defining $\boldsymbol{\eta}_\varepsilon := \boldsymbol{\eta} + \varepsilon \delta \boldsymbol{\eta}$ where $\varepsilon \in \mathbb{R}$ and $\delta \boldsymbol{\eta} \in \mathbb{R}^n$ and taking a functional

derivative of P_η yields

$$\delta P_\eta(\boldsymbol{\eta}) = \delta \boldsymbol{\eta}^T \left(- \sum_i^m k_p \langle (\boldsymbol{\phi}_c^i)^T \boldsymbol{\eta} - g_i^0 \rangle (\boldsymbol{\phi}_c^i) \right). \quad (124)$$

Application of the linear transformation Φ to $T(\dot{\mathbf{x}})$, $U(\mathbf{x})$ and $F(\dot{\mathbf{x}})$ in Eq. (121) yields the following governing equations:

$$\mathbf{M}_\Phi \ddot{\boldsymbol{\eta}} + \mathbf{C}_\Phi \dot{\boldsymbol{\eta}} + \mathbf{K}_\Phi \boldsymbol{\eta} + \mathbf{f}_\Phi(\boldsymbol{\eta}) = \mathbf{Q}_\Phi(t), \quad (125)$$

where the transformed matrices and generalized forces are defined as $\mathbf{M}_\Phi = \Phi^T \mathbf{M} \Phi$, $\mathbf{C}_\Phi = \Phi^T \mathbf{C} \Phi$, $\mathbf{K}_\Phi = \Phi^T \mathbf{K} \Phi$, $\mathbf{f}_\Phi(\boldsymbol{\eta}) = \sum_i^m k_p \langle (\boldsymbol{\phi}_c^i)^T \boldsymbol{\eta} - g_i^0 \rangle (\boldsymbol{\phi}_c^i)$, and $\mathbf{Q}_\Phi = \Phi^T \mathbf{Q}$.

10.2 Proper orthogonal decomposition

For nonlinear systems, it is known that POD can be viewed as a minimization of the error in the choice of a linear representation of the NNM, if the motion is a single synchronous NNM.¹⁶⁵ In this Section, POD of the nonlinear forced response of a piecewise linear system is considered, and a few key properties of the POMs are discussed.

10.2.1 POM construction by the method of snapshots

Let us assume that $\mathbf{x}(t)$ was numerically captured at r ($\ll N$) discrete time instants, and each observation of $\mathbf{x}(t)$ at t_j , $j = 1, \dots, r$ is denoted by $\mathbf{y}_j = \mathbf{x}(t_j)$, which is referred to as a snapshot. We seek an orthonormal basis $\{\boldsymbol{\psi}_i\}_{i=1}^d$ that describe typical members of \mathbf{y}_j better than any other basis of the same size, where $d = \dim(\text{span}(\mathbf{y}_1, \dots, \mathbf{y}_r))$. Such a basis can be found by maximizing the averaged projection of the snapshot vectors \mathbf{y}_j onto a set of orthogonal vectors $\{\boldsymbol{\psi}_i\}_{i=1}^d$ with a suitable normalization, i.e.,

$$\max_{\{\boldsymbol{\psi}_i\}_{i=1}^d} J(\{\boldsymbol{\psi}_i\}_{i=1}^d), \quad (126)$$

$$\text{subject to } \|\boldsymbol{\psi}_i\| = 1, \quad i = 1, \dots, d, \quad (127)$$

where

$$J(\{\boldsymbol{\psi}_i\}_{i=1}^d) = \sum_{j=1}^r \left(\sum_{k=1}^d (\boldsymbol{\psi}_k^T \mathbf{y}_j)^2 \right), \quad (128)$$

and $\|\cdot\|$ represents the 2-norm of a vector: $\|\mathbf{x}\| = (\mathbf{x}^T \mathbf{x})^{1/2}$ for $\forall \mathbf{x} \in \mathbb{R}^N$. The solution of the maximization problem Eq. (126) under the constraints Eq. (127) can be obtained by maximizing a functional

$$L(\{\boldsymbol{\psi}_i\}_{i=1}^d, \{\lambda_i\}_{i=1}^d) = J(\{\boldsymbol{\psi}_i\}_{i=1}^d) - \sum_{i=1}^d \lambda_i (\|\boldsymbol{\psi}_i\| - 1). \quad (129)$$

The necessary condition for the extrema requires that the functional derivatives of L with respect to $\{\boldsymbol{\psi}_i\}_{i=1}^d$ and $\{\lambda_i\}_{i=1}^d$ vanish, which leads to the following eigenvalue problem (see, e.g., Ref.¹⁷⁷)

$$\mathbf{Y} \mathbf{Y}^T \boldsymbol{\psi}_i = \lambda_i \boldsymbol{\psi}_i, \quad (130)$$

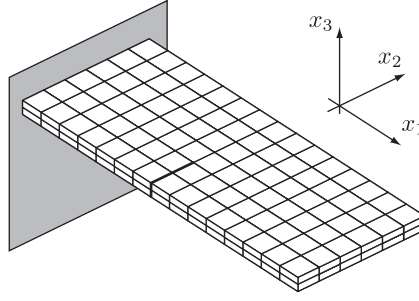


Fig. 62. Finite element model of a cracked plate with $N = 963$ and $m = 6$

where $\mathbf{Y} = [\mathbf{y}_1, \dots, \mathbf{y}_r]$. The eigenvalue problem in Eq. (130) is the POD. The eigenvalues and the eigenvectors of Eq. (130) are referred to as proper orthogonal values (POVs) and proper orthogonal modes (POMs). Solving Eq. (130) requires the eigenvalue and eigenvector extraction of an $N \times N$ matrix, which is not practical for large-dimensional systems. However, the method of snapshots proposed by Sirovich¹⁷⁸ can reduce the problem down to an $r \times r$ eigenvalue problem. It uses a property of the basis where $\boldsymbol{\psi}_i$ can be represented as a linear combination of snapshots, i.e.,

$$\boldsymbol{\psi}_i = \mathbf{Y}\boldsymbol{\pi}_i, \quad i = 1, \dots, r, \quad (131)$$

where $\boldsymbol{\pi}_i \in \mathbb{R}^r$ is yet to be determined. Substituting Eq. (131) into Eq. (130), a sufficient condition for the solution of Eq. (130) can be found as

$$\mathbf{Y}^T \mathbf{Y} \boldsymbol{\pi}_i = \lambda_i \boldsymbol{\pi}_i. \quad (132)$$

Solving the $r \times r$ eigenvalue problem in Eq. (132), and transforming $\boldsymbol{\pi}_i$ back to $\boldsymbol{\psi}_i$ by Eq. (131) yields the POMs. Note that in this paper, the mean of the snapshots is not subtracted from the snapshots when the covariance matrix is formed. In some cases it is useful to subtract the mean from all snapshots,¹⁶⁸ but that is not a requirement for all cases. However, the meaning and interpretation of the POMs has subtle differences in these two approaches.

10.2.2 POD for a piecewise linear system and ROM construction — A cracked plate

The POD is applied to a piecewise linear system derived from a vibration problem of an elastic plate with a crack. The crack is modeled as two geometrically identical surfaces inserted into the elastic plate, which contains m discrete points on each surface. The plate is made of steel with density $\rho_1 = 7,800 \text{ kg/m}^3$, Young's modulus $E_1 = 200 \text{ GPa}$, and Poisson's ratio $\nu = 0.3$. The crack depth is 0.5 relative to the plate width. The length, width, and thickness of the plate are 0.15 m, 0.06 m, and 0.006 m respectively. The motion of the entire plate is subject to the corresponding m inequality constraints represented in Eq. (119), such that the crack surfaces are not allowed to penetrate each other during the motion. The FE model of the cracked plate is shown in Fig. 62 where the plate was discretized with 180 linear brick elements, and $N = 963$ and $m = 6$. A distributed harmonic loading is applied at the tip of the plate, which is parallel to the x_2 direction, such that an NNM (near a resonant frequency corresponding to the first in-plane bending mode) is excited. The resulting initial value problem was solved by a Newmark- β method with contact problem being treated by an augmented Lagrangian method.¹¹⁷ POD was then applied to snapshots ($r = 32$) taken at steady-state. For comparisons, the same calculation was performed with the same plate

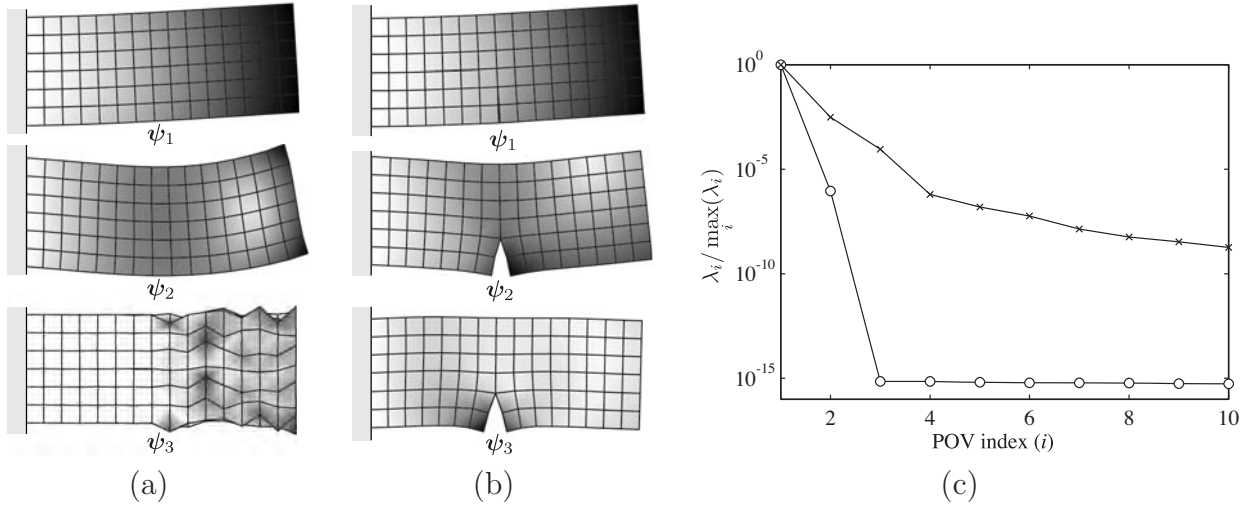


Fig. 63. Results of POD of a linear harmonic response analysis of a plate, and a nonlinear harmonic response analysis of the same plate with a crack. (a) First three POMs from linear harmonic response of healthy plate. (b) First three POMs from nonlinear harmonic response of cracked plate. (c) POV ratio (log scale) from linear and nonlinear harmonic responses: —○— healthy plate; —×— cracked plate.

without the crack, and POD was applied to the snapshots at steady-state. The first three dominant POMs along with their POVs (normalized with respect to the largest POV) are shown in Fig. 63 for both linear harmonic response of the plate and nonlinear harmonic response of the plate with a crack. As can be seen in Fig. 63(a), the most dominant POM, ψ_1 , coincides with the linear vibration mode. The second POM, ψ_2 , is similar to the second in-plane bending mode, but its contribution to the motion is limited, as can be seen in its POV shown in Fig. 63(c). The third POM, ψ_3 is simply due to noises, with the corresponding eigenvalue being negligible. In contrast, for the nonlinear case, although the first two POMs, ψ_1 and ψ_2 , are similar to the linear vibration modes of the cracked plate, the third POM, ψ_3 captures the *local deformation* of the motion, which does not appear in the linear counterpart. The contribution from the rest of the POMs gradually decreases as can be seen in Fig. 63(c). However, the decreasing rate is slower than that for the linear case. This indicates that the nonlinearity posed by the inequality constraints added complexity into the vibration response. Hence, if one attempts to construct a ROM with the POMs, one ought to include more POMs than for the linear case, which is true in general for most nonlinear systems.

Next, a ROM was constructed such that $\mathbf{x}(t) = \mathbf{\Phi}\boldsymbol{\eta}(t)$ where $\mathbf{\Phi} = [\boldsymbol{\psi}_1, \dots, \boldsymbol{\psi}_{n_d}]$, where n_d is the number of dominant POMs, and forced response calculations were performed. Furthermore, to study the dependence of the number of dominant POMs on NNM, ROMs were constructed not only for the first (in-plane) bending mode, but also for the second (out-of-plane) bending mode, where the motion of the surfaces of discontinuity (crack) is more complicated than that for the first in-plane bending mode. The POMs for the second (out-of-plane) bending mode were constructed based on the snapshots taken at the corresponding nonlinear resonant frequencies.

The first three dominant POMs in conjunction with the first 10 POVs are shown in Fig. 64 for the second (out-of-plane) bending mode. As seen in Fig. 64(c), the value of the POVs for the second (out-of-plane) bending mode decreases more gradually than those for the healthy/linear first (in-of-plane) bending mode as well as the first in-plane bending mode.

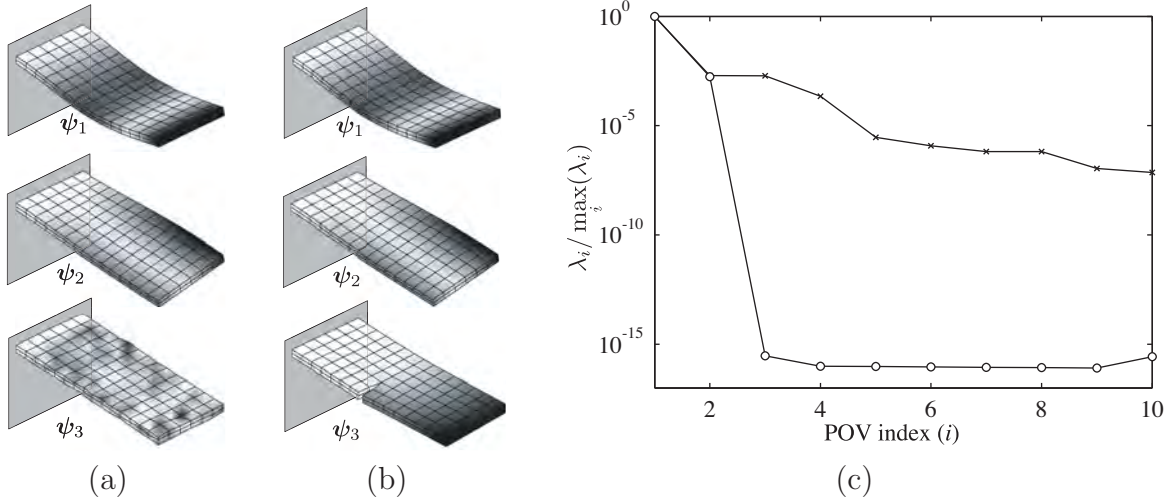


Fig. 64. Results of POD for the second out-of-plane bending modes of the cracked plate. (a) First three POMs for the second out-of-plane bending mode. (b) First three POMs for the second out-of-plane bending mode. (c) POV ratio (log scale): —○— healthy plate; —×— cracked plate.

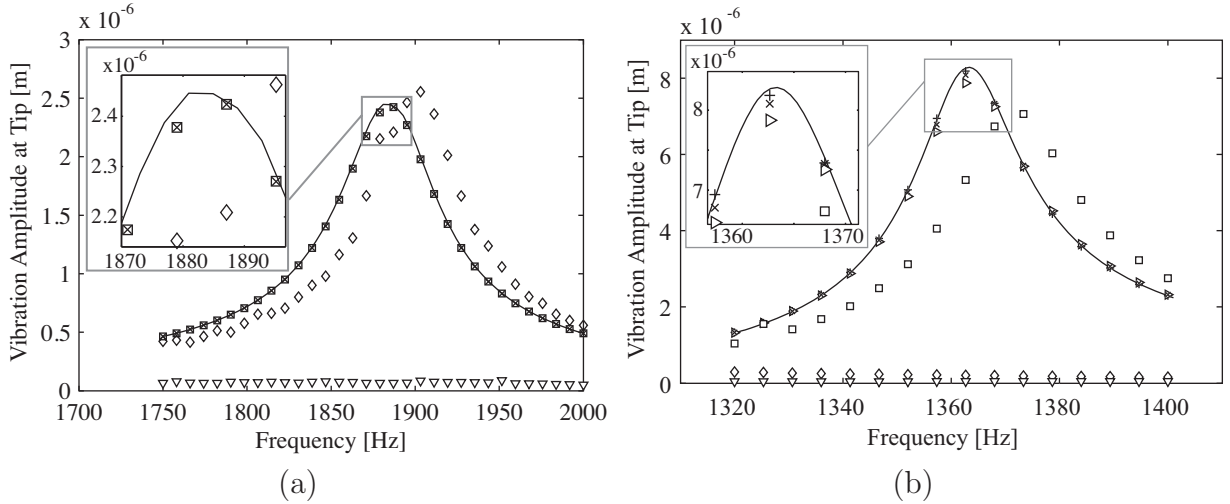


Fig. 65. Nonlinear frequency response. (a) First (in-plane) bending mode. (b) Second (out-of-plane) bending mode. — FEM (963 DOF), + 6 POMs (6 DOF); ▷ 5 POMs (5 DOF); × 4 POMs (4 DOF); □ 3 POMs (3 DOF); ◇ 2 POMs (2 DOF); ▽ 1 POM (1 DOF)

The nonlinear forced response was then computed with the constructed ROMs using a variable step Runge-Kutta method, and the results are shown in Fig. 65 along with the forced response results calculated with the full-order FE model. First, using the POM corresponding to the largest POV did not produce the accurate response at all, mostly due to the fact that the opening and closing of the discontinuous surfaces caused by the inequality Eq. (119) cannot be precisely captured by using the most dominant POM alone. Second, the number of POMs required to obtain satisfactorily accurate results is dependent on the NNM involved in the physical response, as expected from the observations of the POVs. As can be seen in Fig. 65(a), the number of POMs required to capture well the response is three. In contrast, as shown in Fig. 65(b), one needs at least four POMs to accurately capture the second (out-of-plane) bending mode. It is noted that the number of dependent variables involved in the system of nonlinear ODEs is much less than that with the original FE model. For instance, with six POMs for the second (out-of-plane) bending mode, the number of dependent vari-

ables to be integrated is only 12, including the generalized coordinates corresponding to the POMs and their velocities, whereas that for the FEM that number is 963.

10.3 Bilinear modal representation of the proper orthogonal modes

As shown in Section 10.2, the POMs can form a good basis for constructing a ROM which captures well the dynamics of the piecewise linear system. However, the greatest disadvantage of the ROM constructed from the POMs is that it requires a priori knowledge of the nonlinear response, which is oftentimes the solution itself which one is seeking. Typically, the solution involves computationally expensive calculations. In order to circumvent this difficulty, we propose an approximation method of the POMs, based on an augmentation of a set of linear normal modes. The fundamental idea is to construct a set of linearly independent vectors which approximately span the space spanned by the dominant POMs, i.e., $D = \text{span}(\boldsymbol{\psi}_1, \dots, \boldsymbol{\psi}_{n_d})$. Such a set of vectors is derived as follows. Let us assume that the system is undergoing a vibratory motion and subject to the constraints in Eq. (119). At every time step, equality might be enforced for some of the constraints in Eq. (119) whereas the rest of the inequalities are strictly satisfied. Therefore, although the motion is subject to the nonlinear boundary condition, the system can be considered as a linear system at every time step. Depending on which equalities hold, the underlying linear system is different, and such a system (with the equality constraints) is herein referred to as a linear subregion. If there are m such constraints, then there are $\sum_{k=1}^m m!/((m-k)!k!)$ possible linear subregions. If one is concerned with the motion where strictly only two of such linear subregions are present during the motion, it is feasible to represent the configuration of all the DOF by a linear combination of eigenvectors of each of these subregions. Hence, one can construct a ROM using the eigenvectors of these linear subregions. A similar concept has been examined by Chati *et al.*⁹¹ for a piecewise linear oscillator with a single discontinuity, by patching the mode of each linear subregion together at the discontinuity. The constructed mode was comparable to the NNM. However, with the presence of multiple discontinuities, it is not obvious if it is even possible to find such a set of linear subregions, whose eigenvectors span a subspace D . In this study, this concept is generalized to the case where there are more discontinuities than one, and there are multiple states arising from a gradual opening and closing of the contact/discontinuous surfaces.

10.3.1 Definition: bi-linear modal approximations of POMs

Let the eigenvalue problem of the system be written as

$$\mathbf{K}\boldsymbol{\varphi}_o = \lambda_o\mathbf{M}\boldsymbol{\varphi}_o, \quad (133)$$

where λ_o and $\boldsymbol{\varphi}_o$ are eigenvalues and the eigenvectors (mode) of the system without imposing any constraints at the contact/discontinuous surface. This state of the system is herein referred to as *open*, and designated by the subscript o . Considering that in the limit of using all N normal modes as a basis, the space spanned by the dominant POMs can be contained in the subspace spanned by all $\boldsymbol{\varphi}_o$, i.e., $D \subset \text{span}(\boldsymbol{\varphi}_{o1}, \dots, \boldsymbol{\varphi}_{oN})$. Furthermore, if the motion is on the NNM near a linear normal mode, one can always choose at least one $\boldsymbol{\varphi}_o$ that

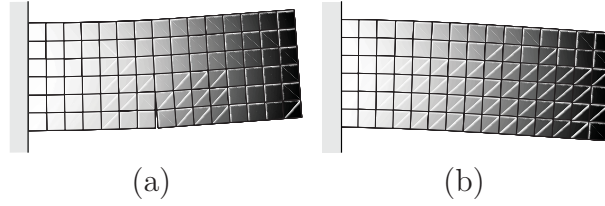


Fig. 66. An example of the extrema of the motion. (a) No equality imposed. (b) All equalities imposed.

resembles the most dominant POM, which is the closest linear representation of the NNM. However, as discussed earlier in Sec. 10.2, one may have to include a large number of modes to represent the local deformations at the contact/discontinuous surfaces. There are many methods developed to date to accelerate the convergence of such a basis and capture the local deformations, such as the use of static constraint modes or the use of attachment modes in CMS.¹¹⁸ However, inclusion of the static modes for the compensation of the linear normal modes tends to inflate the size of the ROM, as the number of such vectors is related to the number of DOF on the contact/discontinuous surfaces. Therefore, one may not like to use such vectors for compensating the linear normal modes for constructing ROMs for piecewise linear systems. In this paper, we hypothesize that the subspace D can be well approximated by the basis consisting of n_o ($\ll N$) of the normal modes, $\{\varphi_1, \dots, \varphi_{n_o}\}$, augmented by another set of linear normal modes of a linear subregion, both of which are assumed to be dominant during the motion. The two dominant modes are computed from the two linear subregions corresponding to two extrema of the motion on the NNM. That is, if one defines equality constraints associated with Eq. (119),

$$g_i(\mathbf{x}) = 0, \quad i = 1, \dots, m, \quad (134)$$

then the linear subregion corresponding to an extremum is defined as the system with *none* of Eq. (134) being imposed (i.e., open). The associated eigenvalue problem is Eq. (133). The other subregion is defined as the system with *all* of Eq. (134) being imposed, which is referred to as *sliding* and designated by subscript s . An example of the two extrema is shown in Fig. 66 using the example of the cracked plate with in-plane bending motion. The linear normal modes with all equalities being imposed are designated as $\tilde{\varphi}_s$, and satisfy

$$\mathbf{K}_s \tilde{\varphi}_s = \lambda_s \mathbf{M}_s \tilde{\varphi}_s, \quad (135)$$

where λ_s and $\tilde{\varphi}_s$ are eigenvalues and eigenvectors, \mathbf{M}_s and \mathbf{K}_s are the mass and the stiffness matrices of size $(N - m) \times (N - m)$ with a suitable elimination of redundant DOFs arising from the constraints in Eq. (134). The elimination of variables can be written as a linear transformation, $\mathbf{K}_s = \mathbf{E}^T \mathbf{K} \mathbf{E}$ and $\mathbf{M}_s = \mathbf{E}^T \mathbf{M} \mathbf{E}$, where \mathbf{E} is a matrix of size $N \times (N - m)$. After solving the eigenvalue problem in Eq. (135), the normal mode $\tilde{\varphi}_s$ is mapped to \mathbb{R}^N , such that $\varphi_s = \mathbf{E} \tilde{\varphi}_s$. The set $\{\varphi_{ok}\}_{k=1}^{n_o}$ is augmented by the set $\{\varphi_{sk}\}_{k=1}^{n_s}$, and the resulting set of modes are grouped together and represented as $\mathbf{B}_{n_o, n_s} = [\varphi_{o1}, \dots, \varphi_{on_o}, \varphi_{s1}, \dots, \varphi_{sn_s}]$, which is referred to as bi-linear modes (BLMs). The determination of n_o and n_s , as well as the selection criteria for φ_o and φ_s shall be discussed in detail in Section 10.3.2. Using the notation of BLMs, the hypothesis is restated as follows: for a given set of POMs, $\{\psi_i\}_{i=1}^{n_d}$, one can find a vector $\mathbf{z} \in \mathbb{R}^{n_o + n_s}$, such that

$$\|\mathbf{B}_{n_o, n_s} \mathbf{z} - \psi_i\| / \|\psi_i\| \ll 1, \quad i = 1, \dots, n_d. \quad (136)$$

Algorithm 5. Angle-based BLM selection

[1] Set a frequency range of interest: $f_l \leq f \leq f_u$ Set a desired number of BLMs: n_{blm} Solve $\mathbf{K}_o \hat{\phi}_o = \lambda_o \mathbf{K} \phi_o$ Identify the mode of interest: $(\hat{f}_o, \hat{\phi}_o)$ where $f_l \leq \hat{f}_o \leq f_u$ $i = 1$ to n_o Calculate $\theta_i(\hat{\phi}_o, \phi_{oi})$ (or $\theta_{K,i}(\hat{\phi}_o, \phi_{oi})$) **end** Sort ϕ_{oi} for $i = 1, \dots, n_o$ in ascending order of θ_i (or $\theta_{K,i}$) Solve $\mathbf{K}_s \hat{\phi}_s = \lambda_s \mathbf{K} \phi_s$ Identify the mode of interest: $(\hat{f}_s, \hat{\phi}_s)$ where $f_l \leq \hat{f}_s \leq f_u$ $i = 1$ to n_s Calculate $\theta_i(\hat{\phi}_s, \phi_{si})$ (or $\theta_{K,i}(\hat{\phi}_s, \phi_{si})$) **end** Sort ϕ_{si} for $i = 1, \dots, n_s$ in ascending order of θ_i (or $\theta_{K,i}$) Form $\mathbf{B} = [\Phi_o, \Phi_s]$, where columns of Φ_o and Φ_s are sorted in ascending order of θ_i (or $\theta_{K,i}$)

Algorithm 6. Bilinear mode selection with interpolated POMs

[1] Compute snapshots \mathbf{Y} that represent the dynamics of the system with a reasonably coarse mesh Compute POMs $\{\psi_1, \dots, \psi_{n_d}\}$ using \mathbf{Y} Map the POMs onto the model with a finer mesh $\{\tilde{\psi}_1, \dots, \tilde{\psi}_{n_d}\}$ Solve $\mathbf{K}_o \varphi_o = \lambda_o \mathbf{M}_o \varphi_o$ Solve $\mathbf{K}_s \tilde{\varphi}_s = \lambda_s \mathbf{M}_s \tilde{\varphi}_s$ $\tilde{\mathbf{B}} = [\varphi_{o1}, \dots, \varphi_{on_o}, \varphi_{s1}, \dots, \varphi_{sn_s}]$ $k = 1$ to n_b $i = 1$ to n_p $j = 1$ to $n_{blm} - k$ Compute $R_{ij} = \|\tilde{\psi}_i - \mathbf{B}_j (\mathbf{B}_j^T \mathbf{B}_j)^{-1} \mathbf{B}_j^T \tilde{\psi}_i\|$, where $\mathbf{B}_j = [\mathbf{b}_j, \tilde{\mathbf{B}}]$ **end end** Choose $j = r$ that minimizes R_{ir} Form $\mathbf{B} = [\mathbf{B}, \mathbf{b}_r]$ Form $\tilde{\mathbf{B}} = [\{\mathbf{b}_j\}_{j \neq r}]$ **end**

This assumption means that the subspace D can be represented well by the linear combination of φ_o and φ_s .

10.3.2 BLM selection criteria

Even though the BLMs can be computed before calculating the nonlinear vibration problem of the original system, selecting the appropriate BLMs is not a trivial task, since one may want to find the minimum number of BLMs that span the subspace D , which is not known when selecting the BLMs. Herein, we propose BLM selection criteria, one of which requires no a priori knowledge about the snapshots, and another which uses a priori knowledge of snapshots of a similar but more tractable problem than the real problem of interest. BLM selection criterion without a priori knowledge of snapshots As seen in Section 10.2, for the forced response problems, the first POMs of the nonlinear response tend to resemble the corresponding linear normal modes whose natural frequencies are within or near the frequency range of interest, which are referred to as $\hat{\phi}_o$ and $\hat{\phi}_s$. It is then possible to identify the modes whose natural frequencies are the closest to the frequency range of interest for both boundary conditions. However, these linear modes alone are not enough to span D . Therefore, other modes have to be chosen to compensate the space spanned by $\hat{\phi}_o$ and $\hat{\phi}_s$. Such modes may be chosen based on their similarity to modes $\hat{\phi}_o$ and $\hat{\phi}_s$ in some metric. The simplest metric may be the Euclidean angle $\theta(\mathbf{x}, \mathbf{y})$ for $\forall \mathbf{x}, \mathbf{y} \in \mathbb{R}^N$, defined by $\cos(\theta) = \mathbf{x}^T \mathbf{y} / (\|\mathbf{x}\| \|\mathbf{y}\|)$. In addition, from the observation that the local deformation has to be captured correctly, a metric using a stiffness-based norm defined by $\|\mathbf{x}\|_K = \mathbf{x}^T \mathbf{K} \mathbf{x}$ for $\forall \mathbf{x} \in \mathbb{R}^N$ is considered. Namely, the angle is defined as $\cos(\theta_K(\mathbf{x}, \mathbf{y})) = \mathbf{x}^T \mathbf{K} \mathbf{y} / (\|\mathbf{x}\|_K \|\mathbf{y}\|_K)$. The BLM selection algorithm based on these metrics is shown in Algorithm 5. BLM selection criterion with a limited a priori knowledge regarding snapshots If the discrete dynamical systems are the ones derived from an infinite dimensional problem, one may be able to take advantage of the results from the convergence study in terms of computational mesh. That is, given a computational mesh with manageable complexity, one may be able to compute snapshots of a dynamical system, which are less accurate than the ones with the finest possible mesh.

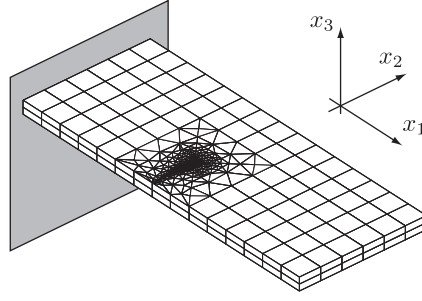


Fig. 67. Cracked plate model with refined mesh where $N = 2835$ and $m = 60$

Next, the POD can be applied to the snapshots, and corresponding POMs can be computed, which are denoted as $\boldsymbol{\psi} \in \mathbb{R}^{Z_c}$, where Z_c denotes the number of DOF of the system from the coarse mesh. The POMs can then be expanded, such that they interpolate the displacement field of the model with the finer mesh (with Z_f DOF). This can be represented as a linear mapping $\mathbb{R}^{Z_c} \mapsto \mathbb{R}^{Z_f}$ given by

$$\tilde{\boldsymbol{\psi}} = \mathbf{N}\boldsymbol{\psi}, \quad (137)$$

where $\mathbf{N} \in \mathbb{R}^{Z_f \times Z_c}$ is a matrix representing the mesh interpolation, and $\tilde{\boldsymbol{\psi}}$ is a POM mapped to the finer mesh. It is noted that $\tilde{\boldsymbol{\psi}}$ is not a POM computed from the snapshots of the system with the finer mesh. Therefore, $\tilde{\boldsymbol{\psi}}$ is not necessarily part of a good basis for constructing the ROM of the finer mesh.

An optimal set of BLMs can then be chosen by finding the BLMs that best approximate the interpolated POMs in the sense of least squares. Namely, for a given interpolated POM, $\tilde{\boldsymbol{\psi}}$, find a set of BLMs, $\mathbf{B} = [\mathbf{b}_1, \dots, \mathbf{b}_{n_b}]$, such that

$$\|\tilde{\boldsymbol{\psi}} - \mathbf{B}(\mathbf{B}^T \mathbf{B})^{-1} \mathbf{B}^T \tilde{\boldsymbol{\psi}}\| = \text{minimum}. \quad (138)$$

In Algorithm 6, this is achieved as follows. First, $\tilde{\mathbf{B}}$ is computed for a frequency range that is slightly wider than the frequency range of interest, where $\tilde{\mathbf{B}} = [\boldsymbol{\varphi}_{o1}, \dots, \boldsymbol{\varphi}_{on_o}, \boldsymbol{\varphi}_{s1}, \dots, \boldsymbol{\varphi}_{sn_s}]$. Second, one of the vectors in $\tilde{\mathbf{B}}$ is selected, and Eq. (138) is examined for the dominant POMs by using \mathbf{B} as the selected vectors. The chosen vector is then renamed as \mathbf{b}_1 and stored in \mathbf{B} . Third, the chosen vector is eliminated from $\tilde{\mathbf{B}}$. Next, the second BLM is selected such that Eq. (138) is achieved for $\|\tilde{\boldsymbol{\psi}} - \mathbf{B}_2(\mathbf{B}_2^T \mathbf{B}_2)^{-1} \mathbf{B}_2^T \tilde{\boldsymbol{\psi}}\|$, where $\mathbf{B}_2 = [\mathbf{B}, \mathbf{b}_2]$. Then, \mathbf{B} is redefined as $\mathbf{B} = [\mathbf{b}_1, \mathbf{b}_2]$. This process is repeated until the number of the chosen BLMs reaches the desired number.

10.4 Case studies

In this section, the proposed method is applied to engineering problems, and its efficiency and validity are discussed. The focus of the case study in Sec. 10.4.1 is placed on the examination of the proposed BLM selection algorithms. The case study in Sec. 10.4.2 is provided to demonstrate the applicability of the BLM representation for other engineering applications such as modeling delaminated plates.

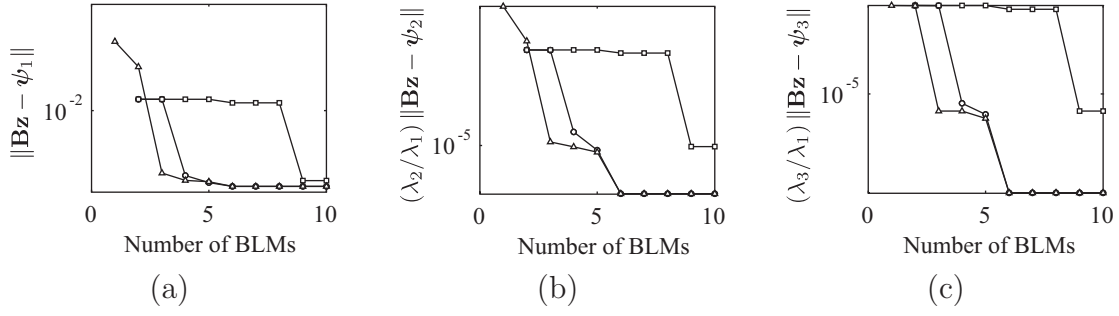


Fig. 68. Convergence of residuals in log scale for first (in-plane) bending mode (first three dominant POMs). (a) POM 1. (b) POM 2. (c) POM 3. \circ — Algorithm 1 (θ); \square — Algorithm 1 (θ_K); \triangle — Algorithm 2.

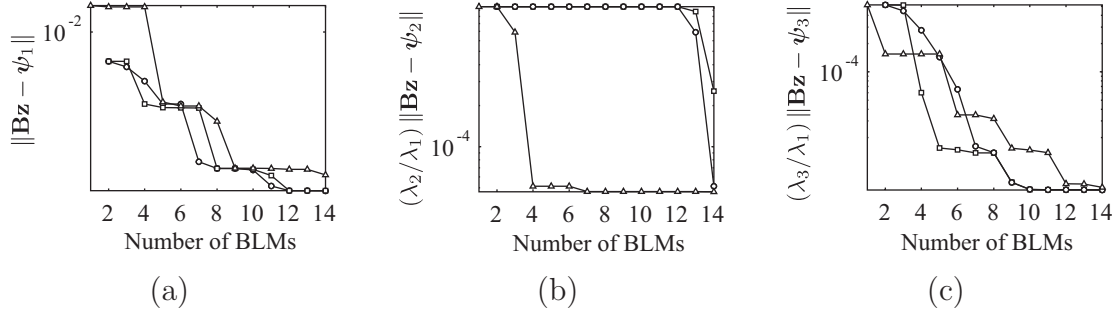


Fig. 69. Convergence of residuals in log scale for second (out-of-plane) bending mode (first three dominant POMs). (a) POM 1. (b) POM 2. (c) POM 3. \circ — Algorithm 1 (θ); \square — Algorithm 1 (θ_K); \triangle — Algorithm 2.

10.4.1 Cracked plate with refined mesh

The first example is the vibration problem of a cracked plate modeled using a refined mesh near the contact surfaces. The associated FE model is shown in Fig. 67. The plate is discretized with 972 solid brick elements, and the system has the total number of DOF of 2835. The number of constraints is 60. The vibration modes of interest in this case study are the first (in-plane) bending that lies in the frequency range $1,750 \text{ Hz} \leq f \leq 2,000 \text{ Hz}$, and the second out-of-plane bending modes in the frequency range $1,362 \text{ Hz} \leq f \leq 1,442 \text{ Hz}$. First, the effectiveness of the proposed BLM selection algorithms is discussed. For comparison, the (usual) dominant POMs are computed from snapshots of the nonlinear forced responses of the FE model. Eq. (136) was then checked to show that the chosen BLMs approximate well the POMs in the sense of least squares, for both algorithms. For Algorithm 6, to obtain the snapshots of the model with a smaller dimensional model, the nonlinear forced response analyses of the same cracked plate model with coarser mesh shown in Fig. 62 were performed. The snapshots obtained were then used to construct the POMs of the system with the coarser mesh, and the POMs were interpolated using Eq. (137). Algorithms 5 and 6 were applied, and the results of Eq. (136) for the first three dominant POMs are shown in Figs. 68 and 69. First, as shown in Fig. 68, Algorithm 5 with θ and that with θ_K generate the BLMs that give the smallest residual for the case with two BLMs. However, the convergence of residuals computed with θ_K is the slowest for all the POMs shown. In contrast, even though Algorithm 6 results in larger residual for the first two BLMs, it converges the fastest among the three methods. For the second (out-of-plane) bending mode, Algorithm 5 with θ_K generates smaller residuals for the first and the third POMs, as seen in Figs. 69(a)

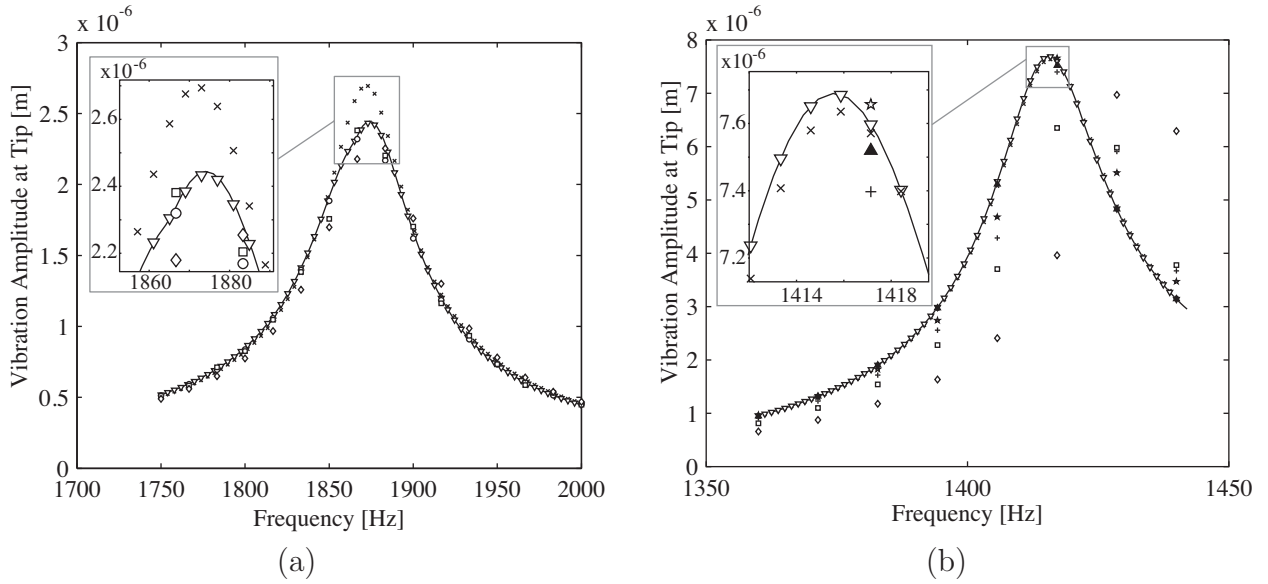


Fig. 70. Nonlinear forced response with various ROMs. (a) First (in-plane) bending mode: — FEM (2835 DOF); \times Craig-Bampton CMS (140 DOF); ∇ Hintz CMS (140 DOF); \diamond 150 φ_o ; \square 3 POMs; \circ 3 BLMs. (b) Second (out-of-plane) bending mode: — FEM (2835 DOF); \times Craig-Bampton CMS (140 DOF); ∇ Hintz CMS (140 DOF); \diamond 150 φ_o ; \square 3 POMs; \blacktriangle 6 POMs; $+$ 10 BLMs; \star 30 BLMs.

and 69(c). However, as can be seen in Fig. 69(b), Algorithm 5 with both angle metrics do not produce satisfactory results for the second POM. This indicates that Algorithm 6 is the only method that consistently shows good convergence for all POMs. This trend was true for other numerical examples, but the results are not shown here for the sake of brevity.

Next, using the BLMs chosen by Algorithm 6, forced response analyses were performed. Namely, ROMs were constructed such that $\mathbf{x}(t) = \mathbf{B}\boldsymbol{\eta}(t)$, where $\mathbf{B} = [\mathbf{b}_1, \dots, \mathbf{b}_{n_b}]$, and the nonlinear forced responses based on Eq. (125) were computed. To compare the proposed ROMs with conventional ROM methods, classical mode superposition method with $\mathbf{x}(t) = \mathbf{\Phi}_o\boldsymbol{\eta}(t)$, as well as CMS methods were examined. The CMS methods have been commonly used for solving nonlinear vibration problems with localized nonlinearities. When CMS methods are applied to dynamical systems with localized nonlinearities, spectral properties of the linear portion of the system are represented by a set of truncated linear normal modes with special boundary conditions. The localized nonlinearities are typically handled by a set of vectors representing local deformations, such as static constraint modes. In this example, two commonly used CMS methods were examined: (a) a CMS method with constraint modes and a truncated set of free-interface normal modes⁹⁸ (Hintz CMS), and (b) a CMS method with constraint modes and a truncated set of fixed-interface normal modes¹¹⁸ (Craig-Bampton CMS). For the numerical integration of the FE model, steady-state response was sought by using a method based on harmonic balance approximations.^{112,153} For the results based on ROMs, a variable step-size Runge-Kutta method was used, as was also done in Sec.10.2.2.

The results of forced response analyses are shown in Fig. 70(a) for the first (in-plane) bending mode, and Fig. 70(b) for the second (out-of-plane) bending mode. First, as can be seen in Figs. 70(a) and 70(b), ROMs with the POMs as small as three (0.1% of the original model size) for the first (in-plane) bending mode, and six (0.2% of the original model size) for

Table 5
CPU time for the selection algorithms

2*Mode	CPU time [s]		
	Algorithm 1 (θ)	Algorithm 2 (θ_K)	Algorithm 2
First bending	$2.59 \times 10^{-2} \pm 4.08 \times 10^{-3}$	$5.47 \times 10^{-2} \pm 7.26 \times 10^{-3}$	$7.77 \times 10^{-1} \pm 1.03 \times 10^{-1}$
Second bending	$7.24 \times 10^{-2} \pm 6.82 \times 10^{-3}$	$1.03 \times 10^{-1} \pm 1.24 \times 10^{-2}$	$3.42 \times 10^{-1} \pm 3.52 \times 10^{-2}$

the second (out-of-plane) bending mode, yielded accurate results. In contrast, CMS ROMs produced accurate results but required much larger ROMs. Indeed, the Hintz CMS method produced accurate results for both modes with a ROM of 140 DOF. The Craig-Bampton CMS ROM with 140 DOF did not even yield accurate results for the first (in-plane) bending mode, as seen in Fig. 70(a). The inflation of the size of the ROMs based on CMS is mostly caused by the retainment of all the DOFs on the contact faces as generalized coordinates in the ROMs. With the standard CMS methods, inclusion of all the DOF on the contact surfaces is unavoidable, unless only a subset of the DOF are sampled and accuracy is sacrificed.¹⁷⁹ Furthermore, as clearly seen in Fig. 70(b), the classical mode superposition method did not yield accurate results with even more modes than in the CMS methods. It is also noted that ROMs made solely from Φ_s do not work at all, because the dynamics is projected onto vectors where the contact interfaces are closed (Eq. (134)). In contrast, BLMs produced as accurate results as those from the POMs, while keeping the ROM size as small as three for the (in-plane) bending mode, and 30 for the (out-of-plane) bending mode. The size of ROMs based on BLM is always larger than or equal to the size of ROMs based on POMs, because the POMs are directly obtained from the nonlinear forced response and they are the optimal linear expression in the sense of least squares. Evidently, BLMs can span the space spanned by the dominant POMs, D , as can be seen in Figs. 70(a) and 70(b). Particularly, the three BLMs used for Fig. 70(a) produced results as accurate as the ones using the ROM with three POMs. The results in Fig. 70(b) require more than six BLMs to capture the response accurately. However, the ROM size (of six) is still much less than the number of φ_o that ended up predicting even less accurate results than the ones obtained with the BLMs. Thus, as long as $n_d \ll N$, the corresponding BLMs can reduce the system size significantly.

To evaluate the computational time for this procedure, the algorithms were implemented in the Matlab environment, and the CPU time was measured on a computer with an Intel Core 2 Duo 2.2 GHz processor and 4.0 GB of RAM. The CPU time was measured for 500 trials for the first and the second bending modes. The results are shown in Tab. 5. As can be seen in Tab. 5, the CPU time required for Algorithm 1 with θ_K requires slightly more time than Algorithm 1 with θ as it requires the inner product between \mathbf{K} and \mathbf{y} . Furthermore, Algorithm 2 requires more CPU time (than Algorithm 1) because it requires successive evaluations of R_{ij} .

10.4.2 Delaminated composite laminates

The second case study considered is a vibration problem of a laminated plate. A square plate with 0.5 m long edges shown in Fig. 71(a) is used for the investigation. The plate consists of two layers with different material properties. The thinner plate with thickness $h_1 = 5$ mm is a steel plate with density $\rho_1 = 7,800$ kg/m³, Young's modulus $E_1 = 200$ GPa, and Poisson's ratio

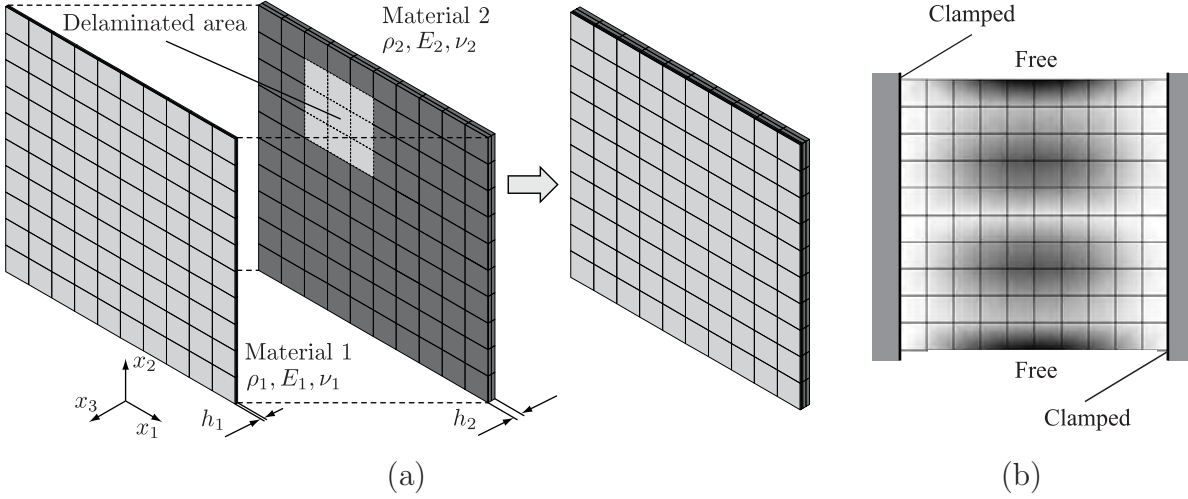


Fig. 71. Partially delaminated composite plate. (a) Schematics of the model. (b) Sixth vibration mode of the healthy plate with natural frequency 2621.5 Hz.

$\nu = 0.3$ (material model 1). The thicker plate with thickness $h_2=15$ mm is a silicon carbide plate (SiC) with density $\rho_2 = 3,230$ kg/m³, Young's modulus $E_2 = 400$ GPa, and Poisson's ratio $\nu_2 = 0.17$ (material model 2). The plate is discretized with 400 brick elements, resulting in 1,497 DOF. We further consider that there is a delaminated area between the two plates, as shown in Fig. 71(a). Namely, the delamination of the layers is modeled by disconnecting the finite element nodes between the plates in the designated area. The plate is subject to a clamped-clamped boundary condition along the edges parallel to the x_2 - x_3 plane, where displacements along x_1 , x_2 , and x_3 are all constrained. The sixth mode was used for this study. The corresponding linear normal mode of the healthy plate is shown in Fig. 71(b). From a mathematical viewpoint, the vibration problem of this structure is the same as the one treated in Sec. 10.4.1, in the sense that the dynamical system is subject to the nonlinear force due to intermittent contact. However, it is expected that the response is much more complicated than the ones observed for the cracked plate, mostly due to the flexibility of the structure in the plane parallel to the nonlinear forces. The increased complexity is manifested in the number of dominant POMs extracted from the nonlinear response, as discussed next.

First, snapshots were obtained by nonlinear harmonic response analyses to examine the number of dominant POMs. Namely, harmonic loadings with unit amplitude were applied on points on both edges parallel to x_1 -axis, where the amplitude of vibration was expected to be the largest in the mode shape of interest, as seen in Fig. 71(b). The frequency of the loadings was swept in a range from 2,000 Hz to 3,000 Hz. The snapshots were then taken at 32 discrete time instants equally spaced over one cycle of oscillation when the system was forced near the resonant frequency. POD was employed and the first three dominant POMs for both the healthy and the damaged plates are shown in Figs. 72(a) and 72(b). The corresponding POVs are shown in Fig. 72(c). As can be seen in Figs. 72(a) and 72(b), the first two POMs are similar to the linear normal modes for both the healthy and the damaged plate. In contrast, the third POM is very localized at the damaged region, as seen in Fig. 71(b). Note that this is similar to the trend observed in the POMs for the cracked plate shown in Figs. 63(b) and 64(b).

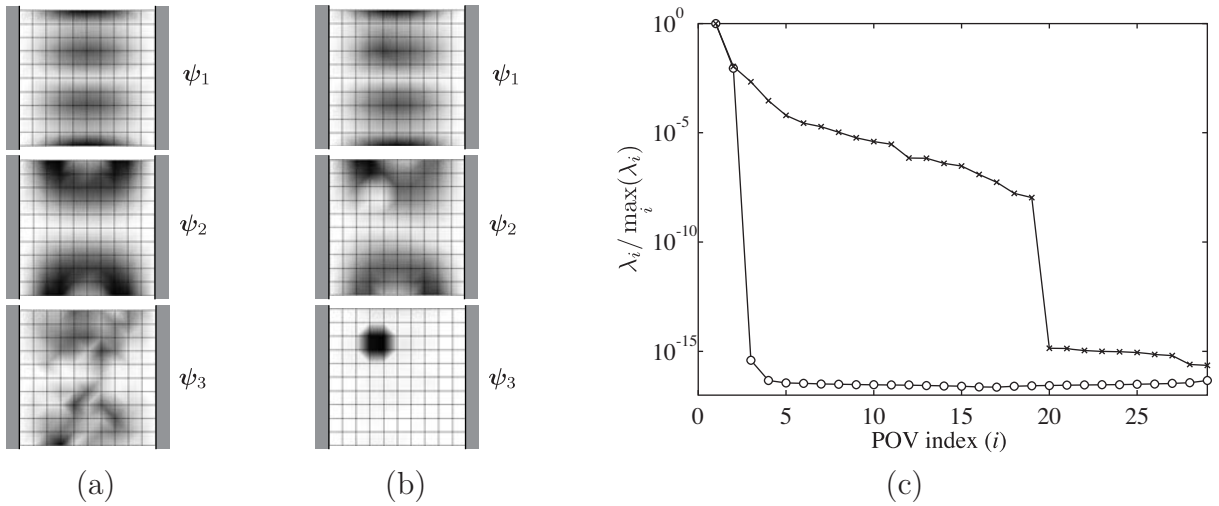


Fig. 72. First three dominant POMs and convergence of POV ratio. (a) Linear harmonic response of healthy plate. (b) Nonlinear harmonic response of delaminated plate. (c) POV ratio (log scale) from linear and nonlinear harmonic responses: \circ — healthy plate; \times — cracked plate.

Second, ROMs were constructed by using the computed POMs, and forced response computations were performed for different numbers of POMs. Converged results were obtained when the number of POMs was 19, where a huge drop in the POV ratio can be observed in Fig. 72(c). The forced response results computed with 2 POMs and 19 POMs are shown in Fig. 73. Finally, ROMs were constructed based on the BLMs chosen by Algorithm 5, and forced response calculations were carried out. To highlight the accuracy and the compactness of the BLM representation, forced response results with the FE model, as well as the ROM constructed only from Φ_o are also shown in Fig. 73. As can be seen in Fig. 73(a), both ROMs with 19 POMs and with 60 BLMs produce very accurate results near the resonant frequency. Even though the ROM with 60 φ_o also produces accurate results, the results produced from the ROM with 60 BLMs are much closer to the results of the FE model than those produced from the ROM with 60 φ_o alone.

It is noteworthy that the results computed from the ROMs with POMs do not show good agreement at lower frequency even with 19 POMs, as can be seen in the lower frequency region in Fig. 73(a). This is because the POMs were constructed based on the snapshots taken only at the resonant frequency. Hence, the POMs are not guaranteed to form a good basis at frequencies far from the resonance, which is typical for ROMs constructed using POMs. In contrast, the ROM constructed using BLMs shows excellent agreement over the entire frequency range of interest. This indicates that the BLMs could effectively embed NNMs for different frequencies, which is difficult to achieve with the ROMs based on the POMs.

In general, the dominant POM subspace changes not only with the frequency but also with the amplitude. As was shown in this example, the BLM-based ROMs can capture the frequency response very well over the frequency range of interest. In this paper, the variations in the amplitude of the excitation has not been investigated. Nonetheless, amplitude variations in general affects the behavior of piecewise-linear oscillators especially when there are static gaps at the discontinuous surfaces.⁸⁸ However, the initial gaps at the discontinuous surfaces are all zero for the specific cases presented in this paper (i.e., $g_i^0 = 0, \forall i$, in Eq. (120)).

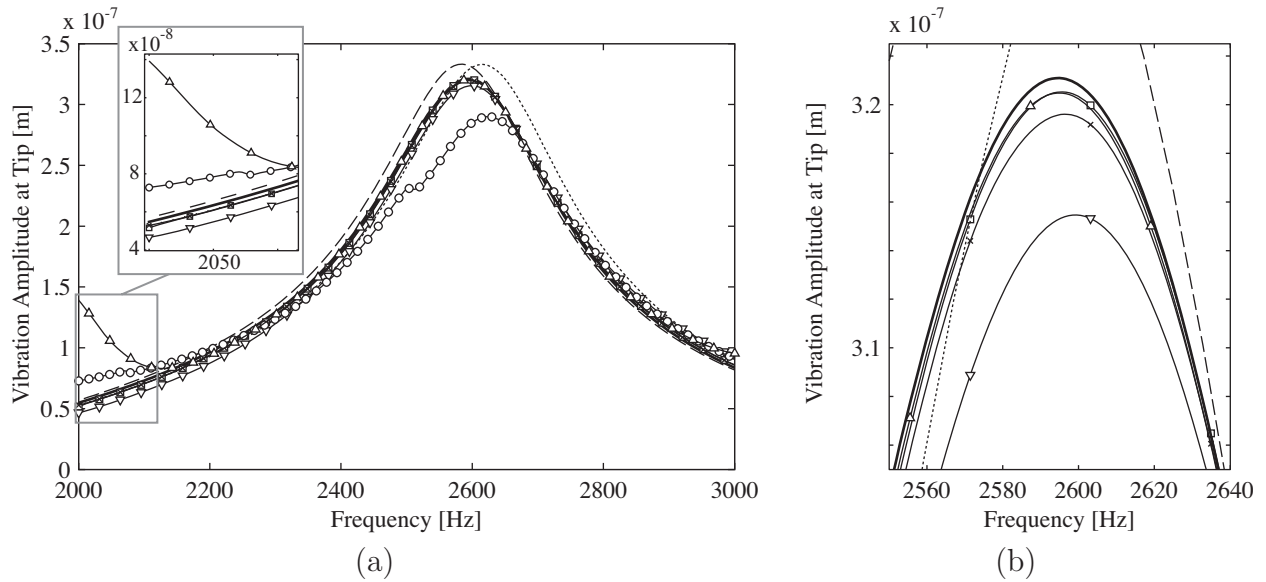


Fig. 73. Forced response results with ROMs. (a) Forced response. (b) Magnified view near the resonant peak. ---- Healthy FEM; — Delaminated FEM (linear response ignoring contact); —○—, 2 POMs; —△— 19 POMs; —▽— 20 BLMs; —×— 60 φ_o ; —□— 60 BLMs; — Delaminated FEM, nonlinear harmonic response (1497DOF).

For such cases, it is known that the vibration response can be scaled with the excitation amplitude due to the positive homogeneity of the piecewise linearity.^{93,153} Namely, if the excitation of interest can uniformly be scaled as $\alpha \mathbf{Q}(t)$ (where $\alpha \in \mathbb{R}^+$), then the response can also be scaled as $\alpha \mathbf{x}(t)$. Hence, the POM subspace computed from the system response due to $\mathbf{Q}(t)$ is the same as the POM subspace computed from the system response due to $\alpha \mathbf{Q}(t)$. This is because the POMs for $\mathbf{Q}(t)$ are computed using $\mathbf{x}(t)$ whereas the POMs for $\alpha \mathbf{Q}(t)$ are computed using $\alpha \mathbf{x}(t)$. Thus, the proposed approach can handle variations in the excitation amplitude (at least ones that are uniform scaling) as long as the BLM-based ROM contains the POM subspace. However, examining the effects of more general variations in the amplitude of excitation on the accuracy of the response predicted with the BLM-based ROMs is still necessary for further expanding the capability of this ROM methodology (and that is beyond the scope of this paper).

**11 REDUCED-ORDER-MODELING FOR NONLINEAR ANALYSIS OF CRACKED
MISTUNED MULTI-STAGE BLADED DISK SYSTEMS**

With the concurrent advancement of computer hardware and software with sophisticated physical and mathematical methodologies represented by finite element method, model-based vibration analysis has been extensively applied to the dynamic analysis of turbomachinery rotors. Most turbine engine rotors consist of multiple stages of bladed disks. Vibration modeling of rotors is a classic problem, yet it has been an active research area for structural dynamicists both in industry and academia. In this paper, a novel reduced order modeling method is proposed for the vibration problems of multi-stage bladed disk assemblies, which possess a cracked blade on one of the stages, and is subject to blade-to-blade small mistuning. The methodology allows the use of an efficient cyclic-symmetry based reduced order modeling method for mistuned but non-cracked stages. The modeling framework is developed by generalizing the modeling procedure proposed by Song *et al.*¹⁸⁰ and is described in the *Mathematical Formulation* section.

This paper is organized as follows. First, a brief overview of multi-stage turbomachinery analysis is provided. Then, a mathematical description of the proposed modeling approach is described. Next, the proposed methodology is validated by using a numerical example of an industrial multi-stage bladed disk system. In particular, nonlinear forced response calculations are performed, and the applicability of the proposed method to the vibration problem of multi-stage bladed disks is demonstrated. Finally, conclusions of the work are given.

11.1 Background

An extensive literature survey of linear and nonlinear vibration modeling of mistuned bladed disk systems is given by Castanier and Pierre.¹⁸¹ Bladh *et al.*¹⁸² investigated the effects of multi-stage coupling on the dynamics of bladed disks with blade mistuning. It was pointed out that the mistuning due to inter-stage coupling is inherent in multi-stage systems. Furthermore, it was reported that the inter-stage coupling may be significant and cannot be neglected when the frequency ranges of interest pass *veering regions*, where the motion of the disk is dominant. A novel reduced order modeling technique for multi-stage bladed disk systems was proposed by Song *et al.*,¹⁸³ which enables the use of stage-wise reduced order models (ROMs) by cyclic-symmetry. The method was then incorporated¹⁸⁴ with an efficient mistuning modeling method called component mode mistuning (CMM).¹⁸⁵ It was successfully applied to the modal parameter identification of multi-stage bladed disks,¹⁸⁶ and also to mistuning identification and structural health monitoring.¹⁸⁰ Laxalde *et al.*¹⁸⁷ also proposed a method to deal with multi-stage bladed disk systems with a similar concept as that proposed by Song *et al.*,¹⁸⁰ and successfully applied their method to modal analysis and forced response calculations for industrial bladed disks.¹⁸⁸ However, in that work each stage was assumed to be tuned. Sternchüs *et al.*¹⁸⁹ extended the method proposed by Laxalde *et al.*,^{187,188} by representing the inter-sector elements as super-elements, and by using inter-stage ring elements. The methodology presented in this paper is a generalization of the method proposed by Song *et al.*,¹⁸⁰ which applies the inter-stage compatibility by Fourier coefficients, and handles the mistuning with CMM.¹⁸⁵

Sinha¹⁹⁰ also developed a lumped parameter model of mistuned multi-stage models where inter-stage coupling is handled by discrete springs, and conducted Monte Carlo simulations

on these models. Although the model was shown to be able to simulate the overall dynamics of the multi-stage rotors, its applicability to industrial models with realistic geometry was not discussed.

In addition to the modeling of blades, there have also been efforts to accurately capture the coupling effects between the torsional vibration of shafts and blades. For example, Chatelet *et al.*¹⁹¹ investigated the complicated dynamics of rotors and shafts by assuming that all the rotors and shafts are axisymmetric and by applying cyclic-symmetry analysis. Turhan and Bulut¹⁹² considered the coupling between shaft torsion and blade bending vibrations by using a qualitative model of multi-stage bladed disks, where the disks are modeled as rigid and the blades are modeled as Euler-Bernoulli beams. Their eigenanalysis (of the analytical model) indicated that there are two types of modes: the coupled modes where shaft torsion and blade bending are coupled, and the rigid shaft modes where the dominant motion is a rigid-body motion of the disk and blades. They also reported that the coupled shaft torsion and blade bending modes are subject to eigenvalue loci veering.

Rzadkowski and Sokolowski,¹⁹³ and Rzadkowski and Drewczynski¹⁹⁴ examined the free response of an eight bladed disk assembly connected by a flexible shaft. For that specific model, they reported that the bladed disk modes of nodal diameters zero, one and two are affected by the shaft flexibility, and multi-stage effects are visible. However, they assumed that the bladed disks are all tuned and have the same number of blades. That is a significant drawback which means that the entire multi-stage bladed disk system has to be cyclically symmetric.

Seguì and Casanova¹⁹⁵ also developed a reduced order modeling method for a (single stage) mistuned bladed disk mounted on a shaft. The method utilizes the Craig-Bampton component mode synthesis (CMS) method¹¹⁸ where the blades, the disk, and the shaft are considered to be separate substructures. As was also reported by other researchers, their work suggested that the stage-wise modal analysis is not enough for accurately predicting the global dynamic response of rotating turbomachines. Later, Boulton and Casanova¹⁹⁶ extended the modeling approach of Seguì and Casanova¹⁹⁵ to the dynamical modeling of a two-stage, mistuned, industrial gas turbine model, and showed that the interaction between the bladed disk and shaft contributes to the variations in the modes predicted from the stage-wise modal analysis.

All the references cited above deal with *linear* vibration problems. Nonlinearity comes from various sources in the dynamics of turbomachinery rotors. To date, only a few attempts have been made to deal with a multi-stage bladed disk assembly with nonlinearities. Laxalde and Thouverez¹⁹⁷ investigated the modeling of friction-ring dampers, which cause strong nonlinearity due to friction between the rotors and the dampers. The nonlinear forced response analysis was performed based on a multi-harmonic hybrid-frequency time domain method with an augmented Lagrangian approach.¹⁰² They showed the applicability of the reduced order modeling of the multi-stage bladed disks based on cyclic-symmetry, and the multi-harmonic hybrid-frequency time domain method.

There have been only a few papers published to date regarding the issue of vibration problems of bladed disks with cracked blades. Saito *et al.*¹⁹⁸ investigated the effects of a cracked blade on the forced response vibration of a single stage mistuned bladed disk. They revealed

that there can be a cracked-blade-localized vibration response for some families of modes. Kharyton *et al.*¹⁹⁹ also investigated the effects of a cracked blade on the vibration response of a bladed disk without blade-to-blade mistuning.

11.2 Mathematical Formulation

In this section, the proposed reduced order modeling method for multi-stage bladed disk assemblies is described. When modeling the multi-stage bladed disk assemblies, the challenge is that the entire multi-stage assembly does not possess cyclic-symmetry because the stages do not necessarily have the same number of blades. Therefore, any reduced order modeling method based on cyclic-symmetry suffers from this issue. Furthermore, efficient modeling of mistuning is crucial for statistical analyses such as Monte-Carlo simulations for many mistuning patterns. The proposed method addresses these challenges.

Recently, efficient mistuning modeling methods for a single stage bladed disk have been reported. For example the CMM approach proposed by Lim *et al.*¹⁸⁵ was shown to be effective and accurate for single stage bladed disks. Song *et al.*¹⁸⁰ successfully applied CMM for the modeling of multi-stage bladed disks. The methodology is capable of modeling the mistuned bladed disks based on a stage-wise cyclic CMS method, and the application of compatibility conditions at the inter-stage boundaries using Fourier basis functions. In this paper, this modeling framework is further generalized for the cases where the system consists of a mixture of stages that in the absence of small blade-to-blade mistuning can be modeled by cyclic-symmetry, and those that cannot be modeled by cyclic-symmetry. Herein, a bladed disk that can be modeled via cyclic-symmetry is referred to as a *cyclic stage*. Strictly speaking, if there is blade-to-blade mistuning, no stage possesses cyclic-symmetry. However, the small mistuning can be added to a stage modeled by cyclic-symmetry by using CMM.¹⁸⁵ Furthermore, the stage that cannot be modeled via cyclic-symmetry is referred to as a *non-cyclic stage*. These stages cannot be modeled via cyclic-symmetry for various reasons, e.g., the presence of large geometric variations, symmetry-breaking components, or a cracked blade. In this paper, the disk with a cracked blade is treated as a non-cyclic stage.

The modeling framework is designed such that it is capable of modeling each stage separately, and it can handle any small mistuning pattern efficiently. First, the model reduction method is formulated for cyclic stages (with distinct number of blades). Then it is formulated for non-cyclic stages. Finally, the assembly of the stage-wise ROMs is discussed.

11.2.1 Reduced Order Modeling of Cyclic Stages

Modeling of Cyclic Stages

Let us assume that stage 1 of a multi-stage system is cyclic and consists of N identical sectors that are disconnected. Fig. 74(a) shows a cyclic stage where N is equal to 25, and Fig. 74(b) shows one of the N sectors that make up the stage. Let $\mathbf{x}(t)$ denote the nodal displacement of all nodes on all sectors. Their kinetic and potential energies can be written as $T = (1/2)\dot{\mathbf{x}}^T \boldsymbol{\mu}_1 \dot{\mathbf{x}}$ and $U = (1/2)\mathbf{x}^T \boldsymbol{\kappa}_1 \mathbf{x}$, where $\boldsymbol{\mu}_1$ and $\boldsymbol{\kappa}_1$ represent the collections of matrices

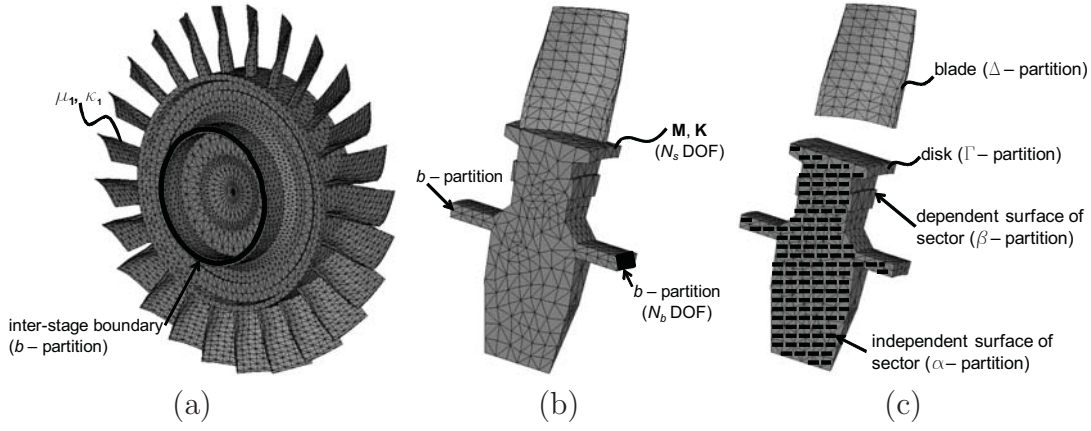


Fig. 74. (a) Cyclic stage with N sectors, (b) single sector of the cyclic stage, (c) blade and disk partitions of the sector model.

of the disconnected sectors, i.e.,

$$\begin{aligned}\boldsymbol{\mu}_1 &= \mathbf{I}_N \otimes \mathbf{M}, \\ \boldsymbol{\kappa}_1 &= \mathbf{I}_N \otimes \mathbf{K},\end{aligned}\tag{139}$$

where \mathbf{M} and \mathbf{K} denote the mass and the stiffness matrices of a sector, \mathbf{I}_N is an identity matrix of size $N \times N$, and \otimes denotes a Kronecker product. Partitioning the displacement vector such that they are ordered based on the order of the sectors, i.e., $\mathbf{x} = [\mathbf{x}_1^T, \dots, \mathbf{x}_N^T]^T$, it is known^{180,185} that the displacements of the n^{th} sector can be exactly described by the following Fourier series

$$\mathbf{x}_n = \frac{1}{\sqrt{N}} \mathbf{u}^0 + \sqrt{\frac{2}{N}} \sum_{h=1}^{\tilde{N}-1} (\mathbf{u}_c^h \cos(n-1)\phi_h + \mathbf{u}_s^h \sin(n-1)\phi_h) + \frac{1}{\sqrt{N}} (-1)^{n-1} \mathbf{u}^{\tilde{N}},\tag{140}$$

where $\phi_h = 2\pi h/N$, $n = 1, \dots, N$ and $\tilde{N} = N/2$ if N is even, or $\tilde{N} = (N-1)/2$ if N is odd. \mathbf{u} denotes a vector of Fourier coefficients, subscripts c and s denote cosine and sine components respectively, and superscripts denote the harmonic number. Also, the last term in Eq. (140) does not exist when N is odd. The transformation from the Fourier coefficients $\tilde{\mathbf{u}}$, to physical coordinates \mathbf{x} can be written as a linear map

$$\mathbf{x}(t) = (\mathbf{F}_{N,N} \otimes \mathbf{I}_{N_s}) \tilde{\mathbf{u}}(t),\tag{141}$$

where

$$\tilde{\mathbf{u}} = [(\mathbf{u}^0)^T, (\mathbf{u}_c^h)^T, (\mathbf{u}_s^h)^T, \dots, (\mathbf{u}^{\tilde{N}})^T]^T,\tag{142}$$

and N_s is the number of degrees of freedom (DOFs) in a sector. For the sake of brevity, let us now partition the nodal displacement vector for a sector, and corresponding Fourier coefficients based on the physical partitions of the finite element model (FEM). Namely, the Fourier coefficients are partitioned as $\mathbf{u}^h = [(\mathbf{u}_\Delta^h)^T, (\mathbf{u}_\Gamma^h)^T, (\mathbf{u}_b^h)^T]^T$, where Δ , Γ and b correspond to the DOF sets for the nodes of the blade part, disk part, and the inter-stage boundary as shown in Fig. 74(c). Substituting Eq. (142) into the kinetic and potential energies, the Lagrangian of this stage can be expressed with the Fourier coefficients as

$$\begin{aligned}L &= \frac{1}{2} \dot{\mathbf{x}}^T \boldsymbol{\mu}_1 \dot{\mathbf{x}} - \frac{1}{2} \mathbf{x}^T \boldsymbol{\kappa}_1 \mathbf{x} \\ &= \frac{1}{2} \dot{\tilde{\mathbf{u}}}^T (\mathbf{F}_{N,N} \otimes \mathbf{I}_{N_s})^T (\mathbf{I}_N \otimes \mathbf{M}) (\mathbf{F}_{N,N} \otimes \mathbf{I}_{N_s}) \dot{\tilde{\mathbf{u}}} - \frac{1}{2} \tilde{\mathbf{u}}^T (\mathbf{F}_{N,N} \otimes \mathbf{I}_{N_s})^T (\mathbf{I}_N \otimes \mathbf{K}) (\mathbf{F}_{N,N} \otimes \mathbf{I}_{N_s}) \tilde{\mathbf{u}}.\end{aligned}$$

Hamilton's principle requires the action integral be stationary, i.e.,

$$\delta \int_{t_1}^{t_2} L(\tilde{\mathbf{u}}, \dot{\tilde{\mathbf{u}}}) dt = 0. \quad (143)$$

Without any constraint between the (identical) sectors, this yields the following set of equations of motion

$$\begin{aligned} \mathbf{M}\ddot{\mathbf{u}}^0 + \mathbf{K}\mathbf{u}^0 &= \mathbf{0}, \\ \begin{pmatrix} \mathbf{M} & \mathbf{0} \\ \mathbf{0} & \mathbf{M} \end{pmatrix} \begin{bmatrix} \ddot{\mathbf{u}}_c^h \\ \ddot{\mathbf{u}}_s^h \end{bmatrix} + \begin{pmatrix} \mathbf{K} & \mathbf{0} \\ \mathbf{0} & \mathbf{K} \end{pmatrix} \begin{bmatrix} \mathbf{u}_c^h \\ \mathbf{u}_s^h \end{bmatrix} &= \begin{bmatrix} \mathbf{0} \\ \mathbf{0} \end{bmatrix}, \quad \text{for } h = 1, \dots, \tilde{N} - 1, \\ \mathbf{M}\ddot{\mathbf{u}}^{\tilde{N}} + \mathbf{K}\mathbf{u}^{\tilde{N}} &= \mathbf{0}. \end{aligned}$$

At this point, all the sectors are assumed to be disconnected. However, the symmetry in the circumferential direction implies that the nodal displacement field of one side of a sector is dependent on that of the other side of the sector. Furthermore, the constraints are dependent on the harmonic number. Namely, the equations of motion are derived by the extremization of the action integral in Eq. (143) subject to the constraints

$$\begin{aligned} \mathbf{u}_{c,\beta}^h &= \mathbf{u}_{c,\alpha}^h \cos \phi_h + \mathbf{u}_{s,\alpha}^h \sin \phi_h, \\ \mathbf{u}_{s,\beta}^h &= -\mathbf{u}_{c,\alpha}^h \sin \phi_h + \mathbf{u}_{s,\alpha}^h \cos \phi_h, \end{aligned} \quad (144)$$

where α represents the boundary considered to be independently moving (on one side of the boundary), β represents the boundary considered to be dependent on the movement of the α boundary (due to the constraints). After the application of Eq. (144) to Eq. (143), the equations of motion of the h^{th} harmonic number can be written in a partitioned format as

$$\left(\begin{array}{cc|c} \mathbf{M}_{i,0}^h & \mathbf{M}_{i,1}^h & \mathbf{M}_{ib}^h \\ \hline (\mathbf{M}_{i,1}^h)^T & \mathbf{M}_{i,0}^h & \\ \hline (\mathbf{M}_{ib}^h)^T & & \mathbf{M}_b^h \end{array} \right) \begin{bmatrix} \ddot{\mathbf{u}}_{c,i}^h \\ \ddot{\mathbf{u}}_{s,i}^h \\ \ddot{\mathbf{u}}_b^h \end{bmatrix} + \left(\begin{array}{cc|c} \mathbf{K}_{i,0}^h & \mathbf{K}_{i,1}^h & \mathbf{K}_{ib}^h \\ \hline (\mathbf{K}_{i,1}^h)^T & \mathbf{K}_{i,0}^h & \\ \hline (\mathbf{K}_{ib}^h)^T & & \mathbf{K}_b^h \end{array} \right) \begin{bmatrix} \mathbf{u}_{c,i}^h \\ \mathbf{u}_{s,i}^h \\ \mathbf{u}_b^h \end{bmatrix} = \mathbf{0}, \quad (145)$$

where

$$\begin{aligned} \mathbf{M}_{i,0}^h &= \begin{pmatrix} \mathbf{M}_{\alpha\alpha} + \cos \phi_h (\mathbf{M}_{\beta\alpha} + \mathbf{M}_{\alpha\beta}) + \mathbf{M}_{\beta\beta} & \mathbf{M}_{\alpha\Delta} + \cos \phi_h \mathbf{M}_{\beta\Delta} \\ \mathbf{M}_{\Delta\alpha} + \cos \phi_h \mathbf{M}_{\Delta\beta} & \mathbf{M}_{\Delta\Delta} \end{pmatrix}, \\ \mathbf{M}_{i,1}^h &= \begin{pmatrix} (\mathbf{M}_{\alpha\beta} - \mathbf{M}_{\beta\alpha}) \sin \phi_h & \sin \phi_h \mathbf{M}_{\beta b} \\ \sin \phi_h \mathbf{M}_{\Delta\beta} & \mathbf{0} \end{pmatrix}, \\ \mathbf{M}_{ib}^h &= \begin{pmatrix} \mathbf{M}_{\alpha b} + \cos \phi_h \mathbf{M}_{\beta b} & -\sin \phi_h \mathbf{M}_{\beta b} \\ \mathbf{M}_{\Delta b} & \mathbf{0} \\ \sin \phi_h \mathbf{M}_{\beta b} & \mathbf{M}_{\alpha b} + \cos \phi_h \mathbf{M}_{\beta b} \\ \mathbf{0} & \mathbf{M}_{\Delta b} \end{pmatrix}, \\ \mathbf{M}_b^h &= \begin{pmatrix} \mathbf{M}_{bb} & \mathbf{0} \\ \mathbf{0} & \mathbf{M}_{bb} \end{pmatrix}, \end{aligned}$$

and i denotes the set of internal DOF defined as $i \triangleq \{\alpha, \Delta, \Gamma\}$, and b denotes the set of DOF on the inter-stage boundary. The structure of the stiffness matrix is omitted here for the sake of brevity because it is the same as the one for the mass matrix.

Reduced Order Modeling of Cyclic Stages by the Craig-Bampton Method

For the reduction of the cyclic stages, the reduction method proposed by Song *et al.*¹⁸³ is employed. That method is based on the cyclic Craig-Bampton method developed by Bladh *et al.*⁶ Namely, the displacement field of the entire stage $\mathbf{x}(t)$ is assumed to be represented as a linear combination of fixed-interface normal modes and constraint modes. The model reduction method with these types of modes is usually referred to as the Craig-Bampton method.¹¹⁸ The fixed-interface normal modes are a truncated set of normal modes of the entire stage with all DOFs on the inter-stage boundary being fixed. A constraint mode for a stage is computed as the static deformation shape of the entire stage due to a unit displacement applied to one of its DOF on the inter-stage boundary (while all the other DOFs on the inter-stage boundary are fixed). A complete set of constraint modes is obtained by repeating such computation for all DOFs on the inter-stage boundary. One disadvantage of this method is that the computation of these constraint modes becomes prohibitively expensive as the model size grows. However, by the application of cyclic-symmetry, these modes can be efficiently computed by solving eigenvalue problems and static problems of a sector and a duplicated sector alone, with appropriate inter-sector boundary conditions. Recalling that the set of DOFs for the inter-stage boundary are denoted by a subscript b , and that all the other DOFs are denoted by a subscript i , the Fourier coefficients can be well approximated by the following coordinate transformation

$$\begin{bmatrix} \mathbf{u}_b^h \\ \mathbf{u}_i^h \end{bmatrix} \simeq \begin{pmatrix} \mathbf{I}_{N_b} & \mathbf{0} \\ \mathbf{\Psi}_i^h & \mathbf{\Phi}_i^h \end{pmatrix} \begin{bmatrix} \mathbf{u}_b^h \\ \mathbf{p}^h \end{bmatrix}, \quad \text{for } h = 0, \dots, \tilde{N}, \quad (146)$$

where N_b is the number of DOFs on the inter-stage boundary (the b -partition), the matrices $[\mathbf{I}_{N_b}, (\mathbf{\Psi}_i^h)^T]^T$ and $[\mathbf{0}, (\mathbf{\Phi}_i^h)^T]^T$ are called the constraint modes and the fixed-interface normal

modes for harmonic number h , and \mathbf{p}^h is the set of modal coordinates associated with the fixed-interface normal modes.

Assuming harmonic motion and substituting $\mathbf{u}(t) = \boldsymbol{\varphi}e^{\omega t}$ into Eq. (145), then the k^{th} fixed-interface normal mode for harmonic number h can be computed by solving the following eigenvalue problem

$$\begin{pmatrix} \mathbf{K}_{i,0}^h & \mathbf{K}_{i,1}^h \\ (\mathbf{K}_{i,1}^h)^\top & \mathbf{K}_{i,0}^h \end{pmatrix} \begin{bmatrix} (\boldsymbol{\varphi}_{c,i}^h) \\ (\boldsymbol{\varphi}_{s,i}^h) \end{bmatrix}_k = \lambda_k \begin{pmatrix} \mathbf{M}_{i,0}^h & \mathbf{M}_{i,1}^h \\ (\mathbf{M}_{i,1}^h)^\top & \mathbf{M}_{i,0}^h \end{pmatrix} \begin{bmatrix} (\boldsymbol{\varphi}_{c,i}^h) \\ (\boldsymbol{\varphi}_{s,i}^h) \end{bmatrix}_k, \quad \text{for } k = 1, \dots, m_1^h, \quad (147)$$

where $\lambda_k = \omega_k^2$, and m_1^h denotes the number of free-interface normal modes to be kept for stage 1.

In contrast, the i -partition of the constraint modes can be computed by solving the following static problem for $\boldsymbol{\Psi}_{c,i}^h$ and $\boldsymbol{\Psi}_{s,i}^h$

$$\left(\begin{array}{cc|c} \mathbf{K}_{i,0}^h & \mathbf{K}_{i,1}^h & \mathbf{K}_{ib}^h \\ (\mathbf{K}_{i,1}^h)^\top & \mathbf{K}_{i,0}^h & \\ \hline (\mathbf{K}_{ib}^h)^\top & & \mathbf{K}_b^h \end{array} \right) \begin{pmatrix} \boldsymbol{\Psi}_{c,i}^h \\ \boldsymbol{\Psi}_{s,i}^h \\ \mathbf{I}_{N_b} \end{pmatrix} = \begin{pmatrix} \mathbf{0} \\ \mathbf{0} \\ \mathbf{R}_b^h \end{pmatrix}, \quad (148)$$

where \mathbf{R}_b^h represents the forces applied to the inter-stage boundary, which cause a unit displacement at one DOF while keeping the rest of the DOFs along the boundary fixed, and N_b is the number of DOFs along the inter-stage boundary for the sector. Defining $\tilde{\mathbf{p}} \triangleq [(\mathbf{u}^0)^\top, (\mathbf{p}^0)^\top, \dots, (\mathbf{u}^{\tilde{N}})^\top, (\mathbf{p}^{\tilde{N}})^\top]^\top$, the linear transformation between the Fourier coefficients for all harmonic numbers $\tilde{\mathbf{u}}(t)$ and the generalized coordinates $\tilde{\mathbf{p}}(t)$ can be written as

$$\tilde{\mathbf{u}}(t) \simeq \boldsymbol{\Phi}_{CB} \tilde{\mathbf{p}}(t), \quad (149)$$

where

$$\boldsymbol{\Phi}_{CB} =_{h=0, \dots, \tilde{N}} \begin{pmatrix} \mathbf{I}_{N_b} & \mathbf{0} \\ \boldsymbol{\Psi}_i^h & \boldsymbol{\Phi}_i^h \end{pmatrix}, \quad (150)$$

and $_{h=0, \dots, \tilde{N}}(\cdot)$ designates a block-diagonal matrix with the arguments being the h^{th} block of a matrix. Combining the transformations from Eq. (141) and Eq. (149), the physical displacement of the entire cyclic stage can be approximated by $\tilde{\mathbf{p}}(t)$, i.e.,

$$\mathbf{x}(t) \simeq (\mathbf{F}_{N,N} \otimes \mathbf{I}_{N_s}) \boldsymbol{\Phi}_{CB} \tilde{\mathbf{p}}(t), \quad (151)$$

where the size of the vector $\tilde{\mathbf{p}}(t)$ is much less than that of $\mathbf{x}(t)$. It is noted that the motion of the inter-stage boundary is now represented as

$$\mathbf{x}_b(t) = (\mathbf{F}_{N,N} \otimes \mathbf{I}_{N_b}) \tilde{\mathbf{u}}_b(t). \quad (152)$$

11.2.2 Reduced Order Modeling of Non-Cyclic Stages

Let us assume that stage 2 consists of M sectors and does not possess cyclic-symmetry. Fig. 75 shows stage 2 where M equals 23. Furthermore, let us also assume that the dynamics of this

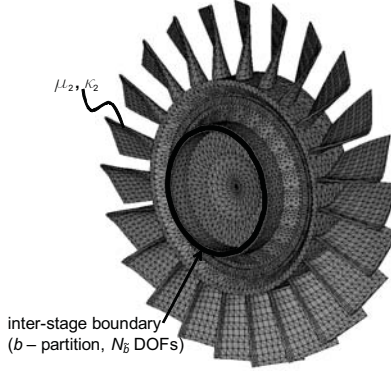


Fig. 75. Non-cyclic stage with M sectors.

stage cannot be projected onto the tuned system modes for this stage. Hence, the model may not be reduced by a method based on cyclic-symmetry as done in the previous section. In this paper, stage 2 is assumed to have a cracked blade which also induces a nonlinearity caused by the intermittent contact at the crack surfaces. Let all FE nodal displacements of stage 2 be denoted by $\mathbf{y}(t)$. The equation of motion can be written as

$$\boldsymbol{\mu}_2 \ddot{\mathbf{y}}(t) + \boldsymbol{\kappa}_2 \mathbf{y}(t) = \mathbf{f}(\mathbf{y}), \quad (153)$$

where $\boldsymbol{\mu}_2$ and $\boldsymbol{\kappa}_2$ denote mass and stiffness matrices, and \mathbf{f} denotes a vector of nonlinear forces due to the intermittent contact at the crack surfaces. The nodal displacement vector can be partitioned as

$$\mathbf{y}(t) = \begin{bmatrix} \mathbf{y}_b(t) \\ \mathbf{y}_i(t) \end{bmatrix}, \quad (154)$$

where \mathbf{y}_b contains all the displacements of the nodes on the inter-stage boundary, and \mathbf{y}_i contains the rest of the internal DOFs. There are various ways to reduce the number of DOFs in the i -partition. In this paper, the motion of \mathbf{y} is expressed as a linear combination of static constraint modes $\boldsymbol{\Psi}$ associated with the inter-stage boundary, and a set of modified free-interface normal modes $\hat{\boldsymbol{\Phi}}$ as was employed by Saito *et al.*¹⁹⁸ Namely,

$$\begin{bmatrix} \mathbf{y}_b(t) \\ \mathbf{y}_i(t) \end{bmatrix} \simeq \begin{pmatrix} \mathbf{I}_{N_b} & \mathbf{0} \\ \boldsymbol{\Psi}_i & \hat{\boldsymbol{\Phi}}_i \end{pmatrix} \begin{bmatrix} \mathbf{y}_b(t) \\ \mathbf{q}(t) \end{bmatrix}, \quad (155)$$

where N_b is the number of DOF along the inter-stage boundary for stage 2, $\hat{\boldsymbol{\Phi}}_i = \boldsymbol{\Phi}_{ii} - \boldsymbol{\Psi}_i \boldsymbol{\Phi}_{ib}$, with $\boldsymbol{\Phi}_{ii}$ and $\boldsymbol{\Phi}_{ib}$ denoting the interior and the inter-stage boundary partitions of $\boldsymbol{\Phi}$ respectively. Herting⁹⁹ provides a detailed formulation of this type of CMS.

11.2.3 Inter-Stage Coupling

After constructing the ROMs of all cyclic and all non-cyclic stages, the next step is to assemble the stages, which means that the geometric compatibility conditions should be applied to the inter-stage boundary nodes. However, the FE meshes of all stages do not necessarily match at the inter-stage interfaces. Most importantly, the stages do not necessarily have the same number of sectors, which means that the stages do not possess the same periodicity.

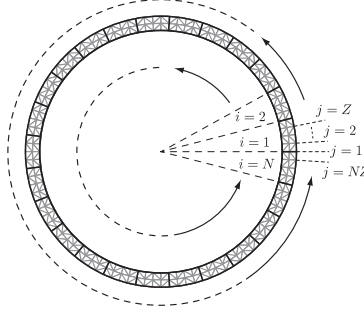


Fig. 76. Inter-stage boundary (b -partition) for a cyclic stage (i denotes a sector, j denotes a radial line segment).

In this paper, the method proposed by Song *et al.*¹⁸³ is extended for the case with coupling between cyclic and non-cyclic stages. Namely, the motion of the inter-stage nodes are projected onto harmonic functions that are periodic in the circumferential direction. For the cyclic stage, let us first partition the displacement vector for the inter-stage boundary DOF as follows

$$\mathbf{x}_b = \begin{bmatrix} \mathbf{x}_{b_1} \\ \vdots \\ \mathbf{x}_{b_N} \end{bmatrix}, \quad (156)$$

where \mathbf{x}_{b_i} corresponds to the inter-stage boundary partition of the nodal displacements of the i^{th} sector. We also assume that the FE nodes of the inter-stage boundary of each sector are aligned such that the nodes can be divided into another kind of groups of nodes having the same angle in a cylindrical coordinate system. The number of such groups in each sector is denoted here as Z , and each group is referred to as a radial line segment in this paper. This means that the inter-stage boundary of stage 1 consists of NZ radial line segments. Each radial line segment for stage 1 is considered to have N_r DOF, and each radial line segment for stage 2 is considered to have M_r DOF. The schematic depicting the inter-stage boundary and the radial line segments is illustrated in Fig. 76. Namely, \mathbf{x}_b can also be partitioned as

$$\mathbf{x}_b = \begin{bmatrix} \mathbf{x}_{r_1} \\ \vdots \\ \mathbf{x}_{r_{NZ}} \end{bmatrix}, \quad (157)$$

where the subscript r stands for the radial line segment. Note that there is a relationship between \mathbf{x}_{b_i} and \mathbf{x}_{r_j} such that \mathbf{x}_{b_i} contains \mathbf{x}_{r_j} for $1 + (i - 1)Z \leq j \leq iZ$.

Next, we assume that the motion of the j^{th} radial segment can be *approximated* by a truncated Fourier series. Namely, defining $\theta_h \triangleq 2\pi h/(NZ)$,

$$\mathbf{x}_{r_j} \simeq \frac{1}{\sqrt{B}} \mathbf{z}^0 + \sqrt{\frac{2}{B}} \sum_{h=1}^{P-1} (\mathbf{z}_c^h \cos(j-1)\theta_h + \mathbf{z}_s^h \sin(j-1)\theta_h) + \frac{1}{\sqrt{B}} (-1)^{j-1} \mathbf{z}^P, \quad (158)$$

where \mathbf{z} represents the Fourier coefficients with superscript denoting the harmonic number and subscript denoting either cosine or sine term, and B is the number of basis harmonic functions used for the Fourier expansion. Note that $P = B/2$ if B is even. If B is odd,

$P = (B - 1)/2$ and the last term in Eq. (158) does not exist. Therefore, in matrix form,

$$\mathbf{x}_b = \begin{bmatrix} \mathbf{x}_{r_1} \\ \vdots \\ \mathbf{x}_{r_{NZ}} \end{bmatrix} \simeq (\mathbf{F}_{NZ,B} \otimes \mathbf{I}_{N_r}) \tilde{\mathbf{z}}, \quad (159)$$

where recall that N_r is the number of DOF per radial line segment for stage 1, $\mathbf{F}_{NZ,B}$ is a $NZ \times B$ Fourier matrix, and $\tilde{\mathbf{z}} = [(\mathbf{z}^0)^\top, (\mathbf{z}_c^h)^\top, (\mathbf{z}_s^h)^\top, \dots, (\mathbf{z}^P)^\top]^\top$. Inverting Eq. (152) and combining it with Eq. (159),

$$\tilde{\mathbf{u}}_b(t) \simeq (\mathbf{F}_{N,N} \otimes \mathbf{I}_{N_b})^\top (\mathbf{F}_{NZ,B} \otimes \mathbf{I}_{N_r}) \tilde{\mathbf{z}}. \quad (160)$$

For the non-cyclic stage (stage 2), the displacement vector of the inter-stage boundary \mathbf{y}_b can be partitioned as

$$\mathbf{y}_b = \begin{bmatrix} \mathbf{y}_{b_1} \\ \vdots \\ \mathbf{y}_{b_M} \end{bmatrix}. \quad (161)$$

Furthermore, as was done for the cyclic stage (stage 1), \mathbf{y}_{b_i} can also be partitioned based on the radial line segments, i.e.,

$$\mathbf{y}_{b_i} = \begin{bmatrix} \mathbf{y}_{r_1} \\ \vdots \\ \mathbf{y}_{r_W} \end{bmatrix}, \quad (162)$$

where W is the number of radial line segments per sector. Next, the motion of the inter-stage boundary is represented by a truncated Fourier series assuming that the number of basis harmonic functions is the same as the one used for the cyclic stage. Namely,

$$\mathbf{y}_b = \begin{bmatrix} \mathbf{y}_{r_1} \\ \vdots \\ \mathbf{y}_{r_{MW}} \end{bmatrix} \simeq (\mathbf{F}_{MW,B} \otimes \mathbf{I}_{M_r}) \tilde{\mathbf{w}}, \quad (163)$$

where $\tilde{\mathbf{w}}$ is a vector of Fourier coefficients, i.e., $\tilde{\mathbf{w}} = [(\mathbf{w}^0)^\top, (\mathbf{w}_c^h)^\top, (\mathbf{w}_s^h)^\top, \dots, (\mathbf{w}^P)^\top]^\top$. Recall that M_r is the number of DOF per radial line segment for stage 2. In this paper, it is assumed that $N_r = M_r$.

At this point, the displacement of the inter-stage boundary of the cyclic and non-cyclic stages are represented by vectors of Fourier coefficients $\tilde{\mathbf{z}}$ and $\tilde{\mathbf{w}}$. The geometric compatibility condition is now enforced as

$$\tilde{\mathbf{z}} = \tilde{\mathbf{w}}. \quad (164)$$

Even though the compatibility conditions are enforced approximately, as long as a sufficient number of Fourier coefficients B are used, the geometric compatibility conditions are very well imposed.¹⁸⁰

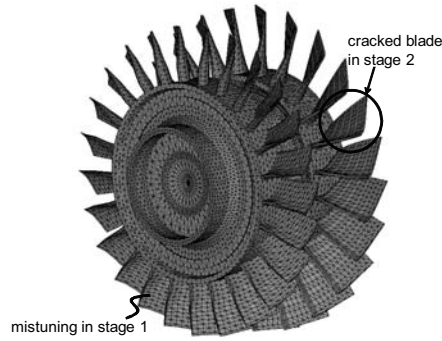


Fig. 77. FEM of multi-stage turbomachinery rotor.

11.3 Analysis

Two ROMs were developed using the methodology presented in the *Mathematical Formulation* section and are numerically validated in this section. Both ROMs were developed only from FEMs of single stage models created in ANSYS. To validate the ROMs, two full-order multi-stage FEMs were also created in ANSYS. These two multi-stage systems differ only in stage 2. A full-order multi-stage FEM of one of the two multi-stage systems is shown in Fig. 77.

Stage 1 of both full-order multi-stage FEMs has 25 identical blades and 63,996 DOFs. Stage 1 also has blade-to-blade small mistuning (in the blade stiffness) with standard deviation of 0.04%. Stage 2 of one of the full-order multi-stage FEM has 23 identical blades and 74,886 DOFs. Stage 2 of the other full-order multi-stage FEM has 23 identical blades (one of which has a cracked blade), and has 76,404 DOFs. The crack occurs at the leading edge of one of the blades and has a length of about one third of the chord.

To create the multi-stage FEMs, multi-point constraint equations were applied at the inter-stage boundaries to connect the individual stages in ANSYS. The total number of DOFs for the FEM of the multi-stage system with a crack is 138,006. The corresponding ROM for the system with a crack contains 705 DOFs (0.5% of the original FE size). The total number of DOFs for the multi-stage system without a crack is 136,488. The corresponding ROM for the system without a crack is 592 DOFs (0.4% of the original FE size). Each ROM uses 23 basis functions to model the dynamics at the interface between stages (as discussed in the *Inter-Stage Coupling* section).

The ROMs were developed to be valid over a frequency range of 0 – 20 kHz. The bulk of the results below are focused on a narrower frequency range of 0 – 5 kHz, where multi-stage modes and crack effects interact. In this work, multi-stage modes refer to modes that are not dominated by motion in a single stage, rather both stages respond at these frequencies. Note that the effects which multi-stage phenomena have on the dynamics in the presence of cracks are of particular interest since this topic has not yet been explored. Also, in this work nonlinear forced response results were computed for the ROMs using a hybrid frequency/time domain method, which prevents inter-penetration at the crack surfaces using a penalty coefficient as done by Saito *et al.*¹⁹⁸

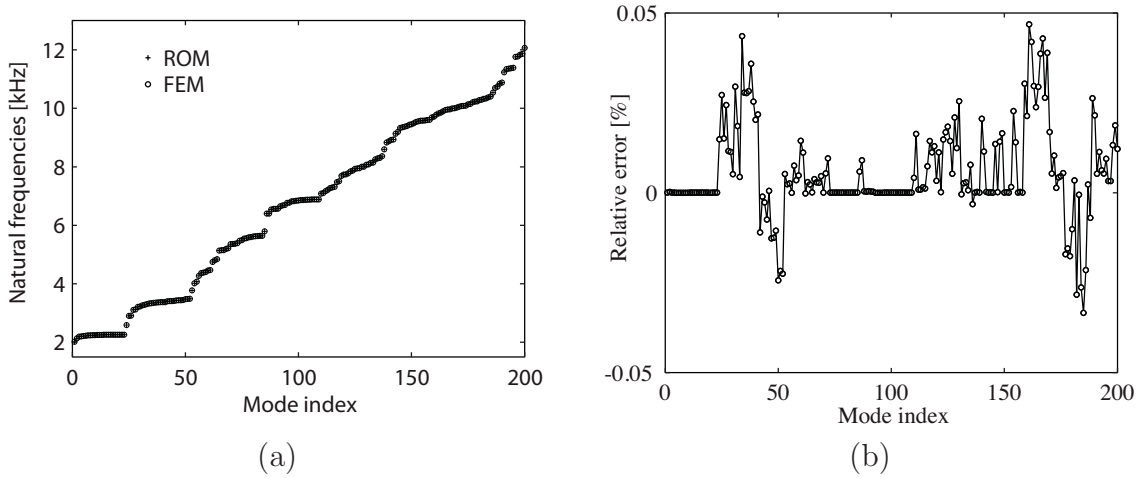


Fig. 78. (a) Natural frequencies of the ROM (+) and the FEM (o). (b) Relative error in the natural frequencies between the FEM and the ROM.

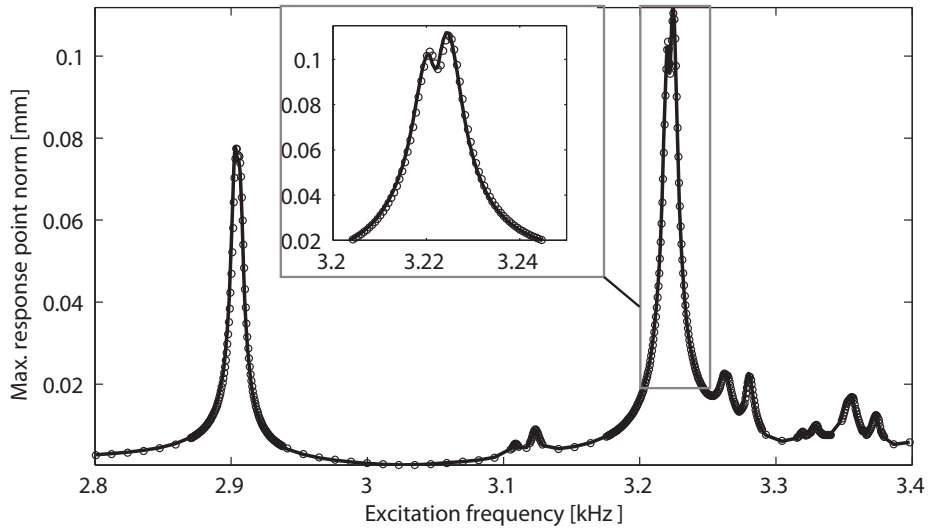
11.3.1 Model Validation

This section demonstrates the accuracy of the ROMs with respect to the full FEMs. To show the accuracy in the frequencies of the ROM of the system with a crack, the first 200 frequencies of the ROM and the FEM are plotted in Fig. 78(a). The corresponding relative error in these frequency estimates is less than 0.05% for all 200 frequencies, and is shown in Fig. 78(b). These frequencies are computed under the assumption that the crack is always open so that a linear analysis (allowing inter-penetration of the crack surfaces) can be carried out using the full FEM. Note that fully nonlinear forced response results have also been obtained and are discussed in the next section.

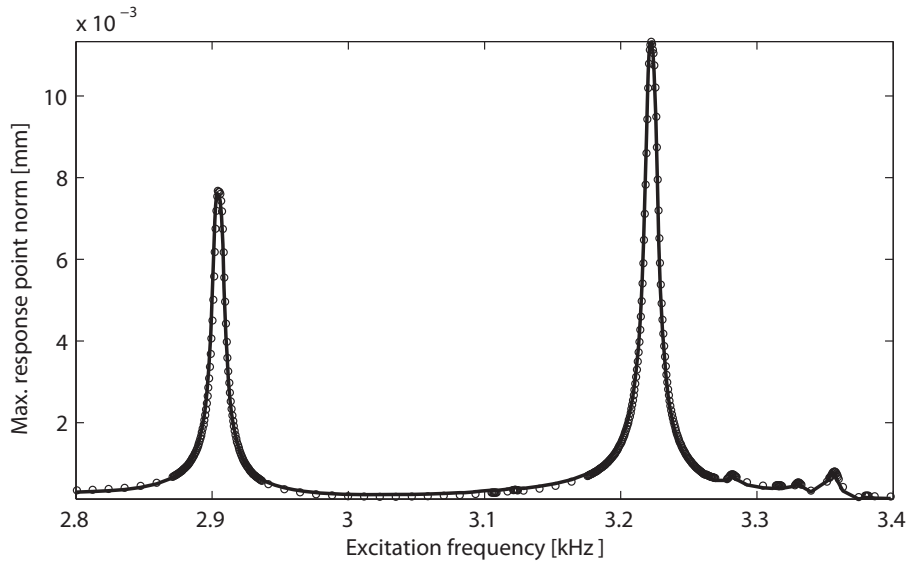
To show the overall accuracy of the ROMs, linear forced response analyses were conducted on the FEMs and ROMs. A proportional damping $\mathbf{C} = \alpha\mathbf{M} + \beta\mathbf{K}$ was applied to the system. Here, \mathbf{C} is the damping matrix with $\alpha = 1.9295 \times 10^{-2}$ and $\beta = 5.1340 \times 10^{-5}$. Engine order 1 excitation was applied to nodes at the blade tips of each stage. Since the multi-stage modes were of particular interest, forced responses were calculated at 1,024 evenly sampled frequencies from 2.8 kHz to 3.4 kHz. The response of the excited nodes were calculated for the FEMs and the ROMs. The maximum response norm of all the excited nodes for each stage was then calculated and the results are summarized in Figs. 79 and 80. Fig. 79(a) shows the forced response for stage 1 and Fig. 79(b) shows the forced response for stage 2 for the FEM and ROM for the system without a crack. These plots show the accuracy of the ROM with the largest relative error at the peaks being approximately 1% for both stage 1 and stage 2. Similarly, Fig. 80(a) shows the forced response of stage 1 and Fig. 80(b) shows the forced response of stage 2 for the FEM and ROM of the system with a crack. Again, the ROM performs well with a relative error at the peaks of less than 1% for both stage 1 and stage 2.

11.3.2 Multi-stage Nonlinear Forced Response Analysis

This section explores the interaction of multi-stage and crack effects. Fig. 81 displays the multi-stage forced response results for three different cases. The first case is a forced response



(a)

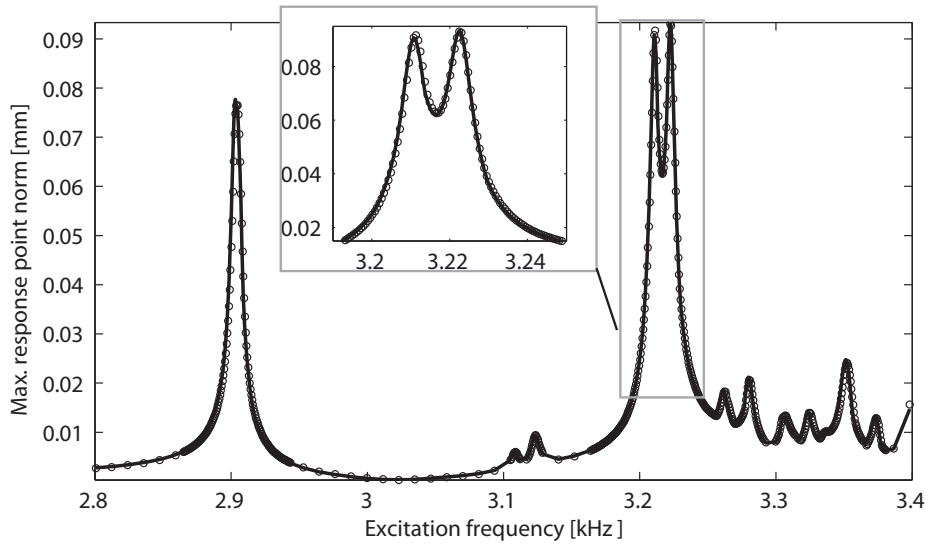


(b)

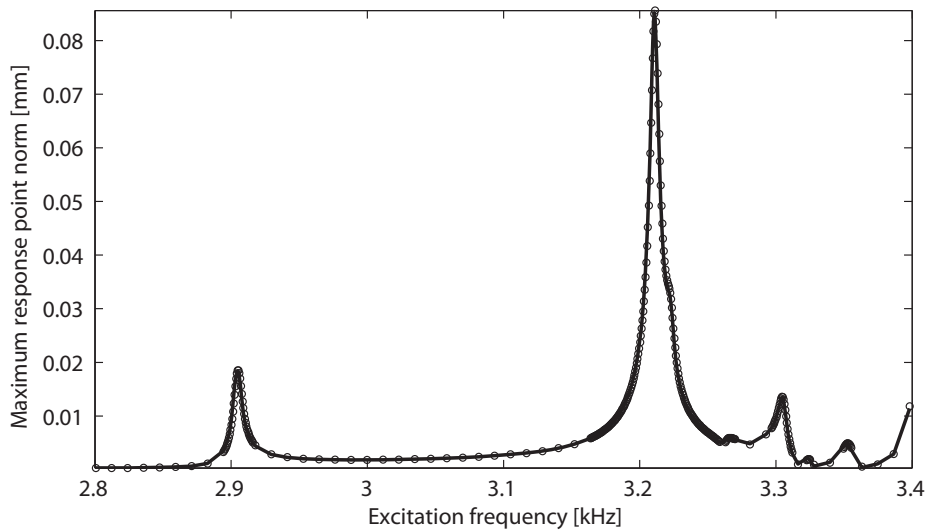
Fig. 79. Comparison of the multi-stage forced response for the FEM (-) and the ROM (o) of the system without a crack for (a) stage 1 and (b) stage 2.

analysis for the ROM of the system without a crack. The second case corresponds to a forced response analysis using a ROM of a system with a crack and a linear analysis (allowing inter-penetration). The final case corresponds to a forced response using a ROM of a system with a crack and a nonlinear analysis (not allowing inter-penetration at the crack surfaces as done by Saito *et al.*¹⁹⁸). The results for stage 1 are shown in Fig. 81(a) and the results for stage 2 are shown in Fig. 81(b).

The differences between the responses for stage 1 are not nearly as large as the differences for stage 2, since the crack is located in stage 2. For stage 1, the largest response for the peak near 3.2 kHz is predicted by the nonlinear forced response analysis. This response is only about 5% larger than the response of the system without a crack and 25% larger than the linear forced response.



(a)

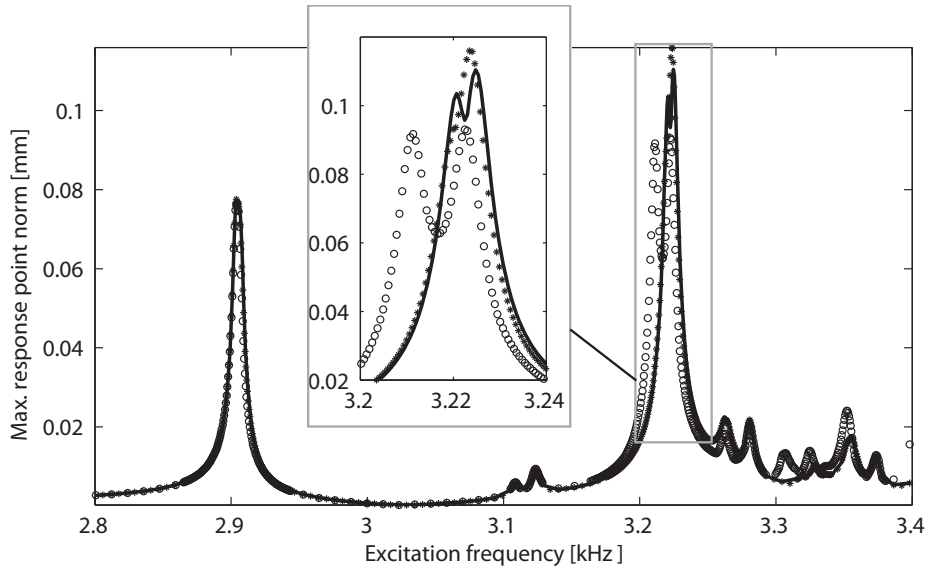


(b)

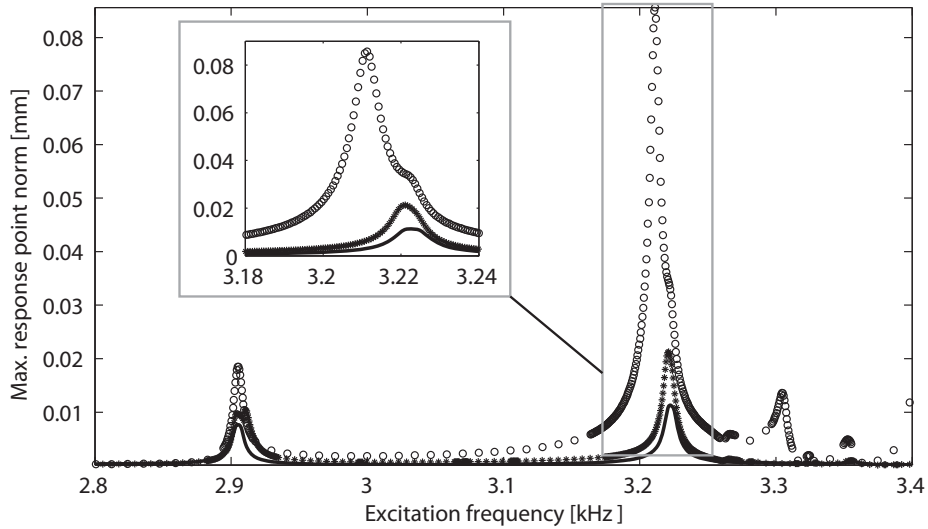
Fig. 80. Comparison of the multi-stage forced response for the FEM (-) and the ROM (o) of the system with a crack for (a) stage 1 and (b) stage 2.

For stage 2, the structural response is as expected for all three cases. The system without a crack is the stiffest and has the lowest amplitude. The linear forced response for the system with a crack is the softest and has the largest amplitude. In fact, the peak response near 3.2 kHz is almost eight times that of the system without a crack. The nonlinear forced response amplitude for the system with a crack is between the other two cases. However, the range of amplitudes between the two cases is very large. Hence, performing the nonlinear analysis is very important in obtaining an accurate response for the stage with a crack. For the peak response near 3.2 kHz, the nonlinear analysis yields a response of just 25% of that obtained using a linear analysis, but double that of the system with no crack.

A plot of the mode shape corresponding to the natural frequency at 3.21 kHz for the FEM of the multi-stage system with a crack is shown in Fig. 82 to better understand the results



(a)



(b)

Fig. 81. Comparison of the multi-stage forced response for the ROM of the system without a crack (-), for the ROM of the system with a crack using a linear analysis (o), and for a ROM of the system with a crack using a nonlinear analysis (*) for (a) stage 1 and (b) stage 2.

in Fig. 81. Fig. 82 shows that the motion in stage 1 is distributed throughout the stage, which explains why the response of stage 1 is not greatly affected by the crack in stage 2. In contrast, the motion of stage 2 is localized to the cracked blade; therefore a full nonlinear analysis is critical in accurately capturing the response of the cracked blade.

To show the importance of the multi-stage modeling, a single-stage analysis was conducted on stage 2 (with both of its inter-stage surfaces being fixed). The results are summarized in Fig. 83. The forced response was computed for 4,092 evenly spaced frequencies in the range 1.5–4.5 kHz. This larger range was chosen since the response is very low. That is because the modes in the range 2.8 – 3.4 kHz are multi-stage modes and are not present when a single-stage analysis is performed. The low level response in the range 2.8 – 3.4 kHz demonstrates

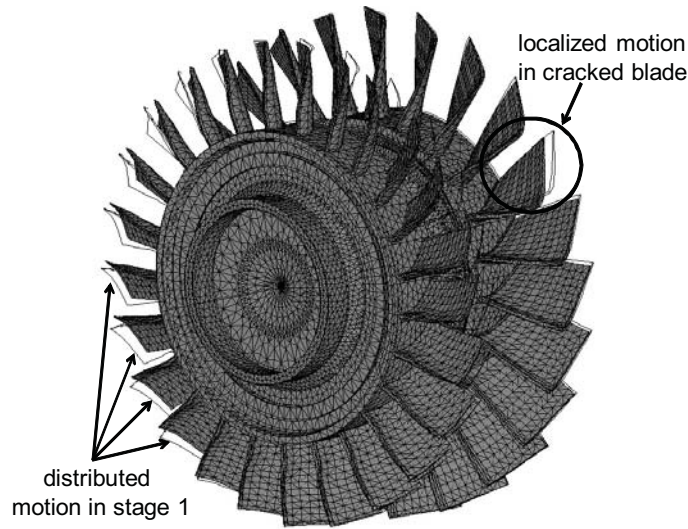


Fig. 82. Mode shape corresponding to a frequency of approximately 3.21 kHz from the FEM of the multi-stage system with a crack.

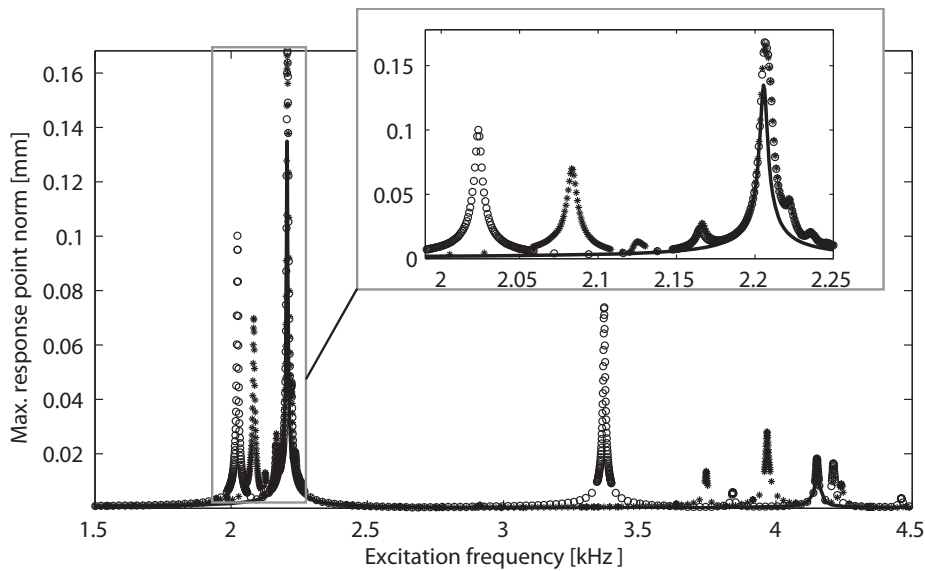


Fig. 83. Comparison of the forced response for stage 2 only for the ROM of a stage that does not have a crack (-), for the ROM of the stage with a crack using a linear analysis (o), and for a ROM of the same stage with a crack using a nonlinear analysis (*).

the need for multi-stage modeling for accurately capturing the dynamics. Three cases are plotted (nonlinear forced response of the stage with a crack, linear forced response of the stage with a crack, and the response of the same stage when it does not have a crack). The behavior is similar to the results in Fig. 81 in that the nonlinear forced response is bounded by the linear forced response and the response of the system without a crack.

A single-stage analysis was also conducted on stage 1 to show the importance of multi-stage modeling. The results are summarized in Fig. 84. Three cases are plotted. The first corresponds to the response of just stage 1 (with both of its inter-stage surfaces being fixed). The next two cases correspond to the response of stage 1 when a full multi-stage analysis is conducted. One of these latter two cases corresponds to the system where there is no crack in stage 2, and the other when there is a crack in stage 2 (and a nonlinear analysis is

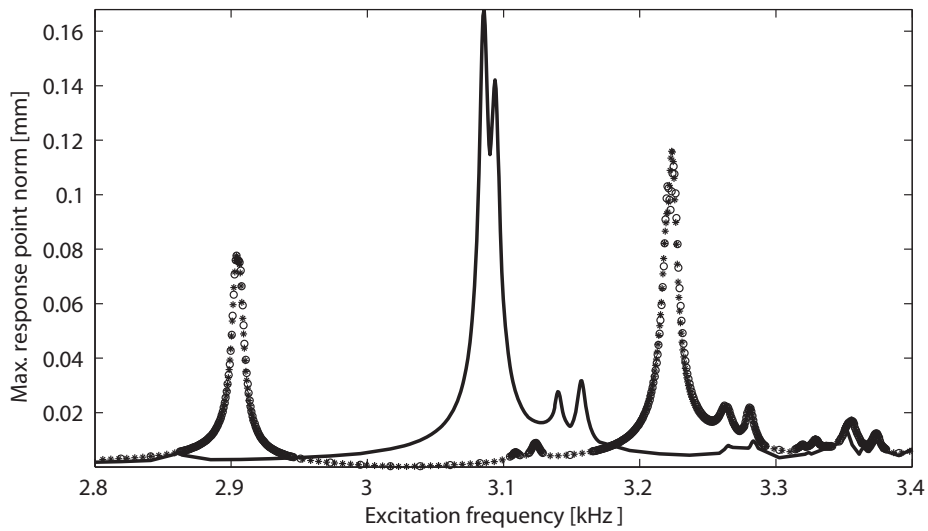


Fig. 84. Effect of multi-stage versus stage-wise only analysis. Stage 1 only forced response (-), multi-stage results for a system without a crack (o), and nonlinear forced response for the multi-stage system with a crack (*).

conducted). It is evident that for stage 1 the effect of single versus multi-stage modeling is very important. However, the effect of modeling the crack (in stage 2) is not that important for stage 1 (although it is important for predicting the response of stage 2).

**12 A STATISTICAL CHARACTERIZATION OF THE EFFECTS OF MIS-
TUNING IN MULTI-STAGE BLADED DISKS**

A significant amount of research has been conducted on the vibration response of bladed disks. An extensive review of this research was conducted by Castanier and Pierre.¹⁸¹ Early work in the area of vibration of bladed disks focused on simple lumped parameter models of single stage bladed disks.^{2-4,200,201} These models were developed in part to understand the effects of mistuning. Mistuning is a random variation in the structural properties of a system, which can be caused by manufacturing tolerances and/or operational wear. Even small levels of mistuning can lead to a localization in the vibration energy to a few blades in the disk, and this localization can lead to a dramatic increase in the amplitude of the force response of these blades. While these simple lumped parameter models were useful in providing a qualitative understanding of certain features of the system such as mistuning, more accurate finite element models (FEMs) of the system were needed to obtain quantitative results. Due to the size of these FEMs, reduced order models (ROMs) of the system were constructed to conduct statistical analyses on these systems.

Early ROMs used component mode synthesis^{118,202} (CMS), which breaks the systems into components for faster analysis, and combines them at the interface using a fixed-interface, free-interface or hybrid method. Early work using free-interface CMS²⁰³ was conducted by Irretier²⁰⁴ and Zheng and Wang²⁰⁵ who found significant savings in computational time relative to the parent FEMs. Eventually, powerful ROMs were developed that have a size of the order of the number of blades in the system yet retain high accuracy over a given frequency range. Yang and Griffin¹⁰ had the first such approach called the subset of nominal modes method. This method used the fact, that when the mistuning is small, the tuned system modes provide an excellent basis for the vibration of the mistuned system. Later, Lim et al.¹⁸⁵ introduced a method called component mode mistuning (CMM), which uses both tuned system modes and blade component modes to construct ROMs. This method handles various types of mistuning in a systematic manner by modeling the mistuning in the blade alone using cantilevered blade modes.

While a great deal of research has been done on the vibration response of single stage bladed disks, far less has been done on multi-stage bladed disk systems. Sinha¹⁹⁰ conducted Monte Carlo simulations on a lumped parameter model of mistuned multi-stage systems to simulate the overall dynamics of multi-stage systems, but did not discuss its applicability to multi-stage systems with realistic geometry for industrial models. An investigation of FEMs of multi-stage bladed disks with blade mistuning was conducted by Bladh et al.¹⁸² It was shown that multi-stage effects due to the inter-stage coupling can occur when the frequency range of interest pass *veering regions*, where the motion of the disk is dominant. Additionally, it was pointed out that, when each stage has a different number of blades, mistuning is inherent in multi-stage systems due to the inter-stage coupling. Song et al.¹⁸³ created a novel reduced order modeling technique for multi-stage systems, and then united it with CMM to efficiently handle mistuning in multi-stage systems.¹⁸⁴ The approach was also used for parameter identification in multi-stage systems¹⁸⁶ and its applicability to structural health monitoring was explored.¹⁸⁰ Laxalde et al.^{187,188} proposed a method similar in concept to Song,¹⁸⁰ and applied the method for modal analysis and forced response calculations for multi-stage industrial bladed disks. Additionally, there has been recent work on multi-stage effects induced by modeling the coupling between flexible shafts and rotors.¹⁹¹⁻¹⁹⁵

In this work new characteristics of multi-stage systems are explored. In particular, a statistical characterization of structural mistuning in multi-stage bladed disks is carried out. The

results were obtained using CMM¹⁸⁵ combined with a new multi-stage modeling approach developed by D’Souza et al.,²⁰⁶ which is based on Song et al.,¹⁸³ however, it only requires the use of full single stage models (i.e. the multi-stage model is constructed in the reduced order space only). In addition to the statistical characterization, a new efficient classification method is detailed for characterizing modes of multi-stage bladed disk systems. Additionally, the effects of structural mistuning on the characterization of the modes is explored.

12.1 Methodology

In this section the modeling methodology is briefly reviewed, and a new classification method is described. The challenge associated with modeling multi-stage systems is caused by the fact that even if each stage is cyclically symmetric the entire multi-stage system is not (when the number of sectors in each stage is different). Song¹⁸⁰ successfully overcame this challenge by projecting the motion of the interface onto a set of Fourier basis functions and then enforcing compatibility. The major drawback associated with his formulation was that full multi-stage modes were needed when including small blade to blade mistuning. That requires the explicit formulation and analysis of the full order FEM. Recently, D’Souza et al.²⁰⁶ proposed a new method to tackle multi-stage systems that can handle a combination of cyclic stages (this includes stages with small mistuning modeled with CMM) and non-cyclic stages (stages including cracks, large mistuning, etc.) by performing only analyses on individual stages (thus completely eliminating the need to form and analyze the full order FEM). This work closely follows the methodology presented in D’Souza et al.,²⁰⁶ but here all the stages are considered to have only mistuning. The following contains a brief review of the method presented in D’Souza et al.²⁰⁶ and Song.¹⁸⁰ Next, a new classification scheme for modes of a multi-stage system is presented.

12.1.1 Multi-Stage ROMs from Cyclic Stages

A significant benefit of dealing with cyclic stages is that the analysis can be performed on sectors (and double sectors) instead of the full stage model, thus greatly reducing the computational cost. Let $\mathbf{x}(t)$ be the nodal displacement on all nodes of all sectors of one stage. $\mathbf{x}(t)$ can be partitioned such that it is ordered based on sectors, i.e. $\mathbf{x} = [\mathbf{x}_1^T, \dots, \mathbf{x}_N^T]^T$, where N is the number of sectors in the stage. The motion of the n^{th} sector can be described by the following Fourier series³⁶

$$\begin{aligned} \mathbf{x}_n = & \frac{1}{\sqrt{N}} \mathbf{u}^0 + \sqrt{\frac{2}{N}} \sum_{h=1}^{\tilde{N}-1} (\mathbf{u}_c^h \cos(n-1)\phi_h + \mathbf{u}_s^h \sin(n-1)\phi_h) \\ & + \frac{1}{\sqrt{N}} (-1)^{n-1} \mathbf{u}^{\tilde{N}}, \end{aligned} \quad (165)$$

where \mathbf{u} denotes a vector of Fourier coefficients with subscripts c and s denoting cosine and sine components, $\phi_h = 2\pi h/N$, and $\tilde{N} = N/2$ if N is even or $\tilde{N} = (N-1)/2$ if N is odd. Note that the last term in Eq. (165) does not exist if N is odd. Grouping the Fourier coefficients in matrix form $\tilde{\mathbf{u}} = [(\mathbf{u}^0)^T, (\mathbf{u}_c^h)^T, (\mathbf{u}_s^h)^T, \dots, (\mathbf{u}^{\tilde{N}})^T]^T$, the physical coordinates can be related

by the following linear map

$$\mathbf{x}(t) = (\mathbf{F}_{N,N} \otimes \mathbf{I}_{N_s}) \tilde{\mathbf{u}}(t), \quad (166)$$

where N_s is the number of degrees of freedom (DOFs) in a sector and $\mathbf{F}_{N,N}$ is an $N \times N$ Fourier matrix.

A cyclic Craig-Bampton method developed by Bladh et al.⁶ can be applied to the displacement field to obtain

$$\tilde{\mathbf{u}}(t) \simeq \Phi_{CB} \tilde{\mathbf{p}}(t), \quad (167)$$

where $\Phi_{CB} = \text{bdiag}_{h=0, \dots, \tilde{N}} \begin{pmatrix} \mathbf{I}_{N_b} & \mathbf{0} \\ \Psi_i^h & \Phi_i^h \end{pmatrix}$, with $\text{bdiag}(\cdot)$ designating a block-diagonal matrix with the argument being the h^{th} block of the overall block-diagonal matrix. The matrix $[\mathbf{I}_{N_b}^T, (\Psi_i^h)^T]^T$ contains the constraint modes for the h^{th} harmonic, b indicates the inter-stage boundary, i denotes the interior of the stage, and N_b is the number of DOF along the inter-stage boundary of a single sector. A constraint mode for a stage is computed as the static deformation of the interior of the stage when a unit displacement is applied to one DOF along the boundary (and the rest of the boundary DOFs are fixed). The matrix Φ_i^h is a truncated set of fixed-interface normal modes of the entire stage with all the boundary DOFs fixed. Finally, $\tilde{\mathbf{p}}(t)$ is the generalized reduced coordinates, where the size of $\tilde{\mathbf{p}}(t)$ is much less than that of $\tilde{\mathbf{u}}(t)$. Combining Eq. (166) and Eq. (167) yields

$$\mathbf{x}(t) \simeq (\mathbf{F}_{N,N} \otimes \mathbf{I}_{N_s}) \Phi_{CB} \tilde{\mathbf{p}}(t). \quad (168)$$

It can be noted that the motion along the inter-stage boundary is

$$\mathbf{x}_b(t) = (\mathbf{F}_{N,N} \otimes \mathbf{I}_{N_b}) \tilde{\mathbf{u}}_b(t). \quad (169)$$

After creating a ROM for each stage, the ROMs must be coupled. Consider the case where two stages are being coupled with the first having N_1 sectors and the second having N_2 sectors. The inter-stage boundary DOF can then be partitioned as $\mathbf{x}_{b_j} = [\mathbf{x}_{b_{j1}}^T, \dots, \mathbf{x}_{b_{jN}}^T]^T$, where j denotes the stage (i.e. $j = 1$ or 2). It is assumed that groups of nodes are aligned so that they have the same angle in a cylindrical coordinate system aligned with the axis of the multi-stage system. These groups of nodes are referred to as radial line segments, and Z_j of them exist in each sector of the j^{th} stage. Therefore, stage 1 has $N_1 Z_1$ radial line segments, and stage 2 has $N_2 Z_2$ radial line segments. The number of DOFs per radial line segment is given by N_{rj} . Figure 85 is a schematic of the radial line segments along the inter-stage boundary. Note that \mathbf{x}_{b_j} can be partitioned as

$$\mathbf{x}_{b_j} = \begin{bmatrix} \mathbf{x}_{r_{j1}} \\ \vdots \\ \mathbf{x}_{r_{j(N_j Z_j)}} \end{bmatrix}, \quad (170)$$

where subscript r stands for the radial line segment and $\mathbf{x}_{b_{ji}}$ contains $\mathbf{x}_{r_{jk}}$ for $1 + (i-1)Z_j \leq k \leq iZ_j$.

Next, the motion of the k^{th} radial line segment is approximated by the following truncated Fourier series

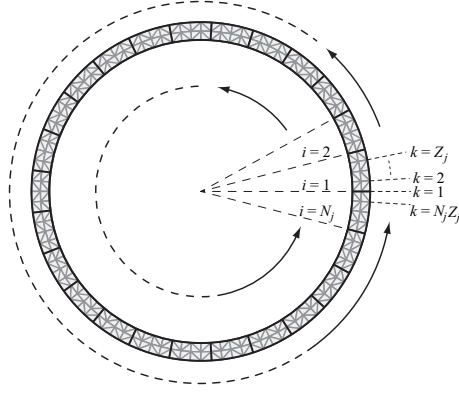


Fig. 85. INTER-STAGE BOUNDARY (*b*-PARTITION) FOR A CYCLIC STAGE (*i* DENOTES A SECTOR, *k* DENOTES A RADIAL LINE SEGMENT).

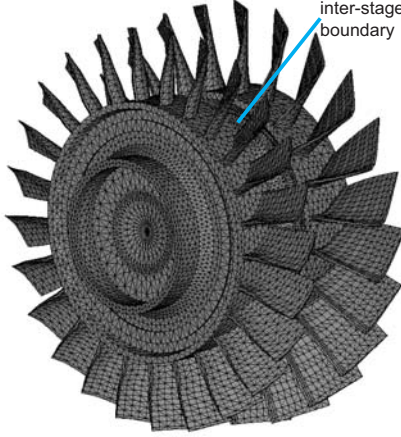


Fig. 86. MULTI-STAGE TURBOMACHINERY ROTOR.

$$\begin{aligned} \mathbf{x}_{r_{jk}} \simeq & \frac{1}{\sqrt{B}} \mathbf{z}_j^0 + \sqrt{\frac{2}{B}} \sum_{h=1}^{P-1} (\mathbf{z}_{jc}^h \cos(k-1)\theta_{h_j} + \mathbf{z}_{js}^h \sin(k-1)\theta_{h_j}) \\ & + \frac{1}{\sqrt{B}} (-1)^{k-1} \mathbf{z}_j^P, \end{aligned} \quad (171)$$

where $\theta_{h_j} \triangleq 2\pi h / (N_j Z_j)$, \mathbf{z} represents the Fourier coefficients with superscript denoting the harmonic number, and subscripts *c* and *s* corresponding to a cosine or sine term, and *B* is the number of basis functions used for the Fourier expansion. Note that if *B* is even $P = B/2$, while if *B* is odd $P = (B - 1)/2$ and the last term in Eq. (171) does not exist. Combining Eq. (170) and Eq. (171) in matrix form gives

$$\mathbf{x}_{b_j} = \begin{bmatrix} \mathbf{x}_{r_{j1}} \\ \vdots \\ \mathbf{x}_{r_{jN_j Z_j}} \end{bmatrix} \simeq (\mathbf{F}_{N_j Z_j, B} \otimes \mathbf{I}_{N_{r_j}}) \tilde{\mathbf{z}}_j, \quad (172)$$

where $\mathbf{F}_{N_j Z_j, B}$ is a $N_j Z_j \times B$ Fourier matrix, and $\tilde{\mathbf{z}}_j = [(\mathbf{z}_j^0)^T, (\mathbf{z}_{jc}^h)^T, (\mathbf{z}_{js}^h)^T, \dots, (\mathbf{z}_j^P)^T]^T$. Inverting Eq. (169) and combining it with Eq. (172) yields

$$\tilde{\mathbf{u}}_{b_j}(t) \simeq (\mathbf{F}_{N_j, N_j} \otimes \mathbf{I}_{N_{b_j}})^T (\mathbf{F}_{N_j Z_j, B} \otimes \mathbf{I}_{N_{r_j}}) \tilde{\mathbf{z}}_j. \quad (173)$$

The final step in the reduced order modeling process is to enforce geometric compatibility along the inter-stage boundary, i.e. $\tilde{\mathbf{z}}_1 = \tilde{\mathbf{z}}_2$. The enforcement of the compatibility conditions is approximate, however, the compatibility conditions are well posed¹⁸⁰ as long as enough Fourier coefficients B are used.

Mistuning can be incorporated into each stage with CMM by using a method detailed by Lim et al..¹⁸⁵ In particular, for stiffness mistuning only, the reduced order stiffness matrix κ_j for the j^{th} stage can be written as

$$\kappa_j = \mathbf{\Lambda}_j + \sum_{n=1}^{N_j} \mathbf{q}_{j,n}^T \sum_{r \in R} (\delta \lambda_{r,n,j}^{CB}) \mathbf{q}_{j,n}, \quad (174)$$

where $\mathbf{\Lambda}$ is a matrix of tuned eigenvalues, $\mathbf{q}_{j,n}$ are modal participation factors, $\delta \lambda_{r,n,j}^{CB}$ is the difference in the r^{th} tuned and mistuned cantilevered blade eigenvalues for sector n of stage j , and R is a set of retained cantilever blade modes.

12.1.2 Classification of Multi-Stage Modes

In this section a new classification scheme for multi-stage modes is discussed to better understand the effects of mistuning and the effects of inter-stage coupling in multi-stage systems. Two factors are used to classify the modes of a multi-stage system. The first factor is the strain energy distribution. The strain energy E of the i^{th} mode of an entire multi-stage system can be calculated very easily and effectively in the ROM coordinates as $E_i = \phi_i^T \mathbf{K} \phi_i$, where \mathbf{K} is the multi-stage reduced order stiffness matrix, and ϕ_i is the i^{th} mass normalized eigenvector of the multi-stage system. A detailed derivation of the reduced order mass and stiffness matrix can be found in previous works.^{183,206} The corresponding energy in the j^{th} stage is given by $E_{ij} = \phi_{ij}^T \mathbf{K}_j \phi_{ij}$, where \mathbf{K}_j is the stiffness matrix for the j^{th} stage, and ϕ_{ij} is the portion of ϕ_i that corresponds to the j^{th} stage. The strain energy ratio for the i^{th} mode of stage 1 in a two stage system is given by

$$ER_{i1} = \frac{E_{i1}}{E_{i1} + E_{i2}}, \quad (175)$$

while for stage 2 it is

$$ER_{i2} = \frac{E_{i2}}{E_{i1} + E_{i2}}. \quad (176)$$

The two ratios ER_{i1} and ER_{i2} reflect the fractions of strain energy contained in each of the two stages.

The second factor used for classifying the modes of a multi-stage system is a form of the modal assurance criterion (MAC) number. The MAC number is a quantitative measure of the alignment of two modes. If the modes are parallel, the MAC number is one, and if the modes are orthogonal, the MAC number is zero. In this work, a variant of the MAC is used. Specifically, MAC_{ij} corresponds to the MAC number of the i^{th} mode of the j^{th} stage, and it is defined as

$$MAC_{ij} = \max_{k \in n_j} \sqrt{\frac{(\phi_{ij}^T \mathbf{M}_j \varphi_{kj})^2}{|\phi_{ij}^T \mathbf{M}_j \phi_{ij}| |\varphi_{kj}^T \mathbf{M}_j \varphi_{kj}|}}, \quad (177)$$

Mode Classification	Energy Distribution	Modal Alignment	Symbol
Stage 1 - single stage mode ($S1$)	$ER_1 > 0.9$	$MAC_1 > 0.9$	
Stage 1 - multi-stage mode (M_{S1})	$ER_1 > 0.9$	$MAC_1 < 0.9$	
Stage 2 - single stage mode ($S2$)	$ER_2 > 0.9$	$MAC_2 > 0.9$	
Stage 2 - multi-stage mode (M_{S2})	$ER_2 > 0.9$	$MAC_2 < 0.9$	
Multi-stage - double single stage mode ($M_{S1,S2}$)	$ER_1 < 0.9$ AND $ER_2 < 0.9$	$MAC_1 > 0.9$ AND $MAC_2 > 0.9$	
Multi-stage mode ($M_{1,2}$)	$ER_1 < 0.9$ AND $ER_2 < 0.9$	$MAC_1 < 0.9$ OR $MAC_2 < 0.9$	

Table 6

CLASSIFICATION OF SIX TYPES OF MODES USING THE ENERGY DISTRIBUTION AND MODAL ALIGNMENT.

where \mathbf{M}_j is the mass matrix of the j^{th} stage, φ_{kj} is the k^{th} *single stage* mode from the j^{th} stage, and n_j is the set of *single stage* modes within the ROM of the j^{th} stage that are within a particular frequency range. This frequency range is related to the i^{th} multi-stage frequency ω_i and the k^{th} single stage frequency ω_{kj} of stage j . The criteria is that the frequency of the single stage mode must be within a given tolerance ε of the multi-stage mode for the single stage and multi-stage modes to be compared, i.e.

$$\varepsilon \geq \frac{|\omega_i - \omega_{kj}|}{\omega_i} \times 100\%. \quad (178)$$

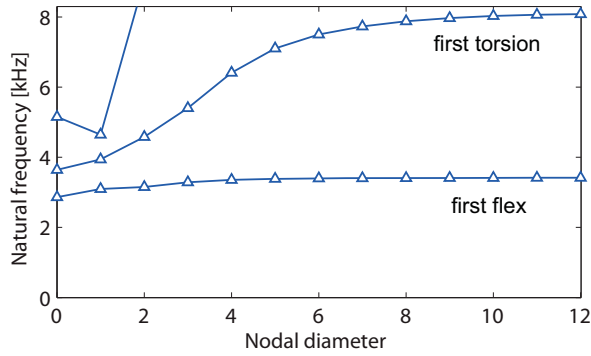
In this work the tolerance ε was set to 10%, which means that the single stage mode must be within 10% of the multi-stage mode in order for the modal alignment to be tested.

Using the information from Eqns. 175, 176 and 177, six types of modes are possible. Essentially, the energy ratio is used to classify the dominance of the mode as stage 1, stage 2, or multi-stage. Then, the MAC number is used to identify if the multi-stage mode is actually aligned with a corresponding single stage mode. A summary of these mode types is given in Tab. 6.

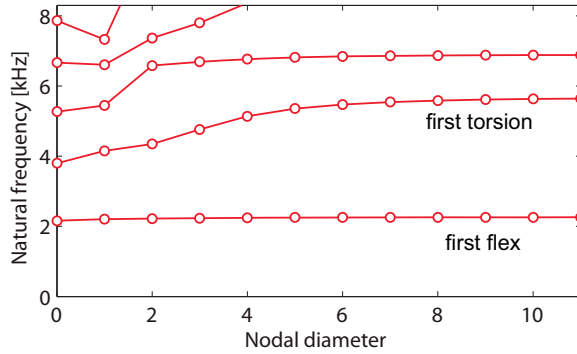
12.2 Analysis

Many ROMs were created using the methodology presented in the *Multi-Stage ROMs from Cyclic Stages* section herein. The system analyzed is a two stage rotor shown in Fig. 86. The first stage of the blisk contains 25 identical blades and the second stage contains 23 blades. Single stage analyses were conducted on each stage to obtain the frequency versus nodal diameter plots shown in Fig. 87. In the frequency range 0 – 8 kHz, there are two mode families for stage 1, and three mode families for stage 2.

The FEM of the multi-stage system contains 136, 488 DOFs, while each of the ROMs contains only 592 DOFs (0.5% of the original FE size). Each ROM uses 23 Fourier basis functions to model the dynamics at the interface between stages. Note that the full multi-stage FEM never needs to be assembled to create the ROMs in this work, it is only constructed for validation purposes. The ROMs were created from 1,000 different mistuning patterns applied to each stage with 20 different mistuning levels with standard deviations ranging from 0% to 10%. While the ROMs were developed to be valid (with respect to the full FEM) over a frequency



(a)



(b)

Fig. 87. NODAL DIAMETER VERSUS FREQUENCY PLOTS FOR (a) STAGE 1 AND (b) STAGE 2.

range of 0–20 kHz, the results below are focused on a narrower frequency range of 0–8 kHz. One mistuned ROM with a 4% standard deviation mistuning level was validated with respect to the FEM. The relative error of the ROM frequencies with respect to the FEM for the first 200 modes was less than 0.05%. Additionally, forced response calculations were carried out in the multi-stage frequency regime 2.8–3.4 kHz. The error at the peak responses was approximately 1% on both stages.

The first set of multi-stage results obtained is a classification of the tuned system modes of the multi-stage system using the criteria given in Tab. 6. The results are summarized in Fig. 88 for the first 120 modes. For Fig. 88(a), the x-axis is the eigenvalue index, while the y-axis is the multi-stage natural frequency. For Fig. 88(b), the x-axis is the eigenvalue index, while the y-axis is the energy ratio in stage 2 ER_2 (a value of 1 indicates that the energy is contained entirely in stage 2, while a value of 0 indicates that the energy is contained entirely in stage 1). For Fig. 88(c), the x-axis is again the eigenvalue index, while the y-axis is the relative frequency difference between modes computed for the multi-stage system and the corresponding modes computed for a single stage system. Note that for all multi-stage modes (M_{S1} , M_{S2} and $M_{1,2}$), no value is plotted because there is no single stage mode to compare with these multi-stage modes.

It is evident that there are a couple of narrow frequency ranges, e.g. 2–2.4 kHz and 6.5–7.0 kHz, where stage 2 only models may be used to model the *tuned* system dynamics. Whereas other regions tend to include a mixture of $S1$, $S2$, M_{S1} , and $M_{1,2}$ modes, which

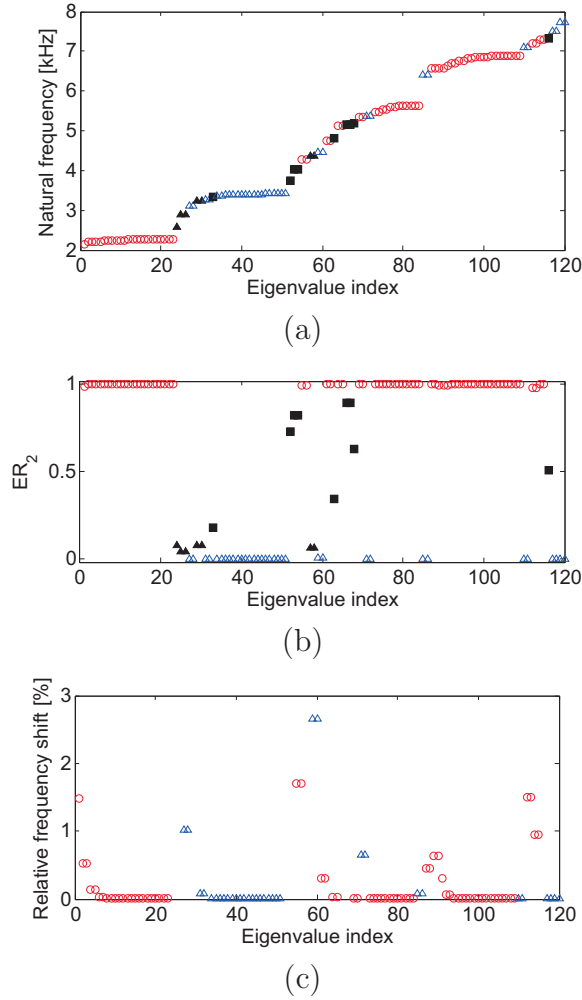


Fig. 88. (a) FREQUENCIES OF THE TUNED MULTISTAGE SYSTEM, (b) ENERGY RATIO IN THE CORRESPONDING MODES, AND (c) RELATIVE FREQUENCY DIFFERENCE BETWEEN THE MULTI-STAGE SYSTEM AND THE SINGLE STAGE SYSTEM MODES.

means that *these regions require a multi-stage analysis* to be valid.

Next we examine the effects of mistuning. Consider the mistuned results for 1,000 distinct mistuning patterns with a standard deviation of the mistuning of 5%. The results are presented in Fig. 89(a) with the same layout as in Fig. 88(a), with the tuned frequencies once again being plotted. All classification symbols are plotted for each index if that classification occurs for at least one mistuning pattern. In Fig. 89(b), the corresponding probability for each classification at each eigenvalue index is plotted. This figure shows the very complex interactions and possibilities that exist when dealing with statistical distributions of mistuning patterns in multi-stage systems. For example, consider the narrow frequency ranges 2 – 2.4 kHz and 6.5 – 7.0 kHz where single stage analyses can be used for the *tuned* system. For mistuned systems, in these ranges there is approximately a 20% chance that some of the modes are multi-stage M_{S2} modes. Outside of those narrow frequency ranges even more complex interactions occur which lead to a probability of the creation M_{S1} , M_{S2} , $M_{S1,S2}$, and $M_{1,2}$ modes.

To investigate the effects of mistuning on the multi-stage system, the alignment of each

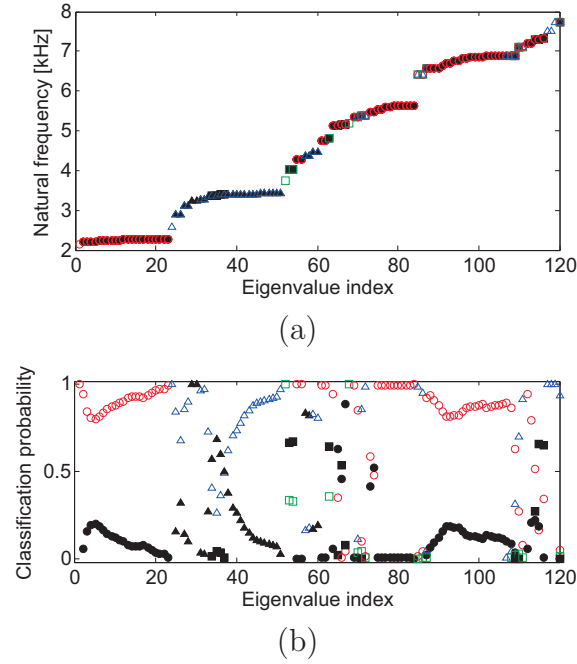


Fig. 89. (a) FREQUENCIES OF THE MISTUNED MULTISTAGE SYSTEM AND (b) THE PROBABILITY OF THE CLASSIFICATION OF THE CORRESPONDING MODES.

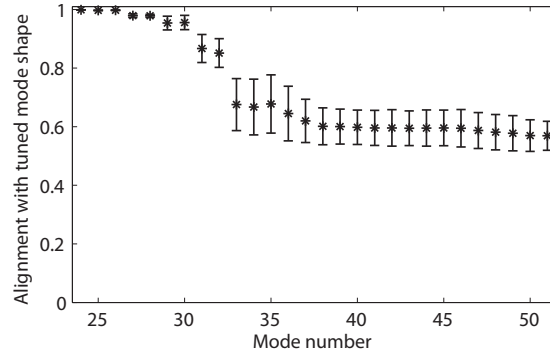


Fig. 90. ALIGNMENT OF MISTUNED MULTI-STAGE MODES WITH TUNED MULTI-STAGE MODES.

mistuned multi-stage mode with its corresponding tuned multi-stage mode was also calculated. The results for the modes in the frequency range 2.5 – 3.5 kHz are plotted in Fig. 90. The mistuning level was 5% and 1,000 different mistuning patterns were simulated. Average alignments and standard deviation bars are plotted in Fig. 90. The alignment is calculated in the reduced space between mass normalized tuned and mistuned eigenvectors using the MAC number. One can observe that the more isolated modes (23 – 27) have a much greater mistuned-tuned alignment than the rest of the modes in this mode family. That is consistent with the intuitive observation that the mistuned modes in the flat region of a mode family can change shape (compared to their tuned versions) more than other modes.

To better understand the results presented in Fig. 88 and Fig. 89, forced response calculations were conducted. A structural damping of the form $j\gamma\mathbf{K}$ was used, where $j = \sqrt{-1}$, $\gamma = 0.002$, and \mathbf{K} is the stiffness matrix. Also, forces were applied at the tip of the blades with specified engine order excitations, and the maximum response of the excited nodes was collected as

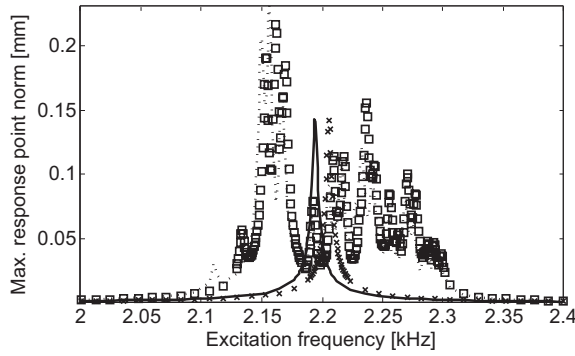
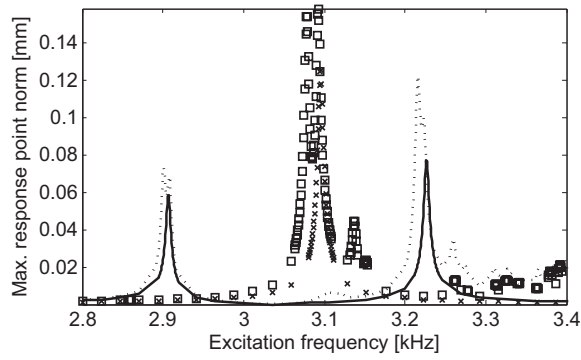


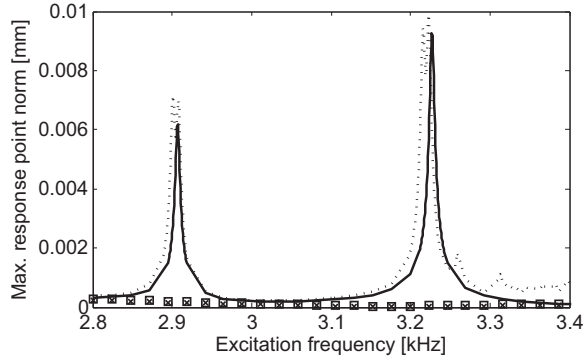
Fig. 91. FORCED RESPONSE OF STAGE 2 FOR A SET OF STAGE 2 DOMINATED MODES, WHICH ARE S_2 WHEN TUNED AND M_{S_2} WHEN MISTUNED (TUNED SINGLE STAGE ANALYSIS [x], TUNED MULTI-STAGE ANALYSIS [-], MISTUNED SINGLE STAGE ANALYSIS [□], AND MISTUNED MULTI-STAGE ANALYSIS [...]).

the maximum forced response. These tip nodes were used for the forced response because the dominant motion on both stages is due to the first flexural modes (see Fig. 87 and Fig. 88) from both stages for the range of frequencies investigated. First an engine order 1 excitation was applied at 512 evenly sampled frequencies from 2 kHz to 2.4 kHz. The y-axis of the plot corresponds to the maximum response of the excited nodes. Figure 91 shows the forced response of stage 2 for four cases. The first case is when a single stage analysis is conducted on the tuned stage 2. The second case is when a multi-stage analysis is conducted on the tuned multi-stage system. The third case is when a single stage analysis is conducted on a mistuned stage 2. The final case is a multi-stage analysis of the mistuned multi-stage system. The tuned single and tuned multi-stage results have a very similar magnitude with just a shift in frequency location, which agrees with the results presented in Fig. 88 (which shows that the MAC is greater than 0.9 over the entire frequency range). Note, due to the difference in frequency between the single and the multi-stage modes (shown in Fig. 88(c)), a slight shift in frequency for the largest responses is to be expected. The mistuned single stage and multi-stage analyses do not match as well as the tuned analyses. They contain significant differences in amplitude and location of peaks. This agrees with Fig. 89 since a mistuning pattern was chosen which would have at least one M_{S_2} mode in the frequency range of interest. This means that at least one MAC number is less than 0.9 in the frequency range of interest, and therefore the single stage modes are no longer aligned with the modes of the multi-stage system over this frequency range. Additionally, the results for stage 1 are not plotted since for all four cases the amplitude of vibration is very low, which is to be expected because $ER_1 < 0.1$ for all modes in the frequency range for all four cases. This highlights that a mode of a multi-stage system can be energetically contained to a single stage and yet may still be significantly different than a single stage mode. Hence, multi-stage calculations must be performed to accurately predict the response of such systems.

Forced response simulations were also conducted at 1,024 evenly spaced points from 2.8 – 3.4 kHz using an engine order 1 excitation. As can be seen from Fig. 88 and Fig. 89 the modes in this frequency range are characterized as stage 1 dominated modes (S_1 and M_{S_1}) and multi-stage modes ($M_{1,2}$). The results for these simulations are presented in Fig. 92 (and the four cases are the same as the ones presented in Fig. 91). Due to important multi-stage effects there is a significant response in both stages. The single stage analyses (tuned and mistuned) cannot capture these multi-stage effects. In Fig. 92(b), the single stage analyses



(a)



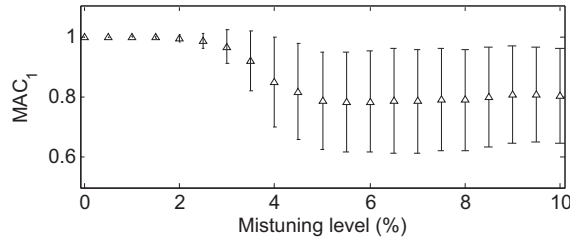
(b)

Fig. 92. FORCED RESPONSE FOR A SET OF S_1 , M_{S_1} , AND $M_{1,2}$ MODES FOR (a) STAGE 1 AND (b) STAGE 2 (TUNED SINGLE STAGE ANALYSIS [x], TUNED MULTI-STAGE ANALYSIS [-], MISTUNED SINGLE STAGE ANALYSIS [\square], AND MISTUNED MULTI-STAGE ANALYSIS [...]).

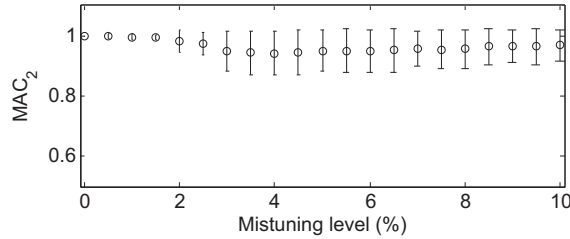
(both tuned and mistuned) predict almost no motion over this frequency range, but the multi-stage analyses (both tuned and mistuned) show that there is considerable motion. In Fig. 92(a), there is motion predicted by the single stage analyses (which is to be expected since single stage dominated modes are present), but the magnitude and frequency are not accurate. Hence, multi-stage calculations are certainly required.

The results in Fig. 92 indicate when the multi-stage analyses (versus single stage analyses) are of primary importance for both tuned and mistuned systems. In contrast, Fig. 91 shows that single stage analyses are valid for tuned systems (with just a slight frequency shift). However, single stage analyses are not valid for arbitrary mistuned systems. To predict the validity of single stage versus multi-stage and tuned versus mistuned analyses one must use Figs. 88 and 89.

A key parameter that affects both the classification of modes and the forced response of the system is the level of mistuning. Figure 93 explores the effect of the mistuning level on the multi-stage mode classification. Figure 93(a) is a plot of MAC_1 versus mistuning level for mode 36 (a stage 1 dominated mode) for 100 mistuning patterns with average and standard deviation bars plotted. Figure 93(b) is a plot of MAC_2 versus mistuning level for mode 6 (a stage 2 dominated mode) for 100 mistuning patterns with average and standard deviation bars plotted. The deviations for mode 36 are larger than for mode 6, which is to be expected



(a)



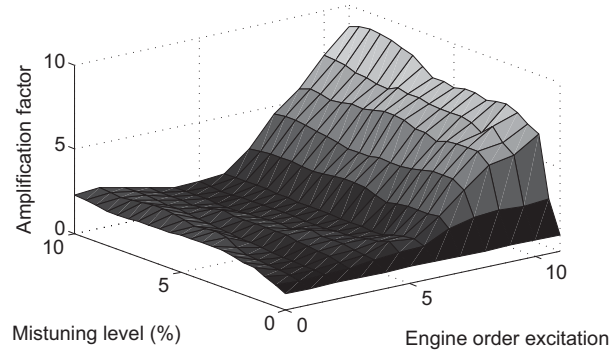
(b)

Fig. 93. MAC NUMBER VERSUS MISTUNING LEVEL FOR (a) MODE 36 [S_1 , M_{S1}] AND (b) MODE 6 [S_2 , M_{S2}] (ERROR BARS INDICATE THE STANDARD DEVIATION OF THESE VALUES FOR 100 MISTUNING PATTERNS).

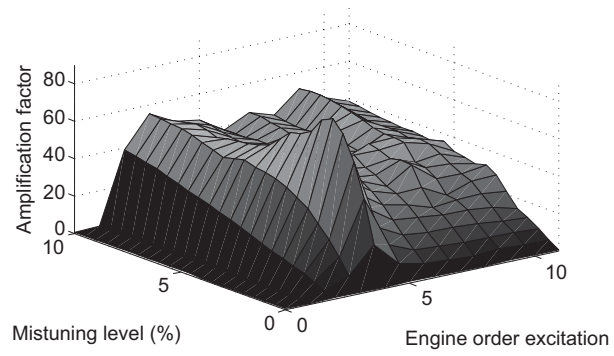
since (from Fig. 89(b)) mode 36 has a 60% chance of changing from S_1 to M_{S1} at a 5% mistuning level, whereas mode 6 has only an 18% chance of changing from S_2 to M_{S2} . Also, as expected, initially the deviations in the MAC number for both modes increases while the actual average MAC number decreases as the mistuning level increases. However, it is interesting to note that the average MAC numbers and the deviations in the MAC number level off at around 4 – 5% standard deviation in the mistuning level.

Figure 94 contains amplification factor plots for stage 1 and 2 of the 99th percentile response of 100 mistuning patterns for engine order excitation 0 to 11 and mistuning levels from 0% to 10% over the frequency range 2.8 – 3.4 kHz. One hundred separate forced response calculations were performed at each unique mistuning level and engine order excitation combination. In this case, the amplification factor for each stage is defined as the number that when multiplied by the tuned response at a given engine order excitation would give the 99th percentile maximum response for this set of mistuning patterns.

The results in Fig. 94 show that stage 2 has a much larger amplification factor than stage 1. This does not mean that the response of stage 2 is larger, in fact it is an order of magnitude lower. The actual 99th percentile response for these mistuning patterns for stage 1 and 2 are shown in Fig. 95. Note that the motion at lower engine order excitations is larger than at higher engine order excitations. This is likely due to the the multi-stage region moving from one family of stage 2 dominated modes to stage 1 dominated modes (see Figs. 87 and 88). This region relates to nodal diameters 0, 1 and 2 (of stage 1) and also corresponds to a kind of veering region where blade and disk motion are coupled, which leads to larger responses.



(a)



(b)

Fig. 94. FORCE AMPLIFICATION FACTOR VERSUS MISTUNING LEVEL AND ENGINE ORDER EXCITATION FOR THE MULTI-STAGE SYSTEM FOR (a) STAGE 1 AND (b) STAGE 2.

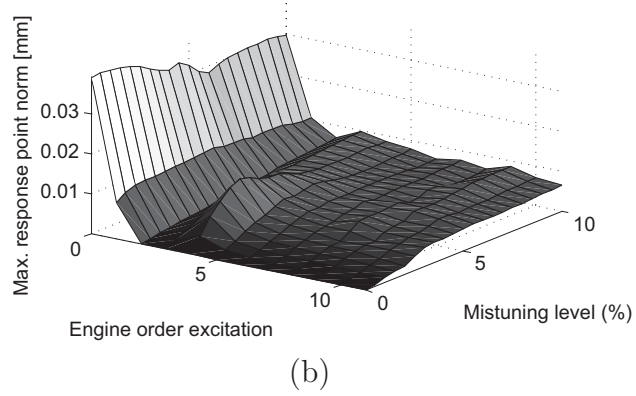
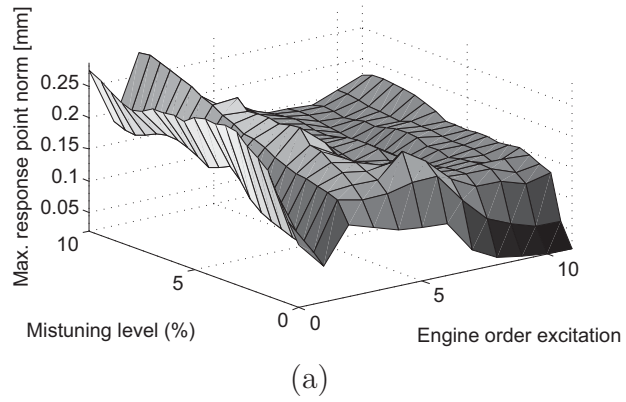


Fig. 95. MAXIMUM FORCE RESPONSE VERSUS MISTUNING LEVEL AND ENGINE ORDER EXCIATION FOR THE MULTI-STAGE SYSTEM FOR (a) STAGE 1 AND (b) STAGE 2.